

FLAME RETARDANCY OF POLYMER NANOCOMPOSITES

A THESIS SUBMITTED TO
THE GRADUATE SCHOOL OF NATURAL AND APPLIED SCIENCES
OF
MIDDLE EAST TECHNICAL UNIVERSITY

BY

NIHAT ALI İŞİTMAN

IN PARTIAL FULFILLMENT OF THE REQUIREMENTS
FOR
THE DEGREE OF DOCTOR OF PHILOSOPHY
IN
METALLURGICAL AND MATERIALS ENGINEERING

MARCH 2012

Approval of the thesis:

FLAME RETARDANCY OF POLYMER NANOCOMPOSITES

submitted by **NİHAT ALİ İŞİTMAN** in partial fulfillment of the requirements for the degree of **Doctor of Philosophy in Metallurgical and Materials Engineering, Middle East Technical University** by,

Prof. Dr. Canan Özgen
Dean, Graduate School of **Natural and Applied Sciences**

Prof. Dr. Tayfur Öztürk
Head of Department, **Metallurgical and Materials Eng.**

Prof. Dr. Cevdet Kaynak
Supervisor, **Metallurgical and Materials Eng. Dept., METU**

Examining Committee Members:

Prof. Dr. Erdal Bayramlı
Chemistry Dept., METU

Prof. Dr. Cevdet Kaynak
Metallurgical and Materials Eng. Dept., METU

Prof. Dr. Necati Özkan
Polymer Science and Technology Dept., METU

Assoc. Prof. Dr. Arcan F. Dericioğlu
Metallurgical and Materials Eng. Dept., METU

Assoc. Prof. Dr. Güralp Özkoç
Chemical Engineering Dept., Kocaeli University

Date : 02-March-2012

I hereby declare that all information in this document has been obtained and presented in accordance with academic rules and ethical conduct. I also declare that, as required by these rules and conduct, I have fully cited and referenced all material and results that are not original to this work.

Name, Last Name: **NIHAT ALI İŞİTMAN**

Signature:

ABSTRACT

FLAME RETARDANCY OF POLYMER NANOCOMPOSITES

Işıtman, Nihat Ali

Ph.D., Department of Metallurgical and Materials Engineering

Supervisor: Prof. Dr. Cevdet Kaynak

March 2012, 255 pages

This thesis is aimed to understand the role of nanofiller type, nanofiller dispersion, nanofiller geometry, and, presence of reinforcing fibers in flame retardancy of polymer nanocomposites. For this purpose, montmorillonite nanoclays, multi-walled carbon nanotubes, halloysite clay nanotubes and silica nanoparticles were used as nanofillers in polymeric matrices of poly (methyl methacrylate) (PMMA), high-impact polystyrene (HIPS), polylactide (PLA) and polyamide-6 (PA6) containing certain conventional flame retardant additives. Furthermore, the influence of nanofiller and flame retardant additives on fiber/matrix interfacial interactions was studied.

Materials were prepared by twin-screw extrusion melt-mixing and ultrasound-assisted solution-mixing techniques. Characterization of nanocomposite morphology was done by X-ray diffraction and transmission electron microscopy. Flame retardancy was investigated by mass loss cone calorimetry, limiting oxygen index measurements and UL94 standard tests. Flame retardancy mechanisms were revealed by characterization of solid fire residues by scanning electron microscopy, transmission electron microscopy, infrared spectroscopy and X-ray diffraction. Thermal degradation and stability was studied using thermogravimetric analysis. Mechanical properties were determined by tension tests and fracture surfaces were observed under scanning electron microscope.

Influence of nanofiller type was investigated comparing the behavior of montmorillonite nanoclay and multi-walled carbon nanotube reinforced PMMA nanocomposites containing phosphorous/nitrogenous intumescent flame retardant. Carbon nanotubes hindered the formation of intumescent inorganic phosphate barrier which caused the samples to be exposed to larger effective heat fluxes during combustion. Contrarily, nanoclays physically reinforced the protective barrier without disrupting the intumescent character, thereby allowing for lower heat release and mass loss rates, and increased amounts of residue upon combustion.

Influence of nanofiller dispersion was studied comparing nanocomposite and microcomposite morphologies in montmorillonite nanoclay reinforced HIPS containing aluminum hydroxide flame retardant. Relative to microcomposite morphology, reductions in peak heat release rates were doubled along with higher limiting oxygen index and lower burning rates with nanocomposite formation. Improved flame retardancy was attributed to increased amounts of char residue and lower mass loss rates. Nanocomposite formation allowed for the recovery of tensile strength reductions caused by high loading level of the conventional flame retardant additive in polymer matrix.

Influence of nanofiller geometry was investigated for phosphorus based intumescent flame-retarded PLA nanocomposites. Fire performance was increased in the order of rod-like (1-D) < spherical (0-D) << plate-like (2-D) geometries which matched qualitatively with the effective surface area of nanoparticles in the nanocomposite. Well-dispersed plate-like nanoparticles rapidly migrated and accumulated on exposed sample surface resulting in the formation of strong aluminum phosphate/montmorillonite nanocomposite residue. Mechanical properties were increased in the order of 0-D < 1-D < 2-D nanofillers corresponding to the order of their effective aspect ratios in the nanocomposite.

Influence of fiber reinforcement was studied for montmorillonite nanoclay containing short-glass fiber-reinforced, phosphorus/nitrogen based flame-retarded PA6 composites. Substitution of a certain fraction of conventional additive with nanofiller significantly reduced peak heat release rate, delayed ignition and improved

limiting oxygen index along with maintained UL94 ratings. Improved flame retardancy was ascribed to the formation of a nanostructured carbonaceous boron/aluminum phosphate barrier reinforced by well-dispersed montmorillonite nanolayers.

Fiber/matrix interfacial interactions in flame-retarded PA6 and HIPS containing nanoclays were investigated using a micromechanical approach, and it was found that the influence of nanoclay on the interface depends on crystallinity of polymer matrix. While the fiber/matrix interfacial strength is reduced with nanoclay incorporation into amorphous matrix composites, significant interfacial strengthening was imparted by large surface area, well-dispersed clay nanolayers acting as heterogeneous nucleation sites for the semi-crystalline matrix.

Keywords: polymer matrix nanocomposite, flame retardancy, thermal degradation, mechanical properties

ÖZ

POLİMER NANOKOMPOZİTLERİN ALEVLENME DAYANIMI

Işıtman, Nihat Ali

Doktora, Metalurji ve Malzeme Mühendisliği Bölümü

Tez Yöneticisi: Prof. Dr. Cevdet Kaynak

Mart 2012, 255 sayfa

Bu tezin amacı, nanoparçacık tipi, nanoparçacık dağılımı, nanoparçacık geometrisi ve elyaf takviyesinin, alev geciktiricili polimer nanokompozitlerin alevlenme dayanımına etkisini incelemektir. Bu kapsamda montmorillonit nanokiller, çok-duvarlı karbon nanotüpler, halosit kil nanotüpler ve silika nanoparçacıklar ile çeşitli alev geciktirici katkı malzemeleri arasındaki etkileşimler poli(metil metakrilat) (PMMA), darbe dayanımlı polistiren (HIPS), polilaktik asit (PLA) ve Poliamid-6 (PA6) matris termoplastikleri kullanılarak incelenmiştir. Kısa cam elyaf takviyeli PA6 kompozitlerde ise montmorillonit nanokil ve alev geciktirici katkının elyaf/matris arayüzey mukavemetine etkisi araştırılmıştır.

İncelenen polimer nanokompozitler, ultrason yardımıyla çözeltide karıştırma ve çift vidalı ekstrüzyon ile eriyik halinde karıştırma yöntemleriyle üretilmiştir. Nanokompozitlerin morfoloji ve dağılımı, X-ışınları kırınımı ve geçirimli elektron mikroskobu ile incelenmiş, alevlenme dayanımı ise kütle kaybı konik kalorimetre yangın testleri, limit oksijen indeksi ölçümleri ve UL94 standart yanma testleri ile belirlenmiştir. Alevlenme dayanımı mekanizmaları, yanma sonrası elde edilen küllerin taramalı elektron mikroskobu, geçirimli elektron mikroskobu, X-ışınları kırınımı ve infrared spektroskopisi analizleri ile açığa çıkarılmıştır. Malzemelerin ısıl kararlılık ve bozunma davranışları termogravimetrik analizler ile incelenmiştir. Mekanik özellikler çekme testleri ile belirlenmiş, kırılma yüzeyleri ise taramalı elektron mikroskobu ile incelenmiştir.

Nanoparçacık tipinin alevlenme dayanımına etkisinin incelendiği montmorillonit nanokiller ve çok-duvarlı karbon nanotüpler içeren fosfor/azot tabanlı alev geciktiricili PMMA nanokompozitlerde, karbon nanotüpler yanma esnasında katı fazda oluşan inorganik kül tabakasının oluşmasını engellemiş ve malzemenin maruz kaldığı efektif ısı akısını yükselterek yangın direncini kayda değer oranda düşürmüştür. Diğer taraftan, nanokiller koruyucu kül tabakasını yapısal olarak güçlendirmiş ve ısı salım hızı, kütle kaybı hızı ve kül miktarı gibi değerleri yükselterek malzemenin yangın direncini arttırmıştır.

Nanokil dağılımının etkisinin incelendiği alüminyum hidroksit alev geciktiricili HIPS karışımlarında, nanokompozit morfolojinin mikrokompozit morfolojiye kıyasla alevlenme dayanımı performansının yaklaşık iki kat üstün olduğu belirlenmiştir. Bu, nanokillerin iyi dağılımı sayesinde etkinleşen bariyer mekanizması ile düşük kütle kaybı hızı elde edilmesine bağlanmıştır. Nanokompozit oluşumu sayesinde alüminyum hidroksit alev geciktiricinin sebep olduğu mukavemet kaybının geri kazanılabileceği gösterilmiştir.

Nanoparçacık geometri etkisinin incelendiği fosfor tabanlı alev geciktiricili PLA nanokompozitlerde, nanoparçacık/polimer matris arayüzey miktarına paralel olarak yangın performansı çubuksu (1-D) < küresel (0-D) << levhamsı (2-D) nanoparçacıklar şeklinde artmıştır. İki boyutlu nanoparçacıklar, matris içerisinde iyi dağılım göstermeleri sayesinde yanma esnasında hızlı biçimde malzeme yüzeyine taşınarak yapısal olarak güçlü bir alüminyum fosfat/kil nanokompozit kül tabakası oluşumu gerçekleşmiştir. Mekanik özellikler ise takviye malzemesinin matris içerisindeki efektif boy/en oranına paralel olarak 0-D < 1-D < 2-D nanoparçacıklar şeklinde yükselmiştir.

Kısa cam elyaf takviyeli, fosfor/azot tabanlı alev geciktiricili PA6 nanokompozitlerin alevlenme dayanımının incelendiği çalışmada, nanokillerin belirli oranlarda alev geciktirici katkının yerine kullanılmasıyla ısı salım hızının azaldığı, tutuşma süresi ve oksijen indeksinin yükseldiği ve UL94 yanmazlık değerlerinin korunabildiği gösterilmiştir. Bu çalışmada nanokiller ile artan yangın direnci, yanma esnasında

oluşan karbonlu bor/alüminyum fosfat tabakasının matris içerisinde iyi dağılmış nanokil tabakaları ve kısa cam elyaflar tarafından güçlendirilmesine bağlanmıştır.

Alev geciktiricili PA6 ve HIPS nanokompozitlerde elyaf/matris arayüzey etkileşimleri, geliştirilen bir mikromekanik yaklaşımla irdelenmiş, nano-boyutlu katkı malzemesinin arayüzeye etkisinin kullanılan termoplastik matrisin kristallenebilme yeteneğine bağlı olduğu anlaşılmıştır. Kristallenmeyen polimer matriste nanokillerin varlığında elyaf/matris arayüzey mukavemeti azalırken, kristallenebilen matriste geniş yüzey alanına sahip nano-düzeyde dağılmış kil tabakalarının heterojen çekirdeklenme bölgeleri oluşturması ile matrisin kristallenme derecesini yükselterek elyaf/matris arayüzeyini güçlendirebileceği gösterilmiştir.

Anahtar Kelimeler: polimer matris nanokompozit, morfoloji, alevlenme dayanımı, ısıl bozunma, mekanik özellikler

To My Parents

ACKNOWLEDGEMENTS

This thesis would not have been successful without the support and guidance of my supervisor Prof. Dr. Cevdet Kaynak. I am grateful that he always appreciated and encouraged my enthusiasm to work independently and make extensive research collaborations. I would also like to express my gratitude to my thesis supervising committee members Prof. Dr. Necati Özkan and Assoc. Prof. Dr. F. Arcan Dericiođlu, as well as Prof. Dr. Jale Hacalođlu, Prof. Dr. Erdal Bayramlı and Assoc. Prof. Dr. Gralp zko for their significant contributions to this thesis.

Behind every great man is an even greater woman. I owe my deepest gratitude to Nagehan Duman for devoting herself to supporting me. I am grateful to Muratahan Aykol, former laboratory mate Hseyin zgr Gndz and my colleagues Dr. Mehmet Dogan and Őebnem Kemalođlu for their endless friendship and research collaboration. I sincerely acknowledge my friends; Serhat n, Mehmet Yldırım, zlem Altıntaş Yldırım and Halil İbrahim Yavuz.

It is my pleasure to thank Dr. Selda Keskin, Serkan Yılmaz, Cengiz Tan, Necmi Avcı, Osman Yaslıtaş, Hlya Yalın and nder Őahin who made this thesis possible by their assistance in testing, characterization and analysis. I am also thankful to METU Metallurgical Engineering Department and METU Central Laboratory for providing the facilities for my research.

I would also like to acknowledge Scientific and Technological Research Council of Turkey (TUBITAK; Grant No: MAG-107M347 and National Scholarship Program for PhD Students), National Boron Research Institute (BOREN, Grant No: 2009--0236) and METU-BAP research grants for their financial support.

TABLE OF CONTENTS

ABSTRACT.....	iv
ÖZ.....	vii
ACKNOWLEDGEMENTS.....	xi
TABLE OF CONTENTS.....	xii
NOMENCLATURE.....	xvi
LIST OF TABLES.....	xix
LIST OF FIGURES.....	xxii
CHAPTERS	
1. INTRODUCTION.....	1
1.1 POLYMER NANOCOMPOSITES	1
1.2 FLAME RETARDANCY	6
1.2.1 Thermal Degradation and Combustion of Polymers.....	6
1.2.2 Evaluation of Flame Retardancy	9
1.2.3 Flame Retardancy Mechanisms	15
1.3 LITERATURE SURVEY	18
1.3.1 Studies on the Effect of Nanofiller Type	20
1.3.2 Studies on the Effect of Nanofiller Dispersion	20

1.3.3	Studies on the Effect of Nanofiller Geometry.....	21
1.3.4	Studies on the Effect of Fiber Reinforcement.....	22
1.3.5	Studies on Interfacial Interactions.....	22
1.4	AIM OF THE STUDY.....	23
2.	EXPERIMENTAL WORK.....	25
2.1	MATERIALS USED	25
2.1.1	Matrix Materials.....	25
2.1.2	Nanofillers.....	27
2.1.3	Flame Retardants.....	29
2.1.4	Fiber Reinforcement.....	29
2.2	PREPARATION OF SAMPLES.....	33
2.2.1	Melt Mixing	33
2.2.2	Solution Mixing	33
2.2.3	Shaping Processes	34
2.3	EVALUATION OF FLAME RETARDANCY.....	35
2.3.1	Mass Loss Cone Calorimeter Fire Testing.....	35
2.3.2	LOI and UL94 Flammability Testing	35
2.4	CHARACTERIZATION TECHNIQUES.....	36
2.4.1	Transmission Electron Microscopy.....	36
2.4.2	Scanning Electron Microscopy	36
2.4.3	X-Ray Diffraction	37

2.4.4	Thermal Analysis	37
2.4.5	Direct Pyrolysis Mass Spectrometry	37
2.4.6	Infrared Spectroscopy	38
2.4.7	Mechanical Testing	38
2.4.8	Fiber Length Distribution.....	38
3.	RESULTS AND DISCUSSION	39
3.1	EFFECT OF NANOFILLER TYPE	39
3.1.1	Nanomorphology	41
3.1.2	Flame Retardancy	50
3.1.3	Flame Retardancy Mechanisms by Residue Analysis	58
3.1.4	Flame Retardancy Mechanisms by Thermal Degradation.....	68
3.1.5	Thermal and Mechanical Properties.....	80
3.2	EFFECT OF NANOFILLER DISPERSION.....	85
3.2.1	Nanomorphology	87
3.2.2	Flame Retardancy	95
3.2.3	Flame Retardancy Mechanisms by Thermal Degradation.....	103
3.2.4	Flame Retardancy Mechanisms by Residue Analysis	106
3.2.5	Mechanical Properties.....	115
3.3	EFFECT OF NANOFILLER GEOMETRY	122
3.3.1	Nanomorphology	123
3.3.2	Flame Retardancy	128

3.3.3	Flame Retardancy Mechanisms by Thermal Degradation.....	133
3.3.4	Flame Retardancy Mechanisms by Residue Analysis	136
3.3.5	Mechanical Properties.....	151
3.4	EFFECT OF FIBER REINFORCEMENT	154
3.4.1	Nanomorphology	154
3.4.2	Flame Retardancy	157
3.4.3	Flame Retardancy Mechanisms by Thermal Degradation.....	168
3.4.4	Flame Retardancy Mechanisms by Residue Analysis	171
3.4.5	Mechanical Properties.....	183
3.5	INTERFACIAL INTERACTIONS	186
3.5.1	Micromechanical Modeling.....	186
3.5.2	Short Fiber Reinforced Amorphous Matrix Nanocomposites	193
3.5.3	Short Fiber Reinforced Semi-Crystalline Matrix Nanocomposites .	206
4.	CONCLUSIONS.....	217
	REFERENCES.....	226
	CURRICULUM VITAE.....	246

NOMENCLATURE

LOI	limiting oxygen index
HRR	heat release rate
MLR	mass loss rate
THE	total heat evolved
TTI	time to ignition
TML	total mass loss
FGI	fire growth index
FIGRA	fire growth rate
TIC	total ion current
FLD	fiber length distribution
XRD	x-ray diffraction
SEM	scanning electron microscopy
TEM	transmission electron microscopy
EDS	energy dispersive spectroscopy
FTIR	Fourier-transform infrared spectroscopy
TGA	thermogravimetric analysis
DTG	differential thermogravimetry
DSC	differential scanning calorimeter
DP-MS	direct pyrolysis mass spectrometry
PMMA	poly(methyl methacrylate)

PA6	polyamide-6
HIPS	high-impact polystyrene
PLA	polylactide
OP	organophosphorus
ATH	aluminum trihydroxide
ALPi	aluminum diethylphosphinate
GF	glass fiber
NC	nanoclay
CNT	carbon nanotube
MF	micro-filler
NF	nano-filler
$\sigma_c(\varepsilon)$	composite stress as a function of strain
σ_m^b	ultimate matrix stress at composite failure
σ_c^b	ultimate composite stress
$\sigma_c^{\text{exp}}(\varepsilon)$	experimental composite stress as a function of strain
$\sigma_m(\varepsilon)$	matrix stress as a function of strain
η_{FOD}	fiber orientation distribution factor
η_{FLD}	fiber length distribution factor
$\eta_{\text{FLD}}(\varepsilon)$	fiber length distribution factor as a function of strain
η_{FLD}^b	fiber length distribution factor at composite break strain
E_f	fiber tensile modulus
E_c	composite tensile modulus

E_m	matrix tensile modulus
ε	strain
ε_b	strain at break
V_f	volume fraction of fibers
ℓ_c	critical fiber length
d	fiber diameter
τ	interfacial shear strength
P_ℓ	probability density of fibers of length ℓ
K	scale parameter of Weibull function
n	shape parameter of Weibull function
$\Gamma(a)$	gamma function
$\Gamma(a,b)$	incomplete gamma function

LIST OF TABLES

TABLES

Table 2.1 Chemical structure of matrix materials.....	26
Table 2.2 Properties of Cloisite 10A and 30B organoclays.....	27
Table 2.3 Properties of multi-walled carbon nanotubes.....	28
Table 2.4 Properties of nanosilica.....	28
Table 2.5 Properties of halloysite nanotubes	28
Table 2.6 Chemical structures of the constituents of OP1312 flame retardant.....	30
Table 2.7 Properties of OP1312 flame retardant.....	31
Table 2.8 Properties of aluminum diethylphosphinate flame retardant.....	31
Table 2.9 Properties of aluminum hydroxide flame retardant	32
Table 2.10 Parameters used for mixing and shaping processes.....	34
Table 3.1 Designations, compositions (wt%) and utilized dispersion techniques to reveal the effect of nanofiller type	40
Table 3.2 Molecular weights of PMMA matrix after processing	41
Table 3.3 Calculated XRD data for PMMA/clay nanocomposites.....	42
Table 3.4 Limiting oxygen index values showing the effect of nanofiller type	50
Table 3.5 Interpreted mass loss calorimeter data showing the effect of nanofiller type	52

Table 3.6 Results of thermogravimetric analysis showing the effect of nanofiller type	69
Table 3.7 DTG data for deconvoluted degradation steps showing the effect of nanofiller type	72
Table 3.8 Glass transition temperatures and ΔC_p of glass transition of PMMA nanocomposites with different nanofiller types	82
Table 3.9 Mechanical properties of neat- and flame-retarded PMMA nanocomposites with different nanofiller types	83
Table 3.10 Designations, compositions (wt.%) and utilized preparation techniques to reveal the effect of nanofiller dispersion	86
Table 3.11 Mass loss calorimeter performance of specimens showing the effect of nanofiller dispersion	98
Table 3.12 Thermogravimetric and differential thermogravimetric data revealing the effect of nanofiller dispersion	105
Table 3.13 Designations and compositions (wt.%) of studied materials to reveal the effect of nanofiller geometry	122
Table 3.14 Interpreted mass loss calorimeter data showing the effect of nanofiller geometry	131
Table 3.15 Results of flammability tests (LOI and UL-94) showing the effect of nanofiller geometry	132
Table 3.16 Results of thermogravimetric analysis revealing the effect of nanofiller geometry	134
Table 3.17 Mechanical properties of PLA nanocomposites with different nanofiller geometries	152
Table 3.18 Designations and compositions (wt%) of studied samples to investigate the effect of fiber reinforcement	155

Table 3.19 Results of flammability tests showing the effect of fiber reinforcement	158
Table 3.20 Interpreted mass loss calorimeter data showing the effect of fiber reinforcement	165
Table 3.21 Thermogravimetric and differential thermogravimetric data of flame-retarded glass fiber reinforced PA6 nanocomposites.....	170
Table 3.22 Designation and compositions (wt.%) of studied materials to reveal the influence of micro- and nano-fillers on interfacial interactions.....	200
Table 3.23 Designations and compositions (wt.%) of studied materials.....	207
Table 3.24 Estimated micromechanical parameters.....	210
Table 3.25 Degree of crystallinity and relative amounts of crystalline phases.....	215

LIST OF FIGURES

FIGURES

Figure 1.1 Different states of nanodispersion and nanomorphology in polymer/clay nanocomposites	4
Figure 1.2 Fire triangle and combustion cycle of polymers [17].....	8
Figure 1.3 Schematic of limiting oxygen index apparatus.....	10
Figure 1.4 Schematic of UL-94 test apparatus.....	11
Figure 1.5 Schematic of the mass loss calorimeter	14
Figure 1.6 A typical mass loss calorimeter curve showing important fire parameters	14
Figure 3.1 XRD patterns of neat- and flame-retarded PMMA/clay nanocomposites	43
Figure 3.2 Gaussian peak deconvolution of XRD profile recorded from NC-PMMA/OP9 sample	43
Figure 3.3 Effect of thermal degradation on clay interlayer spacings; (a) pristine nanoclay, (b) 10 min. at 240°C, (c) 30 min. 240°C, and (d) 1 h at 700°C.....	44
Figure 3.4 TEM micrographs of fully intercalated particles in NC-PMMA nanocomposite; (a) general and (b) closer view of intercalated clay mineral particles	46
Figure 3.5 TEM micrographs of NC-PMMA/OP9 nanocomposite (a) showing partial polymer intercalation and (b) a closer view of partially intercalated aggregate	47
Figure 3.6 (a) and (b) SEM images showing bundles and ropes of as-received multi-walled carbon nanotubes prior to ultrasound-assisted solution mixing	48

Figure 3.7 (a) TEM image of de-bundled carbon nanotubes well-dispersed in PMMA matrix (b) larger magnification TEM image of carbon nanotubes in PMMA	49
Figure 3.8 Effects of nanofillers and organophosphorus flame retardant additive on the heat release behavior of PMMA.....	57
Figure 3.9 Effects of nanofillers on the heat release and mass loss behavior of flame-retarded PMMA	57
Figure 3.10 Appearance of the whole surfaces of mass loss calorimeter fire residues from PMMA with different nanofillers.....	58
Figure 3.11 SEM micrographs of the char residue from CNT-PMMA nanocomposite; (a) general and (b) closer view images	59
Figure 3.12 SEM images of the char residue from NC-PMMA nanocomposite; (a) general and (b) closer view images.....	60
Figure 3.13 ATR-FTIR spectra, XRD patterns and photographs of fire residues showing the effect of nanofiller type	62
Figure 3.14 (a-b) SEM images and (c) energy dispersive spectrum of mass loss calorimeter residue from PMMA/OP18 sample.	64
Figure 3.15 (a-c) SEM images and (d) energy dispersive spectrum of mass loss calorimeter residue from CNT-PMMA/OP18 sample	66
Figure 3.16 (a-c) SEM images and (d) energy dispersive spectrum of mass loss calorimeter residue from NC-PMMA/OP18 sample.....	67
Figure 3.17 Thermogravimetric mass loss curves showing the effects of different nanofillers on the thermal stabilities of neat- and flame-retarded PMMA	69
Figure 3.18 Deconvoluted differential thermogravimetric curves showing the effect of nanofiller type.....	71
Figure 3.19 Total ion current as a function of temperature obtained by direct pyrolysis mass spectroscopy	75

Figure 3.20 Selected single ion evolution profiles obtained by direct pyrolysis mass spectroscopy	76
Figure 3.21 Determination of glass transition parameters (T_g and ΔC_p)	80
Figure 3.22 DSC heat flow curves of nanocomposites based on neat- and flame-retarded PMMA with different nanofillers	82
Figure 3.23 SEM images of tensile fracture surfaces; (a) PMMA/OP, (b) CNT-PMMA/OP, (c) NC-PMMA/OP	84
Figure 3.24 (a) and (b) TEM micrographs of solution intercalated nanocomposites based on neat HIPS (<i>s</i> -NC)	88
Figure 3.25 (a) and (b) TEM micrographs of solution intercalated nanocomposites based on HIPS with 35 wt% aluminum tri-hydroxide (<i>s</i> -NC/35ATH).....	89
Figure 3.26 XRD patterns of solution intercalated nanocomposites based on neat HIPS and HIPS with various levels of ATH.....	91
Figure 3.27 TEM micrographs of nanoclay containing melt-mixed HIPS/clay (<i>m</i> -NC) showing phase-separated microcomposite morphology; (a) low and (b) high magnification images	93
Figure 3.28 XRD patterns of clay containing melt-mixed HIPS and HIPS/ATH; (a) <i>m</i> -NC and <i>m</i> -NC/ATH samples, (b) organoclay and degraded organoclay.....	94
Figure 3.29 Influence of nanoclay dispersion state on the peak heat release rate and char residues in the mass loss calorimeter.....	96
Figure 3.30 Influence of nanoclay dispersion state on the mass loss behaviors of (a) HIPS and (b) HIPS/ATH in the mass loss calorimeter	99
Figure 3.31 Mass loss behavior during combustion in the mass loss calorimeter ...	100
Figure 3.32 (a) Limiting oxygen index values and (b) linear burning rates in UL94 tests showing the effects of flame retardant content and nanofiller dispersion	102

Figure 3.33 Thermogravimetric curves with nanoclay dispersion states of;	104
Figure 3.34 XRD patterns elucidating the decomposition path of ATH and ATH/NC powder mixtures upon annealing	105
Figure 3.35 XRD patterns comparing (a) s-NC/25ATH residue, (b) s-25ATH residue and (c) ATH annealed at 590 °C	107
Figure 3.36 XRD patterns showing montmorillonite interlayer spacings in mass loss calorimeter residues	107
Figure 3.37 (a-c) SEM images and (d) energy dispersive spectra of fire residue from phase-separated microcomposite	109
Figure 3.38 (a-b) SEM images and (c) energy dispersive spectrum of mass loss calorimeter residue from intercalated nanocomposite	110
Figure 3.39 SEM images and energy dispersive spectra of fire residues from (a) HIPS/25ATH, (b-c) phase separated microcomposite based on HIPS/25ATH, and (d-e) intercalated nanocomposite based on HIPS/25ATH	111
Figure 3.40 ATR-FTIR spectra of combustion residues from (a) flame-retarded HIPS and (b) flame-retarded HIPS/organoclay nanocomposite	113
Figure 3.41 Mechanical properties as a function of the nanoclay dispersion state	116
Figure 3.42 Electron back-scattering images of the fracture surface of aluminum trihydroxide flame-retarded high-impact polystyrene; (a) general and (b) closer views	118
Figure 3.43 (a-b) SEM images and (c) elemental mapping of the fracture surface of phase-separated microcomposite	119
Figure 3.44 (a-c) SEM images and (d) Si mapping of the fracture surface of intercalated nanocomposite	120
Figure 3.45 A comparison of the tensile behavior of HIPS/clay nanocomposite and conventional short-glass fiber-reinforced HIPS	121

Figure 3.46 SEM micrographs of nanofillers with different geometries; (a) 0-D nanosilica, (b) 1-D rod-like halloysite, (c) 2-D plate-like montmorillonit	124
Figure 3.47 General (left) and closer (right) view bright-field TEM images of (a) PLA/AlPi/0-D, (b) PLA/AlPi/1-D, and, (c) PLA/AlPi/2-D nanocomposites	125
Figure 3.48 XRD patterns of organo-montmorillonite (OMMT, 2-D nanofiller) and halloysite nanotubes (HNT, 1-D nanofiller), together with corresponding PLA nanocomposites	127
Figure 3.49 (a) Heat release and (b) mass loss rates of samples under 35 kW/m ² irradiation showing the effect of nanofiller geometry.....	129
Figure 3.50 Thermogravimetric curves of PLA, AlPi and PLA/20wt%AlPi	134
Figure 3.51 Effect of nanofiller geometry on thermal stability of nanocomposites based on PLA/AlPi; (a) thermogravimetry and (b) differential thermogravimetry curves	135
Figure 3.52 Macroscopic appearances of the structure and measured thicknesses of mass loss calorimeter residues. Whole sample surfaces (10 x 10 cm ²) for (a) PLA/AlPi, (b) PLA/AlPi/0-D, (c) PLA/AlPi/1-D, and (d) PLA/AlPi/2-D	137
Figure 3.53 XRD patterns of mass loss calorimeter residue from PLA/AlPi/2-D sample; (a) residue at the lower 1mm through the char thickness, (b) residue at the upper 2.5 mm through the char thickness, (c) residue through the full char thickness	141
Figure 3.54 (a) XRD patterns and (b) ATR-FTIR spectra of mass loss calorimeter residues showing the effect of nanofiller geometry	142
Figure 3.55 SEM images and energy dispersive spectra of mass loss calorimeter residues showing (a) aluminum phosphate residue composed of microspheres with non-uniform sizes, (b) aluminum phosphate/montmorillonite nanocomposite formation where the large aspect ratio silicate platelet reinforcing the aluminum phosphate structure is highlighted.....	144

Figure 3.56 (a) and (b) TEM images of char residues formed by combustion of PLA/AlPi/2-D in the mass loss calorimeter	145
Figure 3.57 (a-d) SEM images showing formation of different aluminum phosphate microfibrils as intermediate reaction products during combustion under an atmosphere with O ₂ ~ 28%. Diameters are in the range of 1 μm to 20 μm with lengths extending above a few hundred microns	147
Figure 3.58 General (left) and closer (right) view SEM images from oxygen index tests indicating microporous structures composed of spherical aluminum phosphate nanoparticles; (a) PLA/AlPi/2-D, (b) PLA/AlPi/1-D, and (c) PLA/AlPi/0-D	149
Figure 3.59 (a) General and (b) closer view SEM images showing the evolution of micro-porous residues consisting of spherical aluminum phosphate nanoparticles	150
Figure 3.60 Tensile stress – strain curves of PLA/AlPi and nanocomposites indicating that strengthening efficiency of nanofillers increase with increasing aspect ratio; 0-D < 1-D < 2-D	152
Figure 3.61 SEM images of fracture surfaces from (a) PLA/AlPi, (b) PLA/AlPi/0-D, (c) PLA/AlPi/1-D and (d) PLA/AlPi/2-D	153
Figure 3.62 (a) and (b) TEM images of the PA6/clay nanocomposite	156
Figure 3.63 XRD patterns of (a) nanoclay, (b) <i>n</i> -PA6, (c) <i>n</i> -PA6/GF, (d) <i>n</i> -PA6/GF-OP15, (e) <i>n</i> -PA6/GF-OP10, and, (f) <i>n</i> -PA6/GF-OP5	157
Figure 3.64 Synergistic increases in LOI with the replacement of OP by NC	160
Figure 3.65 (a) Heat release and (b) mass loss rates for reinforced (both at the micro- and nano-scale) and flame-retarded PA6	161
Figure 3.66 Heat release rate curves for flame-retarded/glass fiber reinforced PA6 and nanocomposites	163
Figure 3.67 Heat release rate curves of flame-retarded and glass fiber reinforced PA6 nanocomposites with varying flame retardant content.....	163

Figure 3.68 Mass loss calorimeter data as a function of organophosphorus flame retardant content, (a) peak heat release rate, (b) total heat evolved, (c) time to ignition, and (d) fire growth index. Dashed lines indicate equal nominal filler contents, i.e. organoclay + flame retardant	164
Figure 3.69 Thermogravimetric and differential thermogravimetric curves of flame-retarded glass fiber reinforced PA6 nanocomposites.....	169
Figure 3.70 ATR-FTIR spectra of combustion residues from mass loss calorimeter char residues without nanoclay; (a) PA6/GF, (b) PA6/OP20, and, (c) PA6/GF-OP15	172
Figure 3.71 ATR-FTIR spectra of fire residues from materials with nanoclay, (a) PA6/GF, (b) <i>n</i> -PA6/GF, and (c) <i>n</i> -PA6/GF-OP15.....	174
Figure 3.72 XRD patterns showing the amorphous structure of fire residues from (a) <i>n</i> -PA6/GF-OP15, (b) PA6/GF-OP15, (c) PA6/OP20 and (d) <i>n</i> -PA6/GF	175
Figure 3.73 XRD patterns showing the clay nanomorphology in char residues from (a) <i>n</i> -PA6/GF, (b) <i>n</i> -PA6/GF-OP5, (c) <i>n</i> -PA6/GF-OP10, and (d) <i>n</i> -PA6/GF-OP15.....	176
Figure 3.74 (a-b) TEM images of mass loss calorimeter residue of <i>n</i> -PA6/GF-OP15	178
Figure 3.75 SEM images of mass loss calorimeter residues formed by combustion of (a-b) PA/GF-OP15 and (c-d) <i>n</i> -PA/GF-OP15.....	179
Figure 3.76 Macroscopic appearances of fire residues after mass loss calorimetry; (a) <i>n</i> -PA6/GF, (b) PA6/GF-OP15, (c) <i>n</i> -PA6/GF-OP5, and (d) <i>n</i> -PA/GF-OP15	181
Figure 3.77 SEM micrographs displaying the fire residue morphologies of (a) PA6/OP20, (b) <i>n</i> -PA6/GF, (c) PA6/GF-OP15, and (d) <i>n</i> -PA6/GF-OP15	182
Figure 3.78 Debonding of flame retardant additive / polymer matrix interface as a consequence of poor adhesion	184

Figure 3.79 Mechanical properties of samples showing (a) the effect of GF, OP and nanofiller alone in the matrix, (b) the effect of OP content in GF reinforced PA6 composites, and (c) the effect of OP content in GF reinforced PA6 nanocomposites	185
Figure 3.80 Chart for graphical interpretation of interfacial shear strength	192
Figure 3.81 Compilation of interfacial shear strength estimations of experimental short glass fiber reinforced composite systems.....	192
Figure 3.82 Variation of fiber length distribution in HIPS/GF composites with.....	195
Figure 3.83 Variation of composite tensile strength (σ), interfacial shear strength (τ) and Young's modulus (E) of HIPS/GF composites with (a) fiber volume fraction and (b) screw speed in extrusion.....	196
Figure 3.84 SEM images of fracture surfaces of HIPS/GF composites with short glass fiber contents of (a) 10 wt%, (b) 30 wt%, and, (c) 50 wt%	198
Figure 3.85 (a) η_{FLD} and η_{FOD} vs. strain, and, (b) experimental and predicted stress vs. strain curves of HIPS/GF composites.....	199
Figure 3.86 Variation of (a) fiber length distribution, and, (b) tensile strength, interfacial shear strength and Young's modulus of micro-filler (+MF), nano-filler (+NF) and micro + nano-filler (+MF/NF) modified HIPS/GF composites	202
Figure 3.87 TEM micrograph of HIPS/clay composite showing coarse clay aggregates.....	203
Figure 3.88 SEM images of fracture surfaces of (a) HIPS/GF, (b) +MF, (c) +NF and (d) +MF/NF composites, showing the direct correspondence of estimated interfacial shear strength values and fracture morphology of interfacial zones.....	205
Figure 3.89 TEM micrograph of PA6/organoclay nanocomposite.....	208
Figure 3.90 Fiber length distributions in short glass fiber reinforced PA6/organoclay nanocomposites	208

Figure 3.91 Graphical interpretation of critical fiber length and interfacial shear strength of investigated composites	210
Figure 3.92 SEM images of the fracture surface morphologies of (a) PA/GF, and, (b) +NF composites	211
Figure 3.93 SEM images of the fracture surface morphologies of (a) +MF, and, (b) +MF/NF composites	212
Figure 3.94 Deconvoluted XRD patterns using Gaussian peak profile and linear background; (a) PA6/GF, (b) +NF, (c) +MF, and, (d) +MF/NF	214
Figure 3.95 Variation of interfacial strength with degree of PA6 crystallinity	216

CHAPTER 1

INTRODUCTION

1.1 POLYMER NANOCOMPOSITES

Polymer nanocomposites can be defined as composite materials in which at least one dimension of the reinforcing filler is in the nano-scale (< 100 nm). Common categories of nano-scale fillers used to obtain polymer nanocomposites are nanoclays, layered double hydroxides, extended carbon nanostructures, oxide ceramic nanoparticles and polyhedral oligomeric silsesquioxanes.

Montmorillonite clay minerals are two dimensional crystals in which an octahedral alumina or magnesia lies between two tetrahedral silica via shared oxygen ions. Ion substitutions of lesser charge either at tetrahedral or octahedral sites, e.g. Si^{4+} substituted by Al^{3+} or Al^{3+} substituted by Mg^{2+} , produce net negative layer charges counterbalanced by alkaline or alkaline earth metal cation interlayer species. The extent of van der Waals attraction between successive layers of montmorillonite is fairly low which allows for the interlayer metal cations to be exchanged easily with organic cations. As the clay is transformed from raw to modified form by organic cation exchange, interlayer galleries are expanded and favorable energetic interactions are provided between the clay interlayer and the host polymer matrix. As a consequence, polymer chains might gain access into the clay interlayer to form a polymer/clay or polymer/layered-silicate nanocomposite.

Polymer/clay nanocomposites, discovered by Toyota research group [1], were found to be promising owing to exceptional physical and mechanical properties of the composite at low reinforcement loading levels (generally ≤ 5 wt%) in the matrix. It was shown in numerous studies that polymers incorporating nanodispersed clay minerals possess enhanced mechanical properties [2-6], thermal stability and flame retardancy [7-13].

Characteristically, the lateral dimension of an individual clay layer is in the range of a few tens of nanometers to a few microns [14, 15], whereas the thickness is approximately a nanometer. Accordingly, a brief explanation for the unprecedented improvements in composite properties could be simply based on higher in-plane modulus of an individual silicate layer, and in particular, much larger aspect ratio of exfoliated silicate layers compared to that of conventional micro-scale reinforcing fillers. Besides, the conformational degree of freedom of polymer chains surrounded at nano-scale by rigid silicate walls is largely restricted and chain dynamics is altered. Owing to nano-scale dispersion of silicate layers, polymer chains within the confined environment between layers constitute a large volume fraction of the composite which allows for the modification of overall properties in an unusual manner.

The key to develop unique multi-functional polymer/clay nanocomposites with exceptional properties is to effectively exfoliate and disperse the high-aspect ratio clay layers at the nano-scale in the polymer matrix. Molecular level interactions can then be obtained between polymer chains and clay layers since the clay interlayer separation is comparable to the polymer radius of gyration. Figure 1.1 shows different states of nanodispersion (quality of filler dispersion) and nanomorphology (exfoliated or intercalated nanocomposite, or phase-separated micro-composite) in polymer/clay nanocomposites.

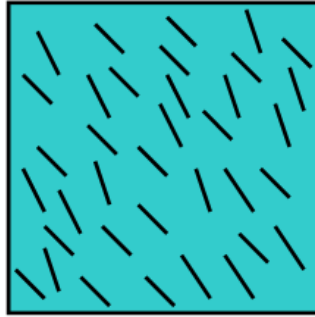
Polymer/clay nanocomposites are most commonly prepared by processes as melt-mixing, solution-mixing and in-situ polymerization techniques. Melt-mixing involves polymer intercalation of clay interlayers facilitated by shear and elongational forces exerted on clay aggregates during screw extrusion processing. Solution-mixing

involves the disruption of clay aggregates, usually with ultrasound assistance, in an appropriate solvent in which the polymer is also soluble. The driving force for solution intercalation of polymers in montmorillonite interlayer is the large gain in entropy by desorption of solvent molecules off the interlayer which compensates for the decrease in the configurational entropy of polymer chains adsorbed on the interlayer. In-situ polymerization entails swelling of the layered silicate within a liquid monomer or a monomer/solvent system which allows polymerization simultaneously at intra-gallery and extra-gallery sites. Intra-gallery polymerization creates an additional driving force for clay layer separation and disruption of large agglomerates providing better dispersion of montmorillonite in the polymer matrix.

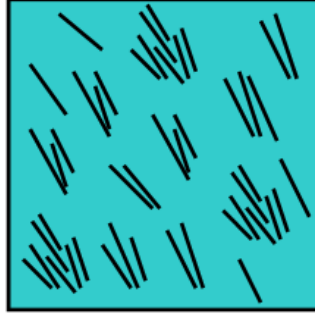
Following their discovery in 1991 [16], enormous research effort was spent on unmatched mechanical and physical properties of carbon nanotubes, cylindrical microtubules of graphitic carbon. Since carbon-carbon covalent bonds are one of the strongest in nature, a structure based on a perfect arrangement of these bonds oriented along the axis of nanotubes would produce an exceedingly strong material.

Carbon nanotubes possess low density, extremely high elastic modulus, high strength and resilience, and high electrical and thermal conductivity. Theoretical studies have suggested that single-walled carbon nanotubes have Young's modulus as high as 1 TPa, which is actually the in-plane modulus value of defect free graphite. However, for multi-walled carbon nanotubes, the actual strength in practical situations would be affected to a large extent by the sliding of individual nanotubes with respect to each other.

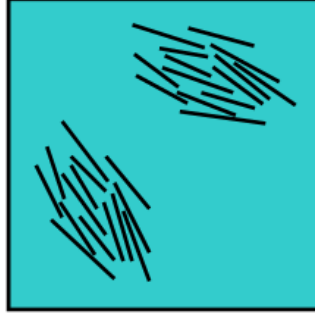
Nanodispersion



Fine dispersion and homogeneous distribution of montmorillonite platelets



Fine dispersion, slightly poor distribution of montmorillonite platelets



Poor dispersion and inhomogeneous distribution of montmorillonite platelets

Nanomorphology

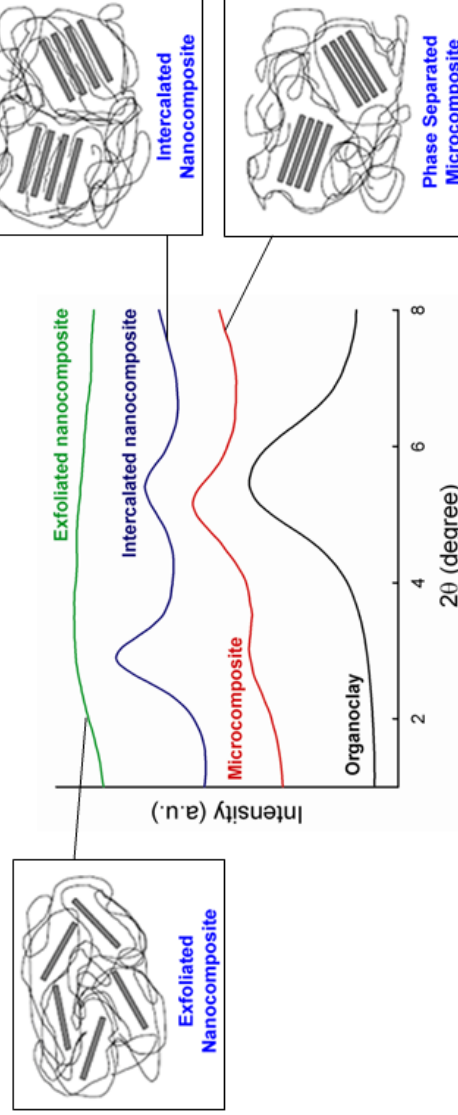


Figure 1.1 Different states of nanodispersion and nanomorphology in polymer/clay nanocomposites

The superior physical and mechanical properties of carbon nanotubes can be tailored to produce novel multifunctional polymer nanocomposites with exceptionally low reinforcement loading levels. Nevertheless, difficulties arise when homogenous dispersion of carbon nanotubes within the polymer matrix is aimed. Carbon nanotubes have a high tendency to form bundles due to strong van der Waals interactions and not to disperse uniformly within the matrix resulting in rather minimized polymer/filler surface interaction area. Processing methods to prepare polymer/carbon nanotube nanocomposites can be summarized as (i) direct-mixing where carbon nanotubes are dispersed into a low-viscosity thermosetting resin followed by curing, (ii) solution-mixing which involves carbon nanotubes dispersed in polymer solution (usually with ultrasound assistance) followed by solvent removal or co-precipitation of polymer and carbon nanotubes, (iii) melt-mixing where carbon nanotubes are mechanically dispersed into a polymer melt using mixers or compounders, and, (iv) in-situ polymerization involving free-radical or condensation polymerization of a monomer or co-monomers taking place in the presence of carbon nanotubes which might also participate in polymerization reactions leading to grafting of carbon nanotubes on polymers.

1.2 FLAME RETARDANCY

Most polymeric materials ignite easily, burn rapidly producing large heats, exhibit flaming drips, and sustain combustion even under oxygen-deficient environments, a characteristic of fires. Unwanted fires, especially those originating from plastic products with poor resistance to ignition and fast flame spread properties could be prevented by the development of novel flame-retarded polymers targeting application areas such as cable insulation, automotive fuel and ignition systems, printed circuit boards, novel textiles and foams, and housings of electrical equipments. Considerable research effort is being exerted both by the academia and the polymer industry on the development of advanced light-weight materials possessing improved flame retardancy together with satisfactory mechanical, thermal, and electrical properties.

1.2.1 Thermal Degradation and Combustion of Polymers

Understanding polymer degradation is of paramount importance for the development of new polymer processing technologies. Of particular interest to this dissertation is that the first step in initiation and growth of a fire is thermal degradation and decomposition in the solid state.

Thermal decomposition of a polymer is an endothermic process which necessitates that binding energy of around 200–400 kJ/mol (typical for most C-C backbone polymers) is supplied to break covalent bonds. It is important to distinguish thermal decomposition in the absence of oxygen (pyrolysis) and in the presence of oxygen (thermo-oxidative decomposition). In thermo-oxidative decomposition, polymer molecules react with oxygen and various lower molecular weight decomposition products are formed along with extremely reactive H• and OH• radical species undergoing further combustion reactions in the gas phase.

However, it has to be noted that at combustion temperatures exceeding 300°C, polymer decomposition takes place via non-oxidizing route since pyrolysis is faster than diffusion of oxygen in the condensed phase. Accordingly, in most flammability and fire tests, rather than thermo-oxidative decomposition, pyrolysis (non-oxidizing thermal decomposition) precedes combustion reactions in the gas phase.

Combustion, defined as the reaction of oxygen and fuel accompanied by heat release, can occur when three essential elements coexist: fuel (combustible), oxygen (combustive) and energy in the form of heat (Figure 1.2). Polymers are long chain macromolecules that generally consist of carbon and hydrogen. When heated to a sufficient temperature, energy barrier for thermal decomposition of a polymer can be overcome leading to extensive changes in the chemical structure. Thermal decomposition, initiated by main-chain or side-group scission, leads to the formation of small volatile fragments that evolve into the gas phase above the decomposing polymer. Those volatiles are mostly flammable and can be ignited when the auto-ignition temperature is attained (temperature at which the activation energy for combustion is reached) in the presence of oxygen gas. Ignition can also be triggered at a lower temperature (termed as the flash point) by an intense external source such as a flame or spark. Once the volatiles are ignited, combustion is self-sustained either by the act of an external source of irradiation or by substantial heat release due to exothermic chain reactions occurring in the gas phase which facilitate the decomposition of polymer thereby maintaining the critical concentration of evolved flammable volatiles in the gas phase.

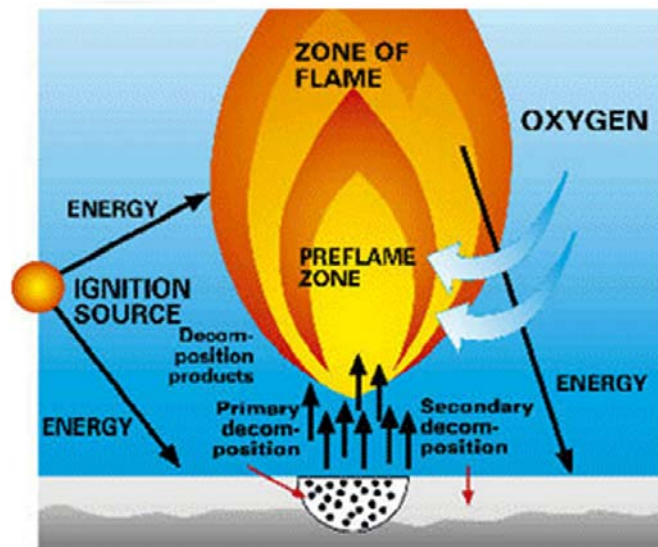
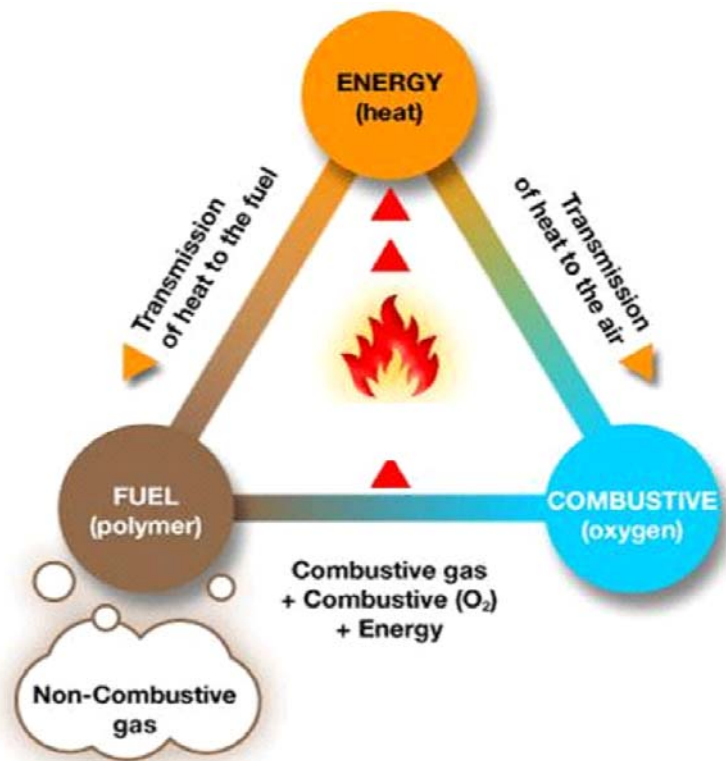


Figure 1.2 Fire triangle and combustion cycle of polymers [17]

1.2.2 Evaluation of Flame Retardancy

A fire evolves through several phases; ignition, sustained combustion, flame spread, flashover and decay. There are several standardized test procedures differing in heat and mass transport conditions, but, all attempt to correctly assess the reaction of polymers in real fire scenarios. Characterization of polymers for their flammability and fire behavior are generally done by three reliable laboratory scale techniques; limiting oxygen index test, UL94 flammability test and cone calorimetry.

(i) Limiting Oxygen Index Test

The limiting oxygen index (LOI) test is used to measure the minimum oxygen concentration in a flowing O_2/N_2 gas mixture that will just support candle-like flaming combustion of polymers. The standardized tests [18, 19] utilize an oxygen index apparatus consisting of a test chimney, a specimen holder, gas measurement/control devices and a flame igniter (Figure 1.3). A test specimen is mounted vertically in a glass chimney and exposed to a quiescent stream of O_2/N_2 mixture having a preset O_2 concentration. The upper end of the specimen is ignited and the subsequent burning behavior is evaluated within specified limits for burning length and duration before extinguishment. Each time before the tests, the equipment is calibrated to measure a minimum (0%, pure N_2) and a maximum (99.5%, pure O_2) oxygen concentration. LOI value is determined by a statistical up-and-down procedure which requires several trials of different O_2 concentrations on the same set of specimens. The higher the LOI value of a polymer, the better it is considered to be flame retarded. Polymers with a LOI value below 21% are categorized as combustible, while those with a LOI value well above 21% might be classified as self-extinguishing.

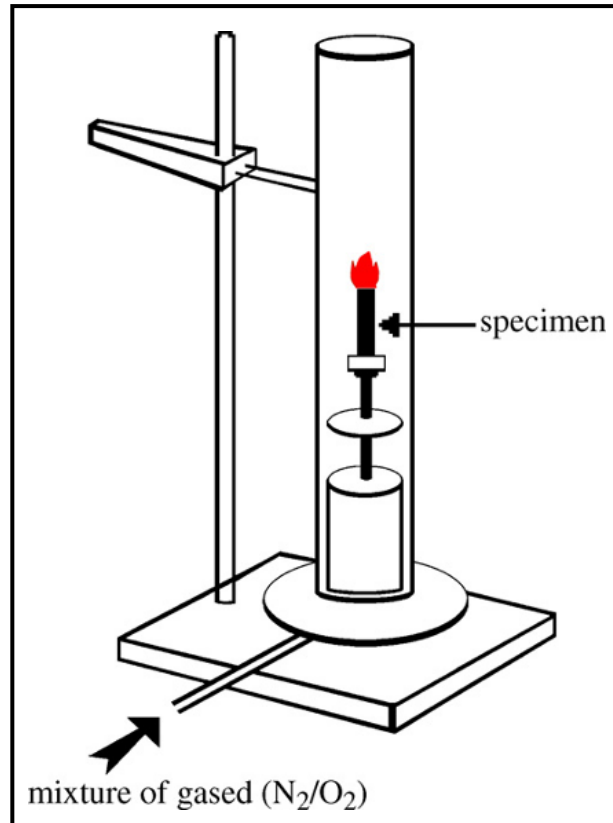


Figure 1.3 Schematic of limiting oxygen index apparatus

(ii) UL94 Flammability Test

UL94 test was developed by Underwriters Laboratory [20] and is the most widely used small-flame, realistic flammability test especially when certain polymeric products are concerned. The standard incorporates a number of different test procedures using alternative configurations, i.e vertical (UL94-V) and horizontal (UL94-HB). Figure 1.4 shows the test apparatus for UL94 vertical testing of a molded plastic. Table 1.1 summarizes the criteria that should be met by a polymer compound to pass the vertical test and be classified with a V-2, V-1 or V-0 rating, in the order of increasing flame retardancy. Materials that cannot pass the stringent vertical test (no-rating or burn-to-clamp) are tested in horizontal orientation in order to quantify the burning rate and to be classified as HB.

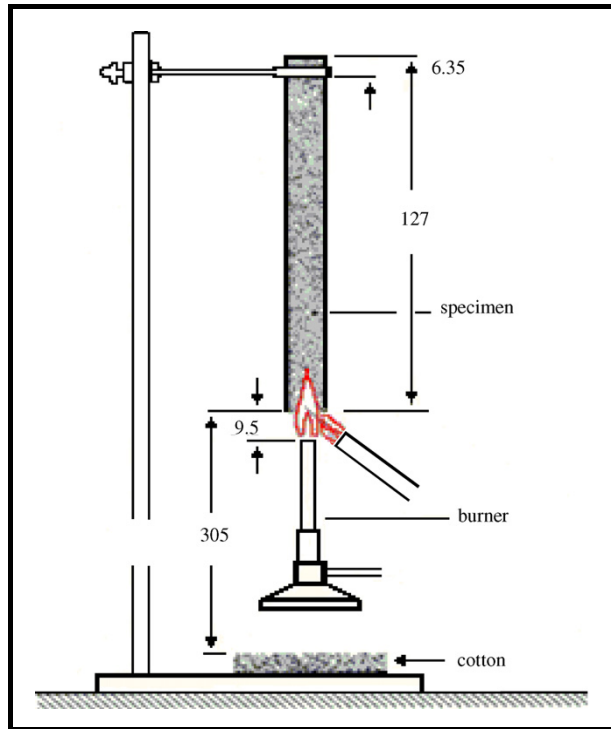


Figure 1.4 Schematic of UL-94 test apparatus

Table 1.1 Materials classifications (ratings) of the UL94-V flammability test

Criteria	Ratings		
	V-0	V-1	V-2
Afterflame time of each individual specimen (t_1 or t_2) in seconds	≤ 10	≤ 30	≤ 30
Total afterflame time for 5 specimens ($t_1 + t_2$) in seconds	≤ 50	≤ 250	≤ 250
Afterflame plus afterglow time for each individual specimen after the second flame application ($t_2 + t_3$)	≤ 30	≤ 60	≤ 60
Afterflame or afterglow of any specimen up to the holding clamp	No	No	No
Cotton indicator ignited by flaming particle or drops	No	No	Yes

(iii) Mass Loss Cone Calorimeter Fire Testing

Mass loss calorimeter is a standardized bench-scale fire test [21-23] to evaluate the performance of polymeric materials under forced flaming combustion conditions. The equipment (Figure 1.5) consists of a sample stage to horizontally mount molded samples for pool fire geometry, a load cell connected to the sample stage to measure sample mass throughout combustion, a conical heater capable of producing external heat flux in the range 20–100 kW/m² on exposed sample surface, a spark discharge igniter to trigger forced flaming combustion, and, an exhaust hood for evolved gas and particle withdrawal.

The equipment is capable of simulating scenarios ranging from mild to large fires which can be adjusted using the heat flux calibration procedure. Additional chimney and thermopile attachments are used to measure the attained temperature on chimney as combustion proceeds. Temperatures measured by the thermopile attachment are recorded using a data-acquisition system and converted to a “heat release rate” value (in kW/m²) using calibration curves obtained prior to testing of each sample batch. Heat release rate calibration of the apparatus is done by using propane gas with known calorific value and volumetric flow rate through a laborious procedure explained in detail elsewhere [24]. The equipment also measures the sample mass throughout combustion and records the data using the acquisition system which can then be used to calculate “mass loss rate” (in g/m²s), and amount of solid fire residue in weight percent.

In the mass loss calorimeter, sustained combustion takes place following ignition and flame spread providing heat for the decomposition and pyrolysis of unburned fuel. The rate at which heat is generated is termed as the heat release rate and is described by the product of burning rate and heat of combustion. Apart from unambiguous effect of presence of flame retardant species, heat release rate from the exposed polymer involves complex contributions from external irradiation, sample orientation, radiative feedback of flame to the pyrolyzing zone and completeness of combustion.

The most important material properties that can be obtained by mass loss calorimeter analysis are listed below and indicated in Figure 1.6.

Peak heat release rate (PHRR): Considered as the most important parameter regarding a material's performance in a fire scenario and determines the contribution of the material to the severity of flashover of a fire. Standard unit of PHRR is kW/m^2 .

Average heat release rate (AHRR): Test average of heat release rate data representing the whole course of combustion process. Standard unit of AHRR is kW/m^2 .

Total heat evolved (THE): Area under the heat release rate versus time curve representing the total fire load of a material. Standard unit of THE is MJ/m^2 .

Time to ignition (TTI): Time elapsed before piloted ignition of a material under external irradiation. Standard unit of TTI is seconds.

Total time of burning (TTB): Time elapsed from the beginning of the test to flame-out (extinguishment). Standard unit of TTB is seconds.

Total mass loss (TML): Change in sample mass upon combustion. Standard unit is grams. It is used to calculate percent fire residue by weight.

Fire growth index (FGI): Ratio of PHRR to TTI. It is an accurate way of describing flame spread rate. Reciprocal of fire growth index is defined as the fire performance index. Standard unit of FGI is $\text{kW/m}^2\text{s}$.

Fire growth rate (FIGRA): Ratio of PHRR to time-to-PHRR. It is another accurate way of describing flame spread rate. Standard unit of FIGRA is $\text{kW/m}^2\text{s}$.

Total-heat-evolved / total-mass-loss ratio (THE/TML): Product of effective heat of combustion (Δh_c) and combustion efficiency (χ). Standard unit is $\text{MJ/m}^2\text{g}$ or kJ/g .

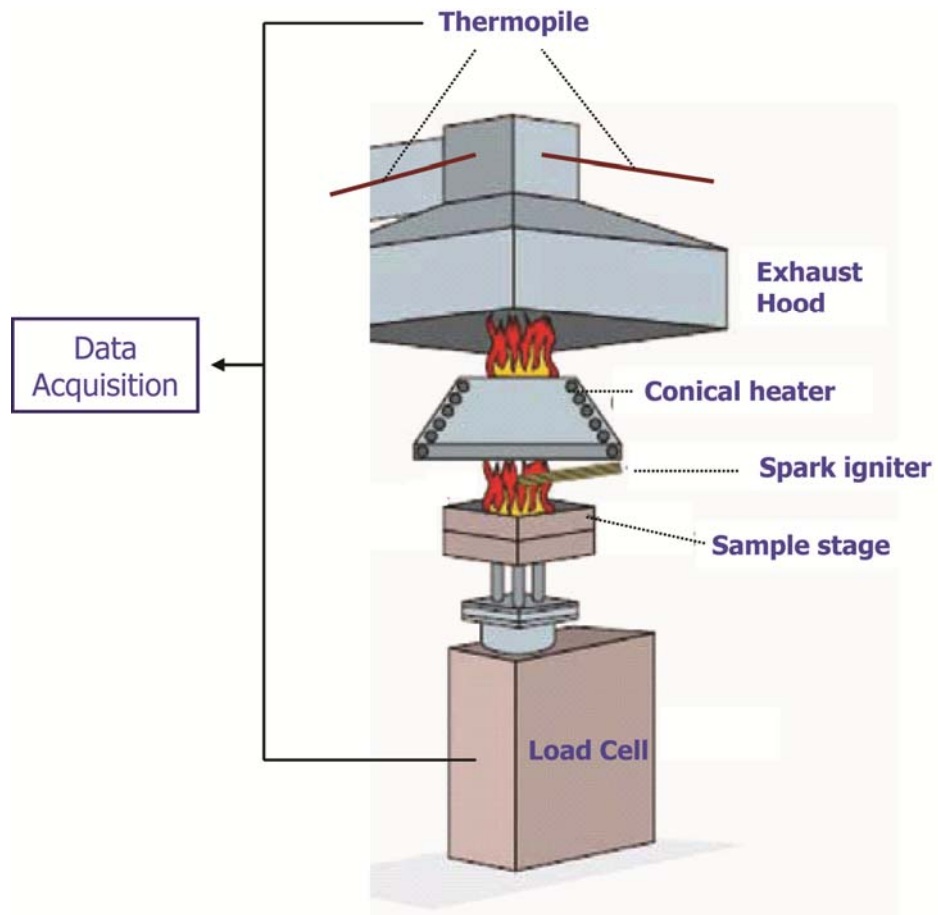


Figure 1.5 Schematic of the mass loss calorimeter

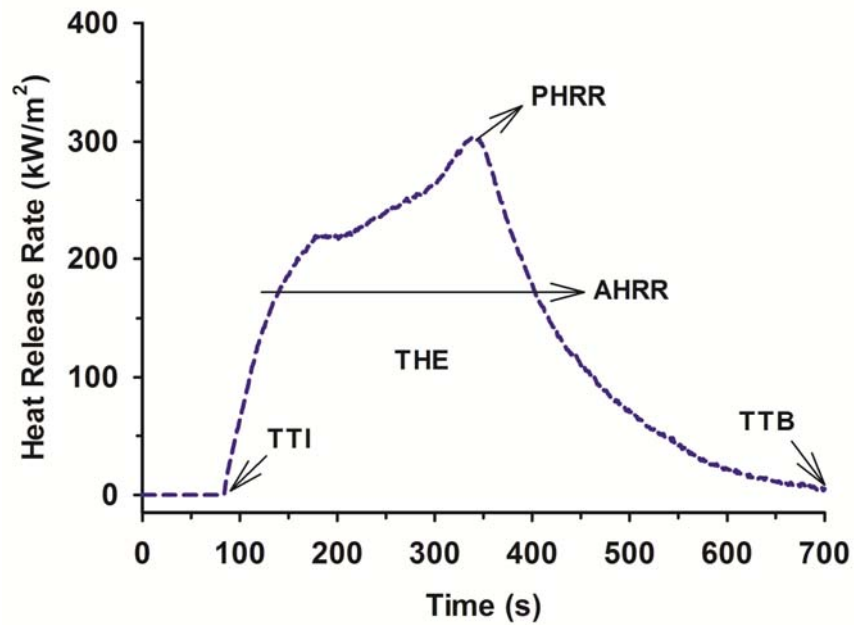


Figure 1.6 A typical mass loss calorimeter curve showing important fire parameters

1.2.3 Flame Retardancy Mechanisms

With the increased consumption of plastics for applications in automotive, aerospace, electrical/electronics, building and cable industries, a wide variety of additive type flame retardants were developed over the past 40 years. It was shown that flame-retarded plastics allow 15 times longer time to escape from a fire compared to neat counterparts. The mechanisms by which flame retardant additives operate are generally classified as “physical” and “chemical” modes of action taking place in the “condensed” or “gas” phases.

Condensed phase activity encompasses several chemical and physical mechanisms including the most common modes of action, i.e. “protective char formation” and “endothermic decomposition”. While the latter takes part in the energy balance of combustion by drawing away heat and cooling the solid fuel, the former involves the formation of a superficial residue facilitated by decomposition of the flame retardant additive. The protective barrier layer suppresses heat and mass transfer between the pyrolysis and flaming zones.

Gas phase active flame retardants strongly interfere with the combustion process either by scavenging of H• and OH• hot radicals in the flaming zone, called as “flame poisoning”, or by generating considerable amounts of less-combustible gases. The general mechanism of common gas phase active flame retardant systems, i.e. “halogenated flame retardants” combined with antimony oxide, is the effective removal of hot radicals from the flame through the release of hydrogen halide and antimony trihalide thereby suppressing exothermic chain reaction of combustion.

(i) Halogenated Flame Retardants

Halogenated compounds have long been considered as by far the most effective flame retardants, especially when used in a synergistic combination with antimony trioxide. However, some of the widely used brominated and chlorinated compounds are proved to have major environmental side-effects such as bioaccumulation in the environment and long-range atmospheric transport, and, some are shown to cause

human health risks due to the release of toxic and corrosive gases by degradation during processing, recycling, and in the case of a fire.

Therefore, it appears that the current restrictions imposed by legal authorities on the use of a number of brominated aromatic flame retardants have increased the demand for halogen-free flame retardants. Accordingly, recent developments in flame retardant chemicals have shifted strongly towards the use of new halogen-free compounds.

(ii) Phosphorus/Nitrogen- (P/N-) Based Flame Retardants

The most common type of condensed phase acting flame retardant systems are based on phosphorus compounds used in conjunction with nitrogen containing substances leading to a phenomenon called “intumescence”. Intumescence is usually referred to as the formation of an expanded superficial char layer during combustion acting as a physical barrier against transport of heat and mass [25]. The intumescent process entails the presence of an acid source for catalytic activity, a carbonization source for char forming, and a blowing agent to obtain expansion of the formed char. The flame retarding efficiency of intumescent systems is dictated, in particular, by the amount, structural integrity, mechanical strength, expansion degree, and thermal stability of intumescent chars [26-28].

Phosphorus based flame retardants can function effectively when incorporated into polymers containing oxygen in pendant groups or in the main-chain backbone. It is generally accepted that phosphorus compounds either react with the polymer during decomposition or get oxidized to phosphoric acid to promote charring in the condensed phase. Phosphorus compounds can also volatilize into gas phase and get oxidized to $\text{HPO}_2\cdot$, $\text{PO}\cdot$, $\text{PO}_2\cdot$ and $\text{HPO}\cdot$ radicals acting as $\text{H}\cdot$ and $\text{OH}\cdot$ scavengers to suppress combustion chain reactions. Common types of phosphorus flame retardants are elemental red phosphorus, inorganic phosphates and organic phosphorus compounds.

Phosphorus-nitrogen synergism is not a general phenomenon but depends on the type of flame retardants involved as well as the structure of the polymer. It is known that certain nitrogen containing compounds such as melamine and its salts interact synergistically with phosphorus flame retardants to enhance the efficiency of intumescent char formation in the condensed phase. Melamine sublimes around 350°C by absorbing significant amount of energy, or it can decompose further in the flame to cyanamid by an endothermic process. Melamine can also undergo condensation reactions releasing ammonia and forming thermally stable condensates. Melamine salts dissociate endothermically upon heating to form melamine which volatilizes similar to pure melamine which might act as a blowing agent in an intumescent system. A common mode of action for melamine cyanurate is the decomposition of the salt to melamine and cyanuric acid, the former catalyzing chain scission of polyamides and polyesters favoring extinguishment of the polymer.

(iii) Metal Hydroxides

Metal hydroxides, the most common type of mineral flame retardants, function both in the condensed and gas phases. There are two major hydrated compounds of high industrial importance, namely aluminum tri-hydroxide $\text{Al}(\text{OH})_3$ and magnesium di-hydroxide $\text{Mg}(\text{OH})_2$. In fact, former is the largest commercially used flame retardant additive by weight, with main application area of wire and cable insulation. It is generally accepted that aluminum and magnesium hydroxides function as flame retardants owing to largely endothermic dehydration reactions acting as a heat sink, cooling the fuel in the condensed phase. Dehydration of aluminum tri-hydroxide starts at ~220°C with a reaction enthalpy of 1050 kJ/kg. Magnesium hydroxide has a higher dehydration temperature ~300°C making it suitable for polymers requiring higher processing temperatures as well as a higher reaction enthalpy of 1300 kJ/kg. In addition to the heat sink effect in the condensed phase, water of dehydration evolves into the flaming zone effectively cooling and diluting the available fuel in the gas phase. Moreover, porous ceramic residues from dehydration reactions, i.e. anhydrous alumina and magnesia, provide heat insulation by forming protective barrier layers on exposed sample surface. The most important drawback of metal hydroxides is that they require very large loading levels ranging from 40 to 70 wt%

in the polymer matrix to provide substantial flame retardancy causing difficulties in processing and also deteriorating the mechanical properties of the polymer matrix.

1.3 LITERATURE SURVEY

Conventional flame retardant additives containing halogen elements are currently being forced by legal environmental obligations to be replaced by halogen-free counterparts such as phosphorus and/or nitrogen-based compounds and inorganic hydroxides. The primary concern with the use of new halogen-free compounds, especially with mineral-type additives, is usually that large filler loadings are required to attain satisfactory flame retardancy which in turn causes deteriorated mechanical properties and processing issues. Moreover, in many circumstances, halogen-free phosphorous and nitrogenous flame retardants were proved inferior to well-established halogenated compounds in providing substantial flame retardancy.

Polymer nanocomposites, especially those incorporating organically modified montmorillonite clay minerals and multi- or single- walled carbon nanotubes, have been proposed to achieve improved flame retardancy with an ascribed mechanism of formation of a superficial physical barrier layer that effectively shields the underlying polymer against external heat exposure and impedes diffusion of volatiles during pyrolysis and combustion. Peak heat release rate was found to be reduced to a significant level with the incorporation of nanoclays at low loading levels into polymer matrices such as polyamide 6 [10, 11], polystyrene [7, 29, 30], poly(methyl methacrylate) [9, 31] and polylactide [32, 33]. Polymer nanocomposites containing carbon nanotubes proved to possess relatively higher flame retardancy when compared to montmorillonite clay minerals due to the formation of denser and crack-free barriers [34-37].

However, results from legitimate tests such as LOI and UL94 still hold to be controversial to those from forced flaming cone calorimetry. No substantial reduction in flammability is likely to be attained in LOI and UL94 tests with nano-scale fillers alone in the polymer matrix. The disappointing results in LOI tests are caused by the

insignificant influence of the barrier formed by the inorganic nanofiller residue when tested under small external heat flux characteristics of those tests.

A different explanation can be postulated for nanocomposites graded fail or non-classified in the UL94 vertical test. As the test entails upwards ignition, melt dripping draws substantial heat by removing fuel being combusted and may result in self-extinguishment as long as the dripping process occurs in a sufficiently rapid manner. However, presence of nanofillers is known to have a pronounced influence on melt viscosity due to nano-scale dispersion and filler-matrix interactions at large surface areas. Consequently, as opposed to neat polymers, it is likely for nanocomposites that dripping is either markedly delayed or completely hindered. It becomes more critical for engineering thermoplastics with semi-crystalline structure such as polyesters and polyamides leading to deterioration of UL94 rating from V-2 to non-classified.

An engineering solution to the disappointing fire-retardant performance of binary polymer nanocomposites (matrix + nanofiller) is to develop novel ternary systems with synergistic combinations of nanoparticles such as nanoclays, carbon nanotubes and oxide ceramics with halogen-free phosphorus/nitrogen- compounds and mineral-type flame retardant additives. The emerging material class that combines micro-scale flame retardant additives and nano-scale fillers has been termed as “flame retarded polymer nanocomposites”. The main purpose of developing those novel nanocomposites is to obtain enhanced flame retardancy that could outperform well established halogenated flame retardants and reduce additive loading levels in polymer matrix along with satisfactory thermal, mechanical, barrier and in some cases electrical or anti-static properties.

The following sections provide only an initial insight into the existing literature on each purpose of the thesis and many other studies in the literature were cited and discussed in relevant results and discussion sections.

1.3.1 Studies on the Effect of Nanofiller Type

There are a number of publications dealing with the use of different types of nanofillers such as organically modified layered-silicate clay minerals referred to as organoclays or nanoclays [28, 38-40], extended carbon nanostructures [38, 39, 41-45], layered double hydroxides [40, 46-52], polyhedral oligomeric silsesquioxanes [53, 54], and oxide ceramic nanoparticles [55-57] to achieve synergistic improvements in flame retardancy of polymers filled with halogen-free flame retardant additives.

Among those publications, attempts to reduce the primary flame-retardant levels in halogen-free cable compounds with the incorporation of well-dispersed nanoclays were successfully commercialized [58]. However, in many previous cases, no synergism or even strong anti-synergism was also encountered [59-61]. Moreover, there are no studies directly comparing the potential synergistic fire retardant interaction of two very important nanofillers, i.e. organo-montmorillonite clays and multi-walled carbon nanotubes with conventional flame retardants.

Therefore, the first aim of this thesis is to reveal the influence of nanofiller type on synergistic fire retardancy in halogen-free flame-retarded polymer nanocomposites.

1.3.2 Studies on the Effect of Nanofiller Dispersion

The incorporation of clay minerals was investigated in a recent publication [62] for the influence of intercalated and exfoliated nanomorphology on the effectiveness of flame retardancy brought in by nanoclays. It was stated that nanomorphology does not play a major role in terms of the reductions in the peak heat release rate in the cone calorimeter as long as the nanodispersion of filler nanoparticles is achieved. On the other hand, poorly dispersed systems where nanoclays form phase-separated microcomposites with the polymer matrix would not significantly improve flame retardancy [63] since the material lacks the formation of an effective barrier layer during combustion.

However, the influence of micro- and nano-composite formation (regardless of the nanomorphology) on the synergistic action between nanoclays and conventional flame-retardant additives has not yet been discussed in flame-retarded polymer compounds. Moreover, although there are some studies on the effect of nanomorphology on the mechanical properties [64], there appears to be no publications comparatively investigating the enhancements in mechanical properties obtained by nanoclays with intercalated nanocomposite and phase separated microcomposite morphologies in a conventional flame retarded polymer.

Therefore, the second aim of this dissertation is to reveal the effect of dispersion of nanofiller at the micro- or nano-scale in terms of synergistic fire retardancy in halogen-free flame-retarded polymer nanocomposites.

1.3.3 Studies on the Effect of Nanofiller Geometry

There are a few studies investigating the role of nanoparticle geometry (spherical, fibrillar or tubular, plate-like) in fire retardancy of polymer nanocomposites [65, 66]. However, the influence of nanofiller geometry has scarcely been evaluated for potential synergistic combination of flame retardant additives and nanofillers.

Spherical (fumed silica) and rod-like (exfoliated attapulgite) nanofillers were used in conjunction with a NASA formulated intumescent flame retardant additive in polystyrene [67]. While both fillers were effective in decreasing heat release rate, different effects were observed in limiting oxygen index performance. Authors emphasized that the combination of spherical and rod-like nanofillers can be an effective route for enhanced fire retardancy. Effectiveness of intumescent fire retardant coatings was evaluated for the influence of fibrillar and plate-like clay morphologies [68]. Sepiolite nanoclay with fibrillar morphology was found to optimize the char structure without restricting intumescence while montmorillonite increased mechanical resistance but reduced the intumescent function.

The third aim of this thesis is to understand the potential synergistic role of all three nanofiller geometries (0-D, 1-D and 2-D) when used in an important engineering bio-based polyester which contains a phosphorus-based flame retardant.

1.3.4 Studies on the Effect of Fiber Reinforcement

Studies on the use of nanoclays and short glass fibers together as reinforcements in thermoplastic matrices are quite limited at the time [16-18]. Although there has been extensive research interest [69-79] in developing flame-retarded short fiber reinforced thermoplastic composites owing to their enhanced mechanical properties, there seems to be no publications concerned with the synergistic flame retardancy effect of nanofillers on glass fiber reinforced thermoplastic composites containing conventional flame retardant additives.

Therefore, the fourth aim of this dissertation is to investigate the flame retardancy effect of using a combination of nanofillers and short glass fibers in a halogen-free flame-retarded polymer.

1.3.5 Studies on Interfacial Interactions

The resistance of the interface between reinforcing fibers and polymer matrix to shear controls the extent of stress transferred to fibers, the reinforcement efficiency of fibers and debonding of the interface under an applied stress. While the interfacial bond strength can be evaluated by experimental micromechanics such as fragmentation, single-fiber pull-out, micro-indentation and micro-tension tests, the in-situ response of the fiber/matrix interface to shear may highly deviate from that isolated interfacial failure. The causes for this deviation were stated to be complex stress state in samples being tested and occurrence of side phenomena rather than pure debonding at the interface [80]. Despite the fundamental basis of these experiments, earlier studies concluded that those indirect interface measurements had no physical meaning [81-86].

Composites contain a great many side effects, the most important being the alterations in the physical properties of polymer matrix either globally or in the vicinity of interface. These alterations are almost always caused by the presence of modifiers, namely micro-filler or nano-filler, the main concern being extension of material properties. In particular, fillers providing substantial improvements in flame retardancy are widely employed to broaden the field of applications. Further modification of fiber reinforced polymers can be achieved using nanofillers to obtain interesting new composite materials exploiting synergistic reinforcement at different length scales, i.e. microscopic fiber reinforcement combined with exfoliated nanoscopic layered silicates. Both types of fillers, either micro-filler or nano-filler can induce significant fiber length degradations during extrusion and can extensively change mechanical, thermal and morphological characteristics of the matrix.

Therefore, the fifth aim of this thesis is to develop a practical theoretical approach to estimate the apparent interfacial shear strength, as a composite property that governs the mechanical properties, to overcome the difficulty of adapting experimental micromechanics to complex systems and to involve the actual contribution originating from conventional flame retardant additives and nanofillers present in fiber reinforced polymer systems.

1.4 AIM OF THE STUDY

As stated in the literature survey, there are five main purposes of this thesis as explained below.

For the first aim investigating the effect of nanofiller type, multi-walled carbon nanotubes and montmorillonite clays are used as different nanofiller types in phosphorus/nitrogenous flame retardant containing poly (methyl methacrylate) matrix.

For the second aim, investigating the effect of nanofiller dispersion, montmorillonite clay nanofillers and aluminum hydroxide flame retardant were used in high-impact

polystyrene matrix processed by different techniques that yielded distinct dispersion states of the nanofiller.

For the third aim, investigating the effect of nanofiller geometry, nanofillers with different geometries (0-D, 1-D and 2-D), namely nanosilica, halloysite clay nanotubes and montmorillonite clays were used in phosphorus/nitrogenous flame retardant containing polylactide matrix.

For the fourth aim, investigating the effect of fiber reinforcement, short glass fibers were used in combination with montmorillonite clays, in phosphorus/nitrogenous flame retardant containing polyamide-6 matrix.

Lastly for the fifth aim, it was attempted to reveal the influence of flame retardant additives and montmorillonite clays on the fiber/matrix interfacial interactions in short glass fiber reinforced polyamide-6 and high-impact polystyrene matrix composites.

Throughout this thesis, materials were prepared by melt mixing or ultrasound-assisted solution mixing techniques. Characterization of nanomorphology and nanodispersion was done by X-ray diffraction (XRD) and transmission electron microscopy (TEM). Reaction to fire of samples was determined by mass loss cone calorimetry, a powerful bench-scale tool to assess forced flaming fire behavior of materials. Flammability properties were evaluated by limiting oxygen index (LOI) measurements and according to the classifications of UL-94 standards. Flame retardancy mechanisms were revealed by observing solid fire residues by scanning electron microscopy (SEM) and transmission electron microscopy (TEM) for barrier morphologies, and characterizing fire residues using attenuated total reflectance – Fourier-transform infrared spectroscopy (ATR-FTIR) for chemical structures and XRD analysis for nanomorphology and phase identification. Thermal degradation behavior was studied using thermogravimetric analysis (TGA). Mechanical properties were measured by tension tests, and fracture surfaces were observed under SEM.

CHAPTER 2

EXPERIMENTAL WORK

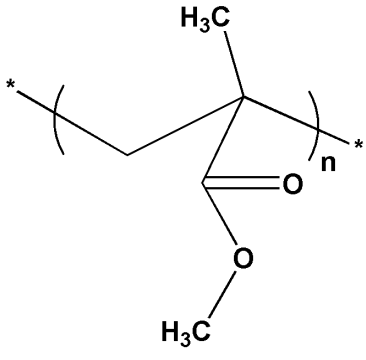
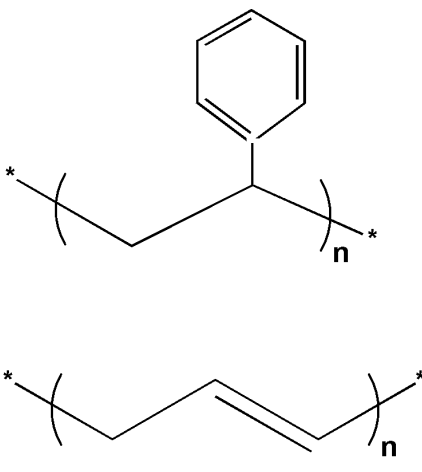
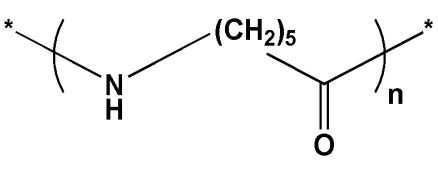
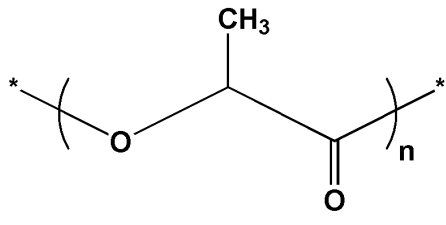
2.1 MATERIALS USED

In this thesis, a variety of thermoplastic matrix materials, nano-scale fillers, conventional flame retardant additives and reinforcing short glass fibers were used.

2.1.1 Matrix Materials

Depending on the particular purpose of each section, one of the four different polymers was used as the matrix material. Poly(methyl methacrylate) (PMMA), obtained from Arkema (Altuglas V 825T), was an injection molding resin with a melt flow index of 2.8 g/10 min (230°C, 3.8 kg) and density of 1.19 g/cm³. High-impact polystyrene (HIPS) was an extrusion grade high-impact resin (Dow Styron, A-Tech 1175) with a melt flow index of 2.8 g/10 min (200°C, 5 kg). Polylactide (PLA), with $M_n \sim 190\,000$ and density of 1.24 g/cm³, was provided by Cargill Dow. Polyamide 6 (PA6), with a density of 1.13 g/cm³, was DSM Akulon K125. Chemical formulae of utilized polymer matrix materials are listed in Table 2.1.

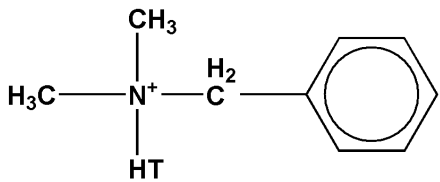
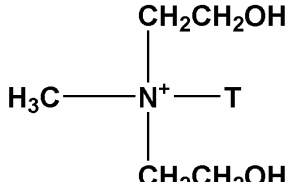
Table 2.1 Chemical structure of matrix materials

Matrix Material	Chemical Structure
Poly(methyl methacrylate) (PMMA)	 <p>The diagram shows the chemical structure of the repeating unit of Poly(methyl methacrylate) (PMMA). It consists of a carbon-carbon backbone where each carbon is bonded to a methyl group (H₃C) and a methoxy group (-OCH₃). The backbone is enclosed in large parentheses with a subscript 'n' and asterisks at the ends, indicating it is a polymer chain.</p>
High-impact polystyrene (HIPS)	 <p>The diagram shows two chemical structures for High-impact polystyrene (HIPS). The top structure is the polystyrene backbone, consisting of a carbon-carbon chain with a phenyl ring attached to each carbon. The bottom structure is the polybutadiene backbone, consisting of a carbon-carbon chain with alternating single and double bonds. Both structures are enclosed in large parentheses with a subscript 'n' and asterisks at the ends, indicating they are polymer chains.</p>
Polyamide 6 (PA6)	 <p>The diagram shows the chemical structure of the repeating unit of Polyamide 6 (PA6). It consists of a six-carbon chain with an amide group (-NH-) at one end and a carbonyl group (-C=O) at the other. The backbone is enclosed in large parentheses with a subscript 'n' and asterisks at the ends, indicating it is a polymer chain.</p>
Polylactide (PLA)	 <p>The diagram shows the chemical structure of the repeating unit of Polylactide (PLA). It consists of a three-carbon chain with a methyl group (CH₃) attached to the middle carbon and a lactide ring (a five-membered ring containing two oxygen atoms) attached to the other two carbons. The backbone is enclosed in large parentheses with a subscript 'n' and asterisks at the ends, indicating it is a polymer chain.</p>

2.1.2 Nanofillers

Nanofillers chosen for different purposes were organically modified montmorillonite clays, multi-walled carbon nanotubes, nanosilica and halloysite nanotubes. Two different montmorillonite nanoclays modified with (i) dimethyl benzyl hydrogenated tallow quaternary ammonium cation (Southern Clay, Cloisite 10A), and (ii) methyl tallow bis-2-hydroxyethyl quaternary ammonium cation (Southern Clay, Cloisite 30B) were used as received. Purified multi-walled carbon nanotubes (Nanocyl NC 7000) produced via catalytic carbon vapor deposition was obtained from Nanocyl (Belgium). Nanosilica was a dimethyldichlorosilane treated fumed silica (Aerosil R 974) obtained from Evonik Degussa. Halloysite, a clay mineral predominantly in the form of nanotubes, was purchased from Aldrich. Some properties of nanofillers used are listed in Table 2.2, Table 2.3, Table 2.4 and Table 2.5.

Table 2.2 Properties of Cloisite 10A and 30B organoclays

	Cloisite 10A	Cloisite 30B
Organic Modifier		
Modifier Concentration	125 meq / 100 g clay	90 meq / 100g clay
Loss on Ignition	~ 39 wt.%	~ 30 wt.%
Tallow Group	~65% C18 ~30% C16 ~5% C14	~65% C18 ~30% C16 ~5% C14
Density	1.90 g/cm ³	1.98 g/cm ³
Color	Off-White	Off-White
Particle Size	d(0.1) < 2 μm d(0.5) < 6 μm d(0.9) < 13 μm	d(0.1) < 2 μm d(0.5) < 6 μm d(0.9) < 13 μm

Data given by the producer.

Table 2.3 Properties of multi-walled carbon nanotubes

Average Outer Diameter ⁺	9.5 nm
Average Length ⁺	1.5 μm
Carbon Content ⁺	90 %
Impurity ^{+,++}	8.6 wt% (in oxide form)

⁺ Data given by the producer.

⁺⁺ Data determined in this study.

Table 2.4 Properties of nanosilica

Surface Modifier	Dimethyldichlorosilane
Primary Particle Size	12 nm
Density	2.24 g/cm ³
Specific Surface Area	170 m ² /g

Data given by the producer.

Table 2.5 Properties of halloysite nanotubes

Nanotube Outer Diameter	30 – 70 nm
Nanotube Length	1 – 3 μm
Specific Surface Area	65 m ² /g
Density	2.53 g/cm ³

Data given by the producer.

2.1.3 Flame Retardants

Certain flame retardant additives were used depending on the purpose of each section and the type of matrix polymer. A multi-component, synergistic mixture of aluminum diethylphosphinate, melamine polyphosphate and zinc borate, was kindly donated by Clariant (Exolit® OP1312). Chemical structures of ingredients and some properties of this organophosphorus (OP) flame retardant are shown in Table 2.6 and Table 2.7 respectively. Aluminum diethylphosphinate (AlPi) with no synergists, properties of which are listed in Table 2.8 was also donated by Clariant (Exolit® OP1240). Aluminum tri-hydroxide (ATH) flame retardant additive was provided with an average particle size of 12 μm (Nabaltec Apyral-16). Properties of ATH are given in Table 2.9.

2.1.4 Fiber Reinforcement

Aminosilane (γ -aminopropyltrimethoxysilane) treated short glass fibers were supplied from CAMELYAF having 4.5 mm initial length and 13 μm nominal diameter.

Table 2.6 Chemical structures of the constituents of OP1312 flame retardant

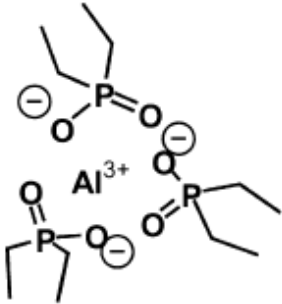
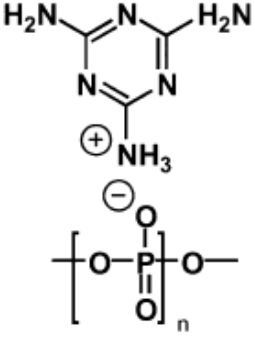
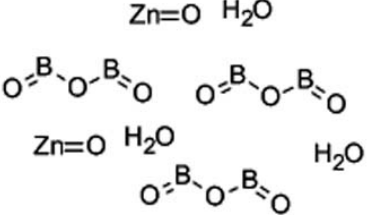
<p>Aluminum diethylphosphinate</p>	
<p>Melamine Polyphosphate</p>	
<p>Zinc Borate</p>	

Table 2.7 Properties of OP1312 flame retardant

Phosphorus Content ⁺	18.7 – 19.7 wt%
Particle Size ⁺⁺	d(0.1) < 18 μm d(0.5) < 40 μm d(0.9) < 71 μm
Color ⁺	White
Density ⁺	1.50 g/cm ³

⁺ Data given by the producer.

⁺⁺ Data determined in this study.

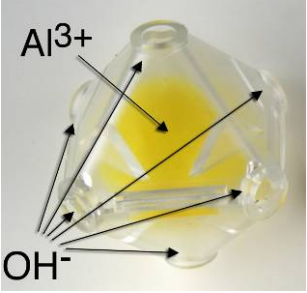
Table 2.8 Properties of aluminum diethylphosphinate flame retardant

Phosphorus Content ⁺	23.3 – 24.0 wt%
Particle Size ⁺⁺	d(0.1) < 19 μm d(0.5) < 50 μm d(0.9) < 98 μm
Color ⁺	White
Density ⁺	1.35 g/cm ³

⁺ Data given by the producer.

⁺⁺ Data determined in this study.

Table 2.9 Properties of aluminum hydroxide flame retardant

<p>Chemical Structure</p>	
<p>Dehydration Onset Temperature ⁺⁺</p>	<p>230 °C</p>
<p>Maximum Dehydration Temperature ⁺⁺</p>	<p>310 °C</p>
<p>Enthalpy of Dehydration</p>	<p>1300 J/g</p>
<p>Water Release ⁺⁺</p>	<p>35 wt.%</p>
<p>Color ⁺</p>	<p>White</p>
<p>Particle Size ⁺</p>	<p>d(0.1) < 1.5 μm d(0.5) < 12 μm d(0.9) < 40 μm</p>
<p>Density ⁺</p>	<p>2.4 g/cm³</p>

⁺ Data given by the producer.

⁺⁺ Data determined in this study.

2.2 PREPARATION OF SAMPLES

Materials were compounded by either mixing the constituents with the polymer in the molten state (melt mixing) or in solution (solution mixing). Samples were then shaped into standard specimen dimensions using compression molding and ram-type injection molding techniques. Details regarding mixing and shaping processes specific to each purpose of the thesis are summarized in Table 2.10.

2.2.1 Melt Mixing

Melt mixing was carried out using lab-scale co-rotating twin-screw extruders (Rondol Microlab 10 mm Twin-Screw Extruder, L/D:20; DSM Xplore 15 ml Micro-compounder; Thermoprism TSE 16 TC Twin-Screw Extruder, L/D:24). All constituents were first mechanically homogenized and fed continuously into the extruders' main feeding zone. Appropriate extruder processing conditions were defined and applied for each batch of samples. When necessary, materials were dried under vacuum overnight prior to melt mixing.

2.2.2 Solution Mixing

Solution mixing was done by first dispersing nanofillers and/or flame retardant additives in toluene using a high-power ultrasonic horn (Bandelin Sonopuls HD3200, 220 W) under amplitude control at full-amplitude. Then, polymers were dissolved in ultrasound treated dispersions under vigorous magnetic stirring (Heidolph MR Hei-tec and IKA RCT basic) to attain 10 % w/v polymer concentration in solvent. Polymer solutions were not exposed to ultrasound in order to avoid molecular weight reductions. These were followed by casting onto glass petri dishes, effective removal of solvent and subsequent milling into small pieces (IKA A11 basic analytical mill) for shaping processes.

2.2.3 Shaping Processes

Solution- or melt-mixed materials were dried under vacuum at 60–80°C at least overnight prior to all shaping processes. Samples for mass loss cone calorimeter studies were produced by compression molding using a custom built hot press. Specimens for flammability and tension tests were produced by lab-scale ram-type injection molding devices (DSM XPlore 12 ml injection molder; Daga Micro-injector).

Table 2.10 Parameters used for mixing and shaping processes

	Melt Mixing	Solution Mixing	Injection Molding
Effect of Nanofiller Type	DSM Xplore Micro-compounder 240 °C, 3 min.	BANDELIN Sonopuls 220 W high-power ultrasonic horn, 3 min full-amplitude	Daga Micro-injector 240 / 65 °C
Effect of Nanofiller Dispersion	DSM Xplore Micro-compounder 210 °C, 3 min.	BANDELIN Sonopuls 220 W high-power ultrasonic horn, 10 min full-amplitude	Daga Micro-injector 210 / 55 °C
Effect of Nanofiller Geometry	Rondol Microlab 10 mm TSE 185 – 205 °C	–	DSM 12 ml injection Molder 190 / 30 °C
Effect of Fiber Reinforcement	Thermoprism TSE 16 TC, 240 °C	–	Daga Micro-injector 240 / 80 °C

2.3 EVALUATION OF FLAME RETARDANCY

All the studied materials were tested for their fire behavior and flammability properties using mass loss calorimetry, limiting oxygen index measurements and UL94 vertical/horizontal burning tests.

2.3.1 Mass Loss Cone Calorimeter Fire Testing

Fire behavior was evaluated using a mass loss calorimeter with chimney and thermopile attachments (Fire Testing Technology, UK) according to the procedure described in ISO 13927. A data acquisition system (Keithley KUSB 3100) was implemented to the mass loss calorimeter to record time dependent heat release rate and sample mass data for further data evaluation. Temperature of the conical heater was adjusted to produce an external heat flux of 35 kW/m^2 on exposed samples. Each time before testing different sample batches, the equipment was calibrated to correlate the measured thermopile temperatures to rates of heat release during combustion. Reference measurements on samples indicated that the obtained heat release rates were repeatable within $\pm 10\%$.

2.3.2 LOI and UL94 Flammability Testing

Limiting oxygen index was assessed according to ISO 4589 on an oxygen index apparatus (Fire Testing Technology, UK) having a paramagnetic oxygen analyzer so that precise adjustments of the oxygen concentration can be performed and repeatable results are obtained. Oxygen concentrations were varied according to Dixon's up-and-down procedure explained in ISO 4589. The method entails the use of a large number of specimens to determine oxygen index with a standard deviation of $\sim 0.2\% \text{ O}_2$.

Samples were classified according to the standards of Underwriters Laboratories (UL94) for their flammability using vertical and horizontal burning tests on a custom flammability meter.

2.4 CHARACTERIZATION TECHNIQUES

In this thesis, a variety of characterization tools were utilized to reveal the morphology, thermal stability, flame retardancy mechanisms and mechanical properties of nanocomposites.

2.4.1 Transmission Electron Microscopy

Transmission electron microscopy of polymer nanocomposite samples was conducted with high-resolution transmission electron microscopes (JEOL JEM-2100 LaB₆ at 200 kV under low dose conditions; FEI TECNAI G² F30 at 100 kV; FEI Tecnai G² Spirit BioTWIN at 80 kV). For TEM studies, thin sections of 100 nm nominal thickness were sliced from injection molded samples using an ultramicrotome (Leica EM UC6) with a diamond knife operated at room temperature and transferred to 400 mesh copper grids. Powdered chars were investigated on holey carbon coated copper grids using a high-resolution field-emission transmission electron microscope (JEOL JEM 2100F) under 200 kV acceleration voltage.

2.4.2 Scanning Electron Microscopy

Fracture surfaces of tension test samples and barrier morphologies of char residues from limiting oxygen index (ignited at O₂ concentrations close to the limiting oxygen index) and mass loss calorimeter analysis were characterized by scanning electron microscopes (JEOL JSM 6400 SEM; FEI Nova NanoSEM 430 field-emission gun SEM). All non-conducting samples were gold-sputtered using sputter coating devices (Anatech Hummle VII and Quorum Technologies SC7640 sputter coaters) prior to analysis. Char residues and fracture surfaces were also analyzed by means of energy dispersive X-ray spectroscopy attached to scanning electron microscopes (SEM-EDS) for the presence of elements such as P, Al, Si, Fe and O.

2.4.3 X-Ray Diffraction

X-ray diffraction was performed on a horizontal goniometer device (Rigaku D-Max 2200 Diffractometer) with Bragg-Brentano focusing optics operating in the $\theta - \theta$ scanning mode. Measurements were done using monochromatic $\text{CuK}\alpha$ radiation (40 kV, 40 mA) by continuous scanning over $1^\circ < 2\theta < 10^\circ$ or $10^\circ < 2\theta < 80^\circ$ diffraction angle ranges with scanning rates of either $1^\circ/\text{min}$ or $5^\circ/\text{min}$, and step size of 0.02° . Nanocomposites were characterized in injection-molded bulk forms whereas nanofillers and mass loss calorimeter fire residues were in homogeneous powder forms.

2.4.4 Thermal Analysis

Thermogravimetric analysis was carried out on thermogravimetric analyzers (Perkin Elmer Pyris1; Shimadzu DTG50H) at $10^\circ\text{C}/\text{min}$ heating rate with flowing nitrogen at a rate of 50–80 ml/min. Heat flow during heating and cooling was determined using a differential scanning calorimeter (Mettler-Toledo DSC1 Star System). Small samples of similar weight were analyzed to avoid sample size effects and to ensure temperature homogeneity throughout samples during TGA and DSC runs.

2.4.5 Direct Pyrolysis Mass Spectrometry

Direct pyrolysis mass spectrometry analyses were performed by Waters Micromass Quattro Micro GC Mass Spectrometer coupled to a direct insertion probe. During pyrolysis, the temperature was increased to 50°C at a rate of $5^\circ\text{C}/\text{min}$, then was raised to 650°C with a rate of $10^\circ\text{C}/\text{min}$ and kept at 650°C for 5 additional minutes. Samples (0.010 mg) were pyrolyzed in quartz sample vials while recording 70eV EI mass spectra at a mass scan rate of 1 scan/s. The analyses were repeated several times to ensure reproducibility. Each time almost exactly the same trends were detected.

2.4.6 Infrared Spectroscopy

Characterization of residues was done by attenuated total reflectance – Fourier-transform infrared spectroscopy using a spectrometer (Bruker Optics Tensor Series FTIR Spectrometer) with 32 scans at an optical resolution of 4 cm^{-1} . Residues were collected from mass loss calorimeter fire tests and ground/homogenized by a mortar and pestle prior to analysis.

2.4.7 Mechanical Testing

Tensile properties were determined on universal testing machines (Shimadzu AGS-J 10 kN; Instron 5565A 5 kN) at a cross-head speed of 1 mm/min according to ISO 527-2 standards. At least three specimens were tested for each studied sample composition. Strain values were obtained directly from crosshead displacement without the use of an extensometer. Young's Moduli were calculated as the slope of tensile stress - strain curves within a strain range of 0.0005 to 0.0025 mm/mm.

2.4.8 Fiber Length Distribution

Fiber length distributions were determined by conducting semi-automated photomicrography on short glass fiber residues deposited on glass slides which were obtained upon burning of the matrix at 650–800°C for 1 h. Following twin-screw extrusion, over 600 fibers were analyzed for each sample to obtain representative residual fiber length distributions in composites.

CHAPTER 3

RESULTS AND DISCUSSION

3.1 EFFECT OF NANOFILLER TYPE

The first aim of this study was to compare the potential synergistic flame retardancy action of different type of nanofillers; nanoclays and carbon nanotubes, used in combination with a halogen-free organophosphorus intumescent flame retardant additive in poly(methyl methacrylate) (PMMA) matrix. The organophosphorus additive is based on phosphorus and nitrogenous salts and it is among the most suitable halogen-free flame retardants for acrylic polymers processed at high temperatures.

In this part of the thesis, samples with compositions and designations given in Table 3.1 were investigated. Melt mixing was utilized for materials that contain nanoclay (NC) and/or organophosphorus (OP) flame retardant whereas high power ultrasound assisted solution mixing was chosen for materials with carbon nanotubes (CNT) to obtain the finest dispersion in the polymer matrix.

Table 3.1 Designations, compositions (wt%) and utilized dispersion techniques to reveal the effect of nanofiller type

Sample Designation	PMMA	Nanoclay (NC)	Carbon Nanotube (CNT)	Flame Retardant (OP)	Dispersion technique
PMMA	100	-	-	-	-
NC-PMMA	97	3	-	-	Melt mixing
CNT-PMMA	99	-	1	-	Solution mixing
PMMA/OP9	91	-	-	9	Melt mixing
NC-PMMA /OP9	88	3	-	9	Melt mixing
CNT-PMMA /OP9	90	-	1	9	Solution mixing
PMMA/OP18	82	-	-	18	Melt mixing
NC-PMMA /OP18	79	3	-	18	Melt mixing
CNT-PMMA /OP18	81	-	1	18	Solution mixing

Characterization of nanomorphology and nanodispersion was done by XRD and TEM techniques. Flame retardancy was evaluated by mass loss calorimeter analysis and limiting oxygen index measurements. Fire residues were analyzed by SEM for microstructure, ATR-FTIR spectroscopy for chemical analysis and XRD for the characterization of stacked montmorillonite structure. Thermal stability was studied by thermogravimetric analysis. In order to reveal the overlapping degradation steps, differential thermogravimetric curves were obtained and further analyzed by carrying out peak deconvolution using mixed Gaussian-Lorentzian line shapes. Thermal degradation mechanisms were studied by direct pyrolysis mass spectrometry. Mechanical properties and glass transition behavior were investigated by tension tests and DSC, respectively. Tensile fracture surfaces were observed under SEM.

In order to confirm that PMMA did not undergo degradation during melt mixing and shaping processes, molecular weights were determined by dilute solution viscosity technique on samples that have been shear mixed (either in solution or in the molten state) and injection molded to the final shape. Samples containing nanofillers and flame retardant additive were first dissolved in toluene, centrifuged and filtered. The solutions were evaporated to dry off the solvent to obtain completely extracted

PMMA. Then, the samples were weighed, dissolved in chloroform and filtered through 0.45 μm PTFE membrane prior to the viscosity measurements. An Ubbelohde type glass capillary viscometer was utilized to determine the intrinsic viscosities at 25°C. Mark-Houwink constants of $a = 0.80$ and $K = 0.0048 \text{ mL/g}$ were used from the Polymer Handbook [87]. Measured viscosity average molecular weights (Table 3.2) ranged between 1.9 and $2.1 \times 10^5 \text{ g/mol}$ indicating that polymer matrix did not undergo notable degradation during processing.

Table 3.2 Molecular weights of PMMA matrix after processing

	Intrinsic Viscosity, $[\eta]$ (dL/g)	Viscosity average molecular weight, M_v (g/mol)
As-received PMMA	0.8662	210 000
Extruded and molded PMMA	0.7886	190 000
CNT-PMMA	0.8700	210 000
CNT-PMMA/OP	0.8328	200 000
NC-PMMA	0.8121	190 000
NC-PMMA/OP	0.8395	200 000

3.1.1 Nanomorphology

Table 3.3 summarizes clay interlayer spacings (d_{001}) and extents of intercalation in nanocomposites of neat- and flame-retarded PMMA calculated using the obtained XRD profiles provided in Figure 3.1. Clay interlayer spacings were calculated at the peak diffracted intensity using Bragg's law as $n\lambda = 2d\sin\theta_B$ where λ is the wavelength used, θ_B is the diffraction angle and d is the interplanar spacing or more specifically the clay interlayer spacing. Extents of intercalation were calculated using Gaussian peak deconvolution of XRD data, as an average of two experiments on each sample (Figure 3.2). Extent of intercalation was taken as the sum of integrated intensities for first and second order reflections (I_{001} and I_{002}) of the intercalated state divided by the total integrated intensity; % intercalation = $(I_{001} + I_{002}) / I_{\text{total}}$

Polymer intercalation in nanoclay interlayers is clear considering the increases in the original value of d_{001} of pristine nanoclay (~1.8 nm) upon melt-mixing with the polymer matrix (~3.6 nm). Interlayer spacings for polymer intercalated nanoclays, designated as d_{001} (intercalated), are almost the same for neat- and flame-retarded nanocomposites. Neat clay nanocomposite displays an additional low intensity peak attributed to a higher order reflection of the intercalated state, i.e. d_{002} (intercalated). However, the additional reflections present in flame-retarded formulations with nanoclays point out some non-intercalation since peak positions referred to as d_{001} (non-intercalated) marked in Figure 3.1 corresponds to the original value of d_{001} for pristine nanoclay rather than the d_{002} (intercalated) of the intercalated state.

Figure 3.3 shows the results of annealing experiments conducted on nanoclays to simulate the degradation of the organic modifier during twin-screw extrusion processing. The gradual collapse of the structure occurs from an initial interlayer spacing of 1.79 nm to 1.25 nm which is close to that of unmodified montmorillonite. Therefore, the additional reflections of flame-retarded nanocomposites around 1.74-1.76 nm which are lower than that of pristine nanoclay can simply be attributed to thermally degraded nanoclays with no polymer intercalation.

Table 3.3 Calculated XRD data for PMMA/clay nanocomposites

	d_{001} intercalated (nm)	d_{001} non- intercalated (nm)	Extent of Intercalation (%)	Nanocomposite Morphology
NC	1.79	-	-	-
NC-PMMA	3.51	-	100	Full Intercalation
NC-PMMA/OP9	3.59	1.74	53.9	Partial Intercalation
NC-PMMA/OP18	3.62	1.76	35.5	Partial Intercalation

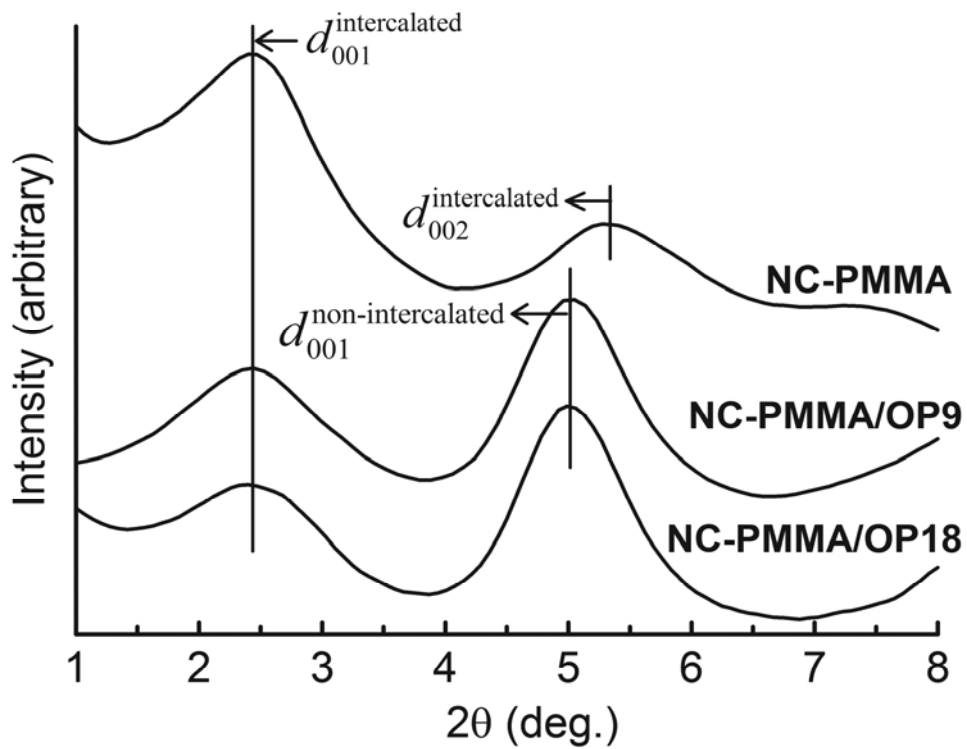


Figure 3.1 XRD patterns of neat- and flame-retarded PMMA/clay nanocomposites

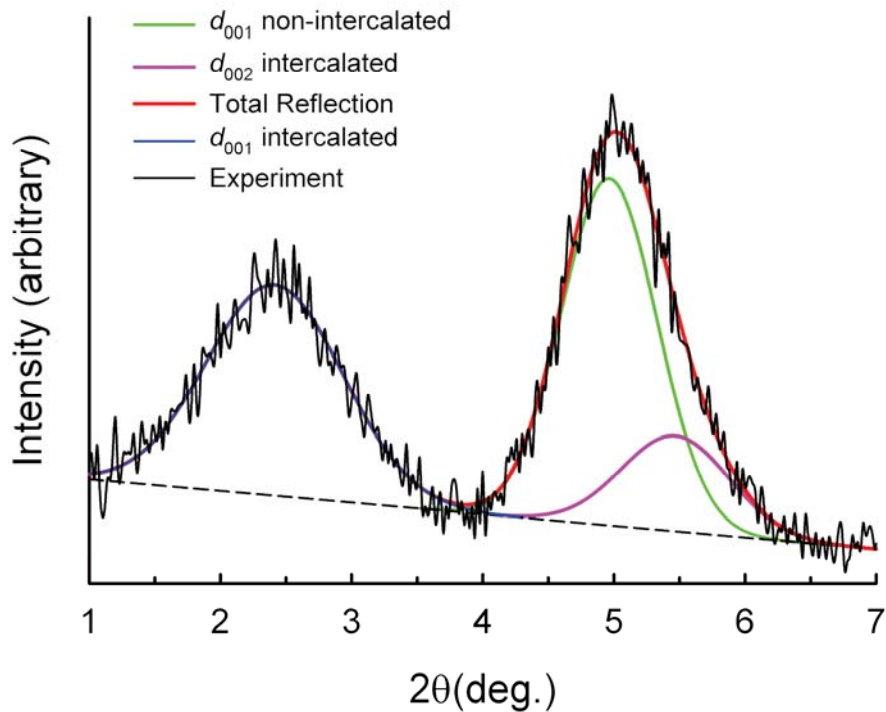


Figure 3.2 Gaussian peak deconvolution of XRD profile recorded from NC-PMMA/OP9 sample

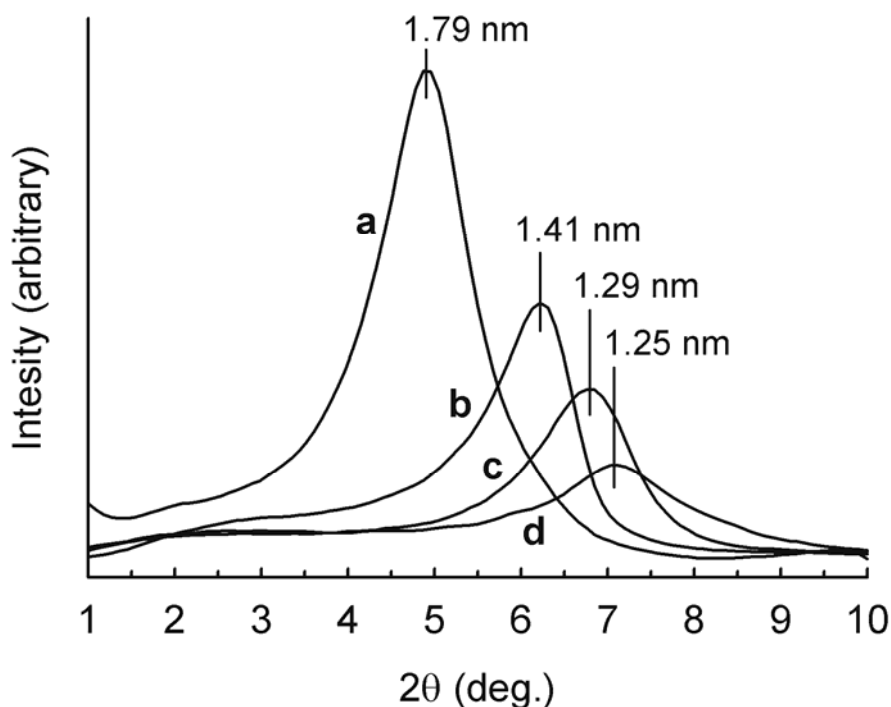


Figure 3.3 Effect of thermal degradation on clay interlayer spacings; (a) pristine nanoclay, (b) 10 min. at 240°C, (c) 30 min. 240°C, and (d) 1 h at 700°C

In light of the above discussions, the extent of intercalation was found to change remarkably from almost full intercalation to partial intercalation with the incorporation of the flame retardant additive in clay nanocomposites. It is fairly disappointing but worth to conclude that the presence of the flame retardant additive significantly deteriorates the dispersion of nanoclays within the polymer matrix. Consequently, non-intercalated microcomposite morphology is partially favored in expense of the intercalated nanocomposite. A convincing explanation for the deteriorated dispersion could be given by considering organoclay agglomeration on the surfaces of flame retardant particles during melt mixing. A detailed study by Samyn et al. [88] investigating the characterization of organoclay dispersion in flame-retarded polymers strongly suggests similar phenomena. They stated that the morphology of poly(butylene terephthalate)/clay system was changed from intercalated nanocomposite to microcomposite with the incorporation of a phosphorus-based flame-retardant additive.

TEM image in Figure 3.4 displays fully intercalated clay mineral particles dispersed in the polymer. A closer view of the particle indicates expansion of the clay interlayers spacing upon polymer intercalation. Figure 3.5 displays the concurrence of clay mineral particles consisting of 1–3 nanolayers and coarser aggregates. A larger magnification image of the aggregate reveals that clay nanolayer stacks display partial polymer intercalation since darker regions within the aggregate remained non-intercalated. Full intercalation in the clay nanocomposite and partial intercalation in flame-retarded nanocomposites, as interpreted by XRD, were confirmed with TEM nanomorphologies.

SEM image in Figure 3.6(a) displays as-received multi-walled carbon nanotubes present in the form of bundles and ropes due to van der Waals interactions between individual nanotubes. Figure 3.6(b) is a closer look showing that a branch of nanotube ropes consists of several bundled nanotubes prior to the dispersion treatment. Upon the ultrasound-assisted solution mixing treatment, CNT-PMMA nanocomposites contained well-dispersed, de-bundled nanotubes embedded in PMMA, as shown in Figure 3.7. The larger magnification image shows isolated nanotubes formed by dispersive mixing that allows for percolating networks to be established.

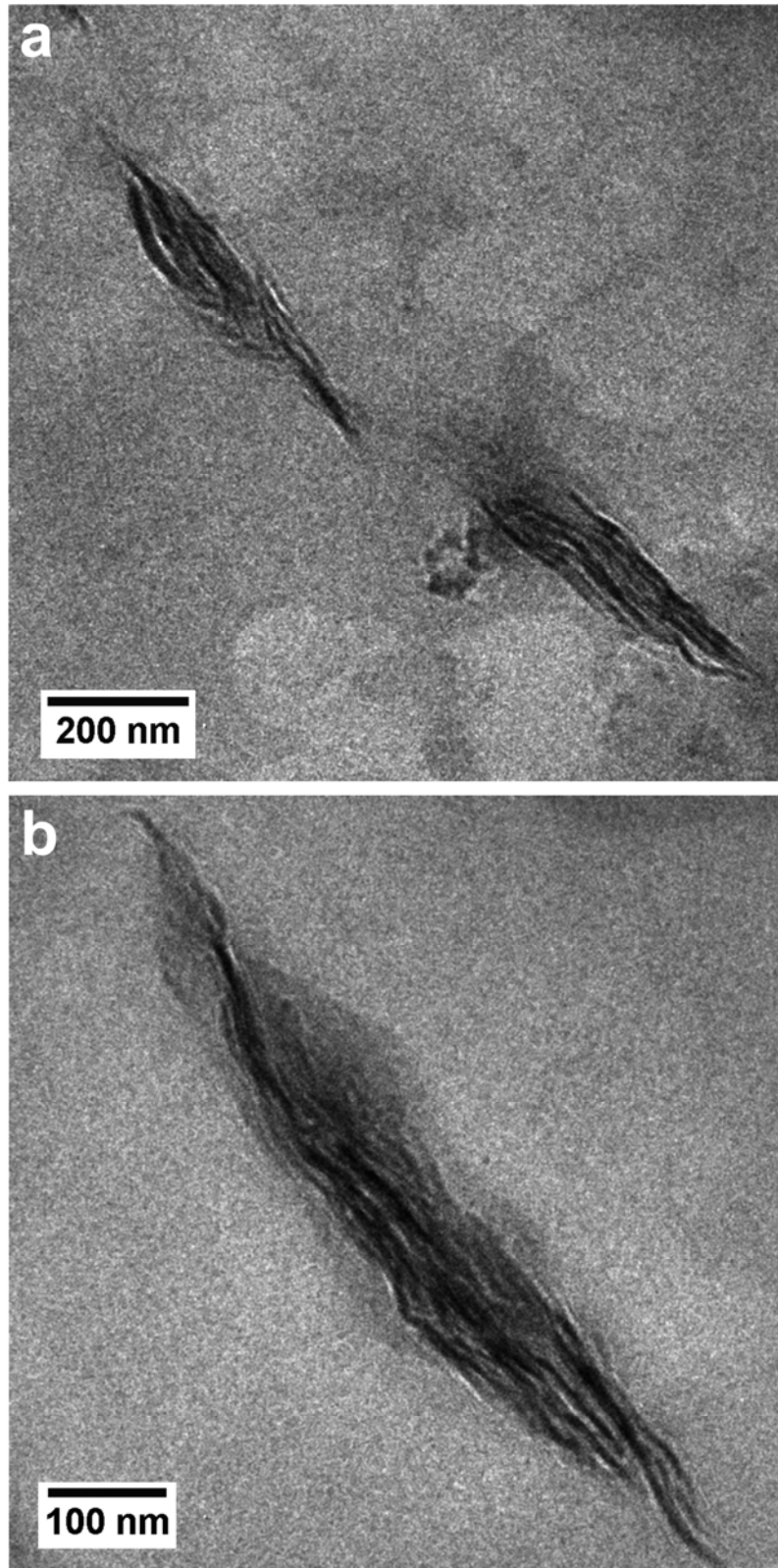


Figure 3.4 TEM micrographs of fully intercalated particles in NC-PMMA nanocomposite; (a) general and (b) closer view of intercalated clay mineral particles

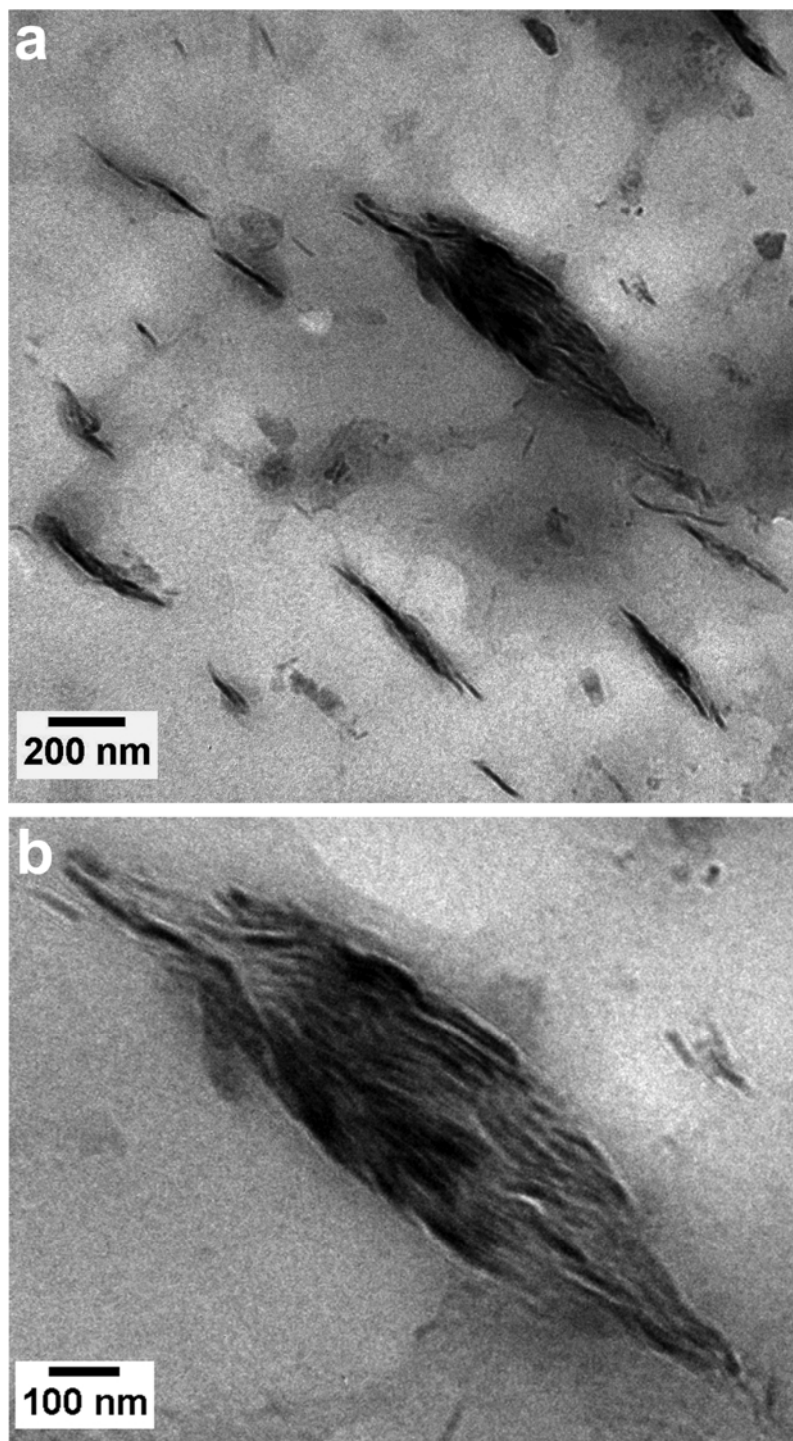


Figure 3.5 TEM micrographs of NC-PMMA/OP9 nanocomposite (a) showing partial polymer intercalation and (b) a closer view of partially intercalated aggregate

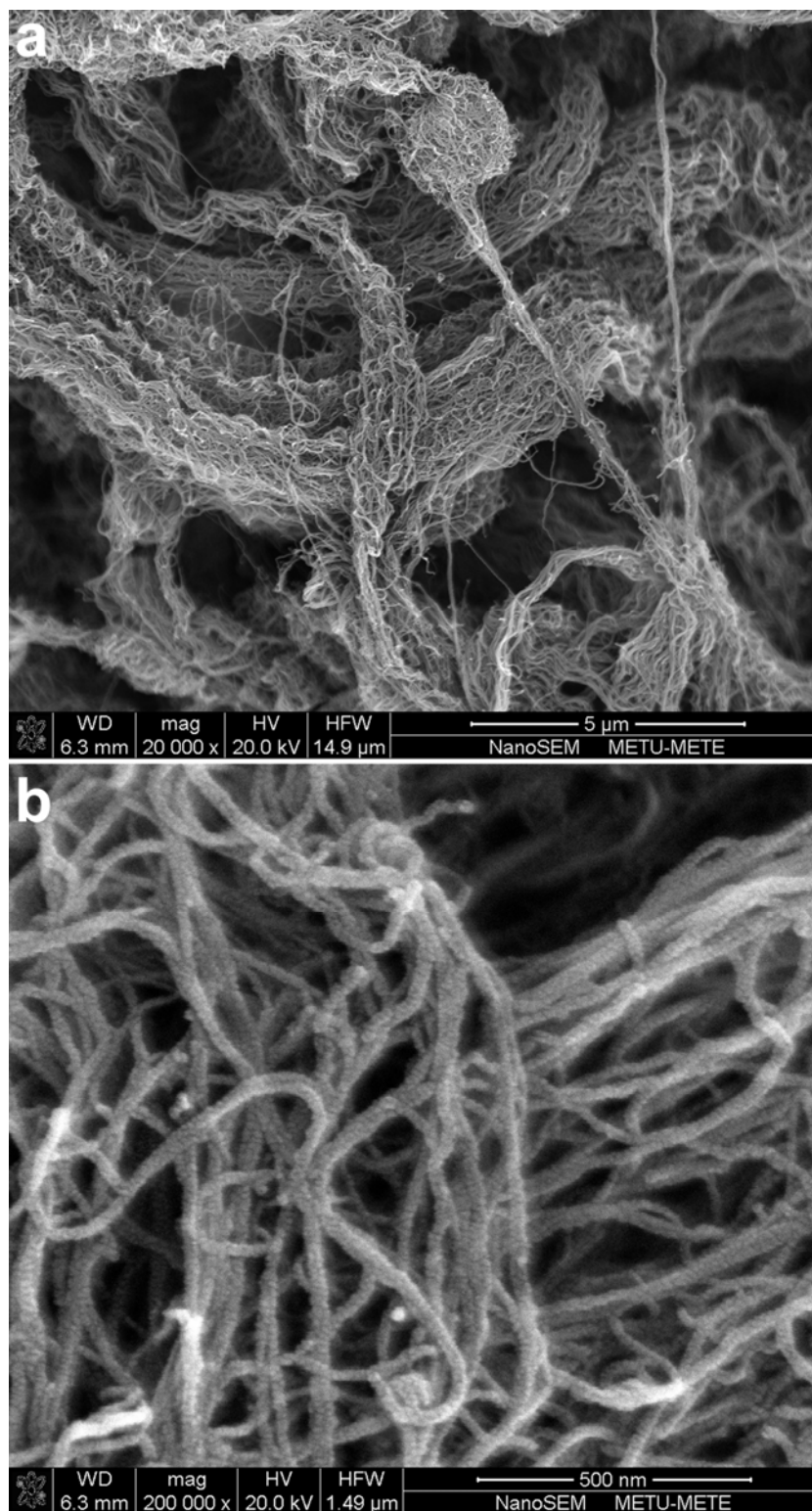


Figure 3.6 (a) and (b) SEM images showing bundles and ropes of as-received multi-walled carbon nanotubes prior to ultrasound-assisted solution mixing

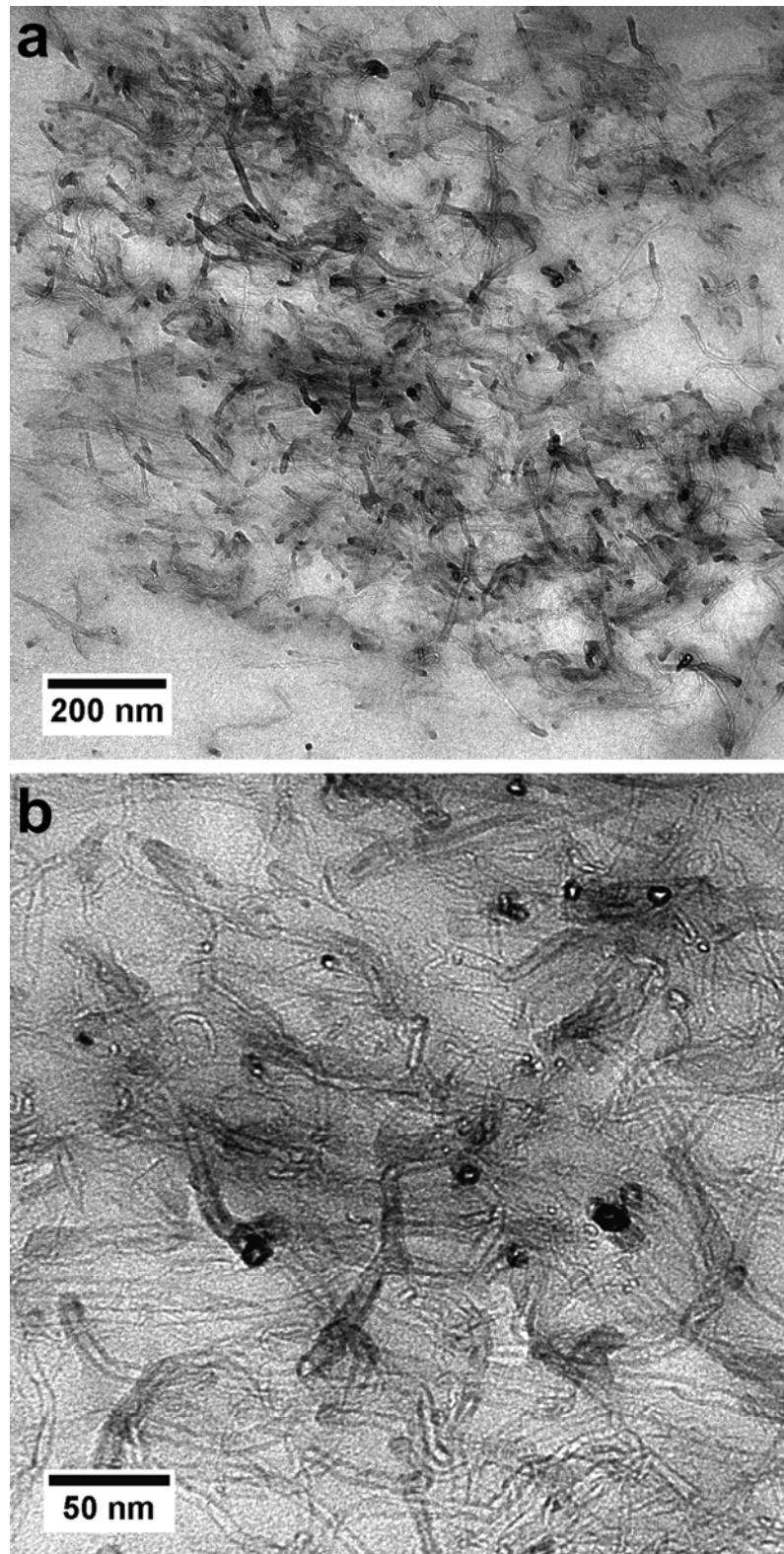


Figure 3.7 (a) TEM image of de-bundled carbon nanotubes well-dispersed in PMMA matrix (b) larger magnification TEM image of carbon nanotubes in PMMA

3.1.2 Flame Retardancy

(i) LOI Flammability Tests

Table 3.4 summarizes the limiting oxygen indices of the investigated materials. Neat PMMA has a considerably low LOI of 17.3% which was slightly improved with the incorporation of nanoclays (18.5%) and carbon nanotubes (19.0%) at small corresponding weight fractions. These slight improvements were obtained through the migration of nanoparticles towards the flaming surface covering and shielding the underlying polymer.

Thin blown chars were developed in the late stages of combustion during the oxygen index tests of PMMA containing the organophosphorus flame retardant additive. These well-blown char structures impede heat transfer from the flame which ensures increased oxygen demand to sustain flaming combustion in proportion with the flame retardant additive content, i.e. from 17.3% of neat PMMA to 20.1% for PMMA/OP9 and 21.9% for PMMA/OP18.

Table 3.4 Limiting oxygen index values showing the effect of nanofiller type

	LOI (%O₂ ± 2σ)
neat PMMA	17.3 ± 0.2
NC-PMMA	18.5 ± 0.2
CNT-PMMA	19.0 ± 0.3
PMMA/OP9	20.1 ± 0.2
NC-PMMA/OP9	20.7 ± 0.2
CNT-PMMA/OP9	21.7 ± 0.2
PMMA/OP18	21.9 ± 0.2
NC-PMMA/OP18	22.5 ± 0.2
CNT-PMMA/OP18	22.9 ± 0.2

Limiting oxygen index of flame-retarded PMMA were further slightly improved by nanoclays, from 20.1% for PMMA/OP9 to 20.7% for NC-PMMA/OP9, and 21.9% for PMMA/OP18 to 22.5% for NC-PMMA/OP18, owing to thicker and stronger chars via clay nanolayer reinforcement, established without losing the blown char structure. It is apparent that carbon nanotubes have a greater influence on LOI compared to nanoclays. LOI were increased from 20.1% for PMMA/OP9 to 21.7% for CNT-PMMA/OP9, and 21.9% for PMMA/OP18 to 22.9% for CNT-PMMA/OP18. The blown structure of char residues were lost with the incorporation of carbon nanotubes due to the restraint of the mechanically strong carbon nanotube network rapidly formed on flaming surfaces. However, protective barriers possessing a consolidated, crack-free and thick character were able to form at much earlier stages of combustion. Thus, carbon nanotubes can be said to provide enhanced flame retardancy compared to nanoclays in terms of the limiting oxygen index.

(ii) Mass Loss Cone Calorimeter Analysis

Table 3.5 lists the important fire properties, as interpreted from mass loss calorimeter analysis. Migration of carbon nanotubes towards the exposed surface provides the formation of a thin but continuous network covering the whole sample. Although the amount of nanoparticles in NC-PMMA is higher than that of CNT-PMMA, the char layer of NC-PMMA forms as a thicker but discontinuous one demonstrating a less effective protective character. However, a slightly lower peak heat release rate (PHRR) could still be attained with respect to neat PMMA by nanoclays ($-\Delta=30\%$) in comparison with carbon nanotubes ($-\Delta=25\%$).

The PHRR reduction provided by carbon nanotubes in this study conforms to those reported earlier by Costache et al. [9] for 3 wt% multi-walled carbon nanotubes ($-\Delta = 29\%$). Reductions in the order of 50–60% were demonstrated by Kashiwagi et al. [34] only by utilizing fine dispersions of single-walled nanotubes ultrasonicated at a very low concentration in solvent (0.2 mg/ml). In their study, a higher and somewhat more feasible concentration of nanotubes in the solvent (1 mg/ml) resulted in a very low efficiency ($-\Delta \sim 10\%$) in terms of the reduction in PHRR.

Table 3.5 Interpreted mass loss calorimeter data showing the effect of nanofiller type

	PHRR (-Δ%) (kW/m²)	THE (MJ/m²)	THE/TML (MJ/m²g)	PMLR (g/m²s)	Residue (%)	FGI (kW/m²)
PMMA	855	78	3.4	27.2	0	20.9
NC-PMMA	602 (30)	78	3.3	21.3	2.9	15.0
CNT-PMMA	644 (25)	74	3.4	20.6	2.7	17.0
PMMA/OP9	425 (50)	74	2.9	15.9	3.7	10.4
NC-PMMA/OP9	409 (52)	69	2.8	15.3	7.9	10.8
CNT-PMMA/OP9	490 (43)	72	3.0	18.2	4.2	12.9
PMMA/OP18	319 (63)	71	2.8	12.2	5.8	7.4
NC-PMMA/OP18	290 (66)	67	2.7	10.2	13.3	7.2
CNT-PMMA/OP18	437 (49)	66	2.8	16.3	6.3	10.9

In the case of clay nanocomposites, PHRR reductions in the range of 20 – 30% were shown with clay loadings of 4 – 6% in PMMA by Jash and Wilkie [89] investigating various clay surface modifiers. A few more studies exist on the fire performance of PMMA/clay nanocomposites reporting reductions in the range of 10–35% with respect to neat PMMA [9, 31, 90, 91]. Accordingly, the performance of the 3 wt% clay nanocomposite of this study ($-\Delta = 30\%$) is consistent with previous studies.

Peak heat release rates were remarkably suppressed by 50% and 63% with the incorporation of 9 and 18 wt% organophosphorus additive, respectively. PHRRs were further lowered by nanoclay additions to PMMA/OP9 and PMMA/OP18 samples in which suppressions were 52% and 66%, respectively. Interestingly, contrary to the common opinion in the synergistic action of carbon nanotubes with conventional flame-retardants [39, 41, 92], a clear anti-synergism was encountered between the organophosphorus flame retardant additive and carbon nanotubes. Consequently, PHRRs were increased compared to flame-retarded samples without nanofillers, and suppressions were lowered to 43% and 49% with CNT-PMMA/OP9 and CNT-PMMA/OP18, respectively. A similar result regarding an increase in PHRR was presented in a recent study [38] investigating the interaction of multi-walled carbon nanotubes incorporated in an intumescent formulation.

It was mentioned above that carbon nanotubes are more effective than nanoclays in terms of limiting oxygen index performance. However, it should be noted that, under the forced flaming conditions of the mass loss calorimeter, intumescence plays a great role in decreasing the effective heat flux on the exposed specimen surface. The perfectly blown, thicker and denser char residues from NC-PMMA/OP samples provide the highest level of flame retardancy in terms of PHRR, compared to CNT-PMMA/OP counterparts. On the other hand, due to the inability of samples containing carbon nanotubes to show intumescence, a synergistic flame retardancy action could not take part between carbon nanotubes and the organophosphorus flame retardant additive.

Apart from the differences in the form of char residues, nanoclay containing neat and flame-retarded PMMA yielded considerably higher amounts of fire residues (approximately two-fold) compared to samples with carbon nanotubes and/or organophosphorus flame retardant additive (Table 3.5), as a verification of thicker chars formed in the presence of nanoclays.

Total-heat-evolved (THE), a measure of material's contribution to the total fire load, were lowered in proportion with the loading level of organophosphorus flame retardant additive. Incorporation of nanoclay and carbon nanotubes in flame-retarded PMMA both had a positive effect on decreasing the total-heat evolved from samples.

Considering total-heat-evolved/total-mass-loss (THE/TML), a ratio that allows for the deduction of availability of any gas phase flame retardancy, the flame retardant acts to some extent in the gas phase in addition to its established condensed phase action in PMMA [55]. THE/TML were reduced from 3.4 MJ/m² for neat PMMA to 2.9 and 2.8 MJ/m² for PMMA/OP9 and PMMA/OP18 samples, respectively. The organophosphorus flame retardant influences the combustion behavior of PMMA primarily by intumescence in the condensed phase accompanied with flame inhibition in the gas phase. In the former mechanism, transport of oxygen and flammable volatiles are impeded, and polymer is shielded from the external radiant heat and the heat feedback of the flame by the act of the protective intumescent layer. The latter mechanism involves the evolution of flame inhibiting phosphorus species together with less-combustible products like melamine contributing to the gas-phase action [93, 94].

In particular, nanoclay and carbon nanotubes act almost completely in the condensed phase as can be inferred from maintained THE/TML values of ~3.4 MJ/m² and ~2.8 MJ/m² with the incorporation of nanofillers in neat and flame-retarded PMMA, respectively. Peak mass loss rate (PMLR) values prove that nanoclays surpass carbon nanotubes by providing further suppressions in rates of mass loss of flame-retarded PMMA as opposed to amplified values with carbon nanotubes.

A reasonable attempt to determine the flame spread as a fire hazard is to consider fire growth index (FGI) defined by PHRR/time-to-ignition [95]. Both nanofillers impeded the growth of a fire when incorporated in neat PMMA owing to the suppressed PHRR. Considering flame-retarded samples, FGI of CNT-PMMA/OP9 and CNT-PMMA/OP18 were remarkably larger than those of PMMA/OP9 and PMMA/OP18, respectively. Higher PHRRs led to significantly increased flame spread of carbon nanotube containing samples in terms of FGI. On the other hand, nanoclays did not significantly alter flame spread.

It can be concluded for both neat and flame-retarded PMMA that carbon nanotubes were more effective compared to nanoclays in terms of the protective barrier formed during combustion in the oxygen index test. Contrarily, as a result of the restraining forces exerted against intumescence by the strongly entangled carbon nanotube network formed on flaming surfaces in the early stages of combustion in cone calorimeter, nanoclays outperformed carbon nanotubes with regard to some major interpreted mass loss calorimetric fire properties; peak heat release rate, peak mass loss rate, fire residue and fire growth index.

Heat release behavior of neat PMMA was compared with PMMA containing the nanofillers and organophosphorus flame retardant additive in Figure 3.8. Heat release curves for CNT-PMMA and NC-PMMA resembles that of neat PMMA with only significant differences in PHRR.

Considering the CNT-PMMA nanocomposite, upon the start of exposure to external heat flux and subsequent ignition of the polymer, carbon nanotubes are rapidly carried towards the exposed surface by the acts of surface free energy and rising bubbles of methyl methacrylate. This provides the enrichment of carbon nanotubes at the surface to form a thin but crack-free, continuous and self-supporting protective layer. Upon formation of the protective surface barrier, vigorous rise and bursting of methyl methacrylate bubbles were inhibited leading to quiescent burning. Thus, the continuous barrier survived without the formation of discontinuous islands observed in an earlier study involving insufficient carbon nanotube concentrations or poor dispersions [34].

Samples containing the organophosphorus flame retardant additive demonstrate well-suppressed, steady heat release plateaus under the influence of protective intumescent char layer. An increase in the flame retardant content from 9 to 18 wt% provides a more stable and better blown intumescent char layer that ensures further decreased rates of heat release throughout combustion in the cone calorimeter. It appears as a conclusion that filler nanoparticles alone could not compete with the organophosphorus flame retardant additive in view of the reductions obtained in rates of heat release in the mass loss calorimeter.

Figure 3.9 displays the changes in heat release and mass loss behaviors of flame-retarded PMMA upon the incorporation of nanofillers. The presence of carbon nanotubes led to significantly decreased burning times, higher rates of heat release and mass loss, as discussed above in depth. Incorporation of nanoclays in flame-retarded samples did not remarkably alter the heat release behavior besides the suppressed rates of heat release.

Reduced values of heat release rates with nanoclay additions were accompanied by significantly suppressed rates of mass loss, indicative of the condensed-phase action of clay nanolayers. It is apparent that the intumescent char is reinforced at the nano-scale by clay nanolayers providing a stronger and thicker char structure that allows for an efficient impediment of mass transport across the protective layer. Contrarily, as a consequence of restricted intumescence, heat release and mass loss rates were amplified with carbon nanotubes showing a clear anti-synergism with the organophosphorus flame retardant additive.

The mass loss rate curves for PMMA/OP18 and NC-PMMA/OP18 are typical for an effective char forming material, in a way that the initial increase in the form of a peak is followed by a gradual smooth decrease with time upon the complete establishment of the intumescent layer. On the other hand, the mass loss rate curve of CNT-PMMA/OP18 possesses rapid mass loss with a peak value even larger than that of flame-retarded PMMA with no filler nanoparticles.

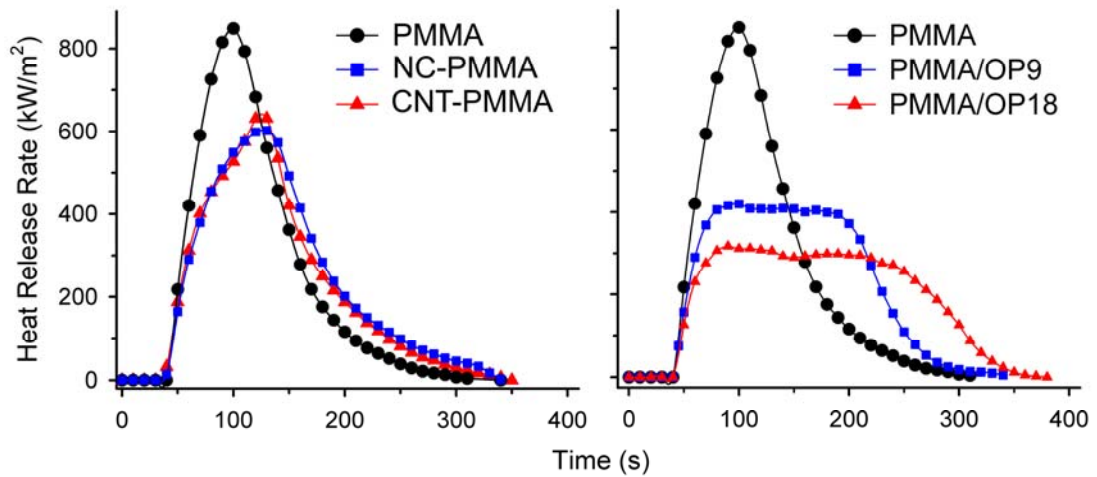


Figure 3.8 Effects of nanofillers and organophosphorus flame retardant additive on the heat release behavior of PMMA

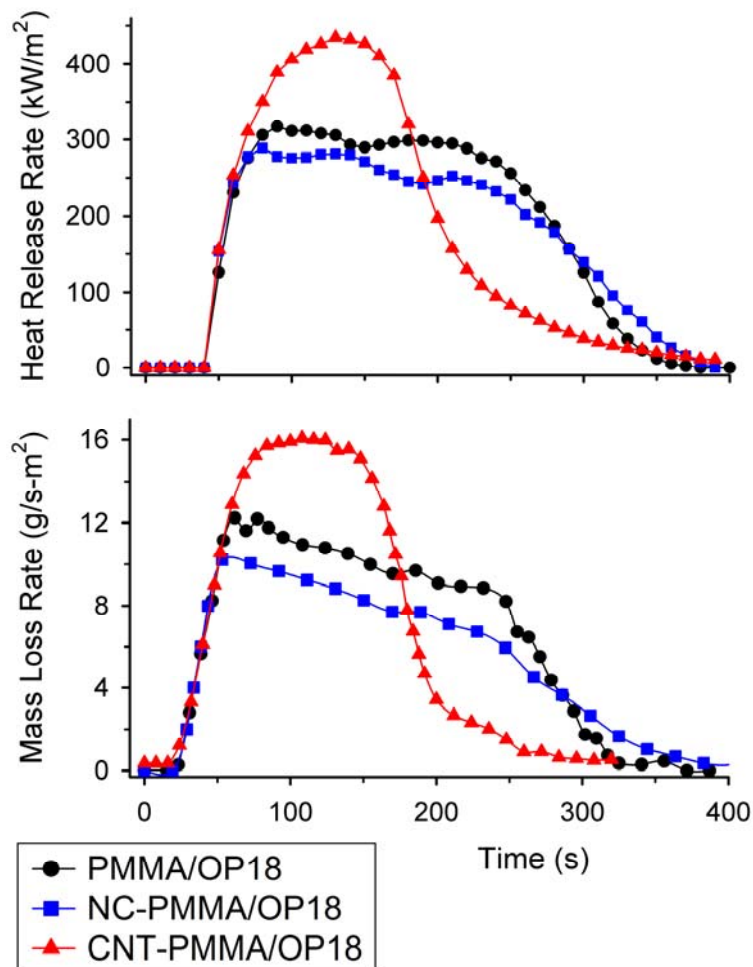


Figure 3.9 Effects of nanofillers on the heat release and mass loss behavior of flame-retarded PMMA

3.1.3 Flame Retardancy Mechanisms by Residue Analysis

The mass loss calorimeter fire residues of CNT-PMMA and NC-PMMA specimens are compared in the macroscopic images provided in Figure 3.10. Carbon nanotubes formed a thin, continuous and crack-free nanoparticle network on the sample surface superior to the thick but discontinuous layer with major voids and lateral cracks formed by nanoclays.

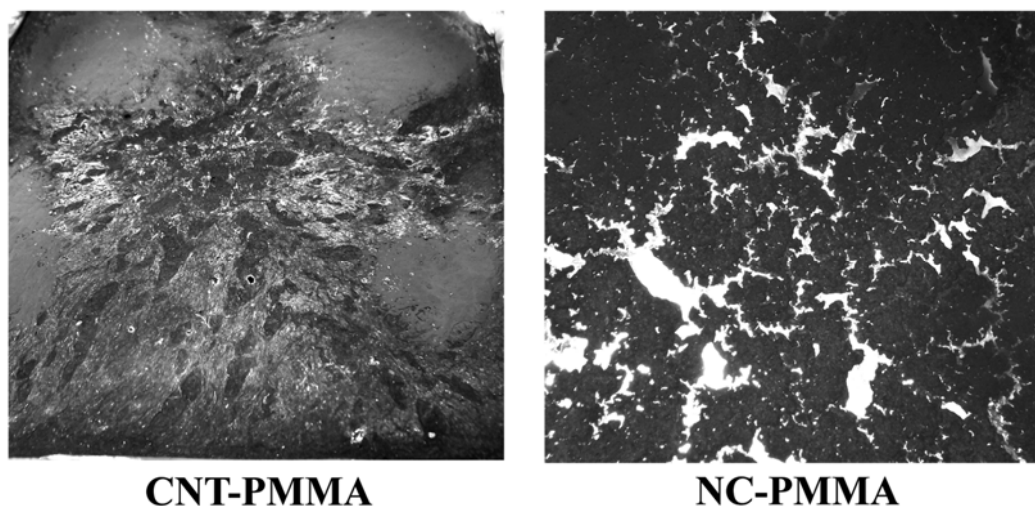


Figure 3.10 Appearance of the whole surfaces of mass loss calorimeter fire residues from PMMA with different nanofillers

Figure 3.11 contains SEM images of the mass loss calorimeter residue of CNT-PMMA nanocomposite displaying the dense network formed by the re-entanglement of carbon nanotubes upon pyrolysis of nearly the whole mass of polymer matrix without charring during combustion. Bare carbon nanotubes are clearly observed in the large magnification image (Figure 3.11(b)) indicating that surfaces of carbon nanotubes and voids in the network formed by carbon nanotubes are free from any carbonaceous char that could act as the char matrix. The mass loss calorimeter residue of NC-PMMA displayed in Figure 3.12 reveals large voids in the char microstructure and flake-like morphology of carbonaceous char. The large magnification image Figure 3.12(b) contains no evidence for montmorillonite particles on the char surface which could indicate that collapsed montmorillonite particles are covered by the carbonaceous char from PMMA decomposition.

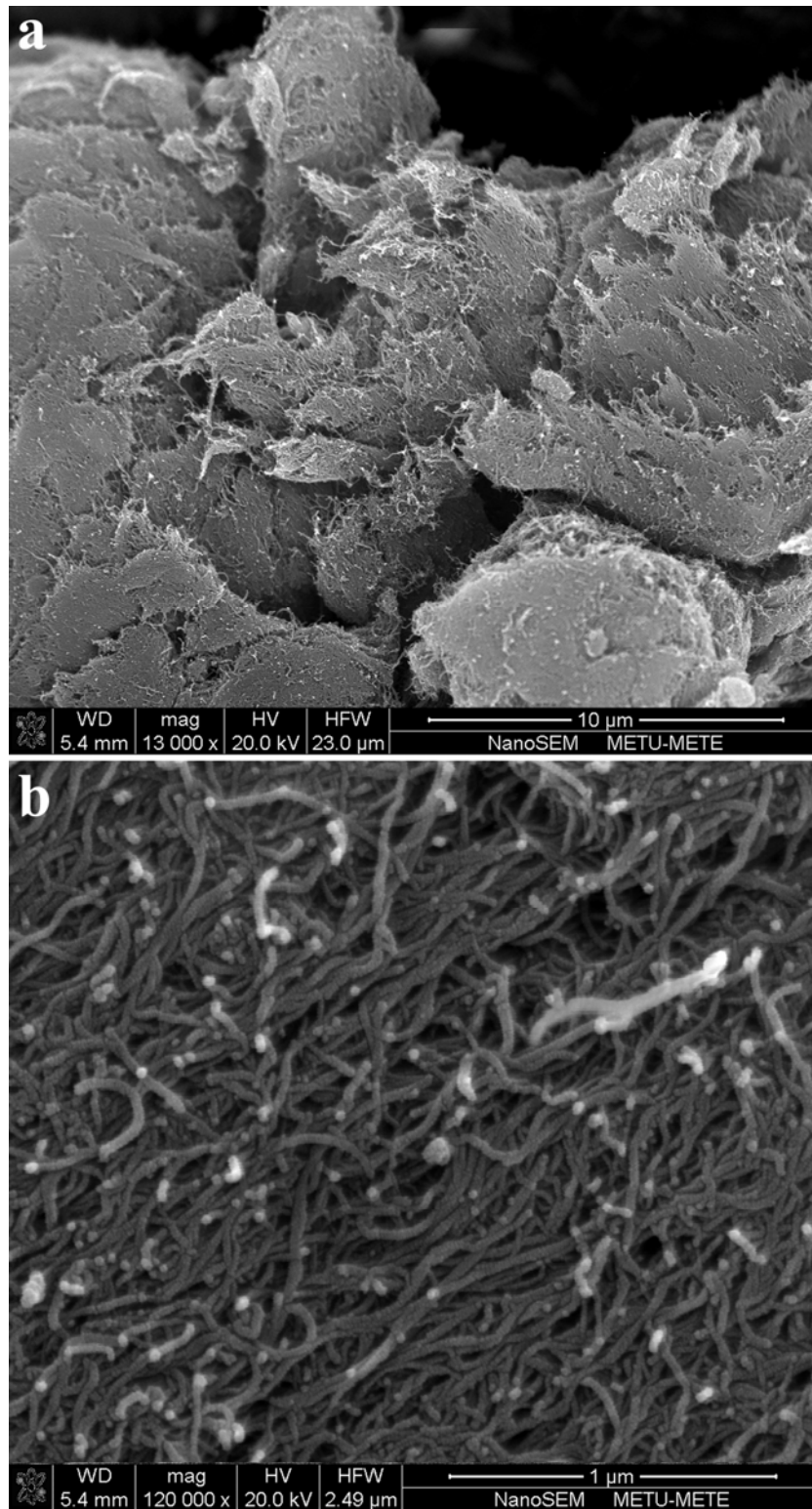


Figure 3.11 SEM micrographs of the char residue from CNT-PMMA nanocomposite; (a) general and (b) closer view images

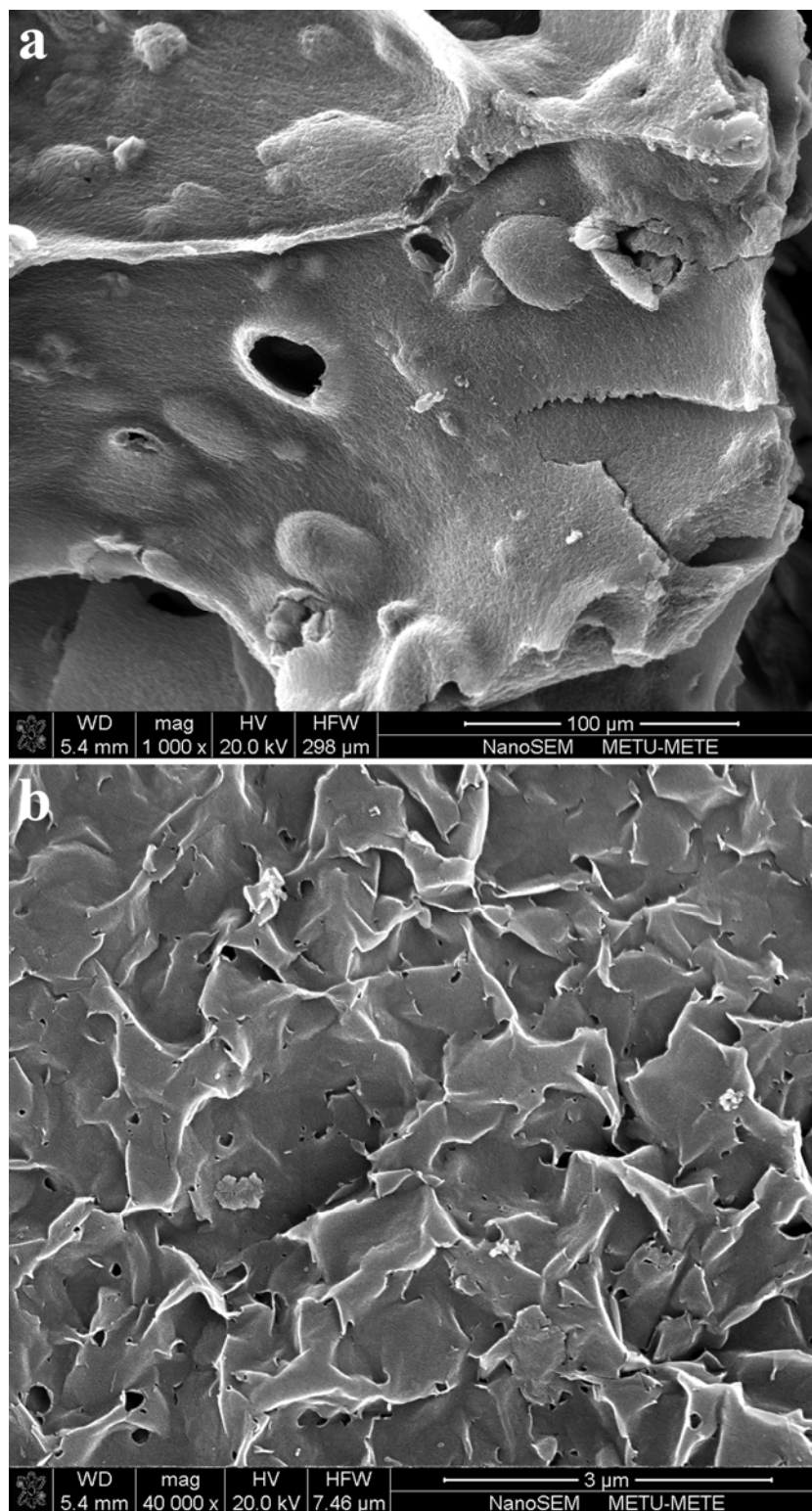


Figure 3.12 SEM images of the char residue from NC-PMMA nanocomposite; (a) general and (b) closer view images

Figure 3.13 shows the ATR-FTIR spectra of fire residues from flame-retarded PMMA with and without the nanofillers. The diffuse band possessing a peak near 1060 cm^{-1} and a shoulder around 960 cm^{-1} in the spectrum for PMMA/OP18 correspond to phosphate stretching vibrations such as that of PO_4^{3-} in boron phosphates [96] and PO_3^{2-} in aluminum phosphates [97]. Bending vibrations of structural OH appear as a small peak at 1620 cm^{-1} and a shallow band peaking at 3100 cm^{-1} (not shown on the spectra), typical of hydrated amorphous aluminum phosphates [97].

The residue from CNT-PMMA/OP18 shows similar phosphate absorption bands with flame-retarded PMMA that contains no nanofillers. The spectrum recorded from NC-PMMA/OP18 includes a peak at 1030 cm^{-1} attributed to the in-plane Si-O stretching vibrations in montmorillonite. Shoulders near 1115 and 915 cm^{-1} correspond to out-of-plane Si-O stretching and OH bending vibrations, respectively [98, 99]. Characteristic absorption bands for phosphates are masked from the strong montmorillonite absorptions which limits further interpretation of the chemical structure of the char residue from NC-PMMA/OP18.

It can be inferred from the XRD patterns in Figure 3.13 that the fire residues from nanoclay containing flame-retarded samples (NC-PMMA/OP9 and NC-PMMA/OP18) possess interlayer spacings around 1.3 nm. This indicates that the protective intumescent layers contain clay nanolayers in the form of collapsed montmorillonite particles [100]. Following the degradation and volatilization of the interlayer species, i.e. organic modifier and intercalated polymer chains, clay nanolayers collapse on each other to show basal reflections close to that of unmodified Na-MMT.

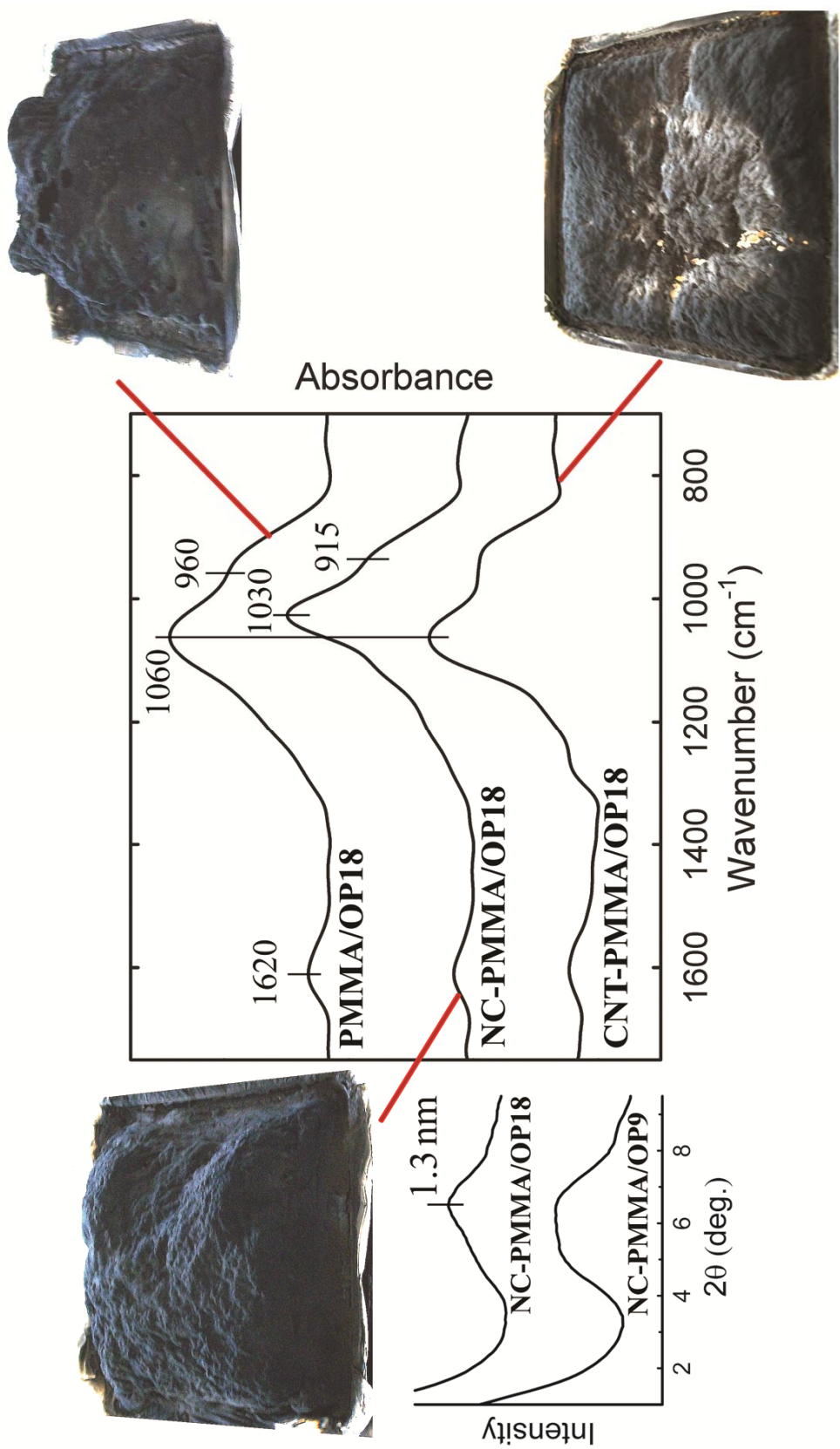


Figure 3.13 ATR-FTIR spectra, XRD patterns and macroscopic appearances of fire residues showing the effect of nanofiller type

Macroscopic appearance of char residues in Figure 3.13 also reveal that flame-retarded PMMA (PMMA/OP18) shows intumescence with a well-blown but thin and weak char layer whereas nanoclay containing flame-retarded sample (NC-PMMA/OP18) displays a thicker, denser and stronger blown char structure. The fire residue from carbon nanotube containing flame-retarded sample (CNT-PMMA/OP18) reveals the restriction of intumescence which leads to poor flame retardancy in terms of cone calorimetric fire properties.

SEM images and elemental analysis of mass loss calorimeter char residues from PMMA/OP18, CNT-PMMA/OP18 and NC-PMMA/OP18 are displayed in Figure 3.14, Figure 3.15 and Figure 3.16, respectively. Upon combustion, PMMA/OP18 transforms to an intumescent, open porous char structure with non-uniform pore size distribution and no interconnection between the pores. The char is composed mainly of Al, P, O, and C (with Al:P mass ratio in the range 0.4–0.6:1) indicating the formation of carbonaceous aluminum phosphate structures. In addition, a minor amount of Zn (< 2 wt.%) was detected in char residues that arise from zinc borate component as a synergist in organophosphorus flame retardant additive.

The char formed by combustion of CNT-PMMA/OP18 contains blown microspheres of carbonaceous aluminum phosphate (Figure 3.15) that might at first be indicative of an intumescent structure. However, closer examination of those blown spheres revealed the presence of homogeneously dispersed carbon nanotubes embedded in aluminum phosphate microsphere walls. The wrapping of phosphate microspheres with strong carbon nanotube networks could physically impede stable char expansion during combustion which explains the non-intumescent macrostructure of the corresponding char in Figure 3.13. Elemental analysis shown in Figure 3.14(d) did not suggest a compositional change of the char by CNT incorporation into PMMA/OP18.

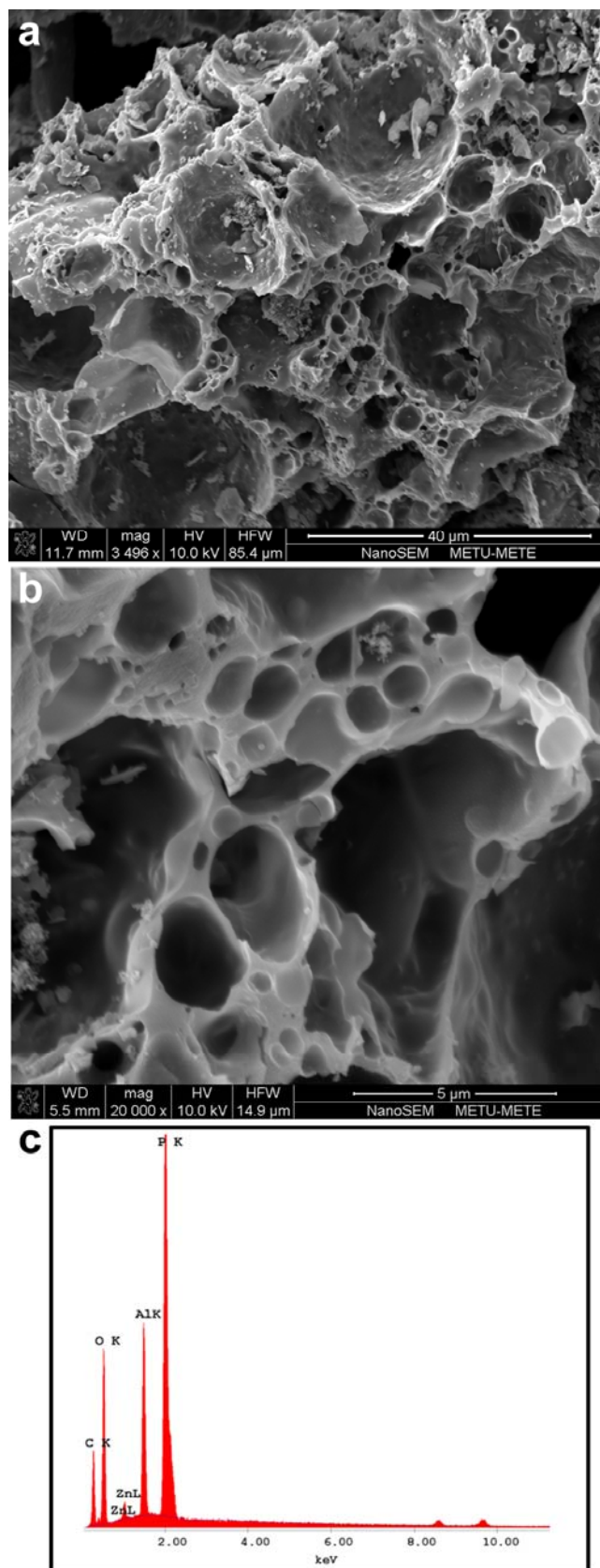


Figure 3.14 (a-b) SEM images and (c) energy dispersive spectrum of mass loss calorimeter residue from PMMA/OP18 sample.

The combustion residue formed by combustion of NC-PMMA/OP18 (Figure 3.16a) also possesses a blown but a more compact structure when compared to that of PMMA/OP18. Elemental analysis (Figure 3.16d) of the char disclosed an increased Al/P ratio to above 0.6:1, and abundance of Si and Fe which arise from montmorillonite particles in the char. The larger magnification images given in Figure 3.16(b-c) revealed the presence of coarse clay tactoids with typical platelet thicknesses in the range 100–200 nm. It can be said that complete collapse of initially intercalated montmorillonite occur upon pyrolysis of decomposition products leading to coarse clay tactoids assembled onto each other forming flake-like structures shown in Figure 3.16(b).

Therefore, in this study, nanofillers were found to modify the micro and the macro-structure of carbonaceous aluminum phosphate chars by physical rather than chemical means.

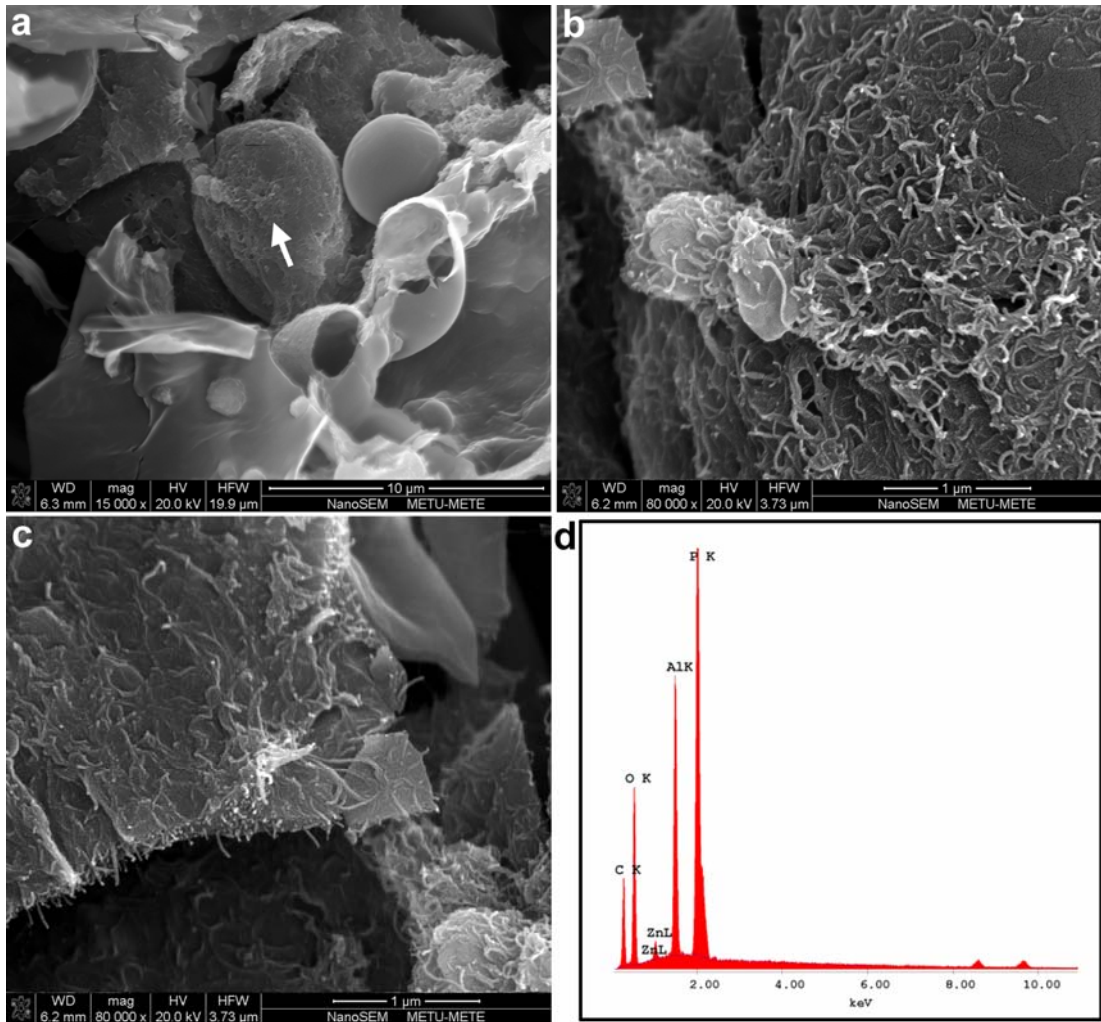


Figure 3.15 (a-c) SEM images and (d) energy dispersive spectrum of mass loss calorimeter residue from CNT-PMMA/OP18 sample

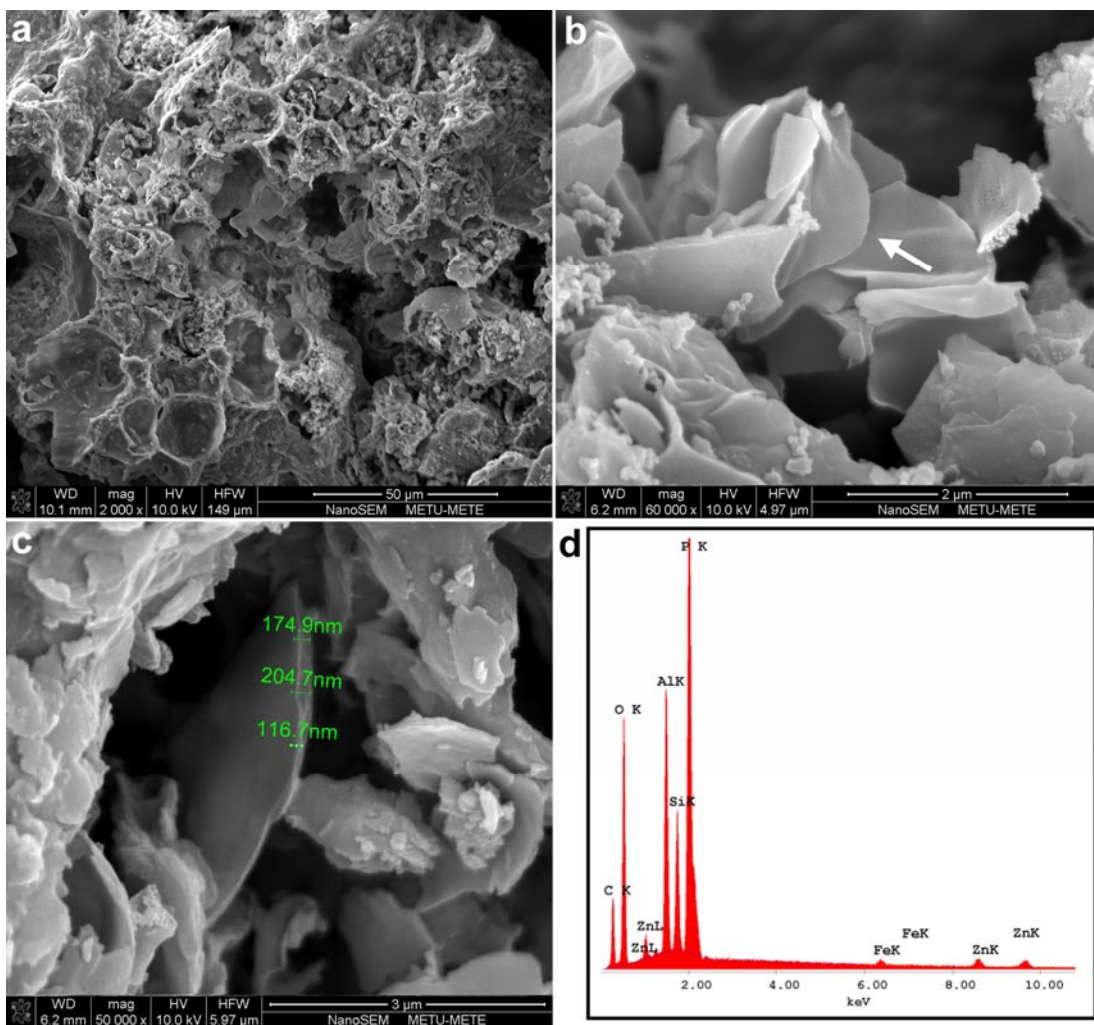


Figure 3.16 (a-c) SEM images and (d) energy dispersive spectrum of mass loss calorimeter residue from NC-PMMA/OP18 sample

3.1.4 Flame Retardancy Mechanisms by Thermal Degradation

(i) Thermogravimetric Analysis

Figure 3.17 displays the changes in thermal stability of neat- and flame-retarded PMMA with the incorporation of nanofillers. PMMA and corresponding nanocomposites apparently decompose in a single mass loss step almost completely by the evolution of methyl methacrylate monomer via de-polymerization [91, 101, 102], whereas flame-retarded PMMA with or without nanofillers possess additional shoulders around 430 - 450°C resolved by differential thermogravimetry. These mass loss rate shoulders might be attributed to the evolution of gaseous decomposition products of the organophosphorus flame retardant additive [93, 94].

Table 3.6 lists some of the important thermogravimetric data. Temperatures corresponding to 10% and 50% mass loss ($T_{10\%}$ and $T_{50\%}$) were shifted by ~15 °C to higher temperatures in the presence of nanofillers in neat PMMA. Incorporation of the organophosphorus flame retardant additive did not show any catalyzing effect on thermal degradation of PMMA considering the unaltered values of $T_{10\%}$. More importantly, the thermal stability of PMMA was enhanced by ~15°C in terms of $T_{50\%}$. Residue yields were increased in proportion with the flame-retardant content by the stabilization of an inorganic char in the condensed phase via the reactions between the constituents of the organophosphorus flame retardant additive.

Nanofillers increased the thermal stability of flame-retarded PMMAs similar to the effect seen for neat PMMA. Particularly, carbon nanotubes demonstrated a more pronounced thermal stabilization compared to nanoclays. Degradation temperatures, $T_{10\%}$ and $T_{50\%}$, were enhanced by ~30°C and ~20°C, respectively, in comparison with PMMA containing 18 wt% organophosphorus flame retardant additive owing to the reinforcement of the protective inorganic char by formed CNT networks.

The residue yields under inert atmosphere for nanoclay and carbon nanotubes containing neat and flame-retarded samples showed no significant differences taking into account the higher nominal weight fraction of nanoclays compared with carbon nanotubes.

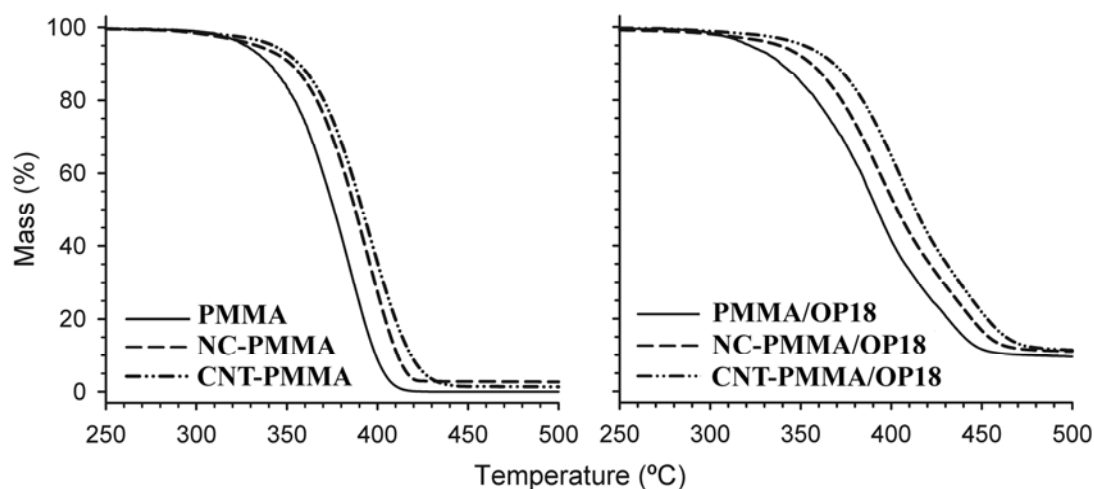


Figure 3.17 Thermogravimetric mass loss curves showing the effects of different nanofillers on the thermal stabilities of neat- and flame-retarded PMMA

Table 3.6 Results of thermogravimetric analysis showing the effect of nanofiller type

	$T_{5\%}$ (°C)	$T_{10\%}$ (°C)	$T_{50\%}$ (°C)	T_{\max} (°C)	Residue at 500 °C (%)
PMMA	327	340	376	385	0
NC-PMMA	334	352	388	393	2.7
CNT-PMMA	343	357	392	397	1.4
PMMA/OP9	323	342	389	394	4.9
NC-PMMA/OP9	343	355	391	390	7.4
CNT-PMMA/OP9	351	366	408	408	6.1
PMMA/OP18	322	339	392	391	9.6
NC-PMMA/OP18	338	356	403	394	11.6
CNT-PMMA/OP18	352	368	413	405	11.3

Differential thermogravimetric (DTG) mass loss rate curves for flame-retarded PMMA and corresponding nanocomposites shown in Figure 3.18 demonstrate additional shoulders at high temperatures unlike the curves for neat PMMA and nanocomposites (curves not shown). In order to reveal the overlapping degradation steps, DTG curves were further analyzed by carrying out peak deconvolution using mixed Gaussian-Lorentzian line shapes. By this means, a three-step degradation behavior was observed; a relatively low-temperature step where the initial mass loss occurs, an intermediate-temperature major degradation step corresponding roughly to the maximum rate of mass loss, and a high-temperature step responsible for the appearance of shoulders in DTG mass loss rate curves.

Table 3.7 contains the DTG data corresponding to each deconvoluted degradation step for flame-retarded PMMA and corresponding nanocomposites. The maximum degradation temperature increased almost for all steps with the incorporation of nanofillers, particularly with carbon nanotubes. The influence of carbon nanotubes on T_{\max} for the initial degradation step (step #1) was of more significance. This shows that carbon nanotubes effectively retard the early stage of degradation in flame-retarded PMMA. The local step-wise maxima and global maximum for mass loss rates were hardly changed by nanofillers.

Mass loss corresponding to the initial degradation step was decreased by nanofillers, especially by nanoclays. The initial step can be said to overlap with the second step in the presence of nanoclays, resulting in lower mass loss rate and corresponding mass loss for the first step, whereas higher mass loss rate and mass loss for the second step (step #2). Most particularly, carbon nanotubes markedly influenced the degradation behavior by increasing the mass loss corresponding to the high-temperature shoulder (step #3). It may be concluded that carbon nanotubes altered the degradation behavior such that a higher yield of thermally stable products was obtained during thermal degradation.

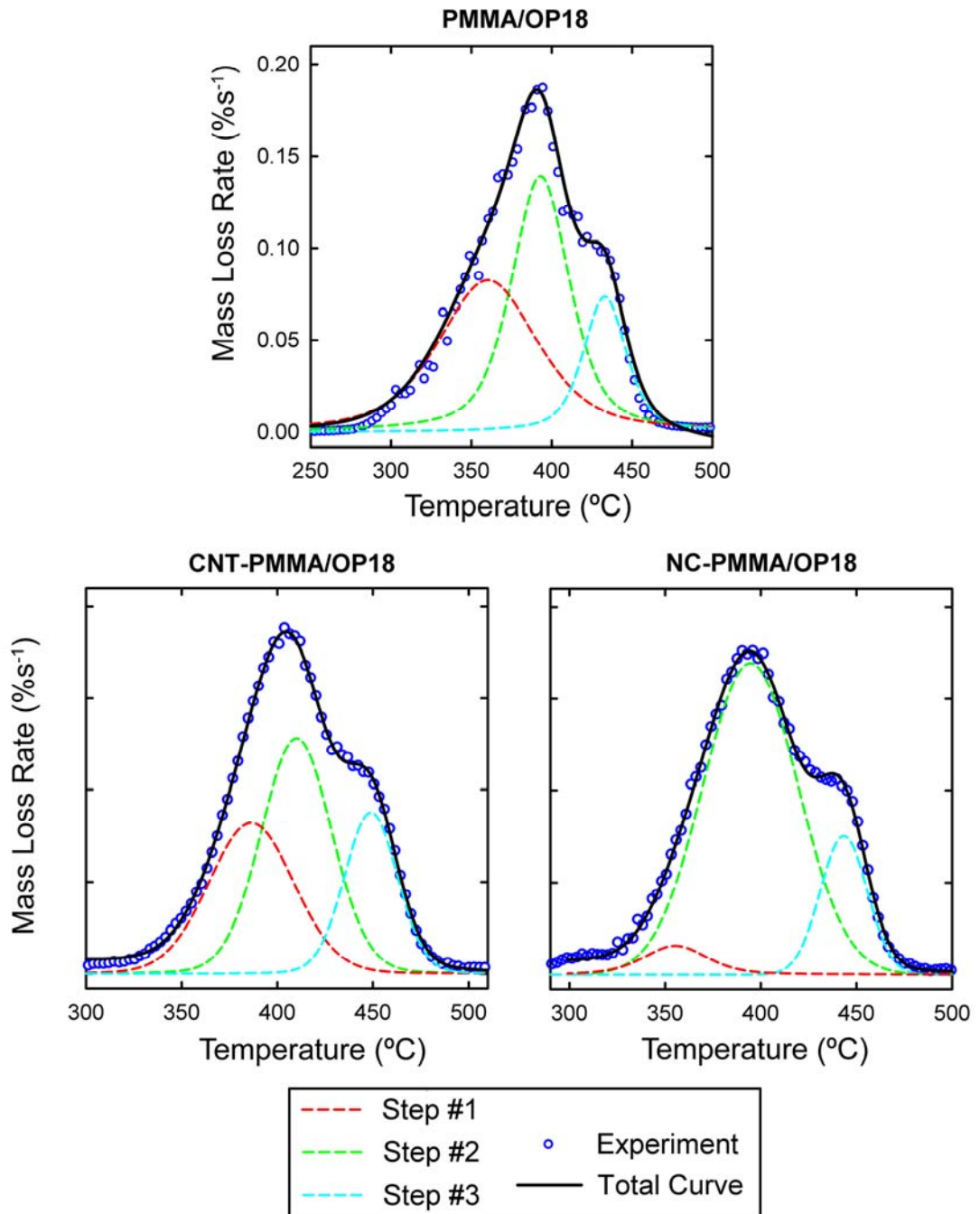


Figure 3.18 Deconvoluted differential thermogravimetric curves showing the effect of nanofiller type

Table 3.7 DTG data for deconvoluted degradation steps showing the effect of nanofiller type

	PMMA/ OP18	NC-PMMA/ OP18	CNT-PMMA/ OP18
T_{\max}^a (step#1)	361	356	387
T_{\max} (step#2)	393	395	410
T_{\max} (step#3)	433	444	449
$-\frac{dm}{dt}^b$ (max.)	0.186	0.176	0.188
$-\frac{dm}{dt}$ (step#1)	0.082	0.016	0.082
$-\frac{dm}{dt}$ (step#2)	0.139	0.169	0.128
$-\frac{dm}{dt}$ (step#3)	0.074	0.075	0.088
Δm^c (step#1)	38.2	5.0	30.0
Δm (step#2)	37.5	68.3	38.7
Δm (step#3)	14.6	14.9	20.0

^a T_{\max} : maximum degradation temperature (°C)

^b $-\frac{dm}{dt}$: maximum mass loss rate (%/s)

^c Δm : mass loss in percent sample mass (%)

(ii) Direct Pyrolysis Mass Spectrometry

Pyrolysis is widely applied to investigate thermal characteristics of a compound such as, thermal stability, degradation products and decomposition mechanism. Pyrolysis mass spectrometry techniques have several advantages such as sensitivity, reproducibility, minimal sample preparation and consumption and speed of analysis. In case of direct pyrolysis, thermal degradation occurs inside the mass spectrometer and pyrolyzates are rapidly transported to the source region and ionized. The high vacuum inside the mass spectrometer favors vaporization and thus, allows the analysis of higher molecular mass pyrolyzates. As the high vacuum system rapidly removes the degradation products from the heating zone, secondary reactions and condensation reactions are avoided. Furthermore, because of the rapid detection system of the mass spectrometers, unstable thermal degradation products can also be detected. Scanning total ion current (TIC) pyrogram as a function of temperature allows separation of components present in the sample as a function of volatilities and/or thermal stability. However, as the mixture of various thermal degradation products further dissociates during the ionization, the mass spectra are usually very complex.

In case of analyses of samples involving high molar mass components, such as polymers, pyrolysis mass spectra may be extremely crowded. Furthermore, all the fragments with the same mass to charge ratio have contributions to the intensity of the same peak in the mass spectrum. Thus, in pyrolysis MS analysis, not only the detection of a peak, but the changes in its intensity (single ion pyrograms, evolution profiles) as a function of temperature has significant importance [103]. Presence of more than one peak in the single ion evolution profile indicates either generation of the same product from polymer chains with different thermal stabilities or evolution of fragments with the same m/z value but different structures.

To investigate the thermal characteristics of flame retardant PMMA nanocomposites containing nanoclay and carbon nanotubes (NC-PMMA/OP18 and CNT-PMMA/OP18) with considerably complex structures, the direct pyrolysis mass spectrometry analyses of pure PMMA, OP flame retardant additive, PMMA/OP18 composite, NC-PMMA nanocomposite and lastly CNT-PMMA nanocomposite were also carried out for comparison.

The TIC (variation of total ion yield as a function of temperature) curve shown in Figure 3.19(a) recorded during the pyrolysis of PMMA showed a broad peak with a maximum at 400°C. The pyrolysis mass spectrum recorded at 400°C showed typical fragmentation pattern of MMA, with intense peaks at $m/z=100$, 69 and 41 Da due to molecular ion of MMA and $\text{CH}_2=\text{C}(\text{CH}_3)\text{CO}$ and $\text{CH}_2=\text{CCH}_3$, respectively. The evolution profiles of $\text{CH}_2-(\text{CH}_3)\text{CH}-\text{C}=\text{O}$ ($m/z=69$ Da), monomer, MMA, ($m/z=100$ Da), dimer (almost absent) ($m/z=200$ Da), CO_2 ($m/z=44$ Da) and C_2OH_3 ($m/z=43$ Da) showed identical trends (Figure 3.20a). It is clear that the thermal decomposition of PMMA took place via de-polymerization yielding mainly the monomer, in accordance with the well known thermal decomposition mechanism [101, 102, 104].

Thermal degradation of organophosphorus flame retardant additive mainly occurred in two regions. The corresponding TIC curve (Figure 3.19b) showed a sharp peak with a maximum at 300°C and overlapping peaks in the temperature range 350-430 °C. The pyrolysis mass spectra recorded at around 300°C were dominated with peaks at 126, 94, 85, 68 and 43 Da that can directly be attributed to molecular ion of melamine, $(\text{C}_3\text{N}_3)(\text{NH}_2)_3$, and to its diagnostic fragment ions, $\text{N}_4\text{C}_2\text{H}_5$, $\text{N}_3\text{C}_2\text{H}_2$ and N_2CH_3 respectively, confirming the loss of melamine at early stages of pyrolysis.

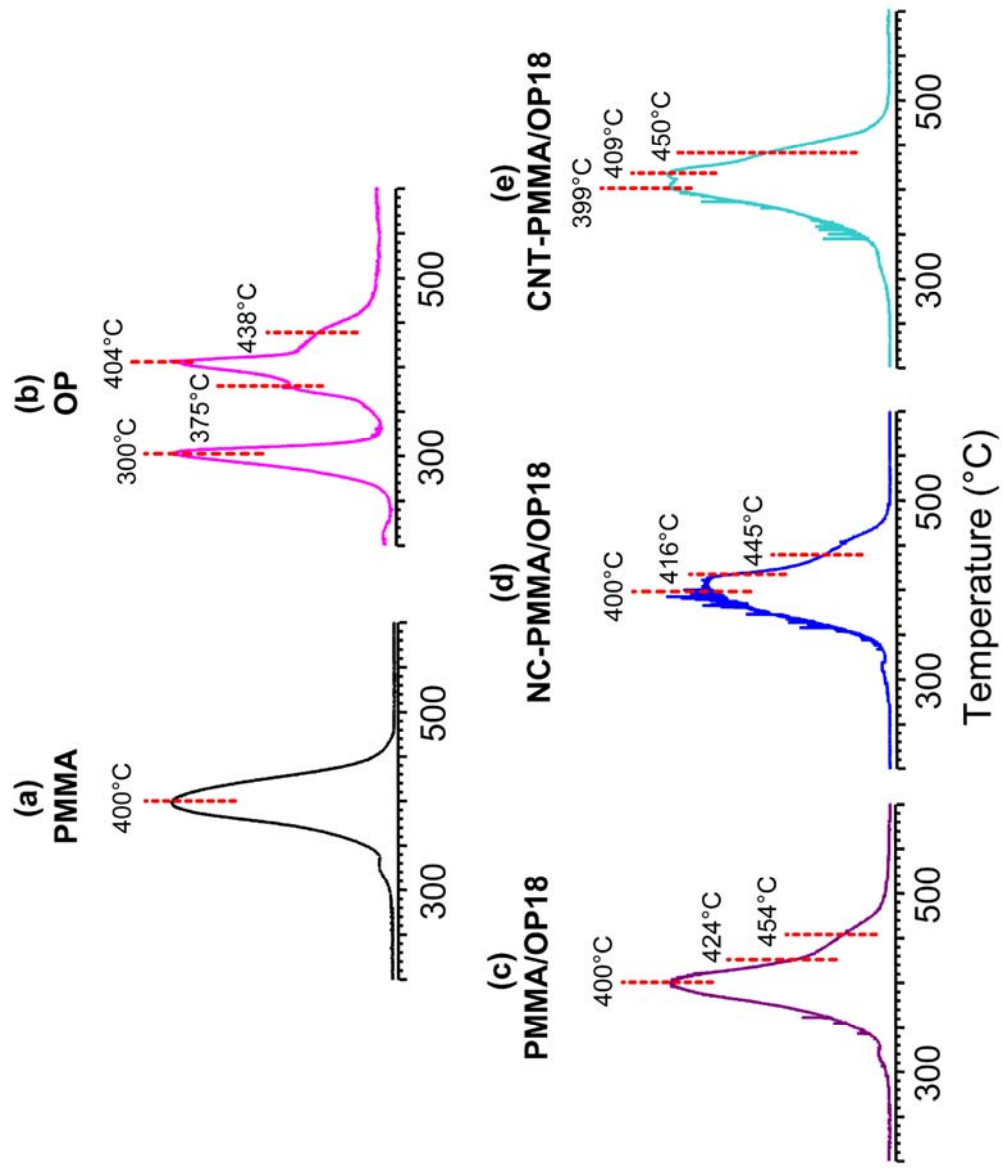


Figure 3.19 Total ion current as a function of temperature obtained by direct pyrolysis mass spectroscopy

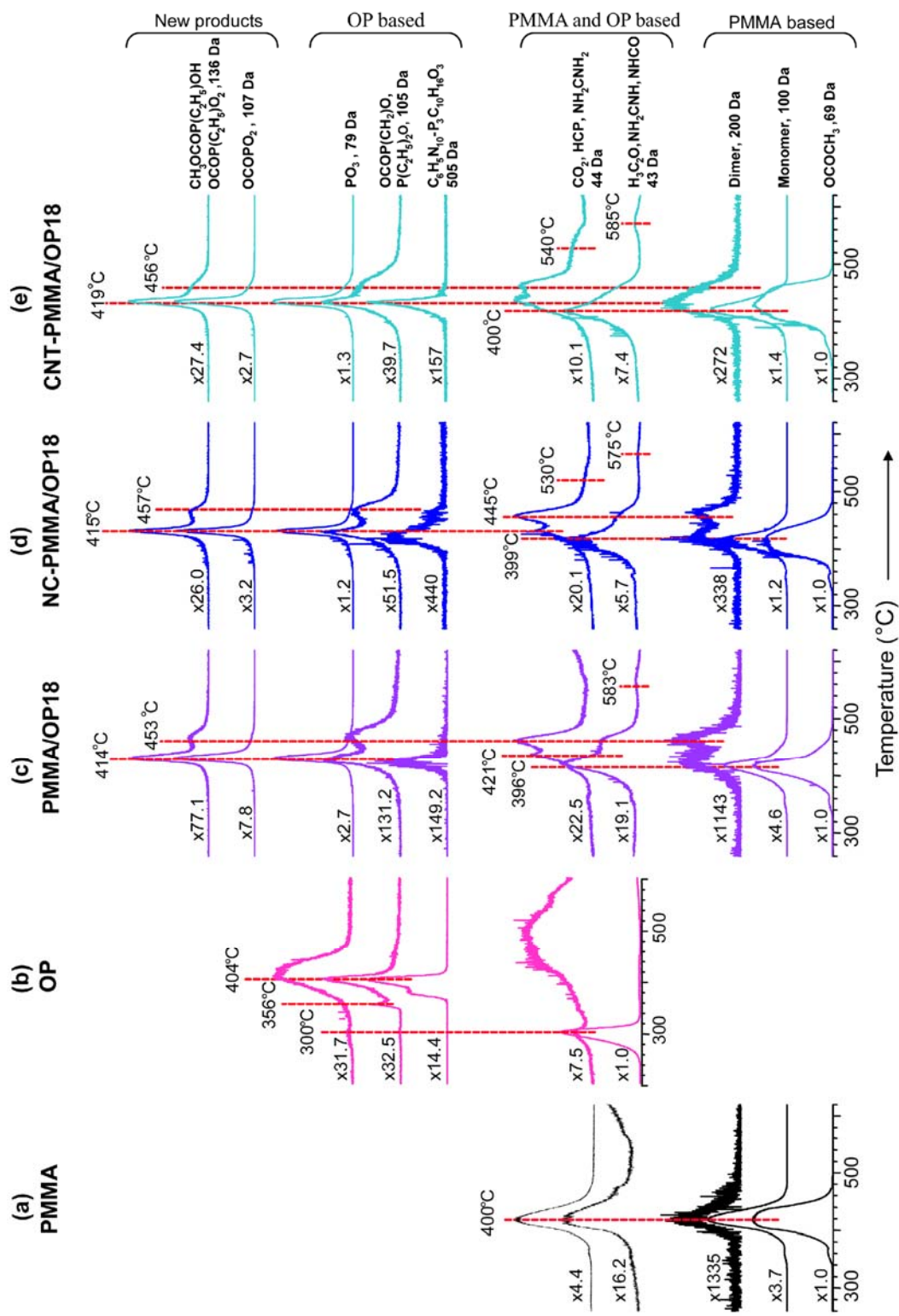


Figure 3.20 Selected single ion evolution profiles obtained by direct pyrolysis mass spectrometry

The relative intensities of peaks due to diethylphosphinic acid and its dimer and trimer were maximized at around 359°C. Whereas, the peaks that can be associated with products due to reactions of melamine and its derivatives with diethylphosphinic acid were detected at slightly higher temperatures, in the range 350-420°C. Release of diethylphosphinic acid, and melamine and its decomposition products throughout the degradation of organophosphorus additive is in good agreement with previously published work [93]. Fragment peaks due to the decomposition of polyphosphate chains were recorded in a broader temperature region, reaching maximum intensities at around 419°C. In Figure 3.20(b), the evolution profiles of some characteristic fragments, namely HCP and/or CO₂ ($m/z=44$ Da), N₂CH₃ ($m/z=43$ Da), PO₃ ($m/z=79$ Da), (C₂H₅)₂PO ($m/z=105$ Da) and C₆H₅N₁₀-P₃C₁₀H₂₇O₃ (a fragment generated from a complex of melamine and diethyl phosphine trimer) ($m/z=505$ Da) are shown.

A broad peak, with a maximum at 400°C and a shoulder at around 450°C was present in the TIC curve of PMMA/OP18 composite (Figure 3.19c). The single ion evolution profiles of PMMA based products were almost identical to those recorded during the pyrolysis of PMMA (Figure 3.20c). On the other hand the evolution profiles of OP based products showed significant differences. Diagnostic peaks of melamine at around 300°C and the low temperature peaks of diethyl phosphinic acid and its dimer and trimer at around 356°C totally disappeared. Furthermore, the evolution profiles of fragments due to melamine derivatives and diethylphosphinic acid complexes became narrower and shifted to high temperature ranges. Even more important was the appearance of new peaks at 136, 109, 108 and 107 Da. It may be thought that transesterification reactions between methyl ester groups of PMMA and free phosphinic acid and/or complexes of phosphinic acid-melamine and its derivatives generated O=COP(C₂H₅)O₂ units that can readily produce these fragments during thermal degradation and/or dissociative ionization processes.

Drastic changes in the evolution profile of 43 Da fragment was noted. 43 Da peak was the base peak in the pyrolysis mass spectra of OP. Although relatively weak, it was also present in the pyrolysis mass spectra of PMMA due to CH₃CO and/or C₃H₇ fragments that can be generated by some rearrangement reactions during

ionization. The evolution profile of 43 Da fragment generated during the pyrolysis of PMMA/OP18 composite, showed two overlapping peaks with maxima at 396 and 453°C and a weak peak at around 583°C. The first peak can readily be assigned to CH₃CO and/or C₃H₇ fragments due to PMMA decomposition. The high temperature evolution of 43 Da fragment may be associated with generation of isocyanic acid (HNCO) by reactions of NH₂ groups of melamine with methacrylic acid units.

Another point that should be noticed was the changes in the evolution profile and the decrease in the relative yield of 44 Da fragment attributed to CO₂ and HC=P for PMMA and OP, respectively. The evolution profile of 44 Da fragment(s) showed a weak shoulder at around 396°C and two peaks with maxima at 421 and 453°C. The weak shoulder may be attributed to evolution of CO₂ as in case of PMMA indicating a considerable decrease in CO₂ generation and supported the above proposed reactions of PMMA and phosphinic acid and its derivatives. The trends in the evolution profile at high temperatures were quite similar to those of 136 and 105 Da fragments and thus, readily assigned to generation of HCP due to decomposition of O=COP(C₂H₅)O₂H units.

Thermal characteristics of NC-PMMA/OP18 nanocomposite (Figure 3.19d) were almost identical to those of PMMA/OP18 composite as shown by the corresponding TIC curve. The mass spectra of NC-PMMA/OP18 were mainly dominated with characteristics peaks detected during the pyrolysis analyses of PMMA/OP18. Yet, noticeable differences were recorded in the relative intensities of MMA monomer and low mass oligomer peaks. In addition, broadening in the evolution profiles of fragments due to dissociative ionization of the monomer was detected (Figure 3.20d). It may be thought that thermal decomposition pathway via random cleavages yielding also low mass oligomers, which can also generate these fragments during ionization, was enhanced in the presence of nanoclay at least to a certain extent. This might be related to the nano-confinement of degrading molecules surrounded by the clay layers leading to a superheated environment that favors random chain scission [91].

Furthermore, the increased yield of products due to the reactions of melamine and its derivatives, and those between PMMA and phosphinic acid are indicative of increased possibility of these reactions in the presence of nanoclay. This could be attributed to the barrier effect of clay nanolayers retarding the evolution of degradation products from the polymer and the constituents of the OP flame retardant additive. This allows for further reactions that lead to increased yield of the mentioned products.

The thermal degradation behavior of CNT-PMMA/OP18 nanocomposite (Figure 3.19e) was quite similar to that of NC-PMMA/OP18 nanocomposite. The evolution profiles of thermal degradation products recorded during the pyrolysis of CNT-PMMA/OP18 nanocomposite are given in Figure 3.20(e). Noticeable increases in the relative intensities of low mass oligomers of MMA and broadening in the evolution profile of CH_3OCO fragment that can also be generated during the dissociative ionization of low mass oligomers were detected. It may be concluded that nano-confinement and barrier effects were more effective with carbon nanotubes having much smaller interparticle spacings compared to nanoclay, as clearly seen from the TEM images in Figure 3.5 and Figure 3.7 which in turn enhances the formation of low mass oligomers.

3.1.5 Thermal and Mechanical Properties

Figure 3.21 shows the method of interpretation of important parameters regarding glass transition from the heat flow curve of a glassy or a semi-crystalline polymer by differential scanning calorimetry. The onset temperature of glass transition, $T_{g,o}$, is the temperature at the interception of C_p (heat capacity) vs. T (temperature) line of the glassy state below T_g and the tangent at maximum rate of C_p change. Similarly, the endpoint of glass transition, $T_{g,e}$, is found by intercepting the C_p vs. T line of the rubbery state above T_g and the tangent at maximum rate of C_p change. The midpoint of the glass transition, $T_{g,m}$, is the temperature corresponding to maximum rate of C_p change during the transition. The changes in the heat capacities of samples upon glass transition (ΔC_p) can be evaluated by calculating the difference in the heat capacities of glassy and rubbery states just at the midpoint temperature.

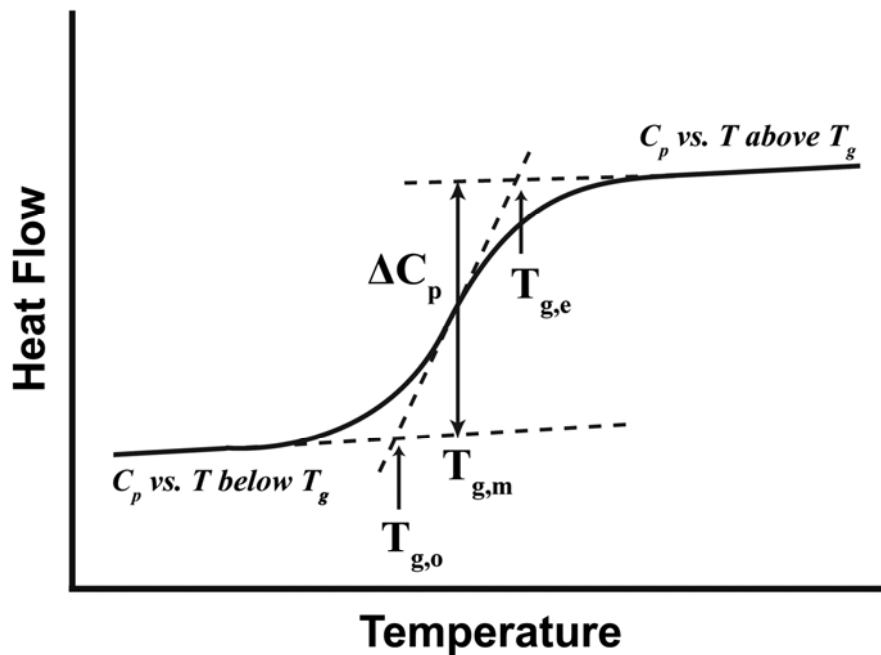


Figure 3.21 Determination of glass transition parameters (T_g and ΔC_p)

For DSC analysis, melt- or solution-mixed and injection molded samples were first heated from 25° to 150°C and then cooled back to 25°C for thermal rejuvenation followed by a second heating from 25° to 150°C at a heating rate of 20°C/min in order to examine the glass transition. Glass transition temperatures were taken as the temperature at maximum rate of C_p change. The changes in heat capacity upon glass transition (ΔC_p) were determined as the difference between the heat capacity of glassy and rubbery states at temperatures corresponding to maximum rate of C_p change.

Glass transition temperatures are marked in Figure 3.22 showing the heat flow curves of injection molded samples during second heating. It is clear that the utilized fillers did not impart a significant change (Table 3.8). In addition, molecular weight of the matrix was almost constant following the utilized shear mixing and molding processes for all formulations, as reported above in the current text. Accordingly, alterations in mechanical properties could confidently be related to the presence of filler nanoparticles and/or the flame retardant additive rather than an influence from the polymer matrix.

The interpreted heat capacity changes of polymer upon glass transition (ΔC_p) were higher for filler nanoparticle containing samples. Polymer single chain configurations might be sufficiently altered in the vicinity of nanoparticles such that a larger ΔC_p was seen upon the glass transition. This has been the discussion of a recent publication by Grady et al. [105] extensively investigating the unresolved phenomenon of increasing heat capacity change of glass transition in the presence of single-walled carbon nanotubes as filler nanoparticles in their case.

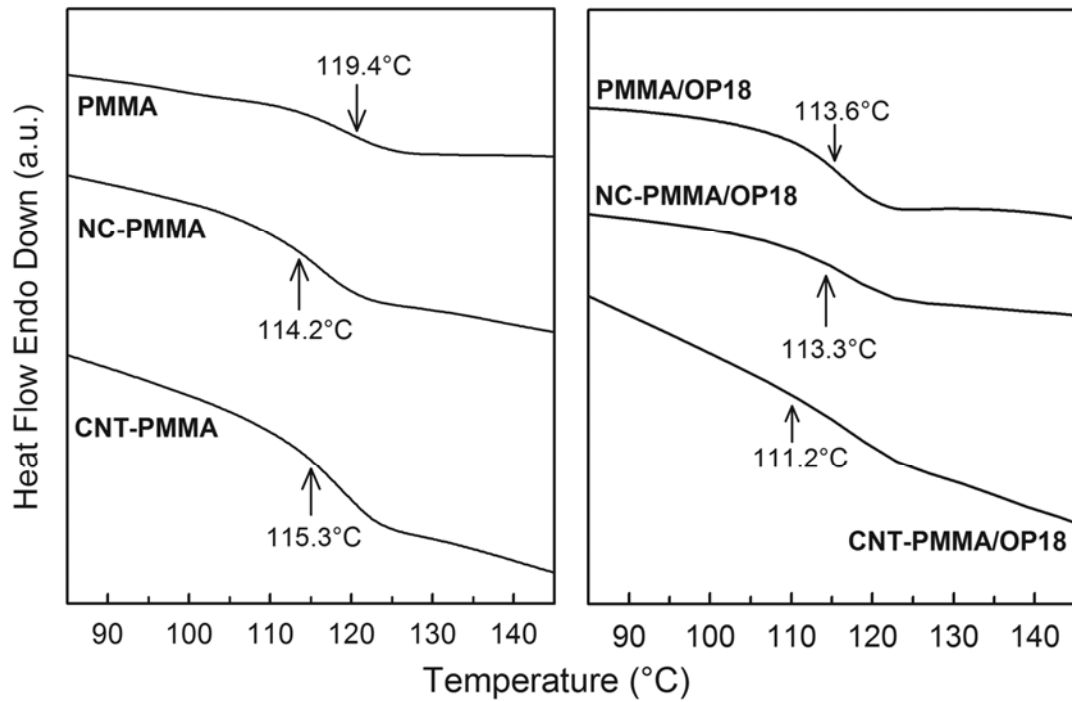


Figure 3.22 DSC heat flow curves of nanocomposites based on neat- and flame-retarded PMMA with different nanofillers

Table 3.8 Glass transition temperatures and ΔC_p of glass transition of PMMA nanocomposites with different nanofiller types

	T_g (°C)	ΔC_p (J/g _{polymer} °C)
PMMA	119.4	0.17
NC-PMMA	114.2	0.28
CNT-PMMA	115.3	0.33
PMMA/OP9	115.6	0.26
NC-PMMA/OP9	111.0	0.32
CNT-PMMA/OP9	114.2	0.31
PMMA/OP18	113.6	0.29
NC-PMMA/OP18	113.3	0.32
CNT-PMMA/OP18	111.2	0.33

Tensile strength, Young's modulus and strain at break values are listed in Table 3.9. Incorporation of organophosphorus flame retardant additive into PMMA matrix slightly lowered the tensile strength and ductility. Nanoclay and carbon nanotubes led to reductions in the tensile strength in all formulations in conjunction with lower elongation at break values. PMMA is a glassy thermoplastic having rather strong and brittle (crack sensitive) character with tensile elongations lower than around 4–5%. Nanofillers leading to agglomeration in the PMMA matrix are likely to act as stress concentration sites which result in crack propagation at lower applied stress levels. Nanoclays were also superior in enhancing Young's moduli of both neat and flame-retarded PMMA due to their intrinsic stiffness.

Figure 3.23 shows the SEM fracture morphologies of flame-retarded PMMA and corresponding nanocomposites. In conjunction with reduced elongation at break, fracture surfaces are smoother indicative of more brittle character of fracture in the presence of nanofillers. The smoother appearance is predominant in the clay nanocomposite where relatively large clay aggregates act as additional stress concentration sites.

Table 3.9 Mechanical properties of neat- and flame-retarded PMMA nanocomposites with different nanofiller types

	Tensile Strength (MPa)	Young's Modulus (GPa)	Elongation at Break (%)
PMMA	93.6 ± 3.3	3.3 ± 0.1	4.4 ± 0.6
NC-PMMA	78.3 ± 2.1	4.1 ± 0.1	2.8 ± 0.3
CNT-PMMA	72.6 ± 4.3	3.4 ± 0.1	2.8 ± 0.2
PMMA/OP9	89.7 ± 1.2	3.6 ± 0.1	3.9 ± 0.2
NC-PMMA/OP9	80.0 ± 2.2	4.1 ± 0.1	2.9 ± 0.1
CNT-PMMA/OP9	80.5 ± 1.6	3.7 ± 0.1	3.2 ± 0.1
PMMA/OP18	82.1 ± 2.6	3.5 ± 0.1	3.4 ± 0.4
NC-PMMA/OP18	76.0 ± 2.3	4.7 ± 0.2	2.3 ± 0.2
CNT-PMMA/OP18	65.4 ± 0.1	3.7 ± 0.1	2.5 ± 0.2

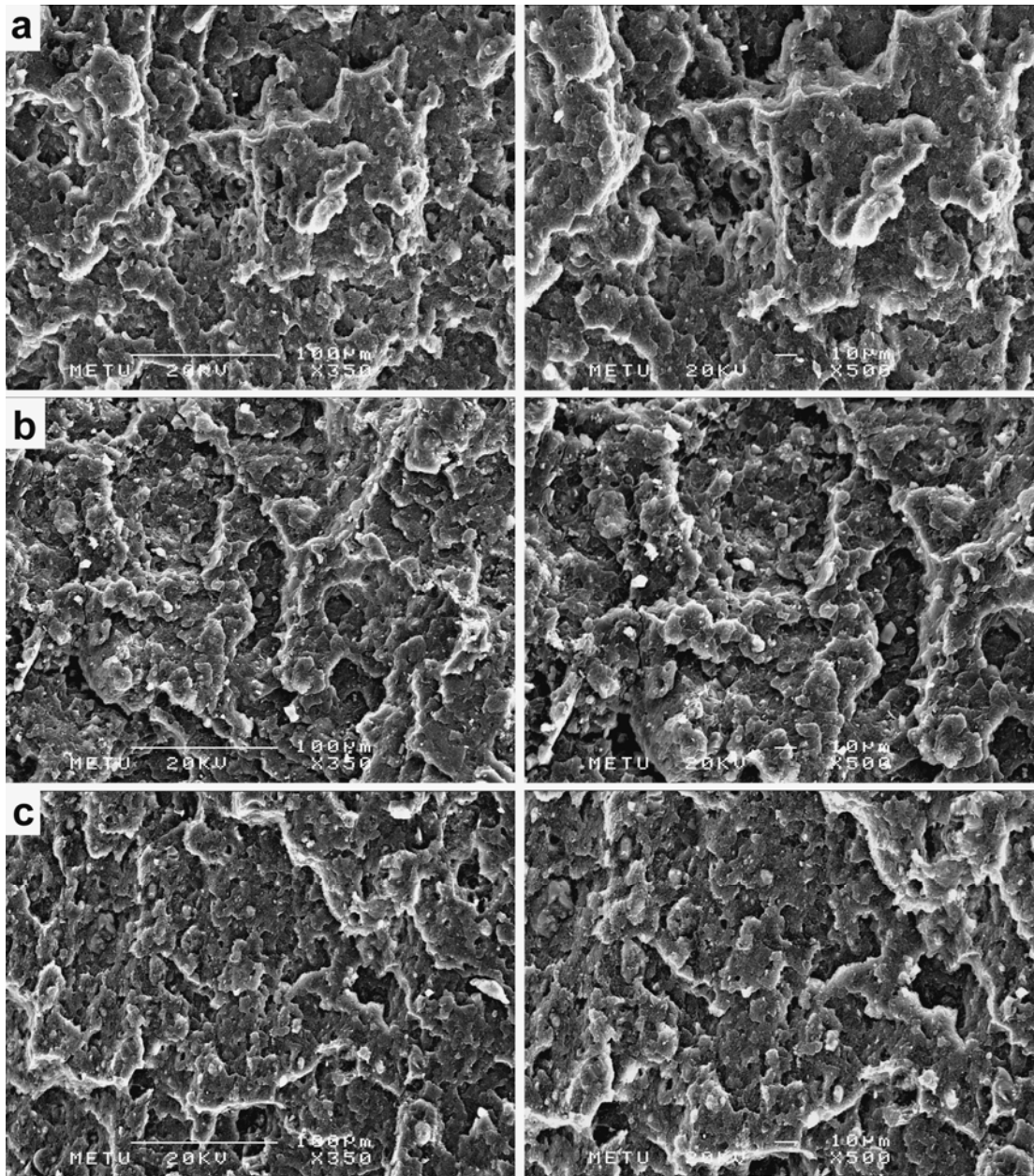


Figure 3.23 SEM images of tensile fracture surfaces; (a) PMMA/OP, (b) CNT-PMMA/OP, (c) NC-PMMA/OP

3.2 EFFECT OF NANOFILLER DISPERSION

Since the second purpose of this study was to reveal the effect of nanofiller dispersion on the synergistic flame retardancy, a flame-retarded thermoplastic polymer (HIPS) containing nanoclays with two different dispersion states, i.e. intercalated nanocomposite and phase-separated microcomposite, were investigated in a comparative manner. Aluminum trihydroxide (ATH) was chosen as the halogen-free flame retardant additive owing to its suitability for processing conditions of HIPS and also to its abundance, low-cost and low environmental impact.

Compositions and preparation techniques of studied materials are listed in Table 3.10. Micro- and nano-composite morphologies of the prepared samples were revealed by TEM and XRD. Influence of the state of nanoclay dispersion, i.e. micro- or nano-composite formation, was monitored on the basis of mass loss calorimeter analysis accompanied by limiting oxygen index and UL94 horizontal burning rate measurements. In an attempt to reveal the flame retardancy mechanism of compounds with different nanoclay dispersion states, thermogravimetric analysis, residue characterization by XRD, SEM and FTIR were carried out. Mechanical properties of samples were compared on the basis of tensile behaviors and fracture morphologies were investigated by SEM.

Table 3.10 Designations, compositions (wt.%) and utilized preparation techniques to reveal the effect of nanofiller dispersion

Sample Designation	HIPS	Aluminum tri-hydroxide (ATH)	Nanoclay (NC)	Preparation Technique
HIPS	100	-	-	-
<i>s</i> -NC	97	-	3	solution-mixing
<i>m</i> -NC	97	-	3	melt-mixing
<i>m</i> -15ATH	85	15	-	melt-mixing
<i>m</i> -25ATH	75	25	-	melt-mixing
<i>m</i> -35ATH	65	35	-	melt-mixing
<i>s</i> -15ATH	85	15	-	solution-mixing
<i>s</i> -25ATH	75	25	-	solution-mixing
<i>s</i> -35ATH	65	35	-	solution-mixing
<i>s</i> -NC/15ATH	82	15	3	solution-mixing
<i>s</i> -NC/25ATH	72	25	3	solution-mixing
<i>s</i> -NC/35ATH	62	35	3	solution-mixing
<i>m</i> -NC/15ATH	82	15	3	melt-mixing
<i>m</i> -NC/25ATH	72	25	3	melt-mixing
<i>m</i> -NC/35ATH	62	35	3	melt-mixing

3.2.1 Nanomorphology

TEM micrograph of the nanocomposite (*s*-NC) obtained via high-power ultrasound-assisted solution intercalation of nanoclays without the conventional flame-retardant is provided in Figure 3.24. Montmorillonite particles with large aspect ratios appear homogeneously dispersed at the nano-scale in polymer matrix and aligned to some extent in the direction of flow during injection molding. The nano-dispersed particles are composed of 2 to 5 stacked polymer intercalated clay nanolayers. The aluminosilicate platelets have a distribution of lengths between 30-150 nm for which image analysis were conducted on several representative images and an apparent number average of ~75 nm was calculated. High-power ultrasonication allowed for the disruption of clay nanolayer registry by overcoming the attractive forces between layers through micro-cavitation effect [106]. By this means, clay nanolayers are dispersed at the nano-scale and homogeneously distributed in the polymer matrix.

Figure 3.25 displays the TEM micrographs of solution intercalated nanocomposites based on HIPS with 35 wt% ATH. The presence of the flame-retardant additive does not significantly alter the nano-morphology and nano-dispersion of montmorillonite in the polymer matrix. Moreover, the preferential orientation of clay nanolayers was not affected by large flame-retardant particles. Therefore, it can be said that no apparent interactions exist between the flame-retardant additive and nanoclay filler nanoparticles during solution processing.

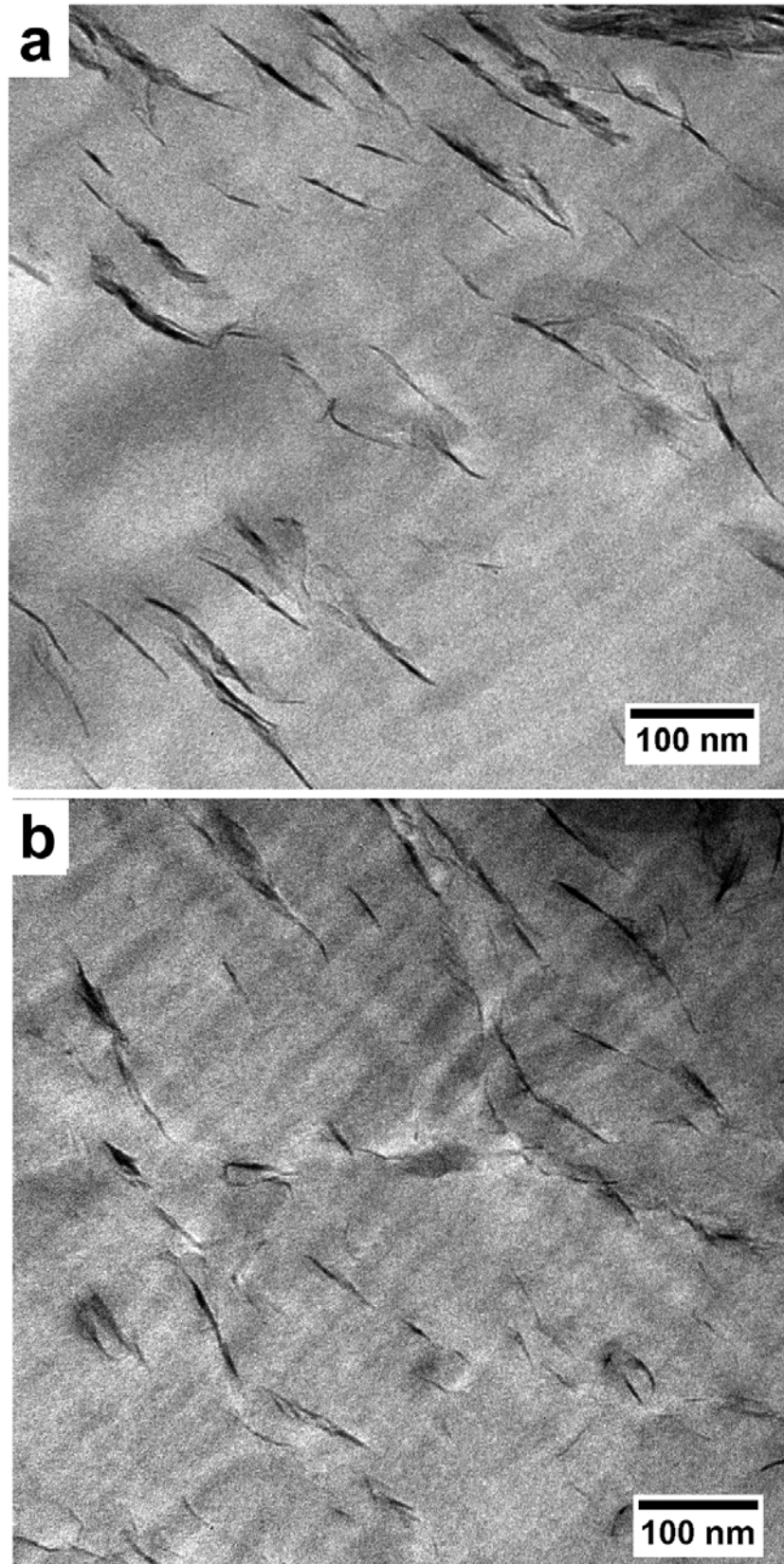


Figure 3.24 (a) and (b) TEM micrographs of solution intercalated nanocomposites based on neat HIPS (*s*-NC)

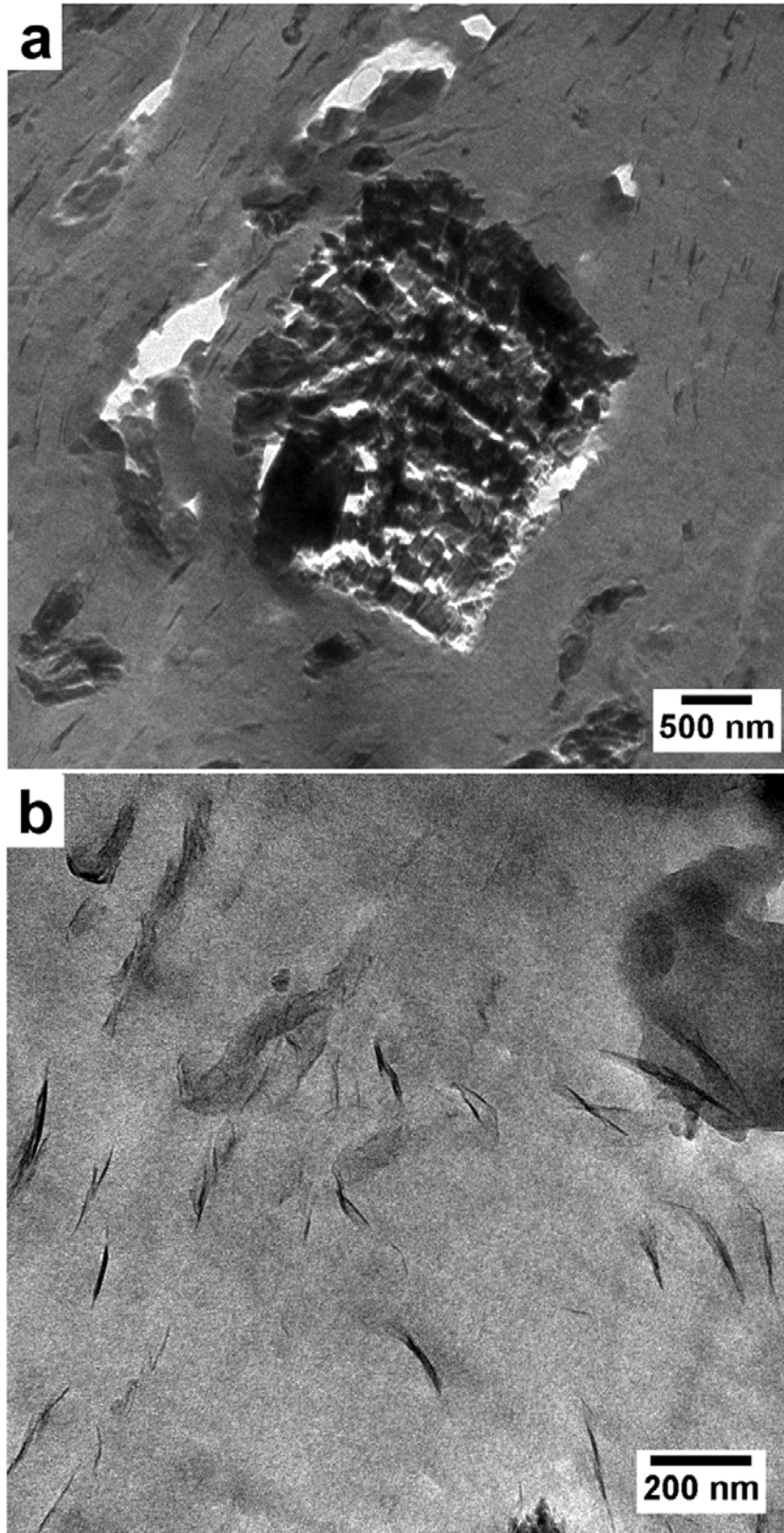


Figure 3.25 (a) and (b) TEM micrographs of solution intercalated nanocomposites based on HIPS with 35 wt% aluminum tri-hydroxide (s-NC/35ATH)

The corresponding XRD pattern given in Figure 3.26 for the solution intercalated nanocomposite (*s*-NC) reveals an increased montmorillonite interlayer spacing (d_{001}) of 3.1 nm which was formerly 1.8 nm prior to the dispersive treatment involving toluene pre-intercalated nanoclays and polymer chains dissolved in toluene. This strongly suggests polymer intercalation in nanoclay interlayers as observed on TEM images when the solution intercalation method is utilized. Higher order reflections from polymer intercalated nanoclays were also detected with peak positions marked with stars in Figure 3.26. The mentioned peaks were attributed to higher order reflections rather than first order reflection of degraded nanoclays (as in the case of melt-mixed samples explained below) since remarkable degradation of organic modifier is not expected during ambient temperature solution processing and following drying and shaping processes.

In the literature, two separate mechanisms were proposed for the solution intercalation of polymers into clay interlayers as exfoliation-adsorption and exfoliation-exchange. Li and Ishida [107] investigating the solution intercalation of nanoclay in polystyrene/toluene systems showed that the governing mechanism is exfoliation-adsorption when the polymer concentration in the solvent equals to or exceeds 10 wt%. In exfoliation-adsorption, solvent molecules intercalated in the interlayer attract the dissolved polymer chains leading to the co-existence of polymer and solvent in the interlayer prior to the removal of solvent. Interlayer spacing decreases gradually during the evaporation of solvent and level off at a value that is significantly larger than that of neat nanoclay when the solvent is completely removed and polymer chains are accommodated in the interlayer.

The presence of the flame-retardant additive leads to significantly lowered intensity of first order polymer intercalated nanoclay reflections accompanied with a slight shift of the peak position from 3.1 to 3.0 nm. The lower recorded intensities could be attributed to scattering and absorption of the diffracted beam by interrupting flame-retardant particles. Such lowering of the diffracted intensity occurs in proportion with the loading level of the flame-retardant which supports the proposed phenomenon of interruption.

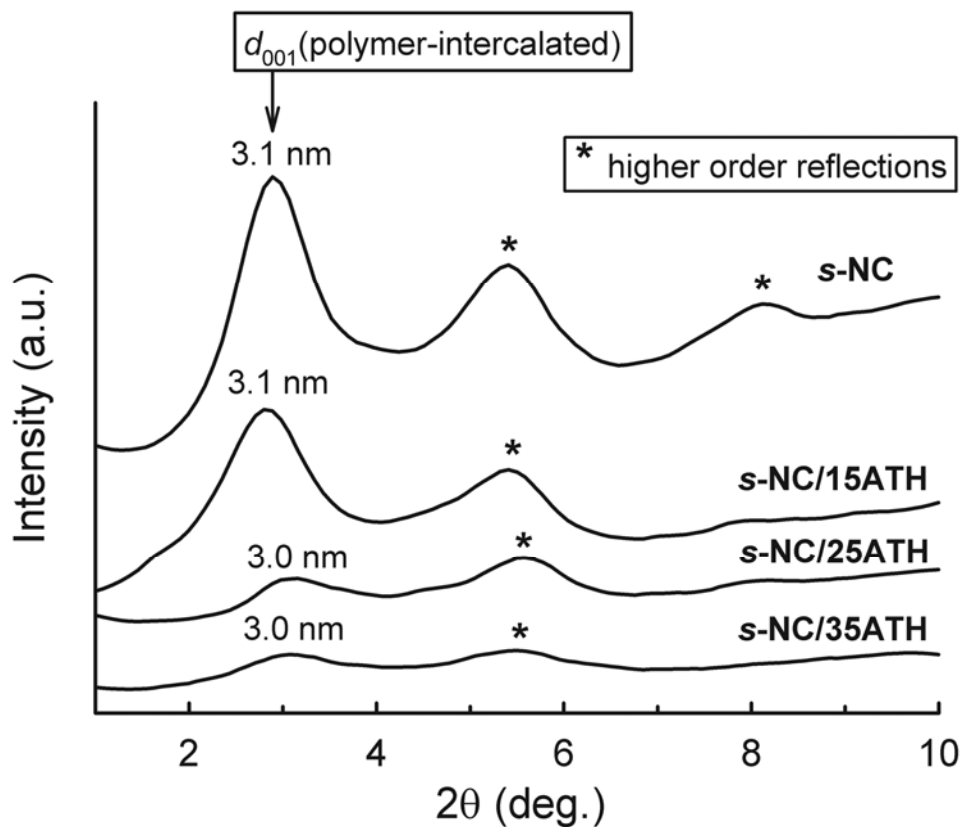


Figure 3.26 XRD patterns of solution intercalated nanocomposites based on neat HIPS and HIPS with various levels of ATH

TEM micrographs of melt-mixed nanoclay composite (*m*-NC) in Figure 3.27 reveal the phase separation of clay mineral particles and polymer matrix, hence the absence of polymer/montmorillonite hybrid nanomorphology. Clay mineral particles are present in the form of aggregates which barely exhibit polymer intercalation. The larger magnification image shows that an aggregate constitutes stacks of large number of clay layers in opposition to solution intercalated samples where montmorillonite particles are composed of only a few clay layers.

XRD patterns of nanoclay containing samples prepared by melt-mixing display single reflections at around $d_{001}=1.6-1.7$ nm (Figure 3.28). In order to reveal the underlying morphology that produces such reflections, a set of annealing experiments were conducted at the exact temperature of twin-screw extrusion and the degradation of organic modifier and corresponding decrease in the interlayer space during melt-mixing with the polymer matrix were simulated. A degraded nanoclay d -spacing of 1.6 nm via the interrupted collapse of the nanoclay was found to correspond to an extent of degradation where the organic modifier loses ~40% of its mass (~17% loss of the overall nanoclay mass) after an annealing treatment for 10 minutes at the particular processing temperature. Accordingly, the reflections observed in the XRD patterns of melt-mixed samples in Figure 3.28 were attributed to the first order reflection (d_{001}) of the degraded nanoclay with only very slight indication of polymer intercalation in clay interlayer.

Therefore, it can be stated that nanofiller dispersion can be significantly altered by using different preparation techniques where intercalated nanocomposites with fine dispersion and phase-separated microcomposites with poor dispersion can be obtained for compounds with same composition.

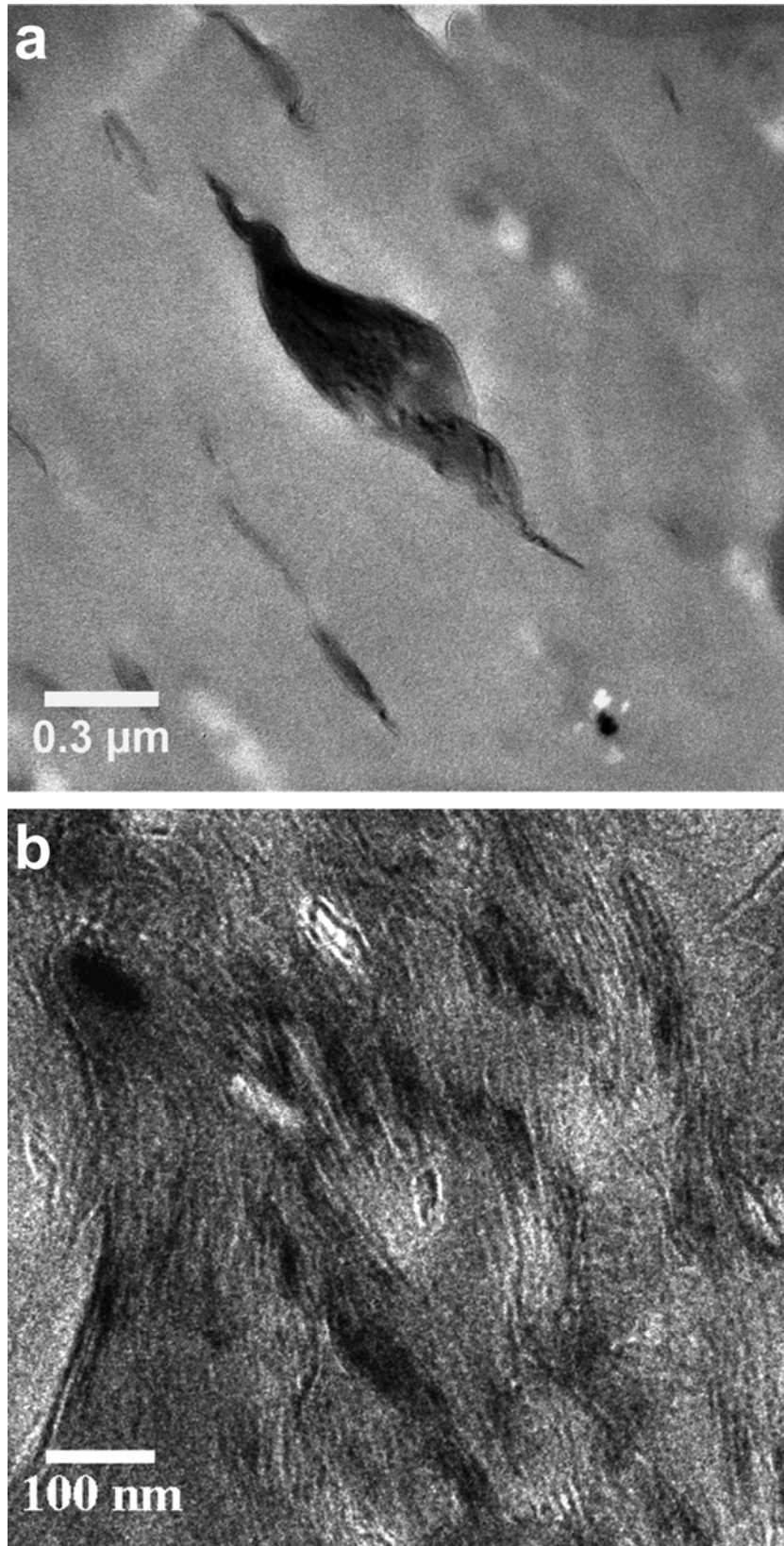


Figure 3.27 TEM micrographs of nanoclay containing melt-mixed HIPS/clay (*m*-NC) showing phase-separated microcomposite morphology; (a) low and (b) high magnification images

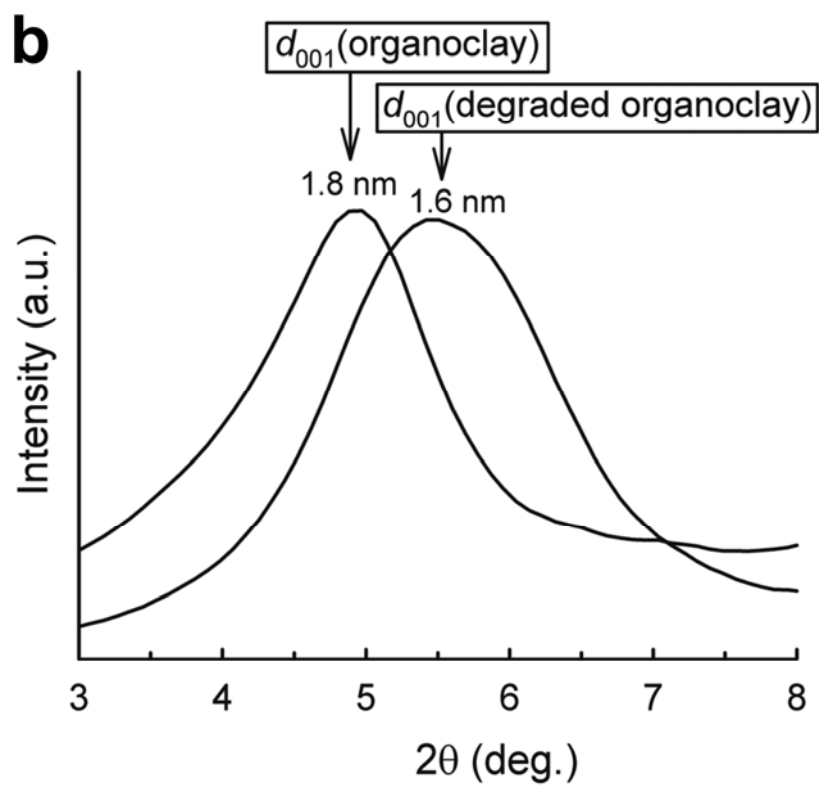
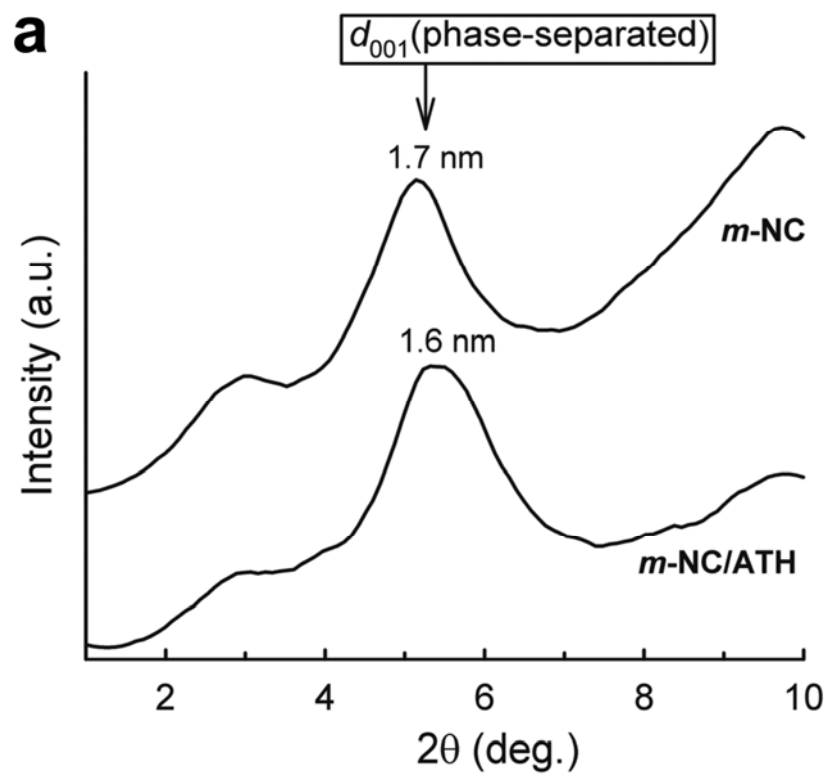


Figure 3.28 XRD patterns of clay containing melt-mixed HIPS and HIPS/ATH; (a) *m*-NC and *m*-NC/ATH samples, (b) organoclay and degraded organoclay

3.2.2 Flame Retardancy

(i) Mass Loss Cone Calorimeter Analysis

Peak value of heat release rate (PHRR) during combustion is an important fire parameter related to the material's contribution to the severity of flashover of a fire. Figure 3.29 displays the influence of nanoclay dispersion state on the PHRR of neat HIPS and HIPS with various loading levels of aluminum hydroxide flame-retardant. It is clear without exception that the lowest PHRRs were obtained when the nanoclays form intercalated nanocomposites when incorporated in neat polymer and flame-retarded compounds. The reduction obtained in PHRR of neat HIPS by the incorporation of 3 wt% nanoclays forming an intercalated nanocomposite were well-comparable to that reported in a previous study [108]. Figure 3.29 also shows that the amounts of char residues remaining at the end of combustion present similar trends with PHRR (actually an opposite trend) where intercalated nanocomposites showed enhanced charring compared to phase-separated microcomposites.

Table 3.11 lists some of the important fire parameters interpreted from mass loss calorimeter analysis. Incorporation of nanoclays with intercalated dispersion state provided the largest suppressions of PHRR (Δ PHRR) with respect to neat HIPS and HIPS with ATH, at least double which was obtained with nanoclays of phase-separated dispersion state. Particularly, peak values of mass loss rate (PMLR) are strongly dependent on the dispersion state of the nanoclay where the largest reductions were attained with intercalated nanocomposites. Reasonable attempts to determine the flame spread as a fire hazard are to consider fire growth index (FGI) defined by the ratio of PHRR to time-to-ignition, or fire growth rate (FIGRA) defined by the ratio of PHRR to time-to-PHRR [109]. The two approaches were in agreement with regard to the effect of nanoclay dispersion state. Intercalated nanocomposites exhibited significantly slower flame spread in all formulations owing to well-suppressed PHRR and retained time-to-ignition or time-to-PHRR.

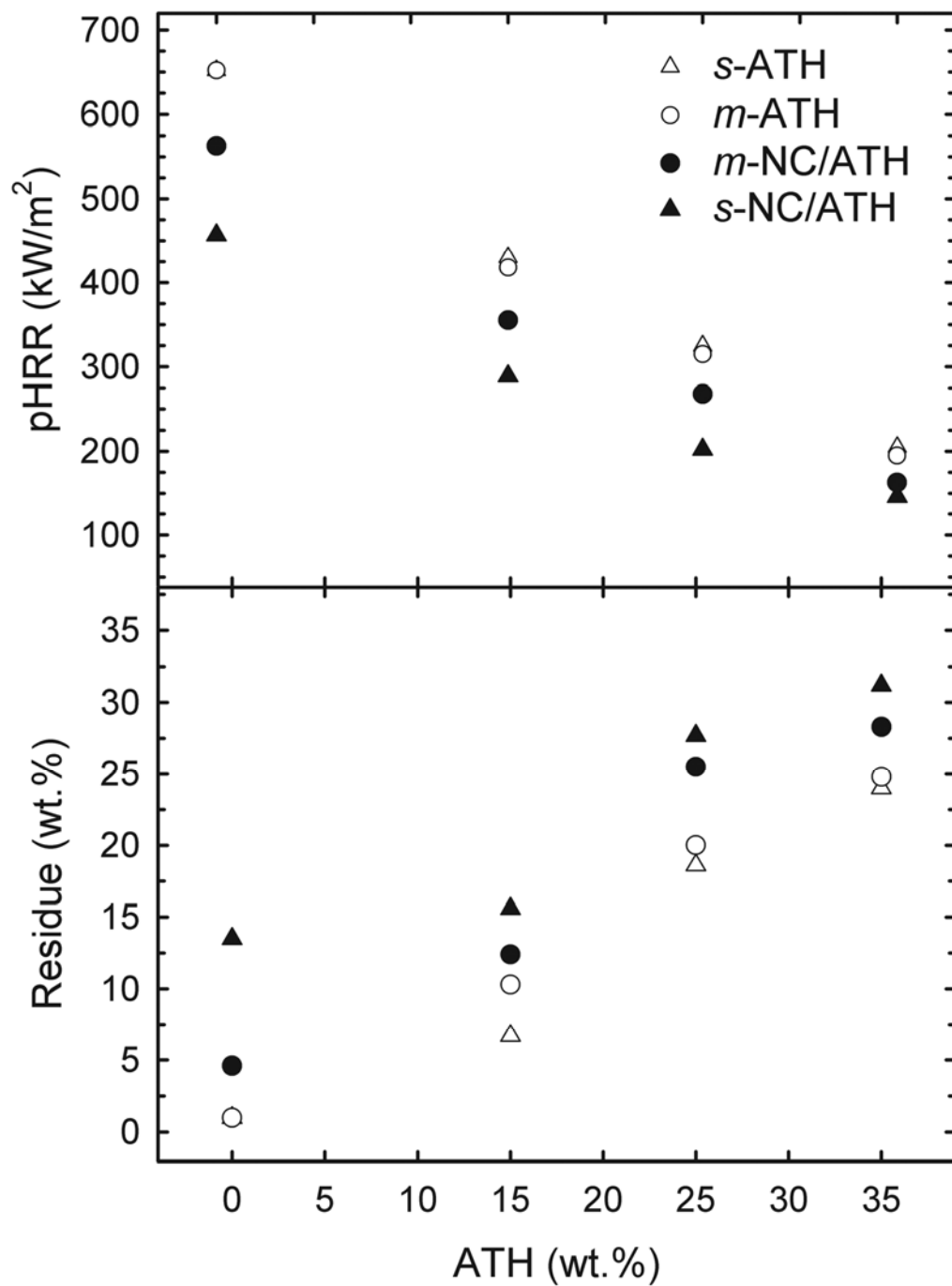


Figure 3.29 Influence of nanoclay dispersion state on the peak heat release rate and char residues in the mass loss calorimeter

It is apparent from Figure 3.30 comparing the mass loss behavior of neat HIPS with *m*-NC and that of *m*-25ATH with *m*-NC/25ATH that no remarkable suppressions could be obtained with the incorporation of nanoclays in phase-separated dispersion state. Contrarily, polymer intercalated nanoclays strongly impede mass loss and provide a plateau-like steady mass loss rate when incorporated in HIPS with ATH (*s*-NC/25ATH), as an indication of effective barrier layers against heat and mass transfer being formed on the flaming surfaces during combustion. It can also be inferred from Figure 3.31 showing the changes in the sample mass with time during forced flaming combustion, that the peak mass loss rate was drastically reduced by organoclays.

Therefore, it can be stated that an intercalated morphology effectively slows down the rate of evolution of volatiles during combustion. This might be ascribed to the nano-confinement of decomposing radicals within the clay interlayer space allowing for further radical recombination reactions which retards volatilization [110]. On the other hand, a phase-separated microcomposite lacks the nano-confinement effect; therefore combustion behavior was significantly altered.

Table 3.11 Mass loss calorimeter performance of specimens showing the effect of nanofiller dispersion

	HIPS	<i>m</i>-NC	<i>s</i>-NC		
-ΔPHRR^a	-	13.7	30.0		
-ΔPHRR^b	-	-	-		
FGI (FIGRA)^c	9.8 (5.7)	13.4 (6.2)	9.7 (4.6)		
PMLR^d	30.7	30.8	23.0		
	<i>m</i>-15ATH	<i>m</i>-NC/15ATH	<i>s</i>-15ATH	<i>s</i>-NC/15ATH	
-ΔPHRR	35.9	45.6	34.0	55.7	
-ΔPHRR	-	15.1	-	32.8	
FGI (FIGRA)	8.7 (3.7)	7.9 (3.8)	7.5 (3.5)	5.8 (2.3)	
PMLR	17.9	16.2	22.7	15.6	
	<i>m</i>-25ATH	<i>m</i>-NC/25ATH	<i>s</i>-25ATH	<i>s</i>-NC/25ATH	
-ΔPHRR	51.7	58.9	50.2	69.0	
-ΔPHRR	-	14.9	-	37.8	
FGI (FIGRA)	6.3 (3.2)	5.6 (2.7)	6.1 (2.7)	4.0 (1.5)	
PMLR	15.3	14.9	19.8	11.9	
	<i>m</i>-35ATH	<i>m</i>-NC/35ATH	<i>s</i>-35ATH	<i>s</i>-NC/35ATH	
-ΔPHRR	70.0	75.0	68.6	77.6	
-ΔPHRR	-	15.1	-	28.8	
FGI (FIGRA)	3.8 (1.8)	3.3 (1.3)	3.6 (1.3)	2.6 (0.9)	
PMLR	11.9	11.7	11.8	9.0	

^a with respect to neat HIPS (kW/m²)

^b with respect to *m*-ATH or *s*-ATH (kW/m²)

^c (kW/s-m²)

^d (g/s-m²)

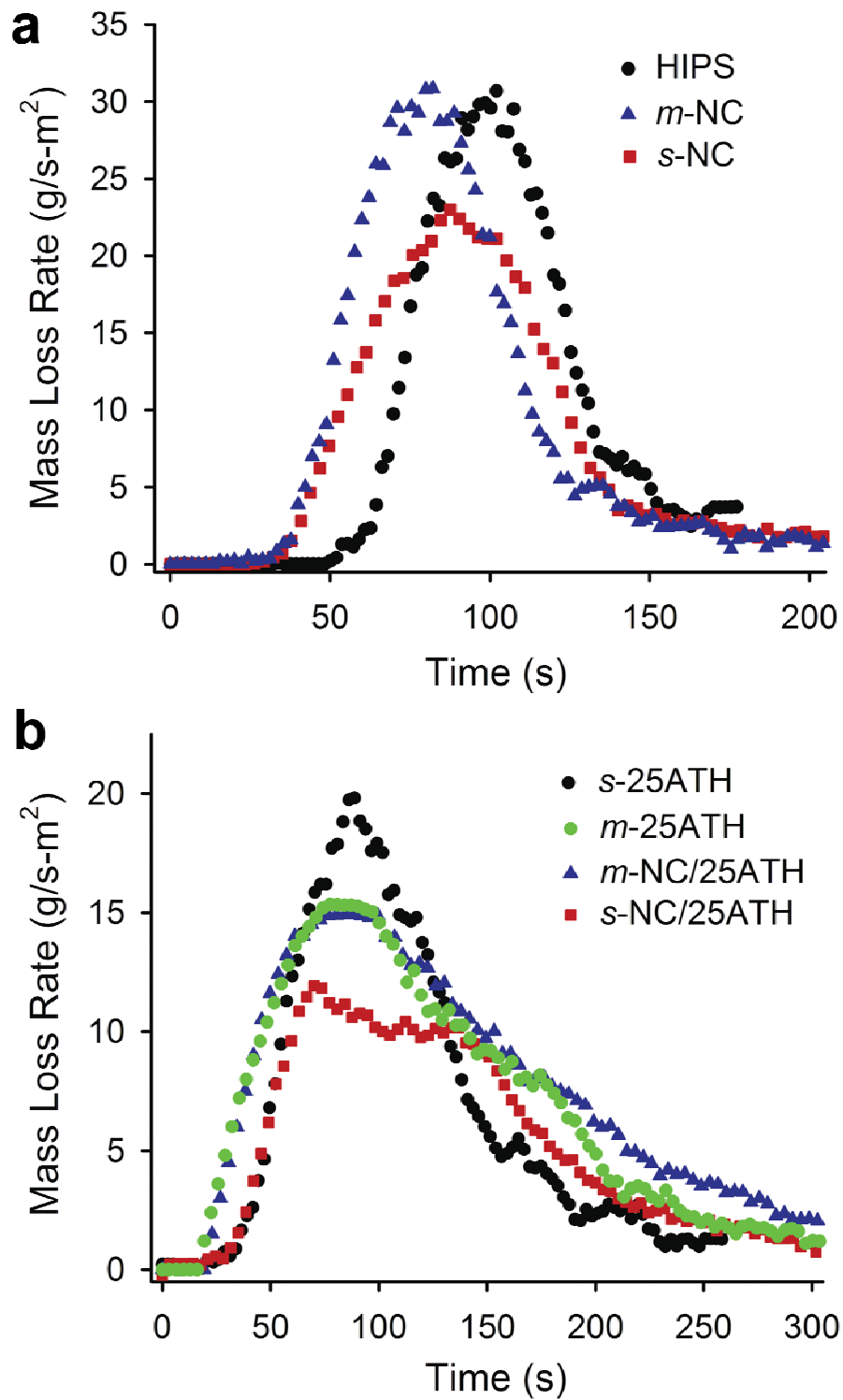


Figure 3.30 Influence of nanoclay dispersion state on the mass loss behaviors of (a) HIPS and (b) HIPS/ATH in the mass loss calorimeter

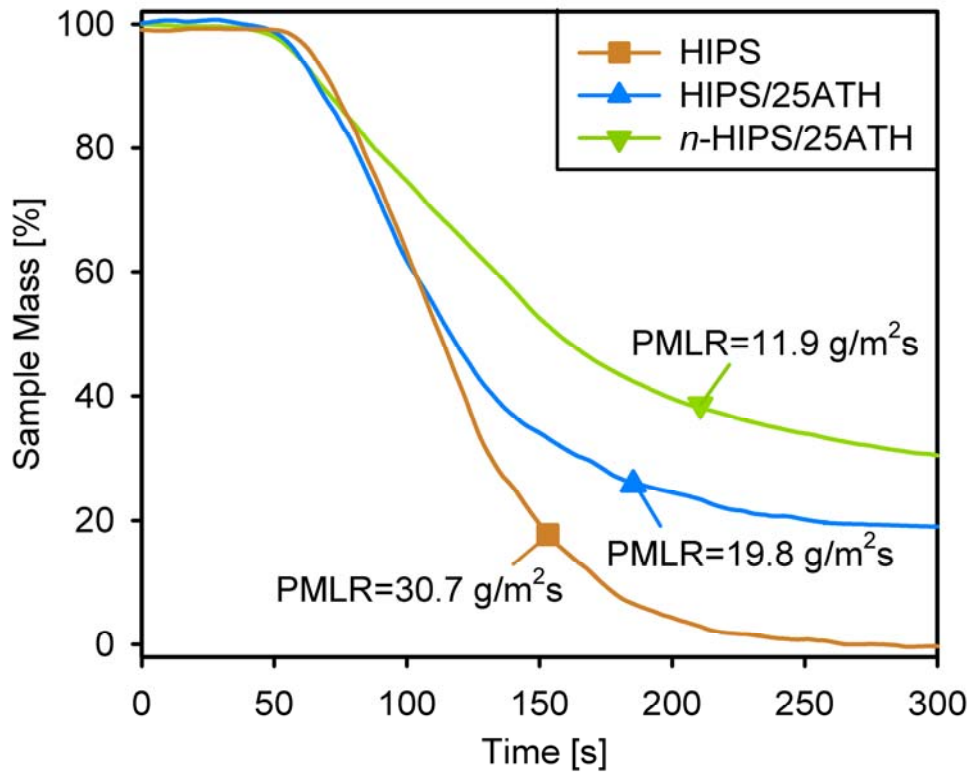


Figure 3.31 Mass loss behavior during combustion in the mass loss calorimeter

(ii) LOI and UL94 Flammability Tests

Flammability of studied materials in terms of the required critical oxygen concentration to support flaming combustion, i.e. the limiting oxygen index, is shown in Figure 3.32(a). High-impact polystyrene is a highly combustible polymer which supports flaming even at a very low oxygen concentration of 17.8%. The ease of combustion is caused by the evolution of highly-flammable styrenic mono-, di- and tri-mers into the gas phase as degradation products [29].

Limiting oxygen index was improved at most by 2.5% compared to neat HIPS with the incorporation of the flame-retardant additive at the highest loading level utilized in this study. Further increases in LOI were obtained in the presence of nanoclay with both dispersion states. It is clear that the state of dispersion notably affects the flammability properties such that an intercalated nanocomposite is superior compared to phase-separated microcomposite at the same level of clay loading in the matrix. In terms of enhancements in LOI, addition of 3 wt% of nanoclay in the intercalated state was shown to perform better than a further addition of 20 wt% of the conventional flame-retardant additive. In addition, the linear burning rates in UL94 horizontal orientation were remarkably lower with intercalated nanocomposite morphology, as shown in Figure 3.32(b).

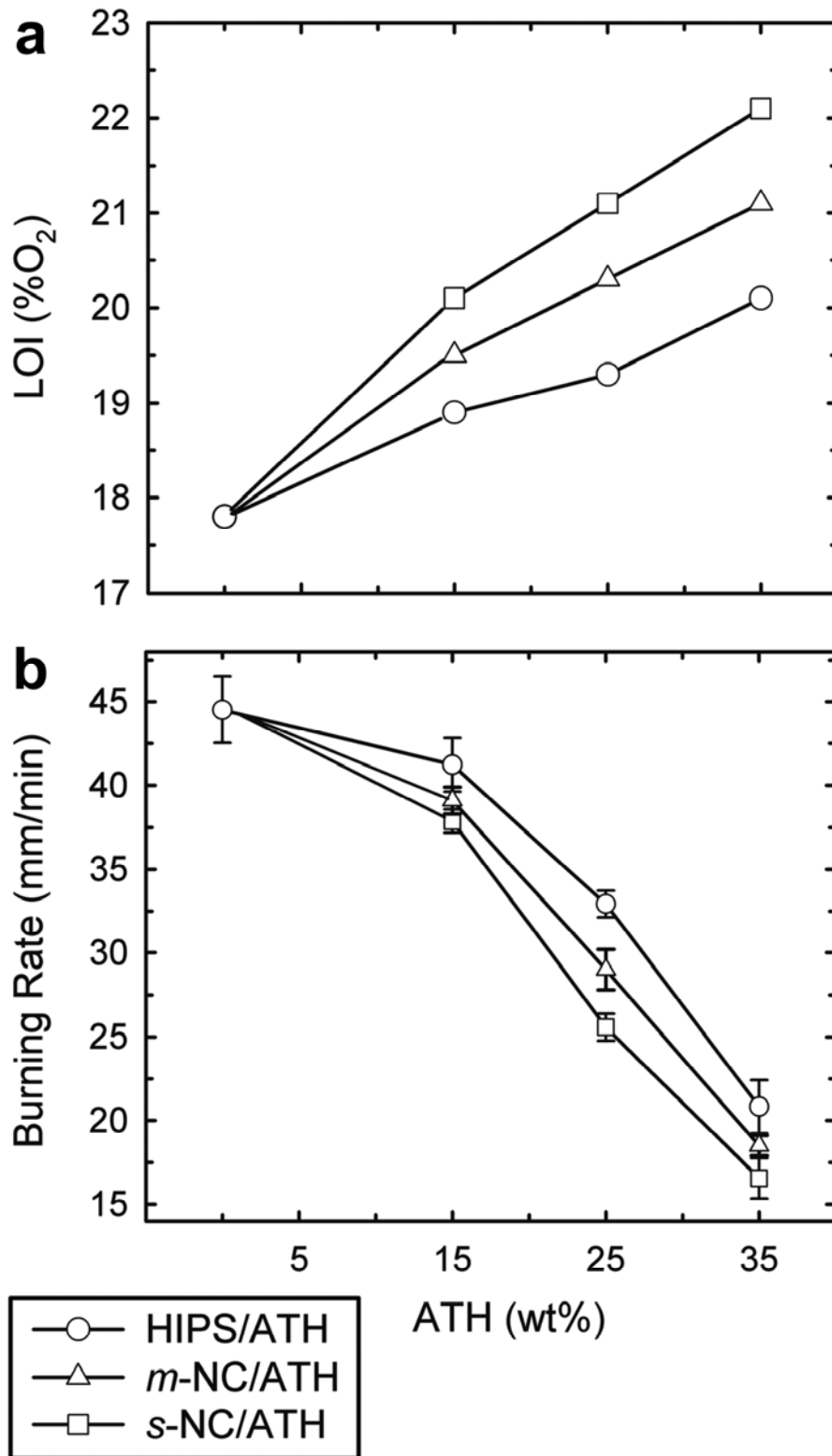


Figure 3.32 (a) Limiting oxygen index values and (b) linear burning rates in UL94 tests showing the effects of flame retardant content and nanofiller dispersion

3.2.3 Flame Retardancy Mechanisms by Thermal Degradation

Single step decomposition was observed for neat HIPS, *m*-NC and *s*-NC in thermogravimetry, as shown in Figure 3.33. The early degradation of the alkyl ammonium clay modifier was evident in thermal degradation of solution-processed nanocomposite (*s*-NC), whereas the melt-processed composite (*m*-NC) did not show such early mass loss due to prior degradation of clay modifier during processing.

Materials containing ATH possessed a two-step mass loss in thermogravimetry. The first step corresponds to the release of water upon the initial low temperature dehydration of aluminum tri-hydroxide into intermediate hydrated species, i.e. boehmite, at around 320 °C. The transformation can be followed from the XRD patterns in Figure 3.34 for samples annealed at 210°C and 400°C indicating aluminum tri-hydroxide and boehmite as the stable phases, respectively. Mass loss in the second step is attributed to overlapping polymer main-chain decomposition and final dehydration of boehmite into anhydrous γ -Al₂O₃. Boehmite to γ -Al₂O₃ transformation was verified via annealing experiments (Figure 3.34) to occur within a temperature range between 400 and 590°C.

Table 3.12 summarizes the interpreted thermogravimetric data for the observed mass loss steps during heating. It is clear that the maximum degradation temperature (T_{\max}) and the onset of degradation (T_0) were increased in the presence of nanoclay both in neat HIPS and HIPS with ATH, independent of nanoclay dispersion state. On the other hand, minor changes could be observed in the degradation temperatures when neat HIPS and HIPS with ATH (*s*-25ATH and *m*-25ATH) were compared.

Remarkable changes in the degradation behavior by nanocomposite formation were observed in terms of mass loss rates in thermogravimetry. The peak mass loss rate corresponding to main-chain decomposition (Step 2) was lower for *s*-NC compared to *m*-NC. This could be attributed to retarded diffusion of volatile degradation products via the tortuous pathway formed by clay layers. More specifically, the radicals from polystyrene decomposition confined in clay galleries undergo further recombination reactions slowing down their release into the gas phase.

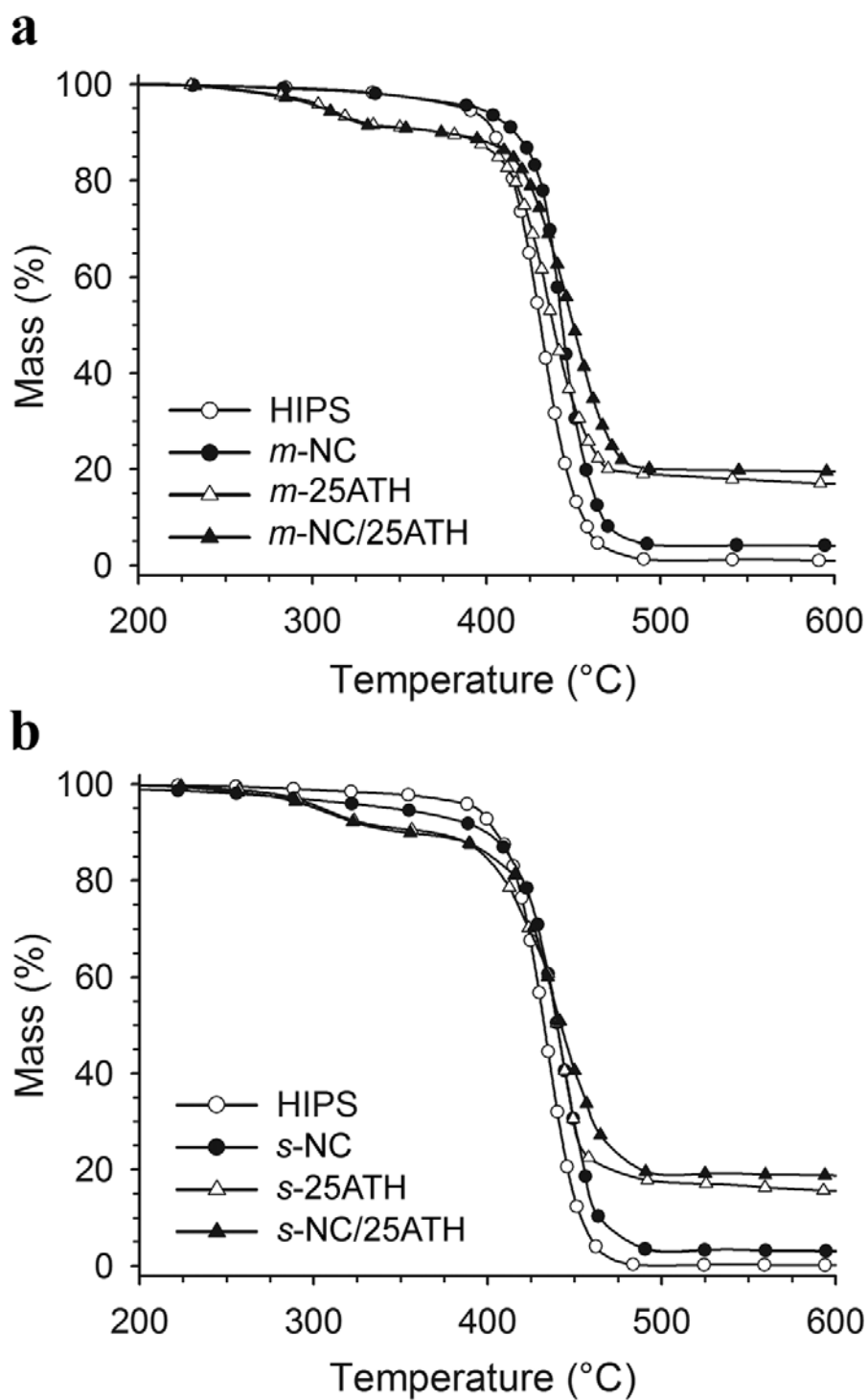


Figure 3.33 Thermogravimetric curves with nanoclay dispersion states of; (a) phase-separated microcomposite and (b) intercalated nanocomposite

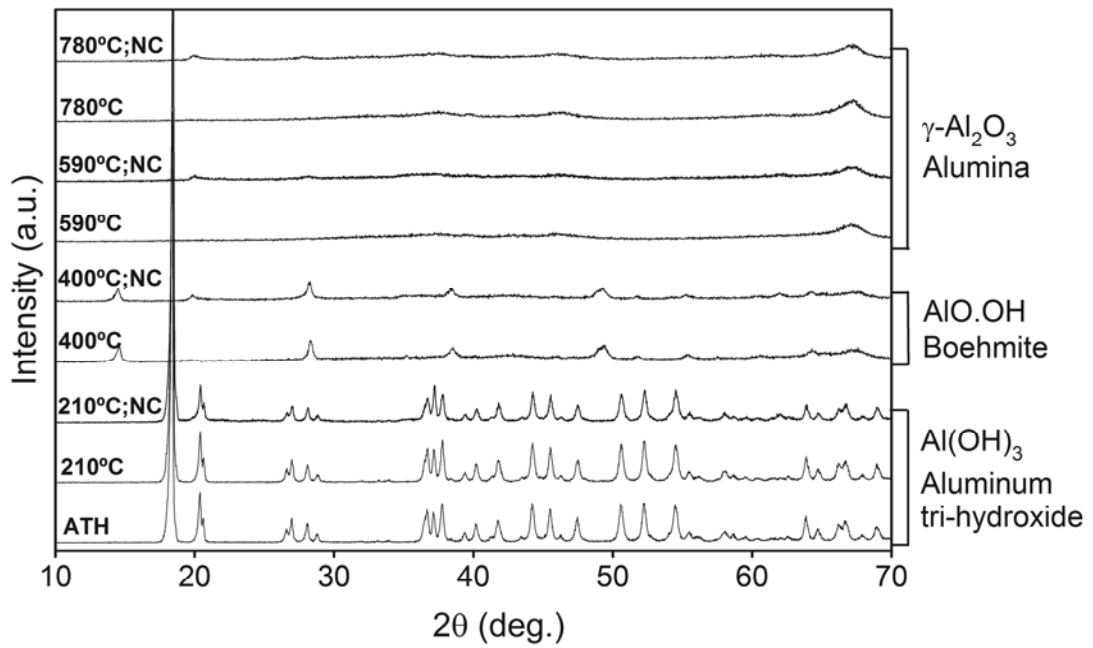


Figure 3.34 XRD patterns elucidating the decomposition path of ATH and ATH/NC powder mixtures upon annealing

Table 3.12 Thermogravimetric and differential thermogravimetric data revealing the effect of nanofiller dispersion

Specimen	T_{\max} (°C)		T_0 (°C)		DTG Peak (% s ⁻¹)		Char (wt.%)
	Step1	Step2	Step1	Step2	Step1	Step2	
HIPS	-	432	-	406	-	0.398	-
<i>s</i> -NC	-	445	-	416	-	0.372	3.1
<i>m</i> -NC	-	441	-	418	-	0.487	4.1
<i>s</i> -25ATH	319	436	270	412	0.031	0.271	15.6
<i>s</i> -NC/25ATH	323	437	269	417	0.029	0.226	18.8
<i>m</i> -25ATH	310	432	282	406	0.031	0.331	16.9
<i>m</i> -NC/25ATH	318	446	284	416	0.028	0.238	19.5

The percentages of char residues upon heating to 600°C, listed in Table 3.12, indicated that charring was not influenced by nanocomposite formation when the values for *m*-NC and *s*-NC are compared. It may therefore be concluded that, although volatile evolution was retarded in the presence of polymer intercalated nanoclay, the radical recombination products could not be stabilized in the condensed phase at high temperatures under flowing nitrogen. It can be inferred from the char percentages of materials containing ATH that, upon dehydration, a residue of around 60% of the initial ATH mass remains in the condensed phase, independent of the presence of nanoclay.

3.2.4 Flame Retardancy Mechanisms by Residue Analysis

Residues from mass loss calorimeter tests, namely fire residues, were similar in structure when compared to ATH and ATH/clay mixtures annealed in furnace. The final stable phase upon the complete decomposition of ATH during combustion in the mass loss calorimeter is a transition alumina, i.e. γ -Al₂O₃, both in the presence and absence of the nanoclay as shown by the XRD patterns in Figure 3.35. Residue of the sample with nanoclay (*s*-NC/25ATH) displays additional reflections from montmorillonite. Figure 3.36 contains XRD patterns showing the intercalation state of montmorillonite in fire residues. Montmorillonite interlayer spacings were found to be around $d_{001} \sim 1.3$ nm being independent of the initial dispersion state (intercalated or phase-separated) or the dispersion technique (solution- or melt-mixing) which indicates that complete montmorillonite collapse takes place by combustion in the mass loss calorimeter.

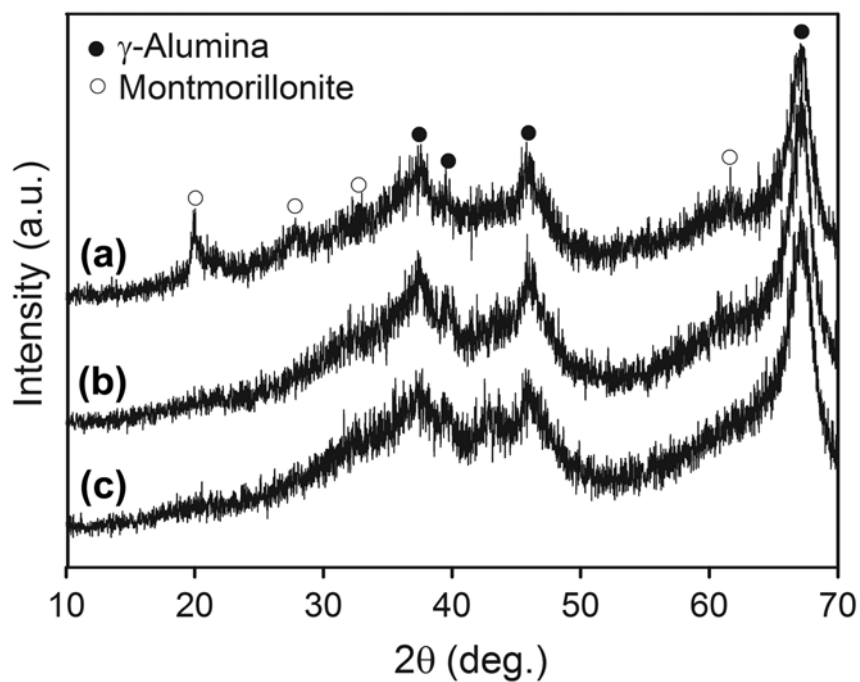


Figure 3.35 XRD patterns comparing (a) s-NC/25ATH residue, (b) s-25ATH residue and (c) ATH annealed at 590 °C

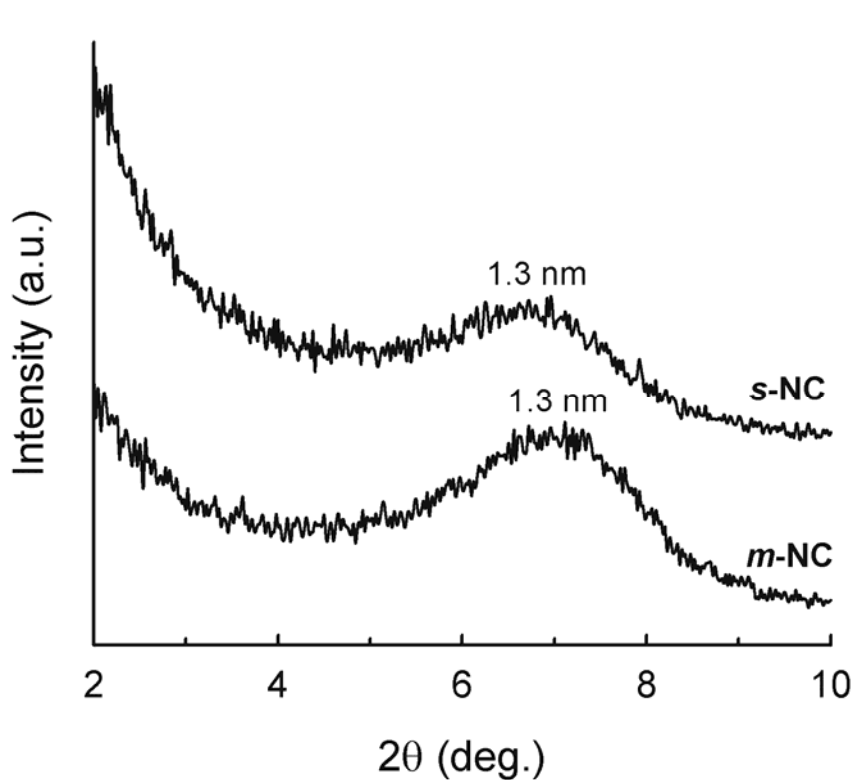


Figure 3.36 XRD patterns showing montmorillonite interlayer spacings in mass loss calorimeter residues

SEM images of fire residue from phase separated microcomposite are shown in Figure 3.37. The residue mainly consists of fine spherical carbonaceous char particles in the size range 60–100 nm and poorly dispersed coarse montmorillonite particles with sizes 5 to 15 μm . The region designated as “A” in Figure 3.37(a) is rich in C with respect to Al and Si whereas the region shown by “B” is enriched by Al, Si and O arising from aggregation of montmorillonite particles. Figure 3.37(b) is a closer view of coarse aggregates of montmorillonite particles which was proved by observing backscattered electron image (Figure 3.37c) of such coarse aggregates showing brighter contrast with respect to carbonaceous char particles. The poor dispersion and coarse aggregate morphology of montmorillonite in the residue stems from poor clay dispersion in the composite prior to combustion. The non-uniform distribution of fine carbonaceous char and montmorillonite particles in the residue leads to a weak char structure that cannot act as an effective barrier against heat and mass transport during combustion.

SEM images of fire residue from intercalated nanocomposite are shown in Figure 3.38. It is clear that fine carbonaceous char particles and flake-like montmorillonite particles with submicron diameters are homogeneously distributed within the residue owing to better dispersion and intercalation in the nanocomposite prior to combustion.

Figure 3.39 displays SEM images of fire residues from HIPS/25ATH and corresponding phase-separated microcomposite and intercalated nanocomposite based on HIPS/25ATH. It can be deduced that faceted $\gamma\text{-Al}_2\text{O}_3$ particles are formed by the decomposition of ATH. The $\gamma\text{-Al}_2\text{O}_3$ particles are densely covered by montmorillonite particles in the residue from intercalated nanocomposite owing to the better initial dispersion of montmorillonite prior to combustion. On the other hand, montmorillonite particles are only rarely attached to the surface of $\gamma\text{-Al}_2\text{O}_3$ particles in the residue from phase-separated microcomposite. In fact, corresponding energy dispersive spectra recorded from $\gamma\text{-Al}_2\text{O}_3$ particles indicate C, Si enrichment of the particles in the residue from intercalated nanocomposite compared to that from phase-separated microcomposite.

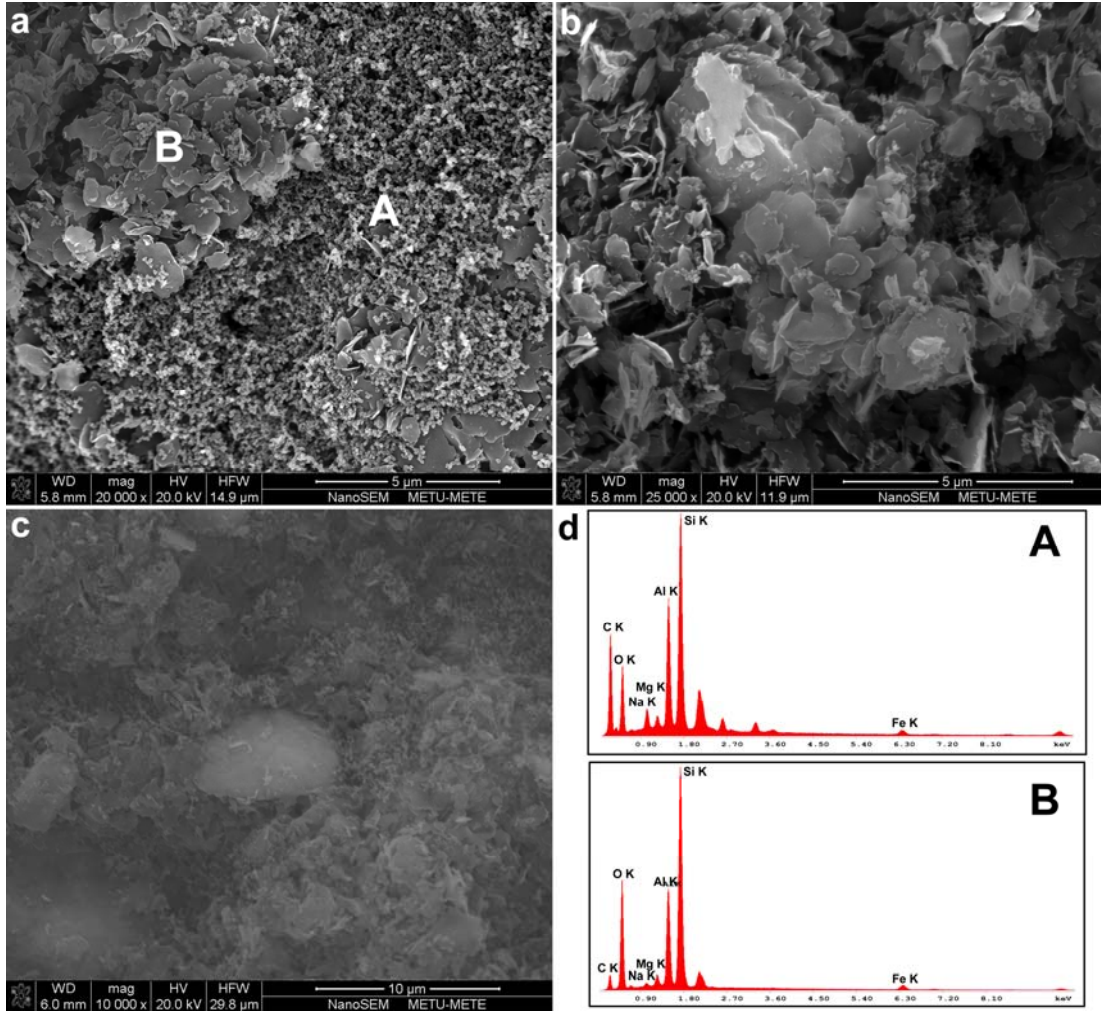


Figure 3.37 (a-c) SEM images and (d) energy dispersive spectra of fire residue from phase-separated microcomposite

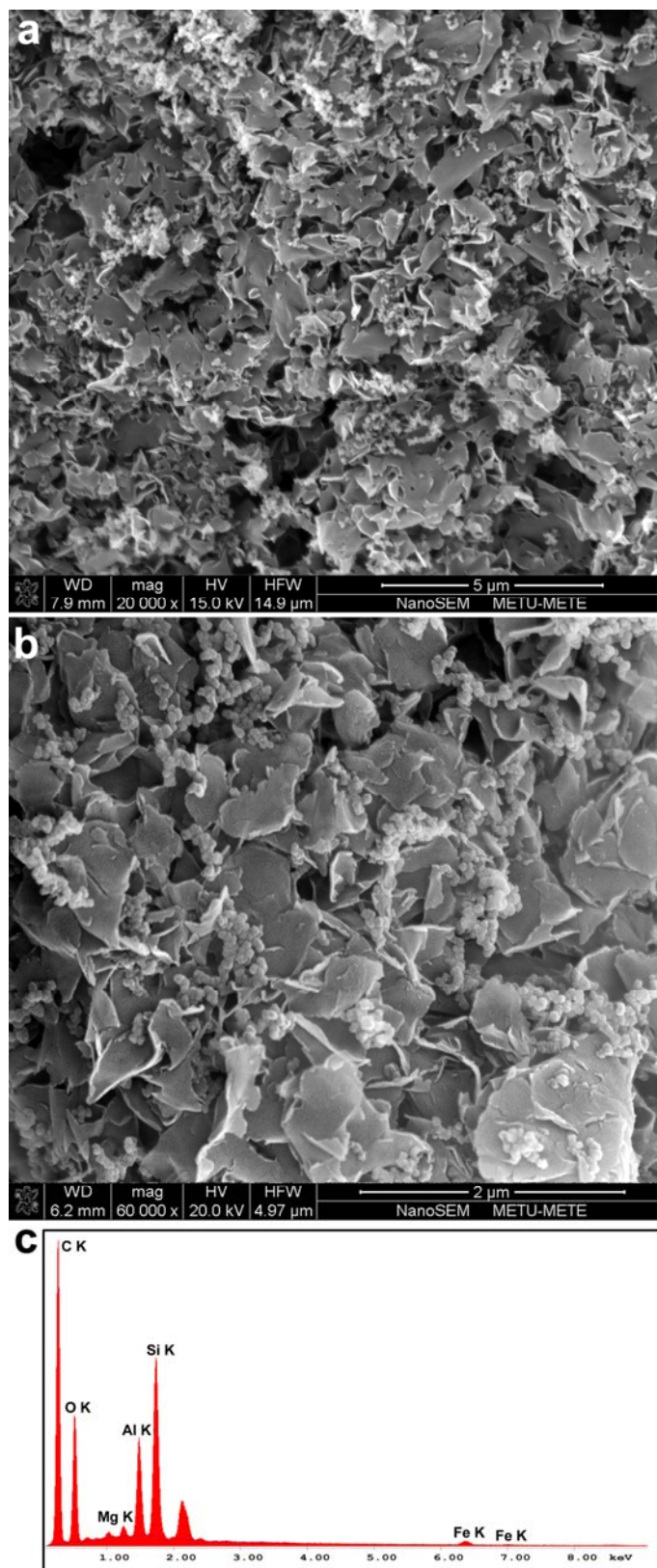


Figure 3.38 (a-b) SEM images and (c) energy dispersive spectrum of mass loss calorimeter residue from intercalated nanocomposite

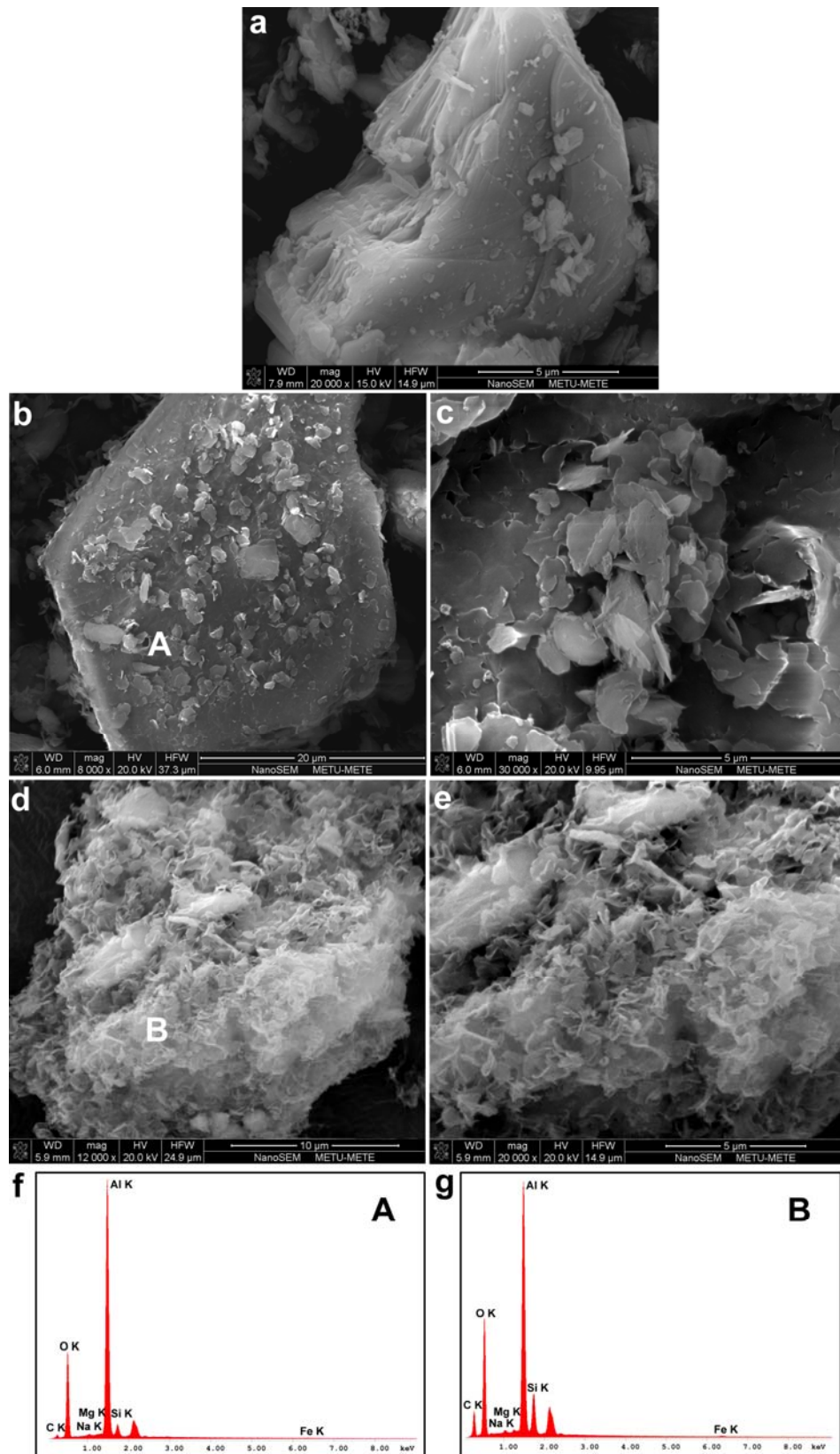


Figure 3.39 SEM images and energy dispersive spectra of fire residues from (a) HIPS/25ATH, (b-c) phase separated microcomposite based on HIPS/25ATH, and (d-e) intercalated nanocomposite based on HIPS/25ATH

In light of the above discussions, the mechanism how nanoclays with intercalated nanocomposite morphology performs remarkably superior to those with phase-separation when used in combination with aluminum tri-hydroxide can be suggested as follows.

The decomposition path of aluminum tri-hydroxide was not altered by nanoclays as can be inferred from annealing experiments. The stable phase in the fire residues was simply γ - Al_2O_3 regardless of the presence of polymer intercalated nanoclays. Slightly increased degradation temperatures and suppressed peak mass loss rates in thermogravimetry were rather weak and questionable implications for the enhanced flame retardancy of intercalated nanocomposites. Fire residues of samples with polymer intercalated nanoclays possessed collapsed microcomposite morphologies implying that chars were reinforced only at the micro-scale by montmorillonite particles rather than clay nanolayer reinforcement. Therefore, structural reinforcement of the chars by montmorillonite particles should not be the governing mechanism for the enhanced flame retardancy presented by intercalated nanocomposites.

The only solid implication for the mechanism of flame retardancy is the remarkable increases in the amounts of char residues in the cone calorimeter with polymer intercalated nanoclays (Figure 3.29). Carbonaceous char residues had been able to form in otherwise little or no char-forming high-impact polystyrene through the incorporation of polymer intercalated nanoclays as in the case of similar studies [111, 112].

In order to confirm the charring and condensed phase stabilization effect by organoclays, fire residues were characterized for their chemical structure by ATR-FTIR as shown in Figure 3.35. The overlapping absorption bands over $600\text{-}1000\text{cm}^{-1}$ range are a characteristic of aluminum oxide structure. Within this range, bands around $650\text{-}700\text{ cm}^{-1}$ of O-Al-O bending vibrations and those around $750\text{-}850\text{ cm}^{-1}$ attributed to Al-O stretching vibrations eventually overlap to form the wide bands observed in the spectra of the residues from flame-retardant HIPS and flame-retardant HIPS/organoclay nanocomposite.

Char residue of the nanocomposite contains an additional absorption peak at 1040 cm^{-1} attributed to in-plane Si-O stretching vibrations of montmorillonite clay [99]. The broad bands around 3400 cm^{-1} are attributed to OH stretching vibrations from free water being more pronounced in the clay containing residue due to the increased clay interlayer hydrophilicity upon degradation of the organic modifier. The feature around 1600 cm^{-1} , which is also more pronounced in the clay containing residue may arise from carbon-carbon double bond stretching in the vinyl group of styrene oligomeric units stabilized in char.

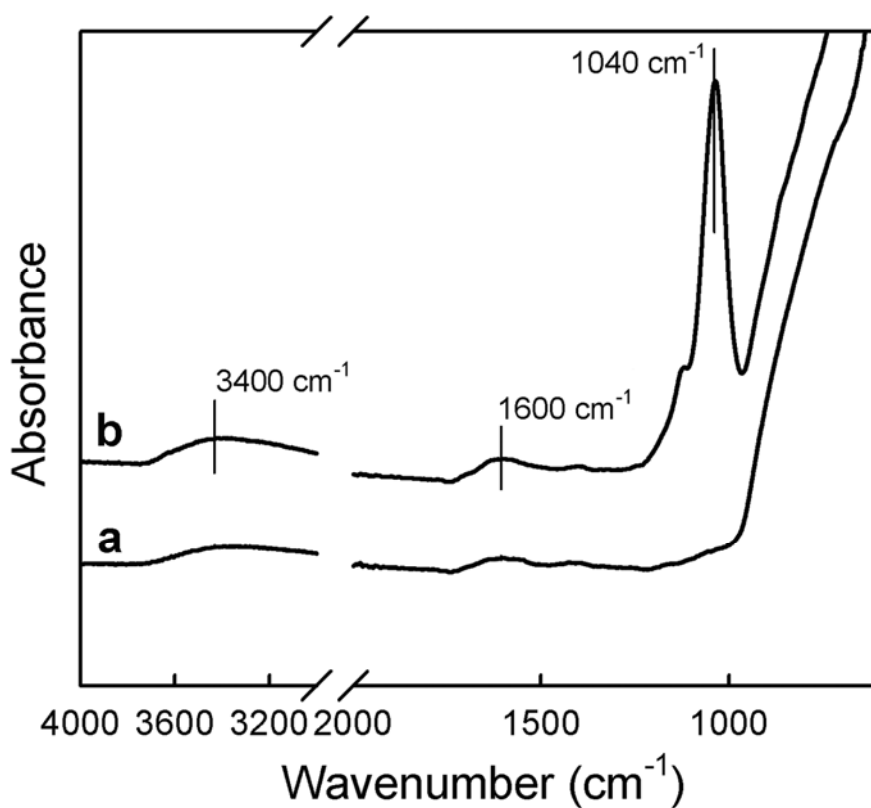


Figure 3.40 ATR-FTIR spectra of combustion residues from (a) flame-retarded HIPS and (b) flame-retarded HIPS/organoclay nanocomposite

Enhanced charring of the polymer enables the formation of thicker and more consolidated protective carbonaceous barrier layers that, in addition, contain collapsed montmorillonite and γ -Al₂O₃ particles. The formed barriers effectively shield the underlying polymer against the external radiant heat and heat feedback from the flaming zone in the cone calorimeter. The insulating barriers also impede the evolution of flammable volatiles into the gas phase and transfer of oxygen required for combustion.

An alternative explanation to the barrier model discussed above for the improved flame retardancy via nanocomposite formation has recently been suggested by Chen et al. [110] as the “nanoconfinement” effect. The concept of nanoconfinement is not limited to the formation of a surface char layer but rather related with hindered diffusion of volatiles from decomposition within the nanocomposite throughout thermal degradation and combustion. Prolonged residence time allowed for intercalated macroradicals from polymer decomposition via the nanoconfinement effect of clay interlayers is thought to allow for bimolecular radical recombination reactions to occur which retard the evolution of volatiles leading to lower rates of mass loss and hence heat release in the cone calorimeter

3.2.5 Mechanical Properties

Figure 3.41 shows that unprecedented improvements are obtained in terms of elastic moduli (up to 53%) and yield strength (up to 51%) when the nanoclay is present in its polymer intercalated state, noting that the reinforcing filler constitutes a very small volume fraction of the composite (1.8 wt% ~ 0.95 vol% on silicate basis). The former is attributed to the very large effective aspect ratio and elastic modulus of an individual nanoclay layer in its intercalated state. The latter is provided by the molecular level entanglements of polymer chains and intercalated nanoclays with very large surface area which impedes the cooperative motion of polymer chains resulting in a larger required stress for yielding. It is expected for intercalated nanocomposites with fine nanofiller dispersion that clay/matrix interactions occur across large total interfacial area with the matrix. However, when the nanoclay is phase-separated, only minor improvements in elastic moduli and yield strength could be seen for the entire range of formulations.

Improvements in the ultimate tensile strength are also evident from Figure 3.41 for intercalated nanocomposites. The nanometric lateral fineness of the reinforcing filler could be an explanation for the cease of stress concentration at clay edges. The corresponding increase in the ultimate tensile strength could then be related to the dispersion state of the highly-stiff, large aspect ratio nanoclays.

Recent studies show that an overall homogenous micron scale distribution is enough for best stiffness improvements rather than a true exfoliated morphology [113, 114]. To support this idea, exfoliated and intercalated nanocomposites were compared and almost the same improvements were achieved in stiffness [64]. However, in the current study, comparisons were made not between different nanocomposite morphologies but between an intercalated nanocomposite and a conventional phase-separated microcomposite. Therefore, the remarkable advantage of the nano-effect [115] was clearly observed in terms of mechanical properties.

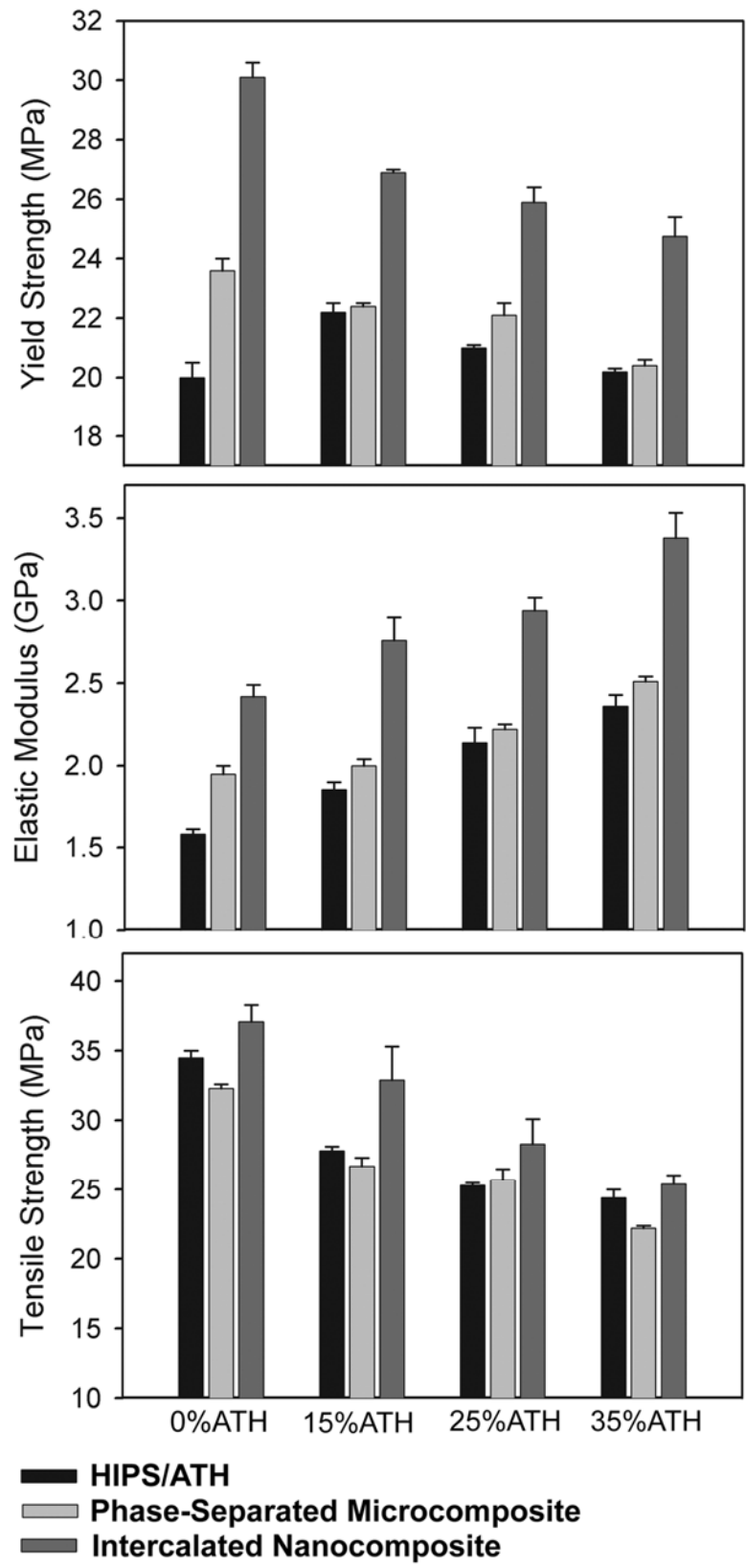


Figure 3.41 Mechanical properties as a function of the nanoclay dispersion state

Fillers that are incompatible with the polymer matrix are generally known to decrease the ultimate tensile strength as a consequence of particle-matrix interfacial de-bonding and stress concentration due to the smaller cross-sectional area of load bearing matrix. This is exactly the case with aluminum tri-hydroxide (Figure 3.41) since it is an inorganic filler having no virtual compatibility with the polymer matrix. Accordingly, the filler debonds at the particle/matrix interface upon loading as shown by the fracture morphologies displayed in Figure 3.42, and clear reductions occur in the ultimate tensile strength in proportion with the ATH content. Similarly, it is apparent from Figure 3.41 that ultimate tensile strength is further lowered in the presence of nanoclays with phase-separated morphologies.

Figure 3.43 shows the tensile fracture surfaces of phase-separated microcomposite (*s*-NC) indicating the presence of coarse second phase particles inside the ductile HIPS matrix. Elemental mapping of Si, Al, O and C verifies that such coarse particles are actually aggregates of montmorillonite particles formed due to poor dispersion of the nanofiller in the matrix. It is also clear from the fractographic images that clay aggregates show severe debonding at the particle/matrix interface upon loading which was evidenced by dark regions formed due to extensive matrix shear deformation in close vicinity of clay aggregates.

The fracture surfaces of the intercalated nanocomposite shown in Figure 3.44 reveals significant ductility of the matrix displaying rough surfaces with fine features formed by shear deformation. Contrary to the case with phase-separated microcomposite, the fracture morphology was notably homogenous throughout the whole sample surface where no coarse second phase particles could be observed. In addition, elemental mapping of the fracture surface for Si (as well as Al, O and C; not shown) indicates evenly dispersed montmorillonite particles within the matrix.

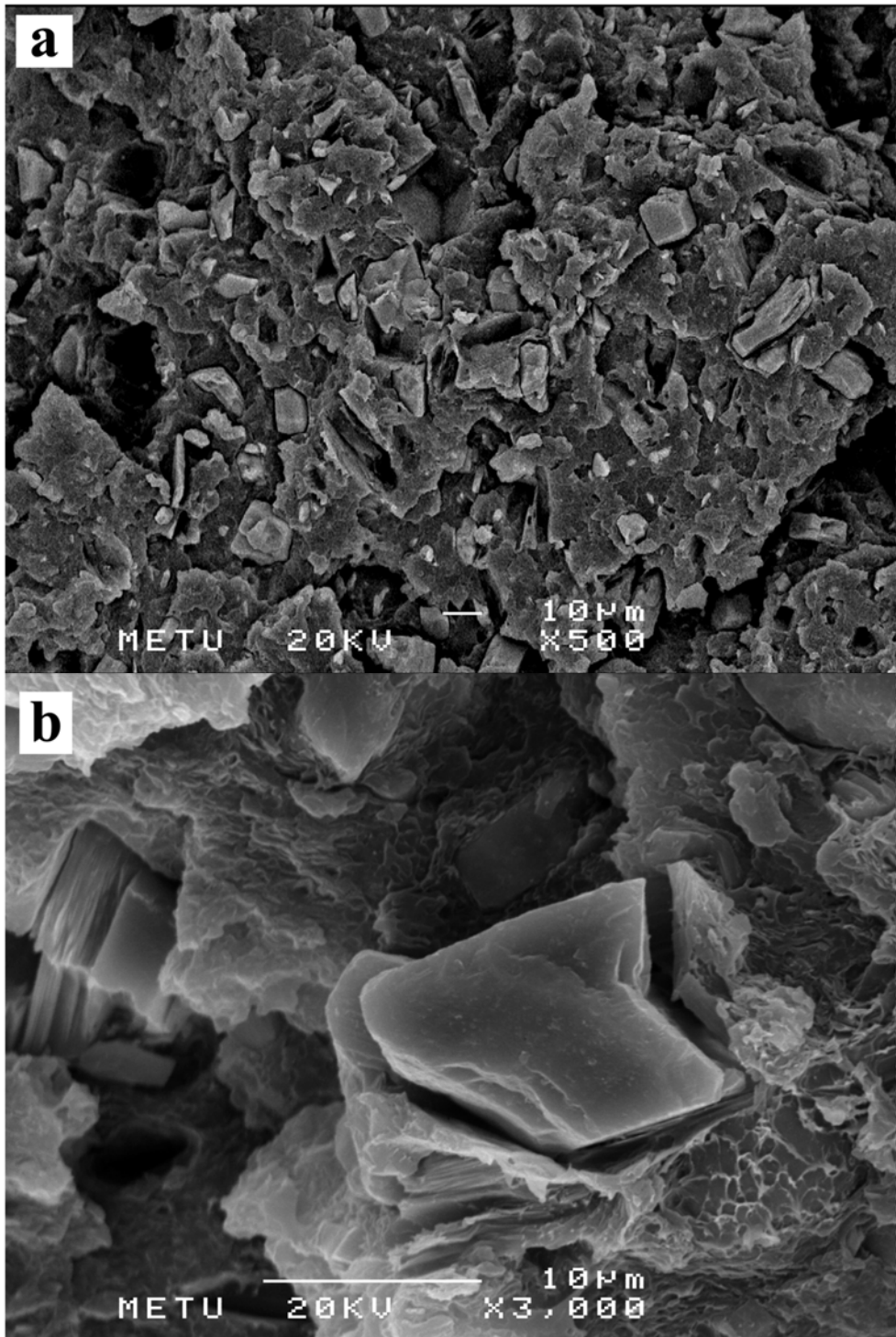


Figure 3.42 Electron back-scattering images of the fracture surface of aluminum trihydroxide flame-retarded high-impact polystyrene; (a) general and (b) closer views

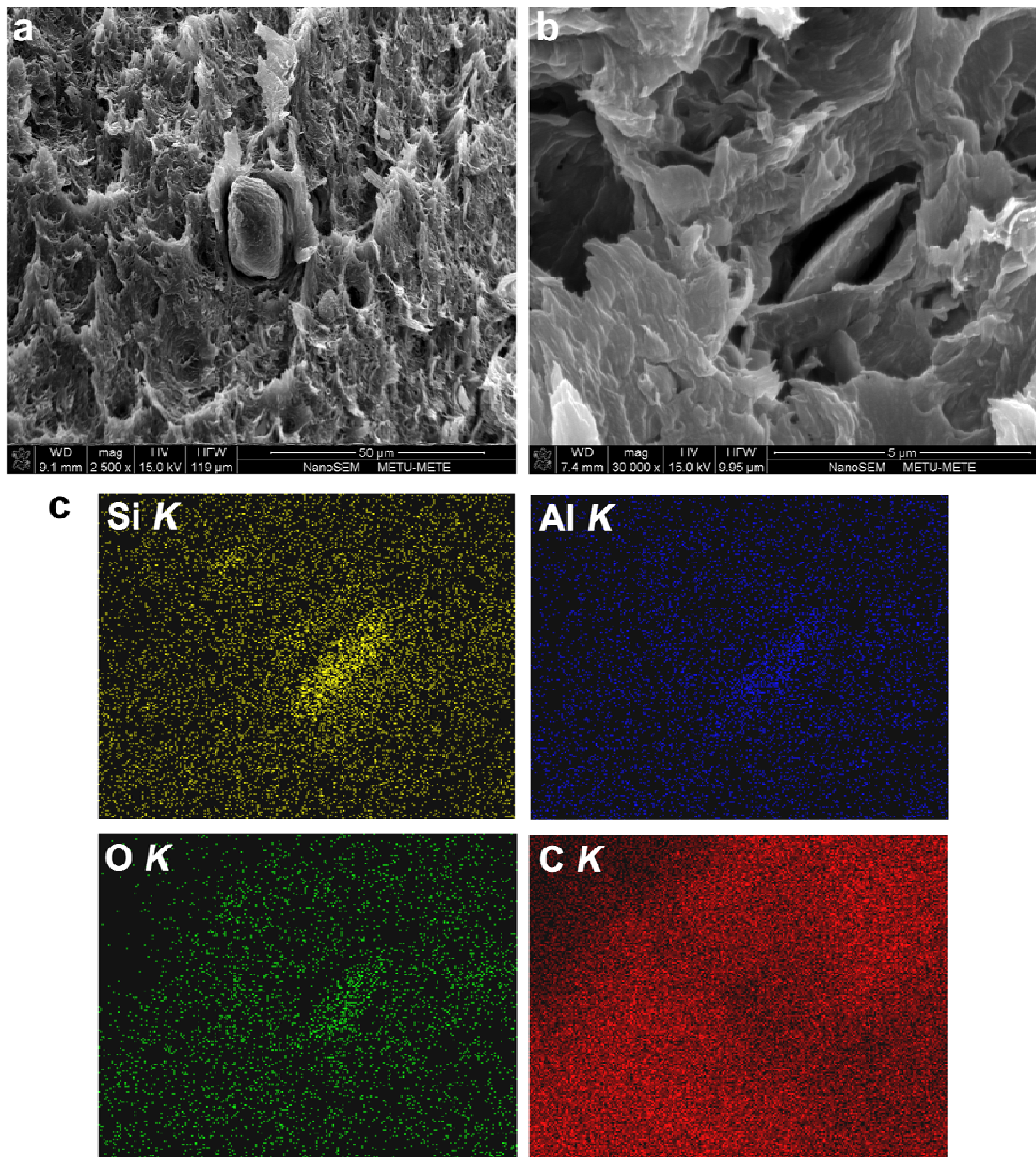


Figure 3.43 (a-b) SEM images and (c) elemental mapping of the fracture surface of phase-separated microcomposite

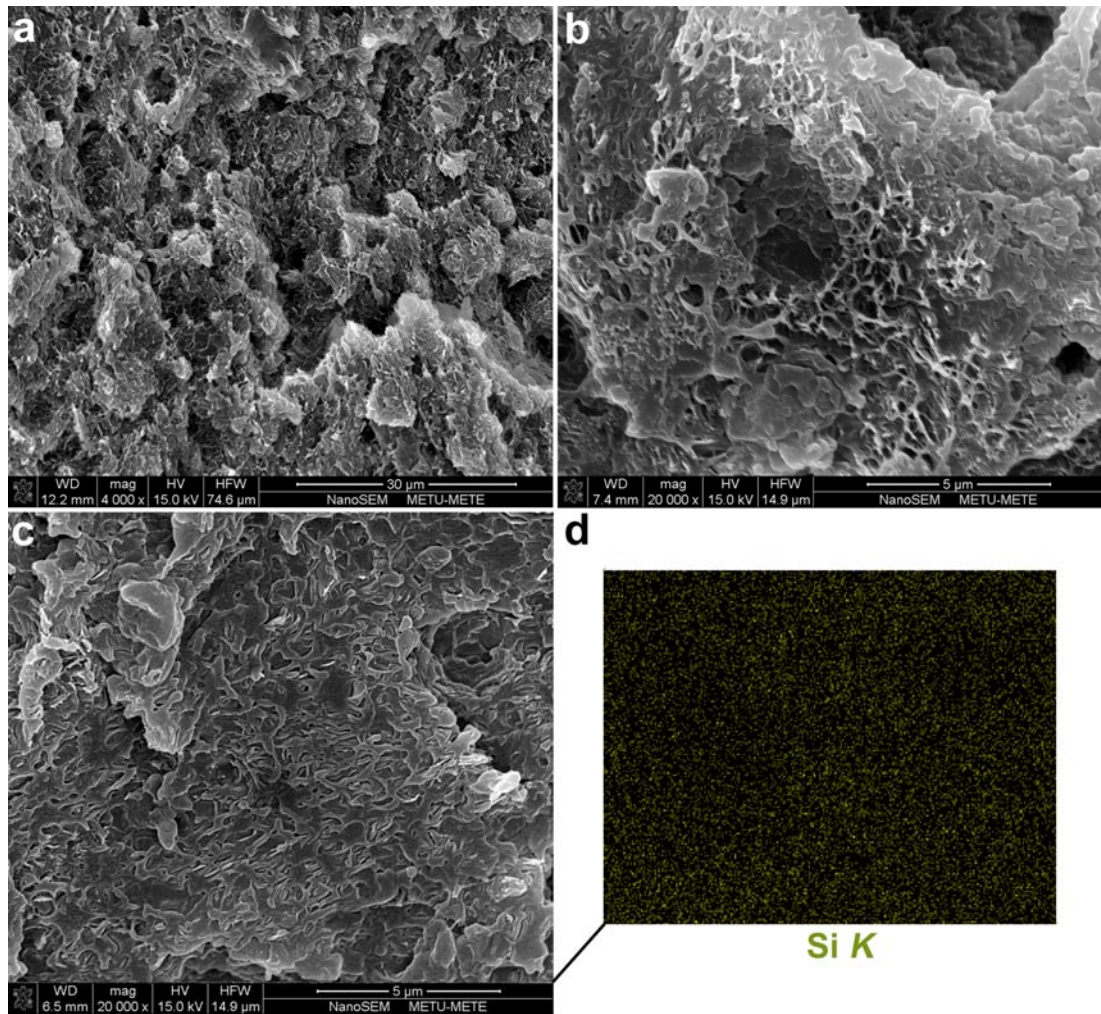


Figure 3.44 (a-c) SEM images and (d) Si mapping of the fracture surface of intercalated nanocomposite

As an additional interesting fact, Figure 3.45 shows that the enhancements in mechanical properties with the incorporation of only 3 wt% nanoclay was well-comparable to that with 30 wt% short-glass fiber (SGF) reinforcement, extracted from a range of 10–50 wt% SGF loadings found in our unpublished work. More importantly, a gain in stiffness and strength with nanoclays did not take place in expense of ductility and toughness as in the case with conventional SGF reinforcement. The nanocomposite possesses homogenous strain along the neck and hence indefinite yielding behavior. Neck formation and definite yielding behavior of the conventional microcomposite are typical signs of stress concentration at fiber ends under an applied load.

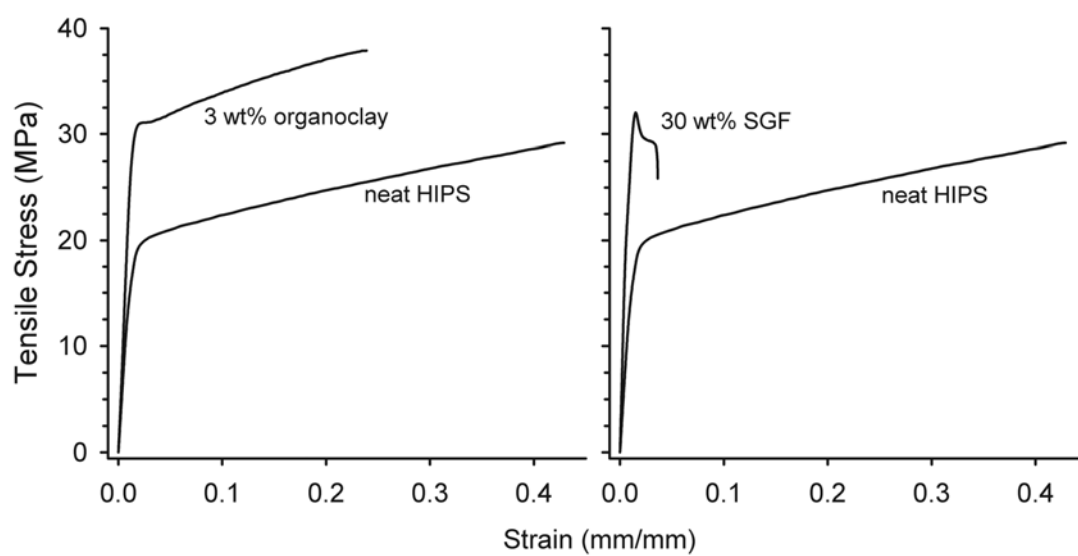


Figure 3.45 A comparison of the tensile behavior of HIPS/clay nanocomposite and conventional short-glass fiber-reinforced HIPS

3.3 EFFECT OF NANOFILLER GEOMETRY

As the third aim of this dissertation, the potential synergistic interactions between aluminum diethylphosphinate (AlPi), a specifically designed phosphorus-based flame retardant for polyesters, and nanoparticles with different geometries (0-D, 1-D and 2-D) were investigated. As the matrix material, poly (lactic acid) also called polylactide (PLA) which is a polyester type biopolymer, was chosen.

Designations and compositions of studied samples are listed in Table 3.13. Morphological aspects of nanocomposites are investigated by TEM and XRD. Flame retardancy is evaluated by mass loss calorimetry, limiting oxygen index and UL-94 vertical burning tests. Mechanisms of fire retardancy are revealed via characterization techniques revealing thermal degradation of compounds and microstructural evolution of residues remained after combustion.

Table 3.13 Designations and compositions (wt.%) of studied materials to reveal the effect of nanofiller geometry

	Aluminum Phosphinate (AlPi)	Silica Nanoparticles (0-D)	Halloysite Nanotubes (1-D)	Montmorillonite Platelets (2-D)
PLA	-	-	-	-
PLA/AlPi	20	-	-	-
PLA/AlPi/0-D	17	3	-	-
PLA/AlPi/1-D	17	-	3	-
PLA/AlPi/2-D	17	-	-	3

PLA/2-D was also produced to reveal the influence of AlPi on nanocomposite morphology and char nanostructure formed by 2-D nanofiller

3.3.1 Nanomorphology

Figure 3.46 contains representative SEM images of utilized nanoparticles having different geometries. Fumed silica is present as spherical nanoparticles (0-D) with an average primary particle size of 12 nm. Halloysite exists in nanorod-like tubular form (1-D) with outer diameters ranging from 40 to 130 nm and lengths from 0.3 μm to above 1 μm . The atomic level stresses due to misfit of the larger tetrahedral and the smaller octahedral sheets [116] induce the formation of hollow multilayered nanotube structures. Montmorillonite particles display a stacked plate-like morphology with lateral dimensions extending above 1 μm .

Figure 3.47 displays the bright-field TEM images of PLA/AlPi nanocomposites with varying nanoparticle geometry. Nanosilica was homogeneously dispersed in the matrix with some agglomeration (Figure 3.47a). The larger magnification image on the right shows that primary silica nanoparticles formed local clusters in the sub-micron scale reducing the effective surface area of nanoparticles in the composite. Halloysite particles are present as aggregates demonstrating small effective surface free energy (Figure 3.47b). Therefore, it was not possible to completely de-bundle and homogeneously distribute these clay nanotubes in PLA matrix via a melt-blending process contrary to the cases reported for polyamide and poly(butylene terephthalate) [117]. When an aggregate is investigated in more detail (image on the right), hollow nanotubules with thick walls made up of successive aluminosilicate layers were detected. Montmorillonite particles are uniformly dispersed at the nano-scale within the matrix in Figure 3.47(c). The larger magnification image on the right shows some regions of montmorillonite aggregates with no exfoliation together with regions of exfoliation containing well-dispersed high aspect ratio second phase particles.

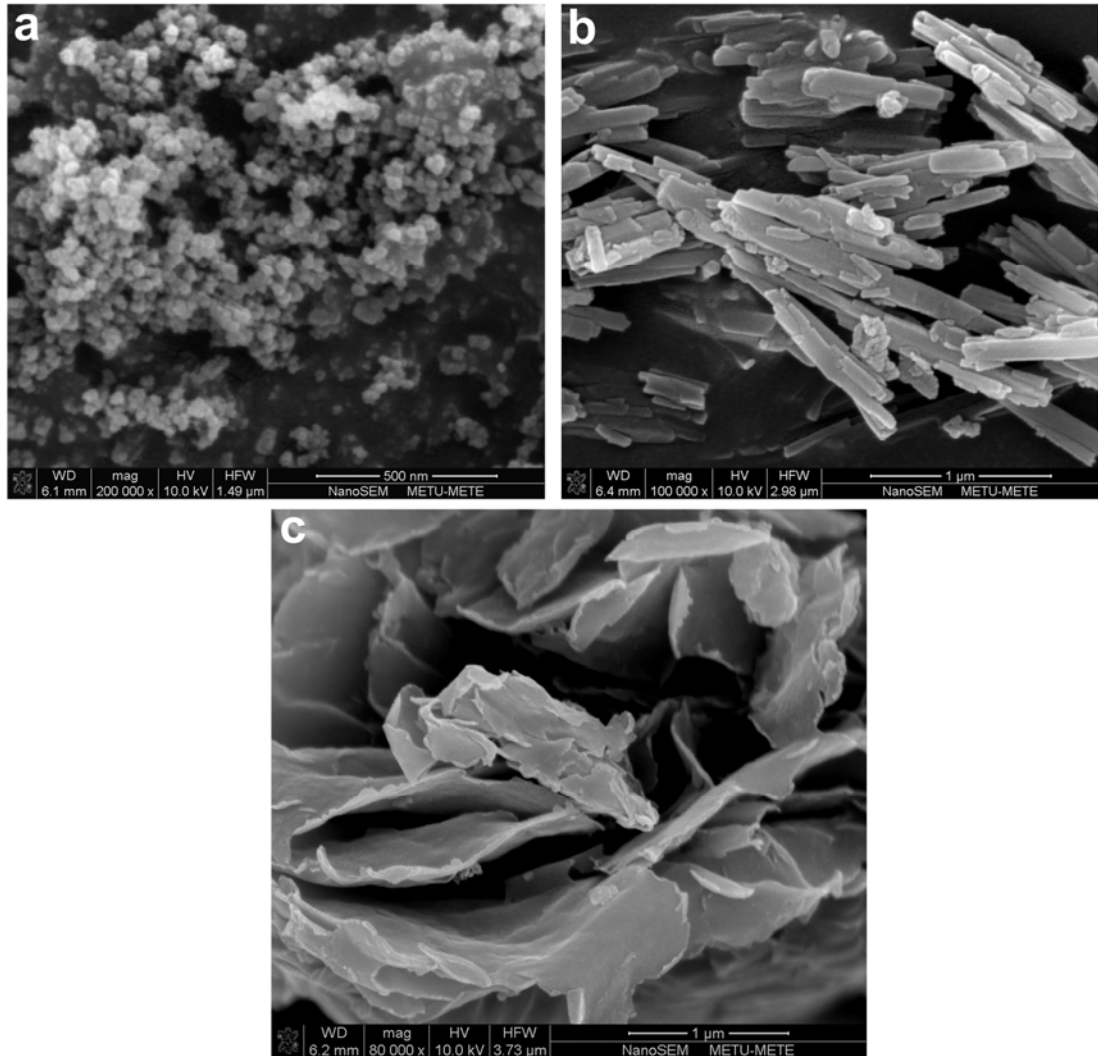


Figure 3.46 SEM micrographs of nanofillers with different geometries; (a) 0-D nanosilica, (b) 1-D rod-like halloysite, (c) 2-D plate-like montmorillonite

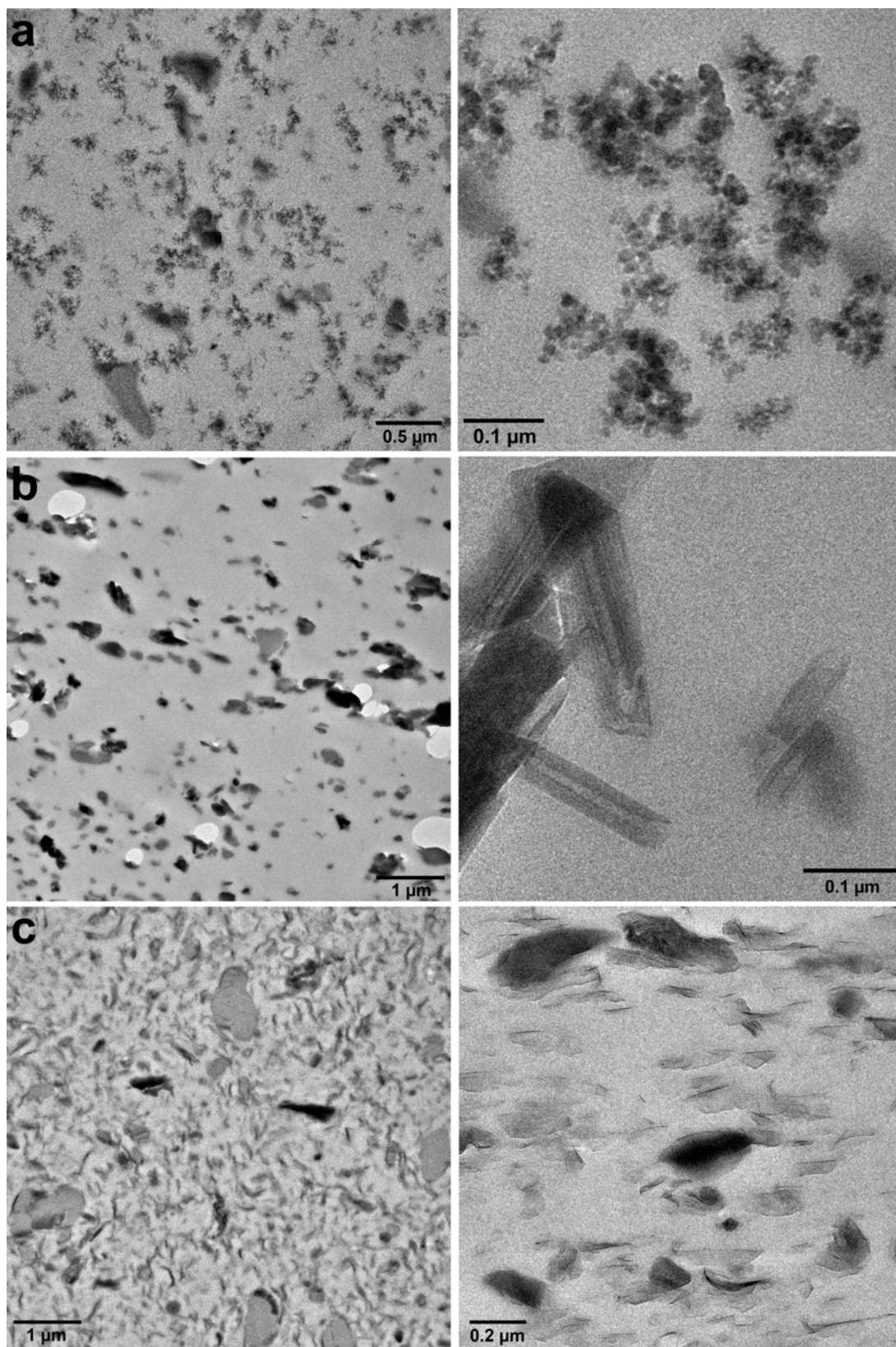


Figure 3.47 General (left) and closer (right) view bright-field TEM images of (a) PLA/AlPi/0-D, (b) PLA/AlPi/1-D, and, (c) PLA/AlPi/2-D nanocomposites

Figure 3.48 contains XRD patterns of organo-montmorillonite and halloysite nanoclays together with corresponding PLA nanocomposites. The pattern for halloysite nanotubes confirm the multilayer structure with an interlayer space of around $d_{001}=0.7$ nm characteristic to dehydrated halloysite [118]. Due to the weak binding of interlayer water, dehydration occurs irreversibly under ambient atmosphere. Almost no change can be seen in the position of (001) basal reflection following melt mixing with PLA which shows that the interlayer is inaccessible to PLA chains.

Prior to melt-mixing, organo-montmorillonite displays a coherent first order basal reflection corresponding to 1.8 nm. Clay interlayer expansion from $d_{001}=1.8$ nm to $d_{001}=3.2$ nm ($\Delta d = 1.4$ nm) for PLA/2-D and to $d_{001}=3.4$ nm ($\Delta d = 1.6$ nm) for PLA/AlPi/2-D was observed due to PLA intercalation of clay galleries. It can be stated that 2-D nanofiller containing samples demonstrate partially intercalated/exfoliated clay nanocomposite morphology rather than full exfoliation, which conforms to previous studies [119-121]. It is clear by comparing XRD patterns of PLA/2-D and PLA/ALPi/2-D that no remarkable change of montmorillonite dispersion, except from a slight increase in basal spacing, was observed in the presence of AlPi.

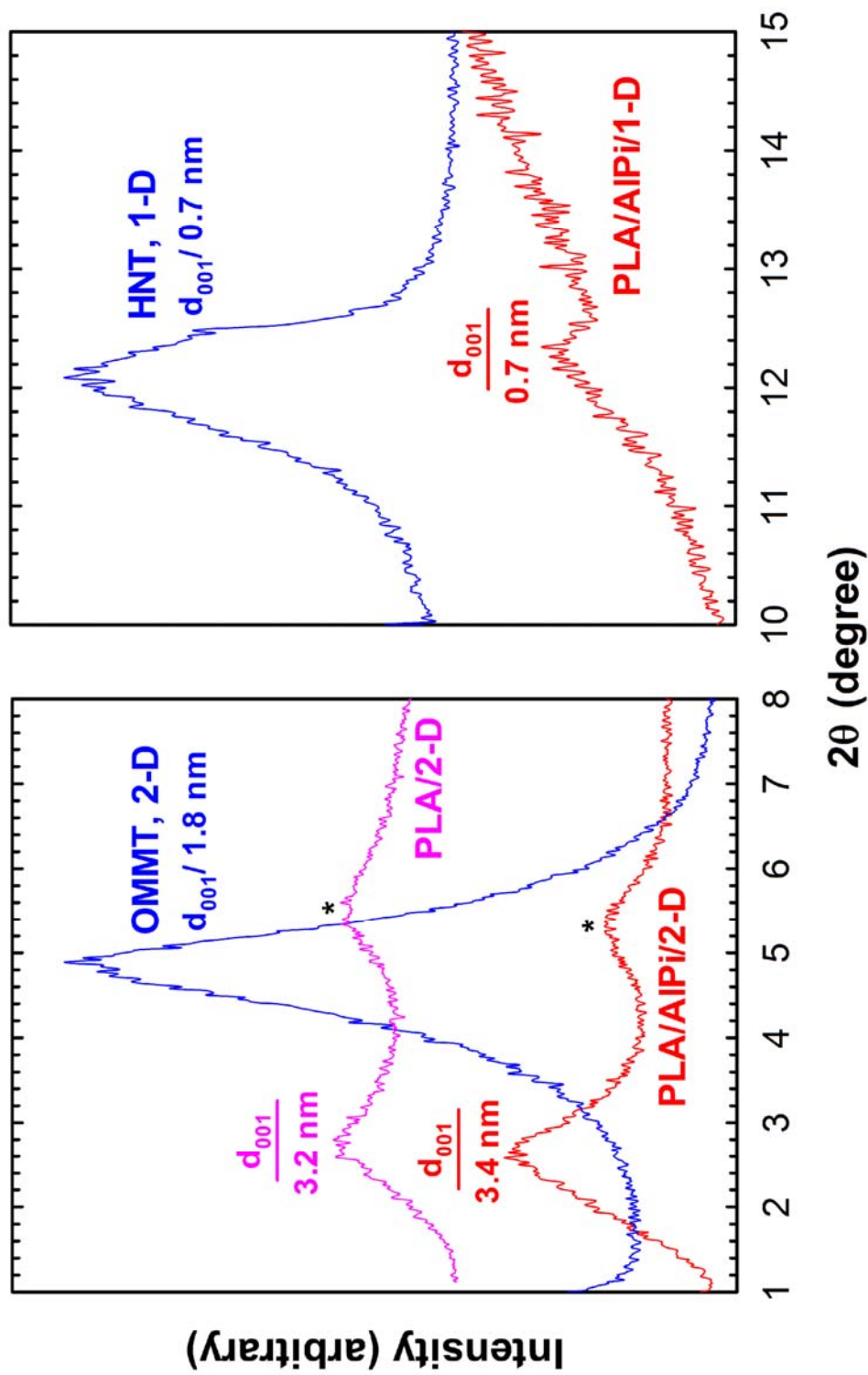


Figure 3.52 XRD patterns of organo-montmorillonite (OMMT, 2-D nanofiller) and halloysite nanotubes (HNT, 1-D nanofiller), together with corresponding PLA nanocomposites

3.3.2 Flame Retardancy

(i) Mass Loss Cone Calorimeter Analysis

Figure 3.49 shows the combustion behavior of samples during a simulated mild-to-intermediate fire scenario using bench-scale mass loss calorimetry. Heat release rates (HRR) were reduced throughout combustion in association with lower mass loss rates (MLR) in the presence of AlPi compared to neat PLA. Although a plateau-like behavior was seen in MLR, HRR increased steadily until flame-out. Partial substitution of AlPi by nanoparticles with varying geometries altered the combustion behavior in different physical ways. Increases in MLR were observed towards flame-out with spherical (0-D) and rod-like (1-D) nanofillers. These were accompanied by steadily increasing HRR during combustion similar to that observed for PLA/AlPi without nanofillers.

Interestingly, the plate-like (2-D) nanofiller remarkably changed the fire behavior such that both HRR and MLR showed similar suppressed plateaus owing to a pronounced condensed phase effect. Contrary to all AlPi containing samples, PLA/AlPi/2-D nanocomposite demonstrated a gradually decreasing MLR plateau that is indicative of char thickening throughout combustion.

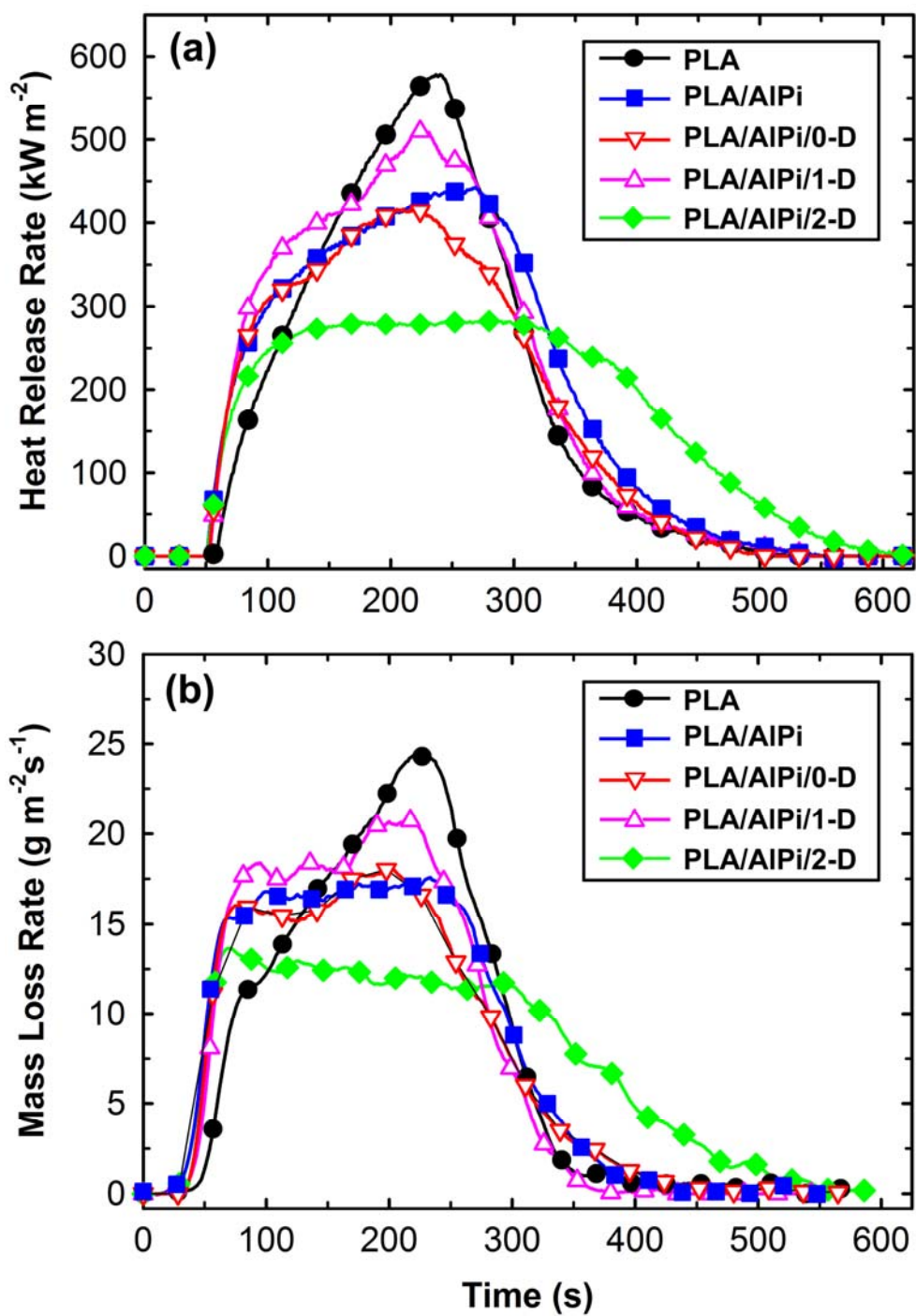


Figure 3.49 (a) Heat release and (b) mass loss rates of samples under 35 kW/m² irradiation showing the effect of nanofiller geometry

Interpreted parameters from forced flaming mass loss calorimetry are listed in Table 3.14. AlPi provided reductions in peak heat release rate (PHRR) and peak mass loss rate (PMLR) to similar extents while almost no changes could be observed in total heat evolved (THE) and effective heat of combustion, i.e. ratio of THE to total-mass-loss (TML). This suggests a dominant condensed phase mode of action for AlPi which is supported by the significantly increased amount of fire residue. The extent of reduction in PHRR obtained with AlPi addition in PLA ($-\Delta = 23\%$) is lower relative to those reported for poly(butylene terephthalate) [72, 122].

Considering fire parameters, while the nanofiller with spherical (0-D) geometry did not provide remarkable improvements, rod-like (1-D) nanofiller had a negative effect on fire retardancy causing increased PHRR and PMLR compared to PLA/AlPi. Strongly altered combustion behavior in the presence of plate-like (2-D) nanofiller enabled significantly lower PHRR and PMLR to be attained. Similar THE/TML values for PLA/AlPi and corresponding nanocomposites indicate that none of the utilized nanoparticles had a gas phase contribution to fire retardancy. Although the incorporation of AlPi led to a slight decrease in time to ignition (TTI) of PLA, no further reductions were caused by nanofillers as partial substitutes of AlPi. It has to be noted that while no remarkable reduction in fire growth index (FGI) was seen with 0-D and 1-D nanofillers, owing to a combination of unchanged TTI and markedly lower PHRR, the nanofiller with 2-D geometry provided a large reduction in fire risks.

Table 3.14 Interpreted mass loss calorimeter data showing the effect of nanofiller geometry

	PHRR (kWm ⁻²)	ΔPHRR (%)	TTI (s)	THE (MJm ⁻²)	THE/TML (MJm ⁻² g ⁻¹)	FGI (kWm ⁻² s ⁻¹)	PMLR (gm ⁻² s ⁻¹)	Residue (wt.%)
PLA	578		58	108	2.4	10.0	24.4	-
PLA/AIPi	443	-23 ^a	50	113	2.5	8.9	17.2	7.8
PLA/AIPi/0-D	416	-28 ^a -6 ^b	52	101	2.4	8.0	18.1	10.4
PLA/AIPi/1-D	511	-12 ^a 15 ^b	52	115	2.6	9.8	20.9	8.9
PLA/AIPi/2-D	283	-51 ^a -36 ^b	50	103	2.4	5.7	13.6	10.3

^a ΔPHRR with respect to neat PLA

^b ΔPHRR with respect to PLA/AIPi

(ii) LOI and UL94 Flammability Tests

Table 3.15 contains the results of LOI and UL-94 vertical burning tests. PLA displayed excessive dripping and no extinguishment can be facilitated by dripping, therefore, it was rated burn-to-clamp (BC) in UL-94. Addition of AlPi markedly increased LOI from ~23% to ~28% and provided extinguishment (V-2 rating, 3.2 mm) via a single large drip during UL-94 tests. The V-2 rating obtained at 20 wt.% AlPi in PLA conforms to a study by Bourbigot et al. [32] reporting that PLA/AlPi formulations exhibit V-2 above 10 wt.% AlPi.

Nanofillers with 0-D and 1-D geometries had a slight deterioration effect on LOI whereas 2-D nanofiller maintained the performance of PLA/AlPi at a lower AlPi content. With 1-D and 2-D nanofillers, dripping is further inhibited and UL-94 rating was downgraded from V-2 to BC. No remarkable change in the dripping behavior was seen in the presence of 0-D nanofiller which enabled to maintain the V-2 rating.

Table 3.15 Results of flammability tests (LOI and UL-94) showing the effect of nanofiller geometry

	LOI (%O₂ ± 0.2)	UL-94 Rating
PLA	22.8	Burn-to-clamp
PLA/AlPi	27.7	V-2
PLA/AlPi/0-D	26.7	V-2
PLA/AlPi/1-D	26.9	Burn-to-clamp
PLA/AlPi/2-D	27.7	Burn-to-clamp

3.3.3 Flame Retardancy Mechanisms by Thermal Degradation

Figure 3.50 shows the thermogravimetric curves of neat PLA, AlPi, and the PLA compound containing 20 wt% AlPi. AlPi decomposes with a maximum decomposition temperature of 484°C, and 27.3% residue remains at 550°C in the condensed phase upon decomposition. It was previously shown that AlPi decomposes to yield aluminum phosphates (ortho-, pyro- and poly-phosphates) accompanied by release of diethylphosphinic acid into the gas phase [72, 122, 123].

PLA has a significantly lower maximum decomposition temperature ($T_{\max} = 396^{\circ}\text{C}$) compared to AlPi. Therefore, PLA/AlPi compound shows a degradation behavior consisting of two distinct steps. The first decomposition step corresponds to almost complete decomposition and pyrolysis of the PLA matrix whereas the second step occurs at a similar temperature ($T_{\max}=495^{\circ}\text{C}$) to that of neat AlPi. It can be inferred from Table 3.16 and Figure 3.51 that nanoparticles did not alter the two-step decomposition behavior apart from slightly increasing the degradation temperatures ($T_{10\%}$, $T_{50\%}$ and T_{\max}) by around 5–11°C, with an exception for 1-D nanofiller which resulted in 6-7°C reductions.

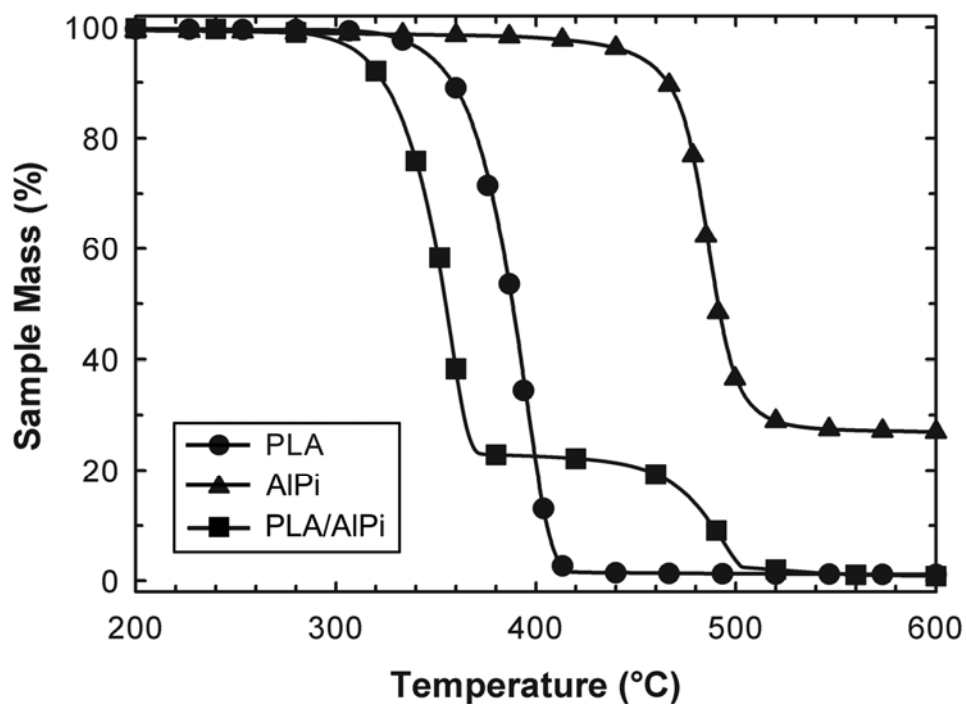


Figure 3.50 Thermogravimetric curves of PLA, AlPi and PLA/20wt%AlPi

Table 3.16 Results of thermogravimetric analysis revealing the effect of nanofiller geometry

	$T_{10\%}$ (°C) ^a	$T_{50\%}$ (°C) ^b	T_{\max} (°C) ^c		Residue (%) ^d
			Step 1	Step 2	
PLA/AlPi	324	355	359	495	1.3
PLA/AlPi/0-D	335	360	364	481	5.0
PLA/AlPi/1-D	318	348	353	495	3.5
PLA/AlPi/2-D	333	365	369	496	4.3

^a Temperature at 10% mass loss

^b Temperature at 50% mass loss

^c Temperature at maximum degradation rate(s)

^d Non volatile fraction at 550°C

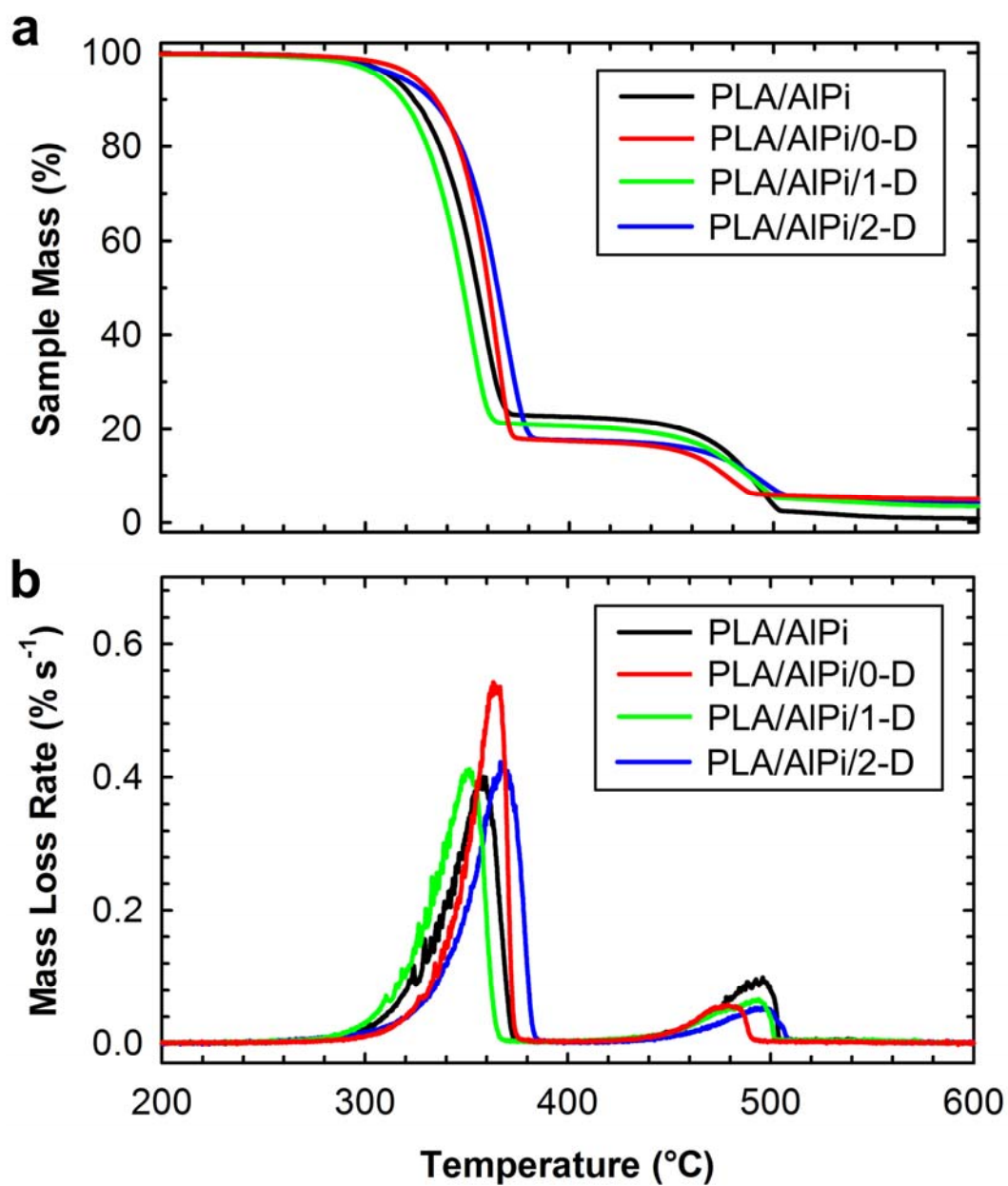


Figure 3.51 Effect of nanofiller geometry on thermal stability of nanocomposites based on PLA/AlPi; (a) thermogravimetry and (b) differential thermogravimetry curves

It should then be clear that PLA/AlPi and corresponding nanocomposites show two-step degradation behavior where the pyrolysis of PLA in the first step is followed by decomposition of AlPi at higher temperatures as the second step. This two-step decomposition behavior was also predominant in forced flaming fire tests where the intumescent char formed at a later stage following significant PLA decomposition and evolution into the flaming zone. This could explain the less effective fire retardancy imparted by AlPi when used in PLA compared to poly(butylene terephthalate).

3.3.4 Flame Retardancy Mechanisms by Residue Analysis

Although the amounts of fire residue were almost unchanged with nanofiller substitution for AlPi, structural integrity, thickness and intumescent function were significantly influenced by nanofiller geometry as shown in Figure 3.52. Incorporation of AlPi resulted in the formation of a thin intumescent char displaying a macro-porous structure. Once the char is formed, combustion proceeds through escaping volatiles from the macro-pores until flame-out. The spherical (0-D) nanofiller inhibited intumescence and resulted in a smoother char surface. However, the char was thinner and weaker compared to that from PLA/AlPi. Rod-like (1-D) nanofiller did not significantly affect the intumescence and char thickness, but there was some reduction in the number and size of macro-pores present in the intumescent char. Most importantly, the plate-like (2-D) nanofiller completely hindered intumescence and promoted the formation of a much thicker char demonstrating strong protective character.

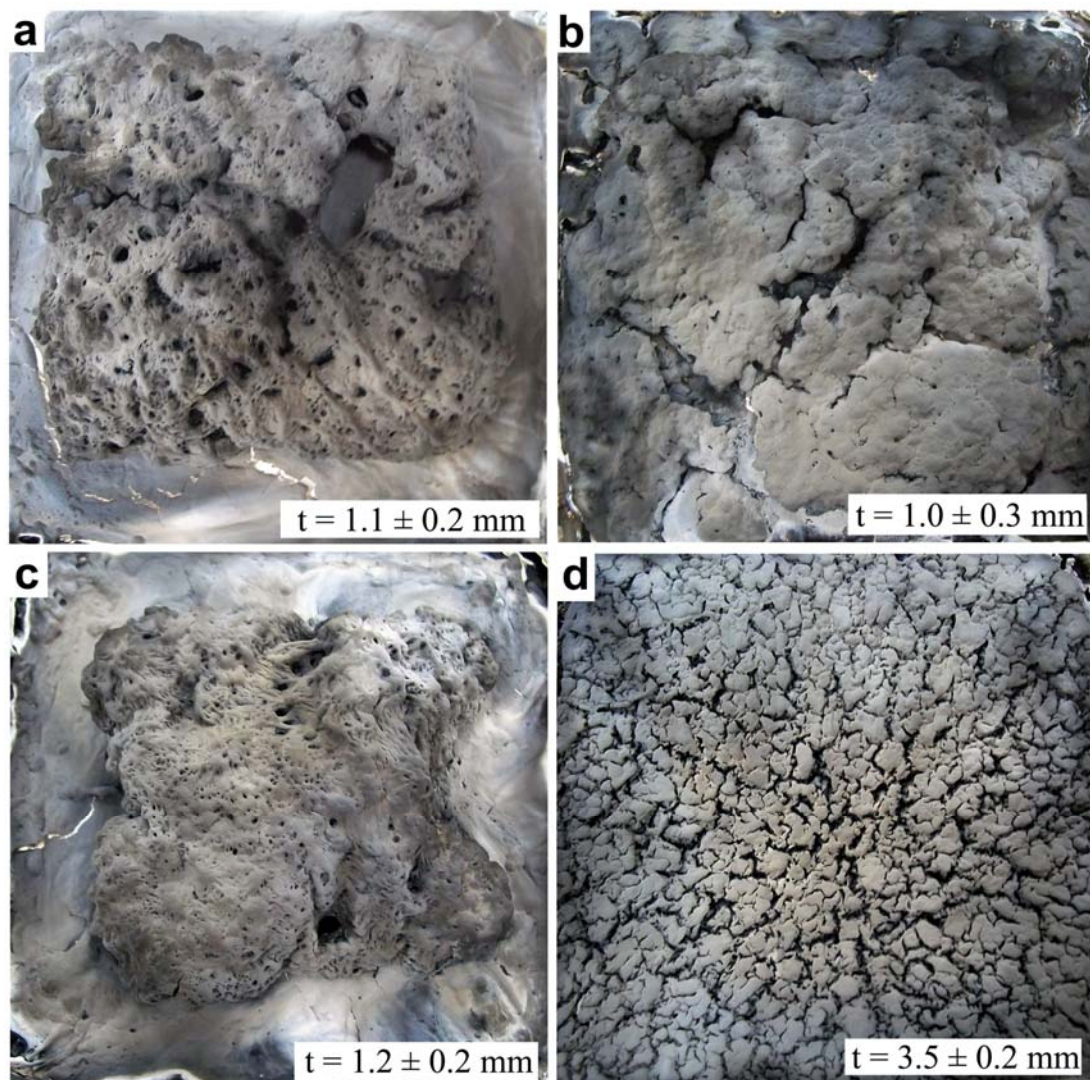


Figure 3.52 Macroscopic appearances of the structure and measured thicknesses of mass loss calorimeter residues. Whole sample surfaces ($10 \times 10 \text{ cm}^2$) for (a) PLA/AlPi, (b) PLA/AlPi/0-D, (c) PLA/AlPi/1-D, and (d) PLA/AlPi/2-D

It was stated above that nanoparticle geometry strongly affects fire retardancy by influencing the structure of the formed chars. The most important factors determining the effectiveness of condensed phase barrier appear to be whether or not the nanoparticles hinder intumescent char formation, how fast the char is formed and how effective insulation character the formed chars demonstrate. Here, it is proposed that char formation and the character of formed chars are controlled by the extent and rate of migration of nanoparticles towards the exposed surface during pyrolysis of PLA prior to formation of intumescent aluminum phosphate residue facilitated by decomposition of AlPi at a higher temperature. In this respect, multi-walled carbon nanotubes were found to completely hinder intumescence through a cage effect due to early migration, accumulation and strong network formation at the surface of intumescent poly(methyl methacrylate) [35].

The most important factor influencing nanoparticle migration and accumulation at exposed surface is the effective surface free energy of the nanoparticle dispersed in the matrix [124]. Considering nanoparticles utilized here, surface free energy and hence the extent of migration and segregation at the exposed surface is expected to increase in the order of halloysite ($65 \text{ m}^2/\text{g}$), nanosilica ($170 \text{ m}^2/\text{g}$), intercalated montmorillonite ($150\text{-}300 \text{ m}^2/\text{g}$ [125]) and exfoliated montmorillonite ($750 \text{ m}^2/\text{g}$).

With rapid migration of exfoliated montmorillonite towards sample surface, concentration of nanoparticles in the vicinity of exposed surface significantly increases at early stages of combustion. And, due to the formation of a rigid non-deformable aluminosilicate ceramic layer and substantial increase in pyrolyzing melt viscosity, intumescent char formation is hindered when a higher temperature is reached to facilitate AlPi decomposition during combustion in the mass loss calorimeter.

Contrary to the case with montmorillonite, halloysite nanotubes with poor dispersion and low effective surface area in the nanocomposite sank in the pyrolyzing melt and showed no significant surface segregation during combustion. Accordingly, intumescent char formation was not hindered in the presence of halloysite nanotubes. With nanosilica, due to relatively large effective surface area of the dispersed phase, some extent of migration was seen such that intumescent char formation is somewhat hindered. However, the formed chars were thin and weak to perform effectively as an insulation layer during combustion. Therefore, only slight improvements were obtained in fire retardancy with spherical silica nanoparticles.

As to how 2-D nanoparticles with nano-scale dispersion in PLA/AlPi matrix impart substantial fire retardancy, following discussions might be useful. The rapid accumulation of montmorillonite particles, primarily those in the exfoliated state, allows for the formation of much thicker aluminum phosphate residue reinforced by montmorillonite platelets (Figure 3.52d) rather than a thin intumescent char. This eventually helps establishing an effective barrier to heat and mass transfer as combustion proceeds and provides an explanation of enhanced fire retardancy with well-dispersed 2-D nanofillers.

In an attempt to support this suggestion, structure of the fire residue from PLA/AlPi/2-D was carefully analyzed by XRD for montmorillonite interlayer distances (Figure 3.53). The upper 2.5 mm along the thickness showing a visually observable different structure (stronger and denser) than the lower 1 mm part were separately scanned. Interestingly, upper part had a larger d -spacing (5.9 nm) while the lower part possessed mostly around $d_{001}=1.9$ nm apart from a shoulder at larger spacing. When the entire residue is analyzed a superposition of montmorillonite d -spacings present in upper and lower parts of the residue were obtained. This conclusion supports the suggestion made above that exfoliated montmorillonite particles will be the first to accumulate at the surface of pyrolyzing melt. Later on during pyrolysis, the char gets thicker by further migration and after the formation of char with a certain thickness with large interlayer spacing, intercalated montmorillonite particles are accommodated towards the bottom of the char with a lower final interlayer space of $d_{001}=1.9$ nm.

Exfoliated montmorillonite layers present in the nanocomposite collapse without completion during pyrolysis of PLA and the char residue showed an average interlayer space larger than that of intercalated montmorillonite particles in the nanocomposite prior to decomposition. This observation supports that PLA/AlPi/2-D has a mixed intercalated/exfoliated nanomorphology as evidenced by TEM (Figure 3.47c). It is also to be noted that montmorillonite fraction with intercalated state in the nanocomposite collapsed to yield a final interlayer space around $d_{001}=1.0$ nm [100].

Mass loss calorimeter residues were further analyzed by XRD (Figure 3.54a) and ATR-FTIR (Figure 3.54b) for possible phase changes and chemical alterations by nanoparticles. Residues were found to be amorphous with no long range order. Although the presence of nanofillers was verified by sharpened absorption peaks due to strong characteristic vibrations such as Si-O in nanofillers, no chemical alteration of aluminum phosphate residue with characteristic peaks at 1130 and 960 cm^{-1} [93] could be detected. Therefore, it can be concluded that nanoparticles influence fire retardancy solely by physical means in the condensed phase.

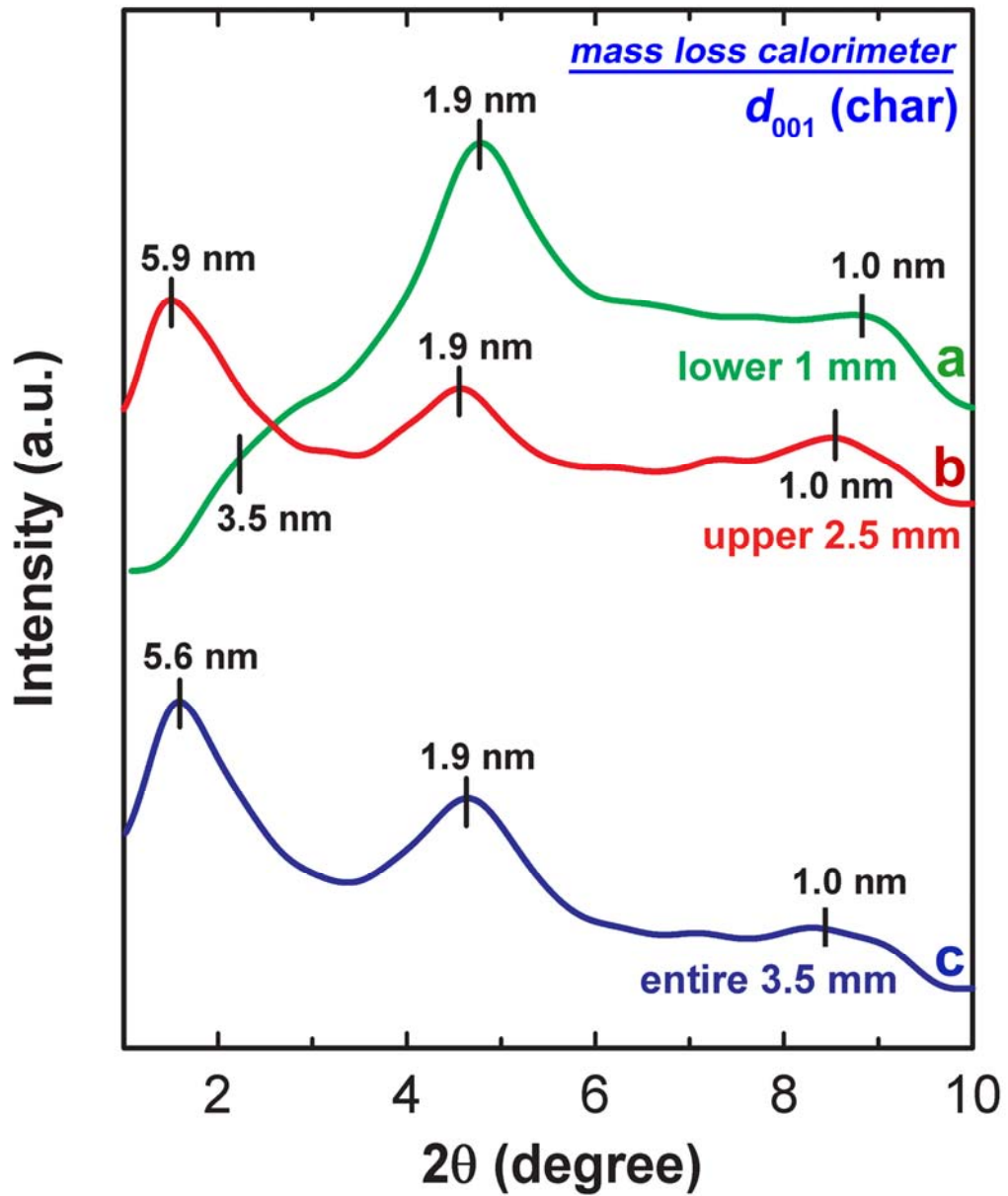


Figure 3.53 XRD patterns of mass loss calorimeter residue from PLA/AIPi/2-D sample; (a) residue at the lower 1 mm through the char thickness, (b) residue at the upper 2.5 mm through the char thickness, (c) residue through the full char thickness

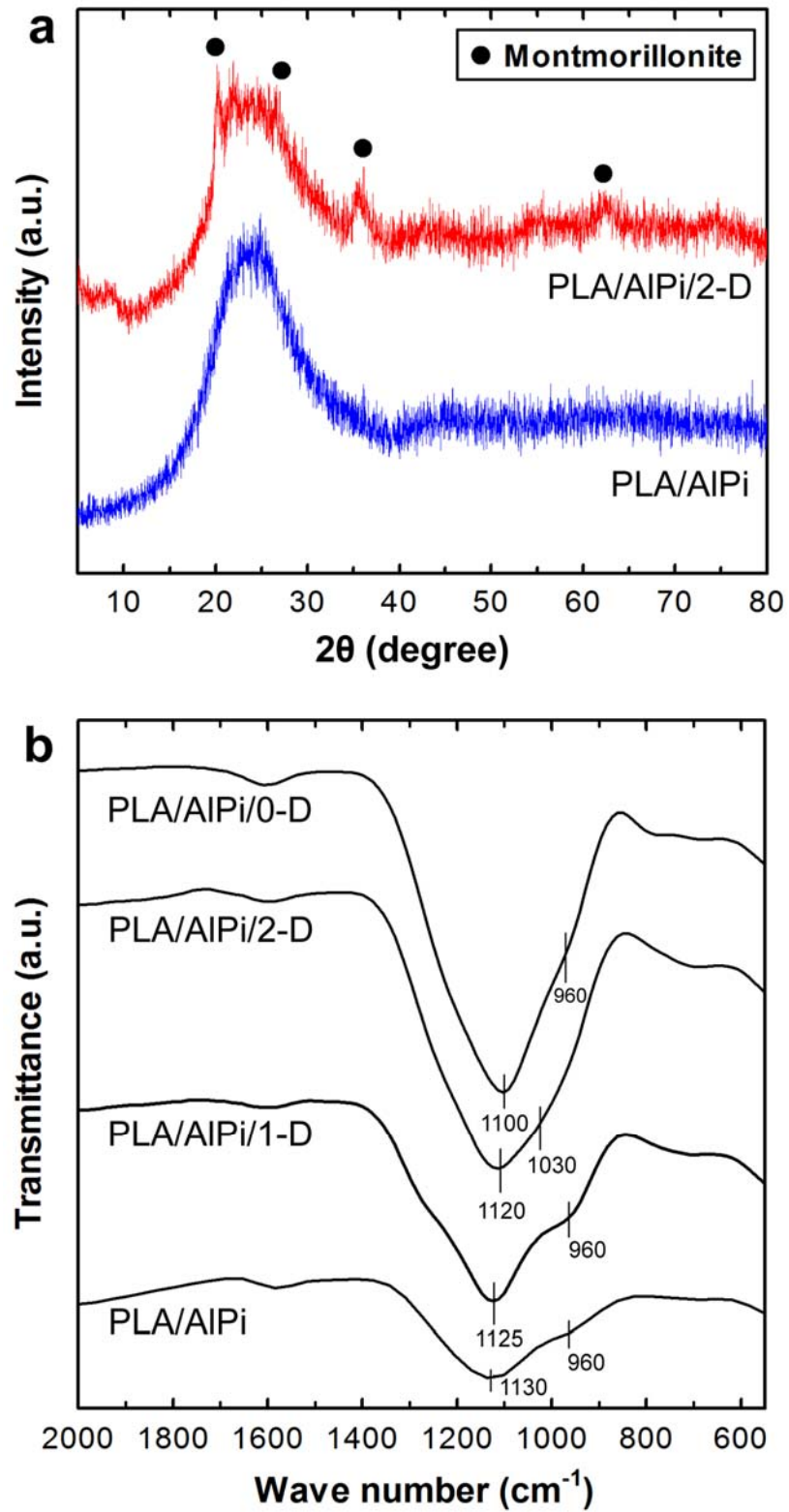


Figure 3.54 (a) XRD patterns and (b) ATR-FTIR spectra of mass loss calorimeter residues showing the effect of nanofiller geometry

The residue formed from PLA/AlPi/2-D was postulated above to be a nanocomposite of aluminum phosphate and montmorillonite platelets. To support this, residues from PLA/AlPi/2-D (upper 2.5 mm part) and that from PLA/AlPi with no nanofillers were observed under SEM (Figure 3.55). Residue from PLA/AlPi is composed of aluminum phosphate microspheres with broad particle size distribution from 0.1 to 0.9 μm averaging 0.34 μm (Figure 3.55a). In the case of PLA/AlPi/2-D, aluminosilicate platelets are present as a dispersed second phase in aluminum phosphate residue reinforcing it at the nano-scale as shown in Figure 3.55(b). The presence of montmorillonite was verified by EDS which revealed extra peaks due to characteristic K-radiation for Si and Fe, and an increased Al to P mass ratio (Al:P \sim 0.6) compared to aluminum phosphate residue from PLA/AlPi (Al:P \sim 0.3). Aluminum phosphate microspheres had a narrower particle size distribution (0.1 - 0.4 μm) and a slightly finer average diameter of 0.27 μm in the presence of montmorillonite reinforcement.

In order to further support the nanocomposite char formation by combustion of PLA/AlPi/2-D, mass loss calorimeter char nanostructure was investigated under TEM as shown by micrographs in Figure 3.56. Montmorillonite crystallites with large aspect ratio which can be thought to possess ordered layer stacking, are observed to assemble into a new structural order by combustion (Figure 3.56a). Besides, regions of exfoliated montmorillonite layers were also observed (Figure 3.57b) maintaining their initial nano-scale dispersion in the nanocomposite after combustion.

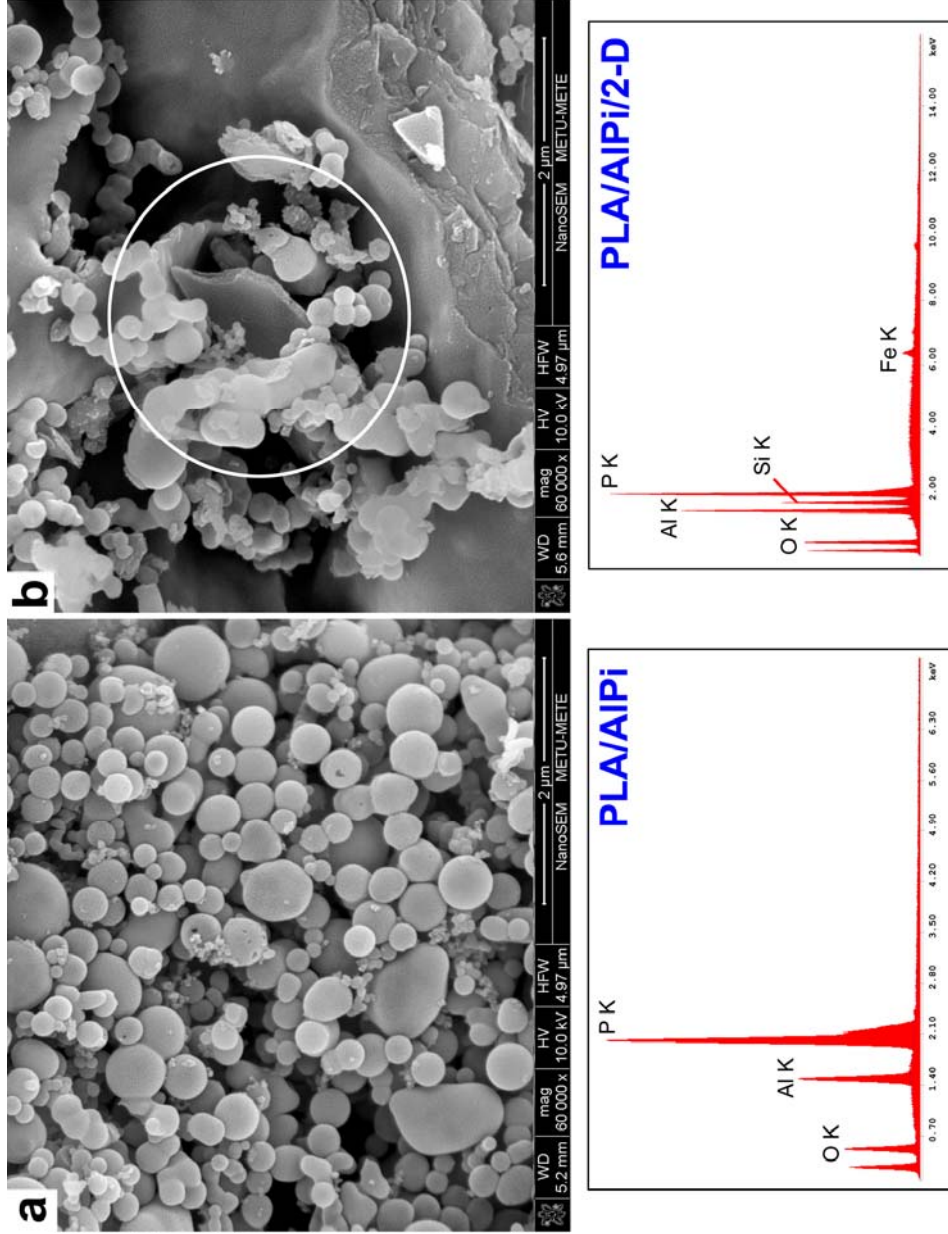


Figure 3.55 SEM images and energy dispersive spectra of mass loss calorimeter residues showing (a) aluminum phosphate residue composed of microspheres with non-uniform sizes, (b) aluminum phosphate/montmorillonite nanocomposite formation where the large aspect ratio silicate reinforcing the aluminum phosphate structure is highlighted

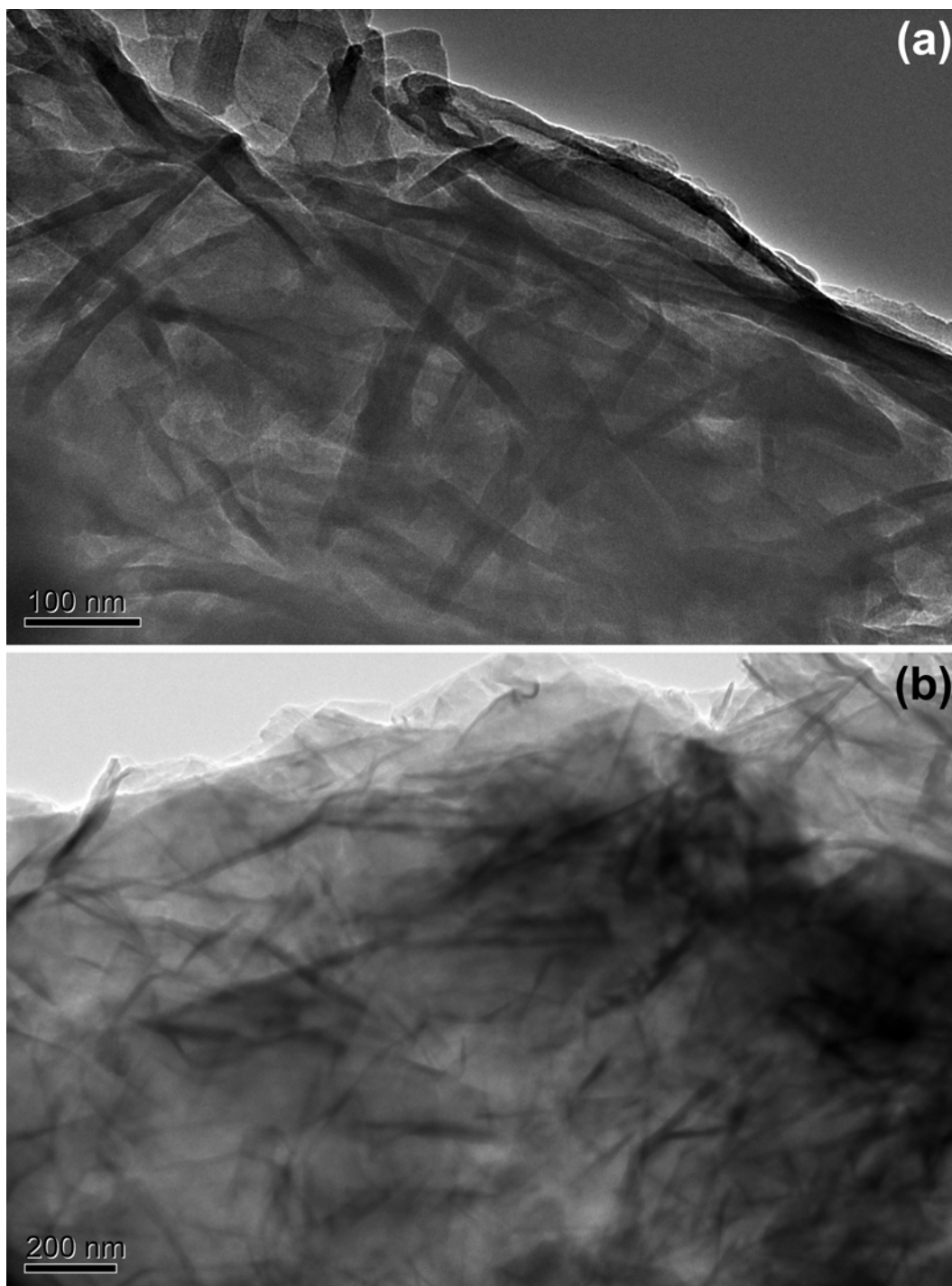


Figure 3.56 (a) and (b) TEM images of char residues formed by combustion of PLA/AlPi/2-D in the mass loss calorimeter

To elaborate on the microstructural evolution of chars, residues obtained from oxygen index tests conducted under an O₂ level close to LOI of samples were further investigated. It is seen in Figure 3.57 that PLA/AlPi char evolution occurs by an unprecedented manner by the formation of transient fibrillar microstructures. Figure 3.57(a) shows a dense forest of microfibrils covering the underlying sample prior to its pyrolysis. At the moment, it is unclear how these extraordinarily regular hollow fibrillar structures with hexagonal cross-section (Figure 3.57b) grow during flaming combustion. Figure 3.57(c) shows that this microfibrillar structure is transformed to a smooth amorphous aluminum phosphate char in the regions closer to flaming zone forming the intumescent char. Lastly, the image provided in Figure 3.57(d) might be an evidence that bare AlPi particles, following pyrolysis of PLA, are subjected to the flame temperature and rapid decomposition takes place under flowing N₂/O₂ mixture resulting in transient spun-like fibrillar geometries as intermediate reaction products. At the moment, however, the discussions are speculative and this intriguingly regular intermediate product formation requires further attention in future studies.

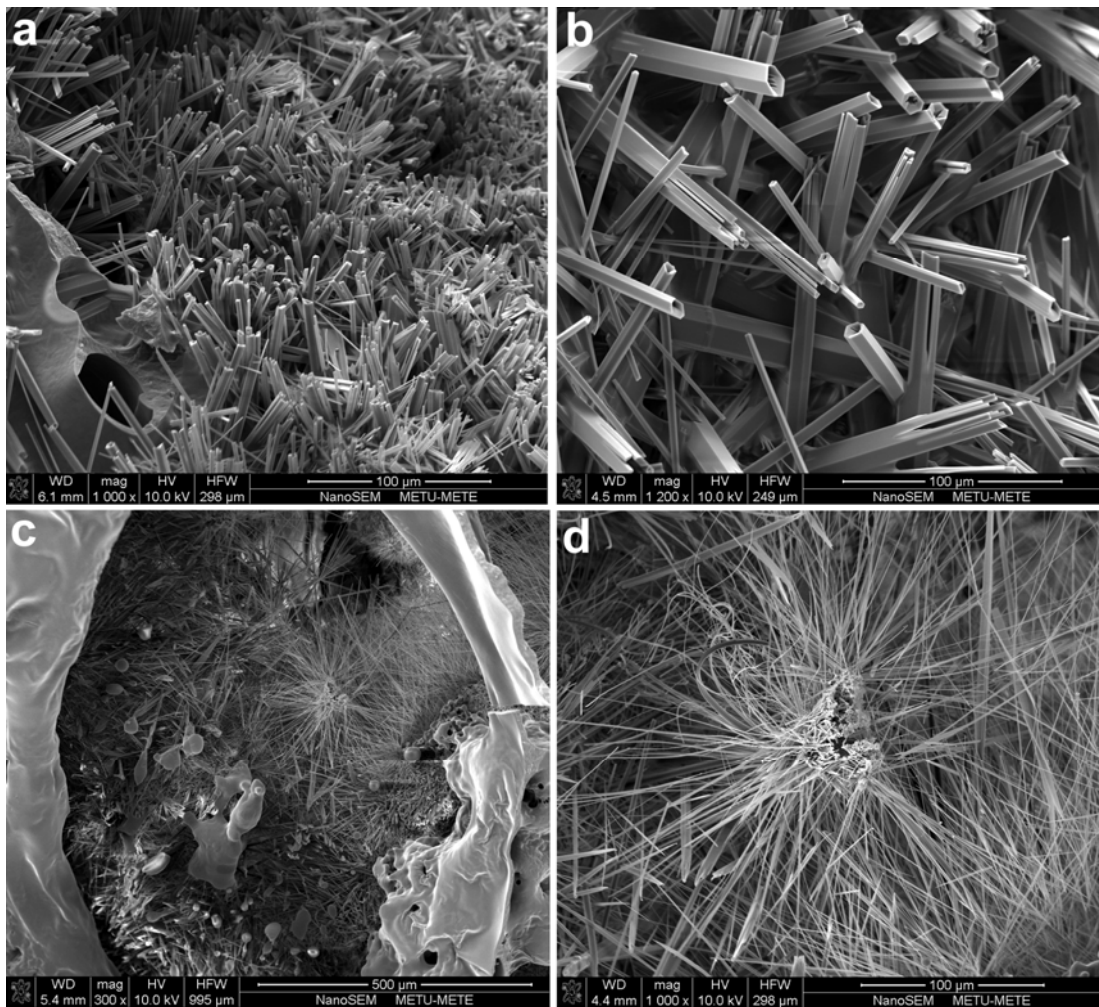


Figure 3.57 (a-d) SEM images showing formation of different aluminum phosphate microfibrils as intermediate reaction products during combustion under an atmosphere with $O_2 \sim 28\%$. Diameters are in the range of $1 \mu\text{m}$ to $20 \mu\text{m}$ with lengths extending above a few hundred microns

The interesting microstructural evolution of chars observed in PLA/AlPi was not present in nanocomposites. Unlike fibrillar microstructure, SEM images of residues revealed micro-porous ceramic structures (Figure 3.58). Higher magnification images showed sintered net-like structure containing spherical primary particles ($\bar{d} \sim 80$ nm) with PLA/AlPi/2-D, isolated islands consisting of coalesced spherical nanoparticles ($\bar{d} \sim 90$ nm) with PLA/AlPi//1-D, and, a more densely packed assembly of slightly coarser spherical particles ($\bar{d} \sim 130$ nm) with PLA/AlPi//0-D. All these microstructures contain no signs of nanoparticle presence (no trace of Si in each case) on top of the residues by migration and accumulation. Therefore, unlike fire performance, LOI rating was not significantly influenced by nanoparticle geometry.

Figure 3.59 indicates that ceramic residues consisting of aluminum phosphate nanoparticle aggregates form on the surface of pyrolyzing melt when the temperature to facilitate decomposition of AlPi ($T_{\max} = 484^{\circ}\text{C}$) is attained. The protective porous ceramic residue with given detailed images in Figure 3.57 isolates the underlying material by covering the surface of pyrolyzing melt. Figure 3.59(b) is an evidence of nanoparticle coalescence during combustion which leads to the formation of coarser aluminum phosphate microspheres ($\bar{d} \sim 270$ nm) in fire tests compared to those formed during LOI test ($\bar{d} \sim 80\text{--}130$ nm).

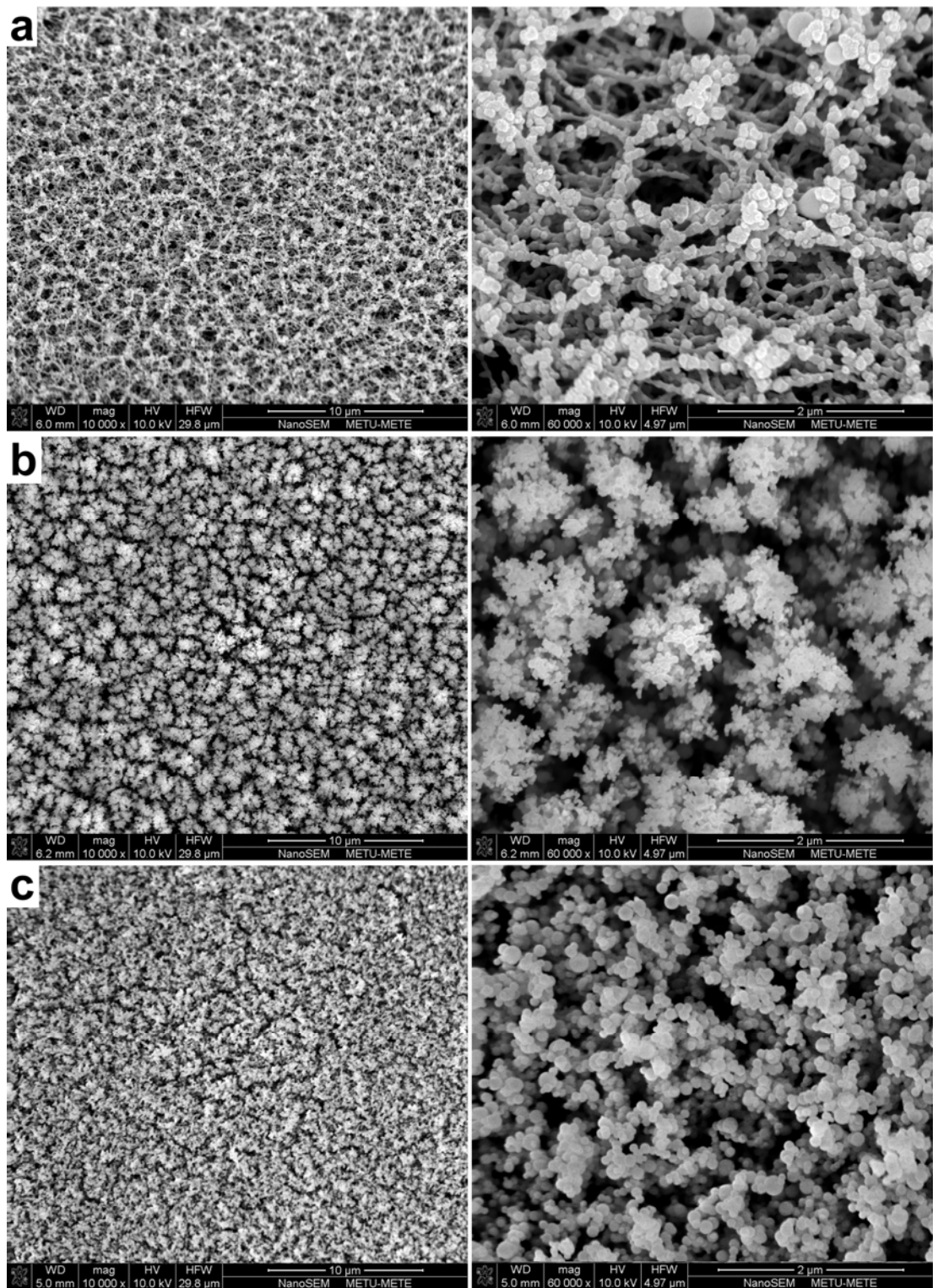


Figure 3.58 General (left) and closer (right) view SEM images from oxygen index tests indicating microporous structures composed of spherical aluminum phosphate nanoparticles; (a) PLA/AIPi/2-D, (b) PLA/AIPi/1-D, and (c) PLA/AIPi/0-D

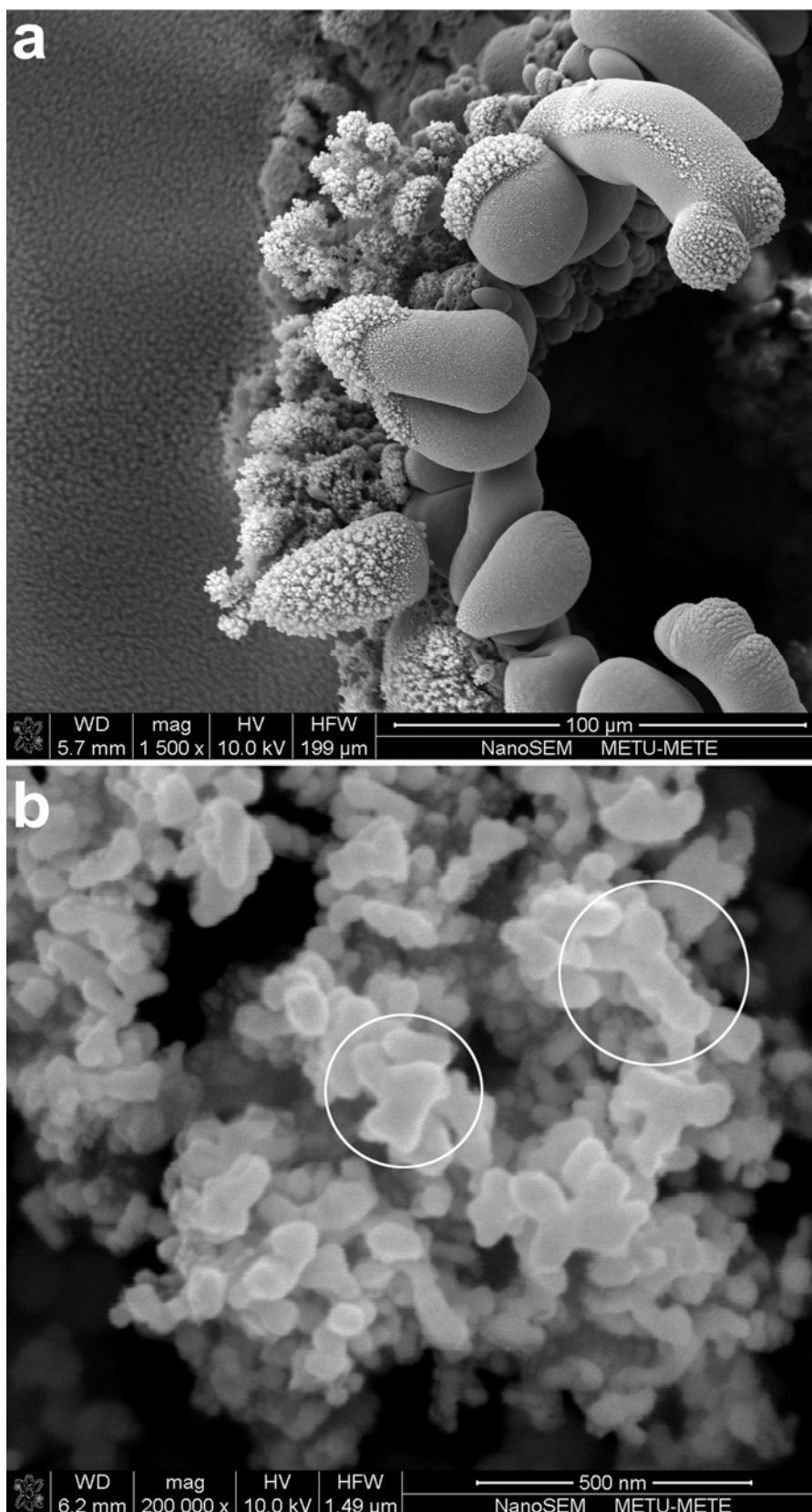


Figure 3.59 (a) General and (b) closer view SEM images showing the evolution of micro-porous residues consisting of spherical aluminum phosphate nanoparticles

3.3.5 Mechanical Properties

It can be inferred from Figure 3.60 and Table 3.17 that mechanical properties (tensile strength and Young's Modulus) are increased in the order of spherical (0-D) < rod-like (1-D) < plate-like (2-D) nanofiller geometries. It is expected that large aspect ratio fillers provide higher level of strengthening. The reason for platelet morphology being more effective could be better dispersion and interfacial interactions via organic modification, and, larger effective aspect ratio obtained with polymer intercalation and exfoliation of montmorillonite. Larger aspect ratio and better interfacial interactions of the 2-D nanofiller strongly hinders polymer chain mobility and improves the load transfer efficiency to the reinforcing filler.

Figure 3.61 contains the SEM images of fracture surfaces showing significant interfacial debonding of AlPi additive and PLA matrix upon loading. Fracture surfaces of samples containing nanofillers demonstrate similar features to that of PLA/AlPi without any evidence of nanofiller agglomerates that undergo debonding, though, energy dispersive spectra verify the presence of nanofillers by increased Al:P and Si:P ratios compared to PLA/AlPi. It can then be concluded that presence of nanofillers has no significant influence on debonding between PLA matrix and AlPi additive and imparts no remarkable change in the fracture morphology.

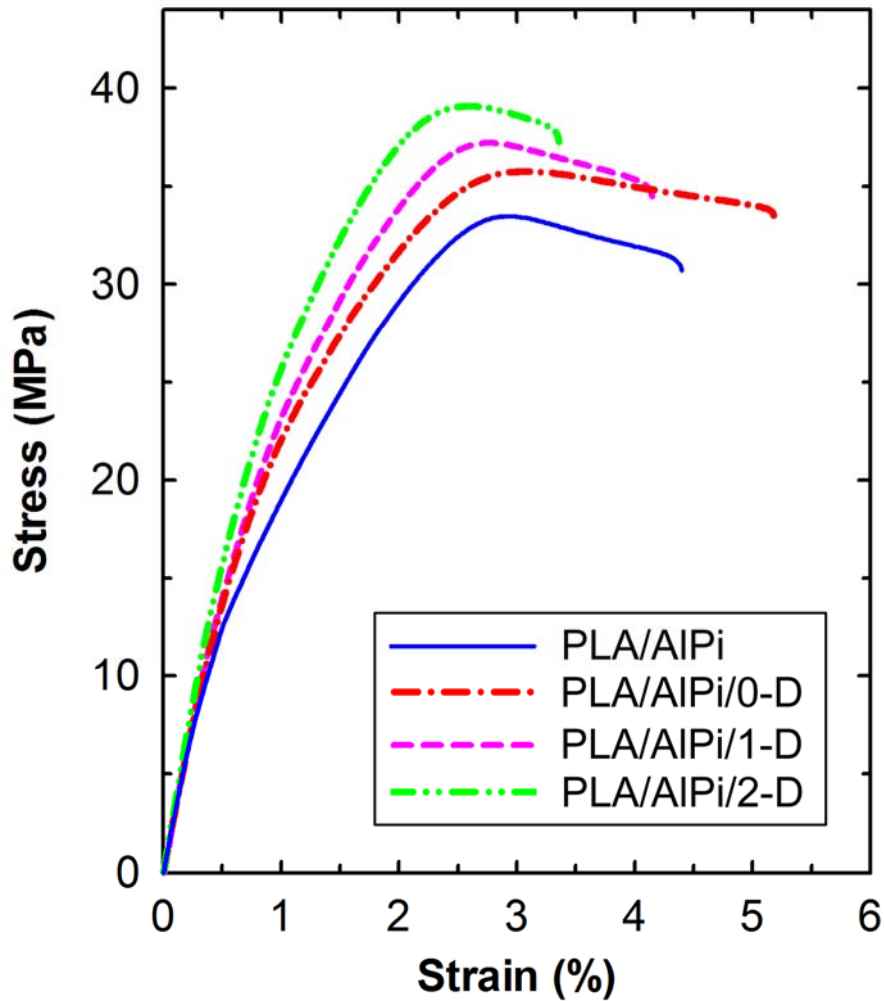


Figure 3.60 Tensile stress – strain curves of PLA/AIPi and nanocomposites indicating that strengthening efficiency of nanofillers increase with increasing aspect ratio; 0-D < 1-D < 2-D

Table 3.17 Mechanical properties of PLA nanocomposites with different nanofiller geometries

	Tensile Strength (MPa)	Young's Modulus (MPa)	Elongation at Break (%)
PLA/AIPi	34.0 ± 0.7	3075 ± 51	4.5 ± 0.2
PLA/AIPi/0-D	36.2 ± 0.5	3131 ± 28	4.9 ± 1.1
PLA/AIPi/1-D	37.0 ± 0.3	3318 ± 88	3.9 ± 0.3
PLA/AIPi/2-D	38.9 ± 0.5	3513 ± 58	3.8 ± 0.9

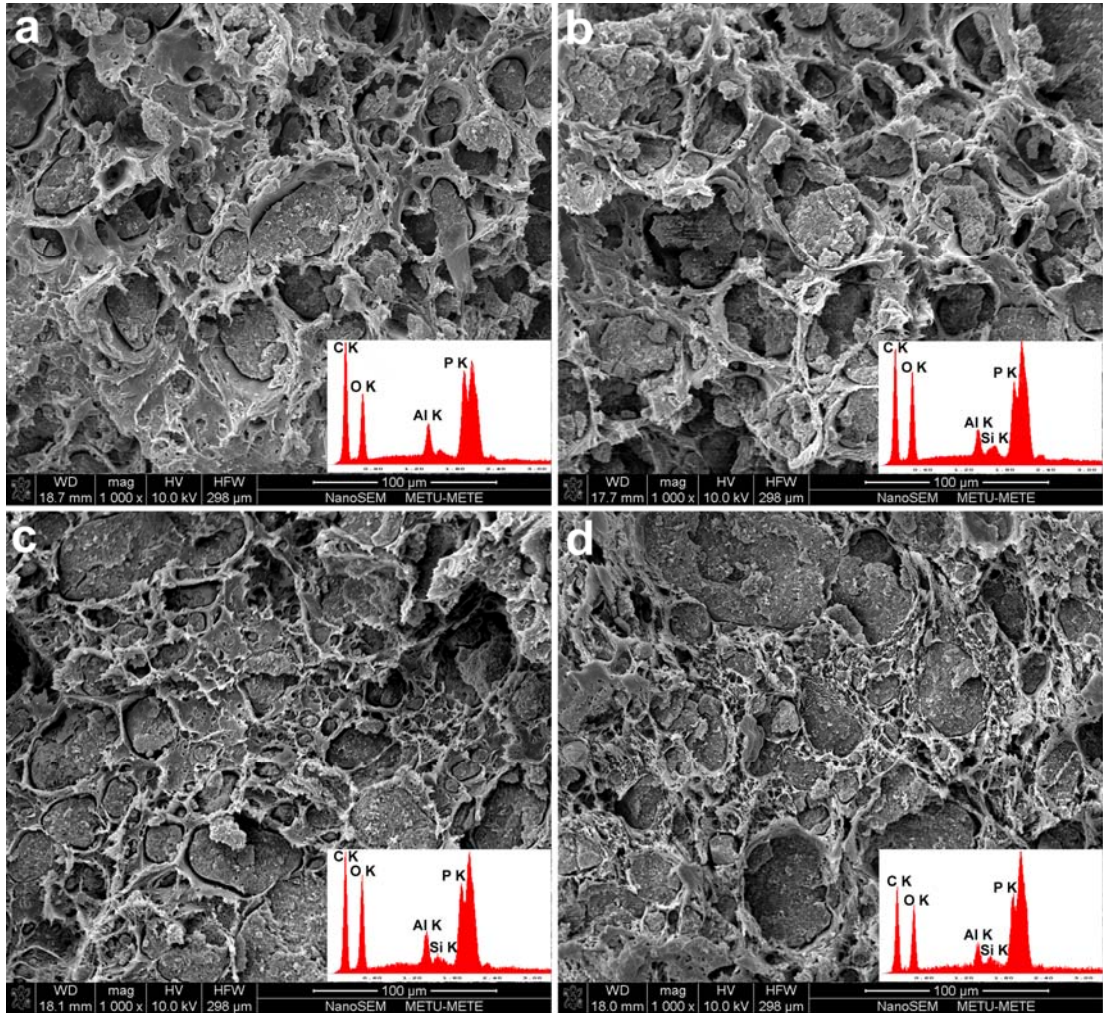


Figure 3.61 SEM images of fracture surfaces from (a) PLA/AlPi, (b) PLA/AlPi/0-D, (c) PLA/AlPi/1-D and (d) PLA/AlPi/2-D

3.4 EFFECT OF FIBER REINFORCEMENT

The fourth aim of this study was to understand the role of fiber reinforcement in synergistic fire retardancy interactions between nanofillers and flame retardant additives. For this purpose, an engineering thermoplastic polyamide-6 (PA6) was chosen as the matrix material, while the fiber reinforcement was silane treated short glass fibers. Organically modified montmorillonite clay and organophosphorus compound were used as the nanofiller and conventional flame retardant additive, respectively. The organophosphorus flame retardant additive is composed of phosphorus and nitrogenous salts and it is known for its high flame retardant effectivity in glass fiber reinforced polyamides.

Designations and compositions of studied samples are listed in Table 3.18. Nanocomposite morphology was characterized by TEM and XRD. Flammability was evaluated by limiting oxygen index tests and classifications of the UL94 standard. Bench-scale fire performance assessment was done by mass loss calorimetry. Flame retardancy mechanisms were investigated using TGA, ATR-FTIR, XRD, SEM and TEM.

3.4.1 Nanomorphology

Morphological analysis of clay nanocomposites based on PA6 was made by TEM and XRD as shown in Figure 3.62 and Figure 3.63, respectively. TEM images reveal exfoliation and nanodispersion of montmorillonite layers in the PA6 matrix. Orientation of individual clay layers along the flow direction of molten polymer during shaping is also evident. Disrupted registry of silicate layers result in the absence of basal reflections in XRD. This suggests exfoliated morphologies for all specimens containing nanoclays. Exfoliation is thermodynamically favored by the large enthalpic contribution of the polar and hydrogen bonding interactions between clay surface modifier (methyl tallow bis-2-hydroxyethyl quaternary ammonium) and PA6 chains [126]. Presence of the flame retardant and/or short glass fibers had no influence on the dispersability of nanoclays, as assessed by XRD.

Table 3.18 Designations and compositions (wt%) of studied samples to investigate the effect of fiber reinforcement

	Polyamide-6 (PA6)	Organophosphorus Flame Retardant (OP)	Short Glass Fiber (GF)	Nanoclay (<i>n</i>)
PA6	100	–	–	–
PA6/OP20	80	20	–	–
PA6/GF	85	–	15	–
<i>n</i>-PA6	95	–	–	5
PA6/GF-OP10	75	10	15	–
PA6/GF-OP15	70	15	15	–
PA6/GF-OP20	65	20	15	–
<i>n</i>-PA6/GF	80	–	15	5
<i>n</i>-PA6/GF-OP5	75	5	15	5
<i>n</i>-PA6/GF-OP10	70	10	15	5
<i>n</i>-PA6/GF-OP15	65	15	15	5

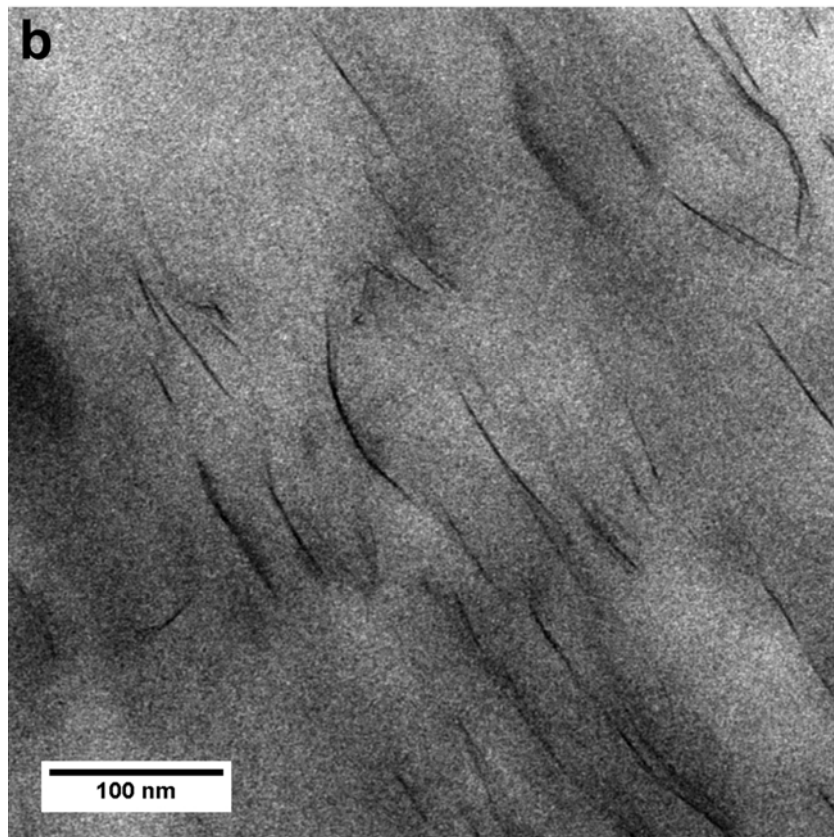
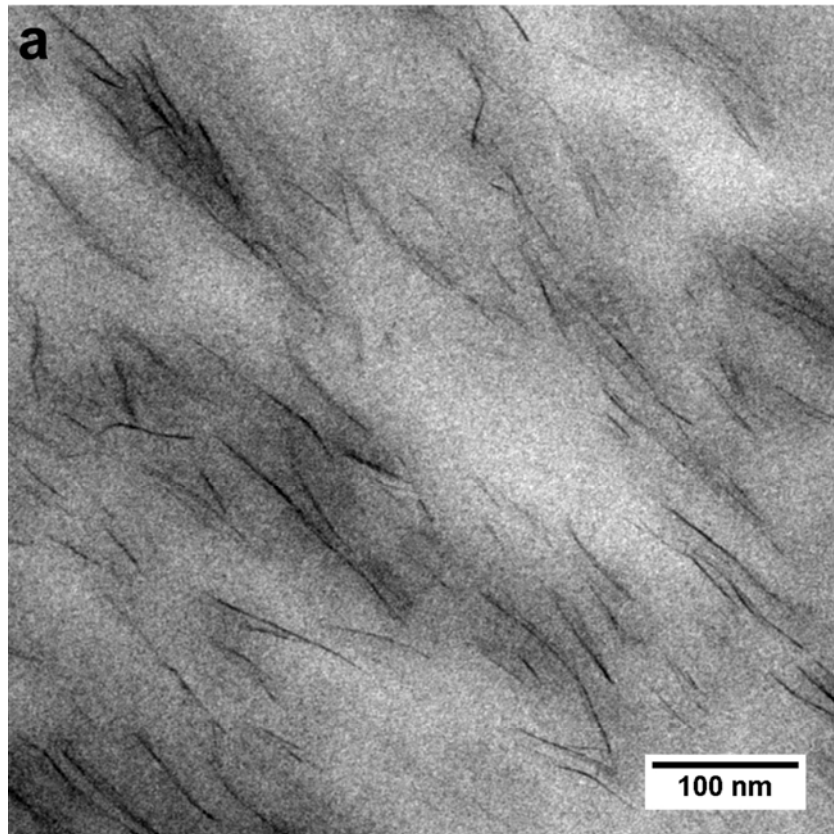


Figure 3.62 (a) and (b) TEM images of the PA6/clay nanocomposite

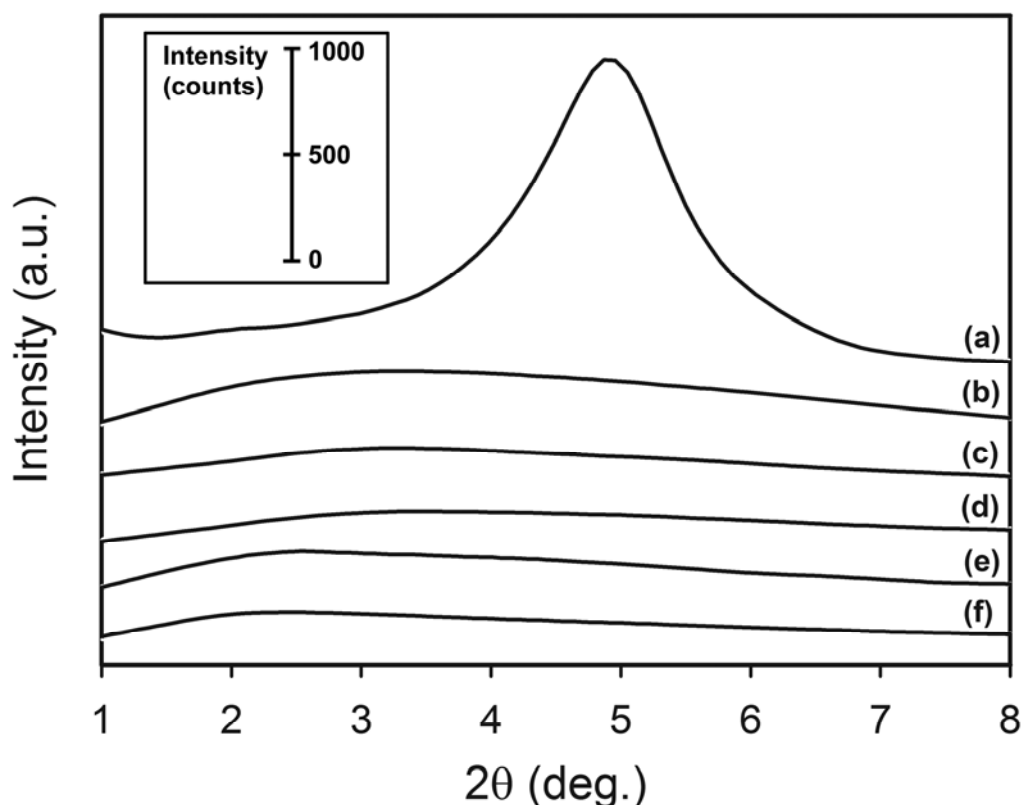


Figure 3.63 XRD patterns of (a) nanoclay, (b) *n*-PA6, (c) *n*-PA6/GF, (d) *n*-PA6/GF-OP15, (e) *n*-PA6/GF-OP10, and, (f) *n*-PA6/GF-OP5

3.4.2 Flame Retardancy

(i) LOI and UL94 Flammability Tests

Results of LOI and UL94 tests are given in Table 3.19. LOI was increased noticeably from 24.9% to 31.7% and UL94 V-0 rating was easily attained with the incorporation of the flame retardant in unreinforced PA6. It is seen that PA6/GF had a considerably lower LOI compared to neat PA6 due to the “candlewick effect” which is well-established in the literature [71, 73]. Short glass fibers, having a loading level of 15 wt% in the composite, were sufficient to stabilize the melt in oxygen index test whereas dripping could not be prevented in UL94 test during which the flammable residue fell off and the V-2 rating of PA6 was retained.

LOI was progressively improved with increasing organophosphorus flame retardant content in flame-retarded/glass fiber reinforced PA6's possessing a jump from 24.9% to 29.3% when the flame retardant concentration was changed from 10 wt% to 15 wt%. Considering flame-retarded/glass fiber reinforced PA6's, V-0 rating was obtained in UL94, except for the lowest flame retardant content, i.e. 10 wt%.

Glass fiber reinforced nanocomposite without the flame retardant showed only a modest enhancement in LOI compared to PA6/GF. Dripping of glass fiber reinforced PA6 was inhibited by nanocomposite formation, thus, the material fails from UL94 vertical burning test. The disappointing results in LOI and UL94 were discussed in a number of studies investigating the flammability of nanocomposites without conventional flame retardants [59, 127].

Table 3.19 Results of flammability tests showing the effect of fiber reinforcement

	LOI (%O₂ ± 2σ)	UL-94
PA6	24.9 ± 0.4	V-2
PA6/OP20	31.7 ± 0.6	V-0
PA6/GF	21.3 ± 0.2	V-2
PA6/GF-OP10	24.9 ± 0.2	V-1
PA6/GF-OP15	29.3 ± 0.4	V-0
PA6/GF-OP20	30.2 ± 0.6	V-0
<i>n</i>-PA6/GF	22.4 ± 0.3	NR
<i>n</i>-PA6/GF-OP5	29.1 ± 0.2	V-1
<i>n</i>-PA6/GF-OP10	30.9 ± 0.4	V-0
<i>n</i>-PA6/GF-OP15	31.7 ± 0.7	V-0

Flame-retarded/glass fiber reinforced nanocomposites have impressive LOI values even at a very low concentration of the flame retardant (5 wt%). Comparing PA6/GF-OP10 and *n*-PA6/GF-OP5 having nominally the same filler concentration of 10 wt% (apart from glass fiber content), LOI of the nanocomposite (29.1%) is unambiguously superior to that of the conventional composite (24.9%). However, the UL94 classification of V-1 obtained by PA6/GF-OP10 was not improved by nanocomposite formation in *n*-PA6/GF-OP5 due to the stringent ignition conditions and geometry of the UL94 test. To generalize, when 5 wt% flame retardant is replaced by the same amount of nanoclays, e.g. for PA6/GF-OP10 and *n*-PA6/GF-OP5, synergistic improvements in LOI are substantial for all three flame retardant contents utilized.

Figure 3.64 reveals the synergistic flame retardancy effect of nanoclays upon replacement of 5 wt% of the organophosphorus flame retardant by nanoclays. It is apparent that LOI values did not follow a simple rule of mixtures (dashed lines) owing to the synergistic interactions (solid lines) between nanoclay and flame retardant. The magnitude of the synergistic improvement in LOI increased with decreasing total filler content (OP + NC).

UL94 classifications of the flame retarded/glass fiber reinforced materials were maintained as either V-1 or V-0 with the mentioned replacements of 5 wt% flame retardant with nanoclay, contrary to the degraded ratings reported earlier [59, 128].

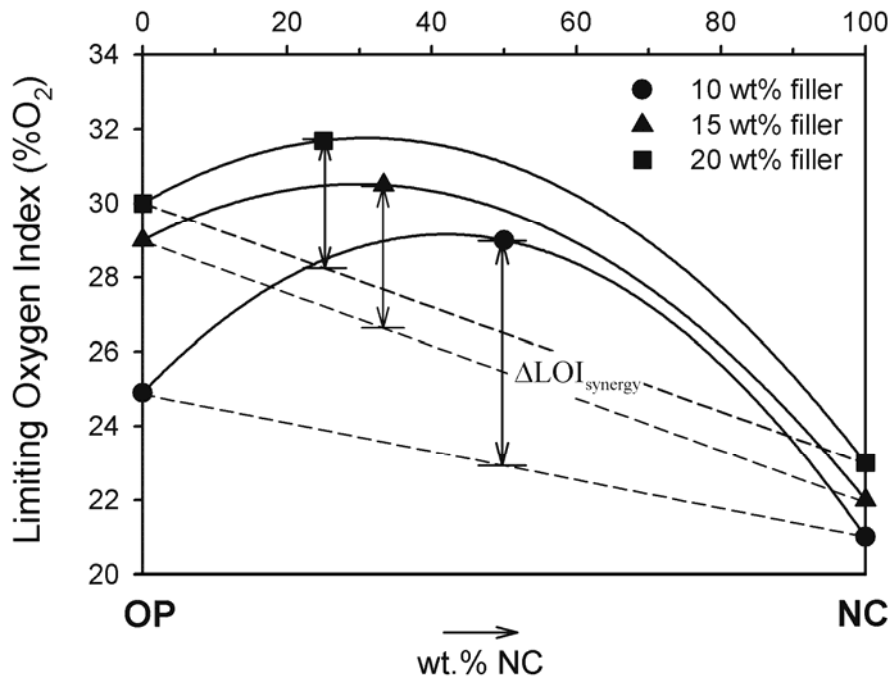


Figure 3.64 Synergistic increases in LOI with the replacement of OP by NC

(ii) Mass Loss Cone Calorimeter Analysis

Figure 3.65(a) displays the heat release rate curves for PA6 reinforced at micro-/nano-scales, i.e. with short glass fibers and nanoclays, and flame-retarded PA6. PA6/GF possessed extended time of burning and a lower peak heat release rate (PHRR) through slowing down of polymer transport into the pyrolysis zone. Formation of clay nanocomposites of PA6/GF reduced the PHRR and increased the burning time. With the incorporation of an active flame retardant in PA6, largest suppression in PHRR together with longest burning time was achieved (PA6/OP20). Longer burning times were previously reported when charring is promoted [129].

Mass loss rate (MLR) curves obtained by mass loss calorimetry, displayed in Figure 3.65(b), shows that for PA6 and PA6/GF, shapes of HRR and MLR curves are similar as an indication of a condensed phase action of glass fibers. Particularly for *n*-PA6/GF, MLR curves possess an initial increase in rate of mass loss followed by a smooth gradual decrease until extinction by the act of the established barrier. More importantly, even though *n*-PA6/GF and PA6/OP20 had similar mass loss rates, heat release rates were different due to the fact that PA6/OP20 shows a gas phase action.

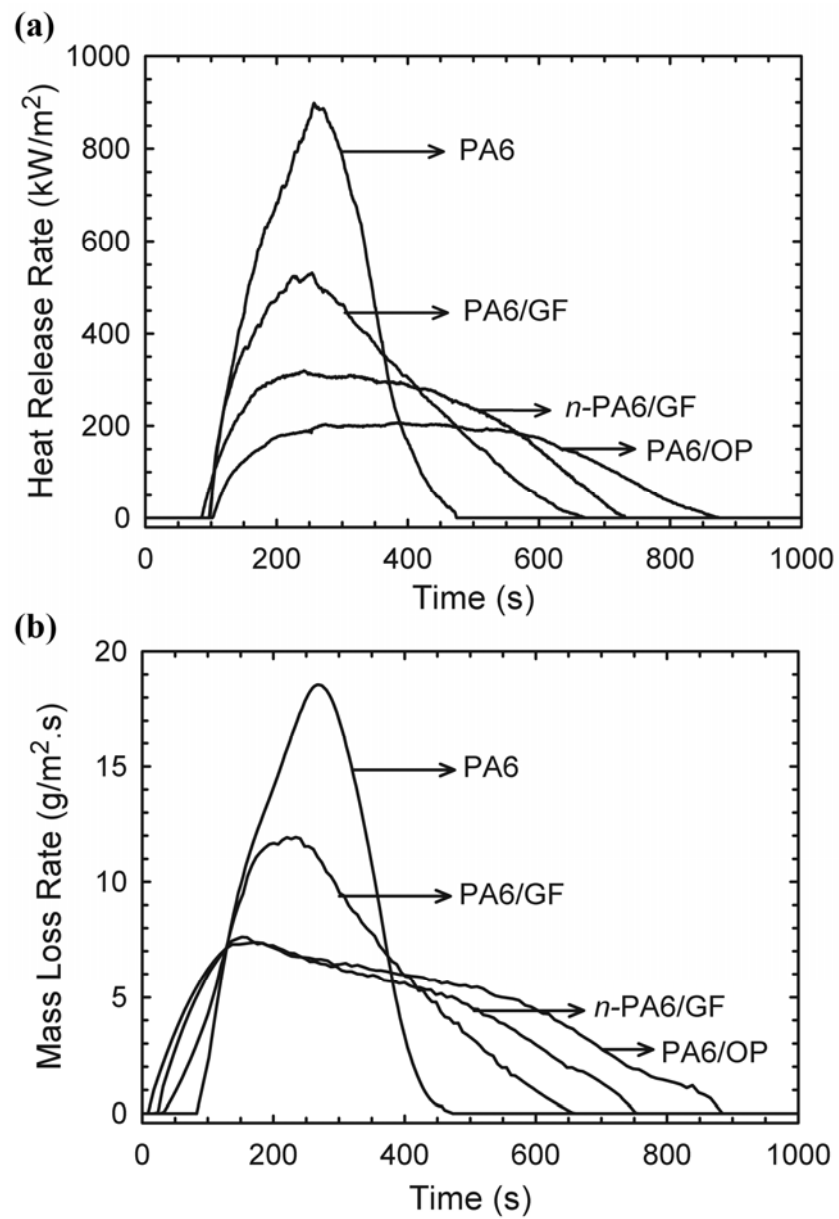


Figure 3.65 (a) Heat release and (b) mass loss rates for reinforced (both at the micro- and nano-scale) and flame-retarded PA6

It can be inferred from Figure 3.66 that burning characteristics of PA6/GF were altered such that peak heat release rate was largely suppressed and burning time was extended with the incorporation of the flame retardant (PA6/GF-OP15). The clay nanocomposite, *n*-PA6/GF-OP10, provided further extension of burning time compared to PA6/GF-OP15 owing to the formation of a thicker char. In fact, the initial increase of heat release rate followed by a steady burning plateau possessed by *n*-PA6/GF-OP10 is a reflection of thick charring on the heat release behavior [130]. At early stages of combustion, the material burns with the highest rate of heat release under the forced flaming conditions of mass loss calorimeter. Then, a plateau of lower heat release rate is formed upon the establishment of the protective barrier layer slowing down the escape of flammable volatiles.

It is apparent in Figure 3.67 that peak heat release rate was suppressed in proportion with the amount of flame retardant in the nanocomposites. A steady heat release plateau was formed by flame-retarded/glass fiber reinforced nanocomposites demonstrating strong charring behavior.

Figure 3.68 and Table 3.20 contain the interpreted mass loss calorimeter data. Figure 3.68(a) shows that formation of PA6/GF nanocomposite suppressed the peak heat release rate by 40% owing to the carbonaceous barrier formed on the exposed surface of the specimen by migration and accumulation of clay layers dispersed at the nano-scale. Considering PA6/GF-OP formulations, peak heat release rate was reduced in proportion to the flame retardant contents of 10 wt%, 15 wt%, and 20 wt% by 52%, 58% and 62%, respectively, compared to PA6/GF. Regarding nanoclay containing materials, similar reductions are obtained with flame retardant contents of 5 wt%, 10 wt% and 15 wt% by 36%, 41% and 45%, respectively, compared to *n*-PA6/GF. When PA6/GF-OP and *n*-PA6/GF-OP with same nominal filler contents (dashed lines in Figure 3.68(a) are considered, further peak heat release rate reductions of 20%, 16% and 13% could be attained with nanocomposite formulations in the order of increasing total filler content.

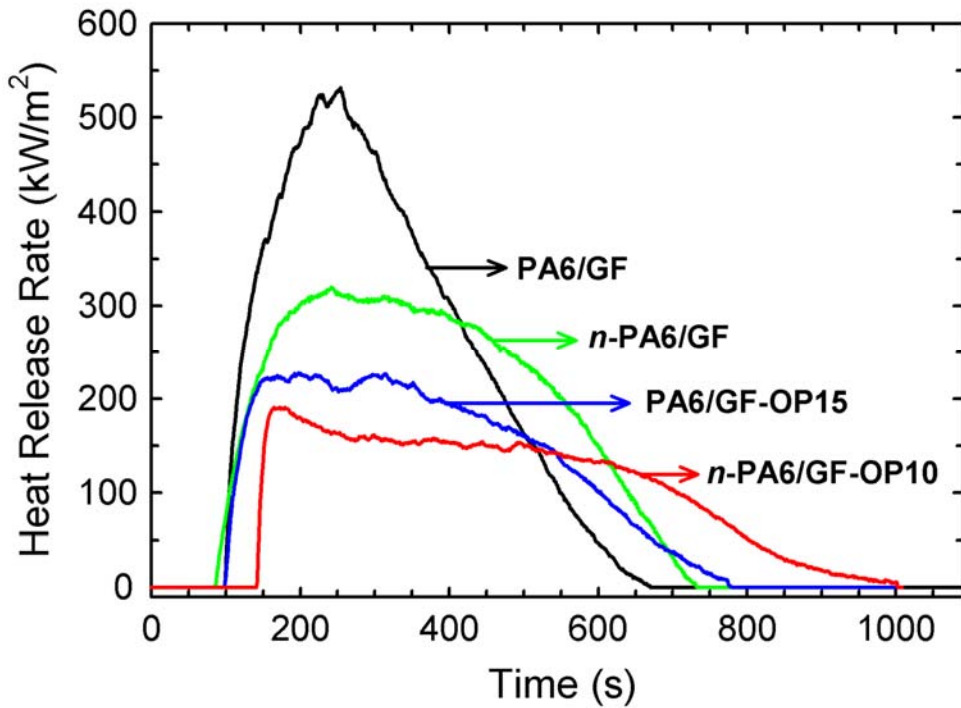


Figure 3.66 Heat release rate curves for flame-retarded/glass fiber reinforced PA6 and nanocomposites

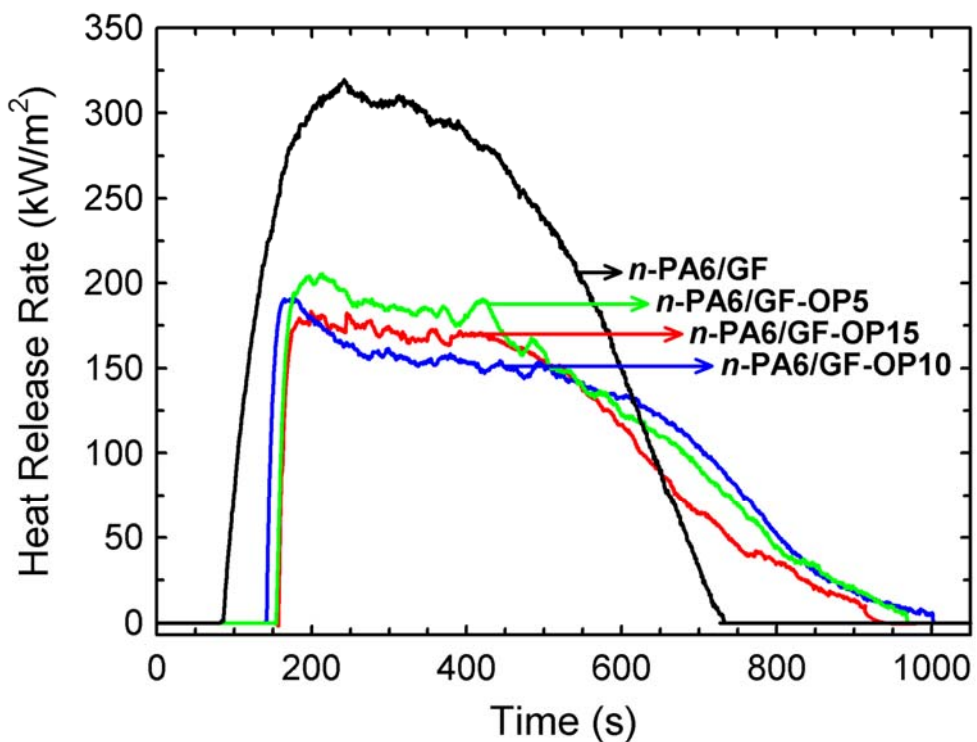


Figure 3.67 Heat release rate curves of flame-retarded and glass fiber reinforced PA6 nanocomposites with varying flame retardant content

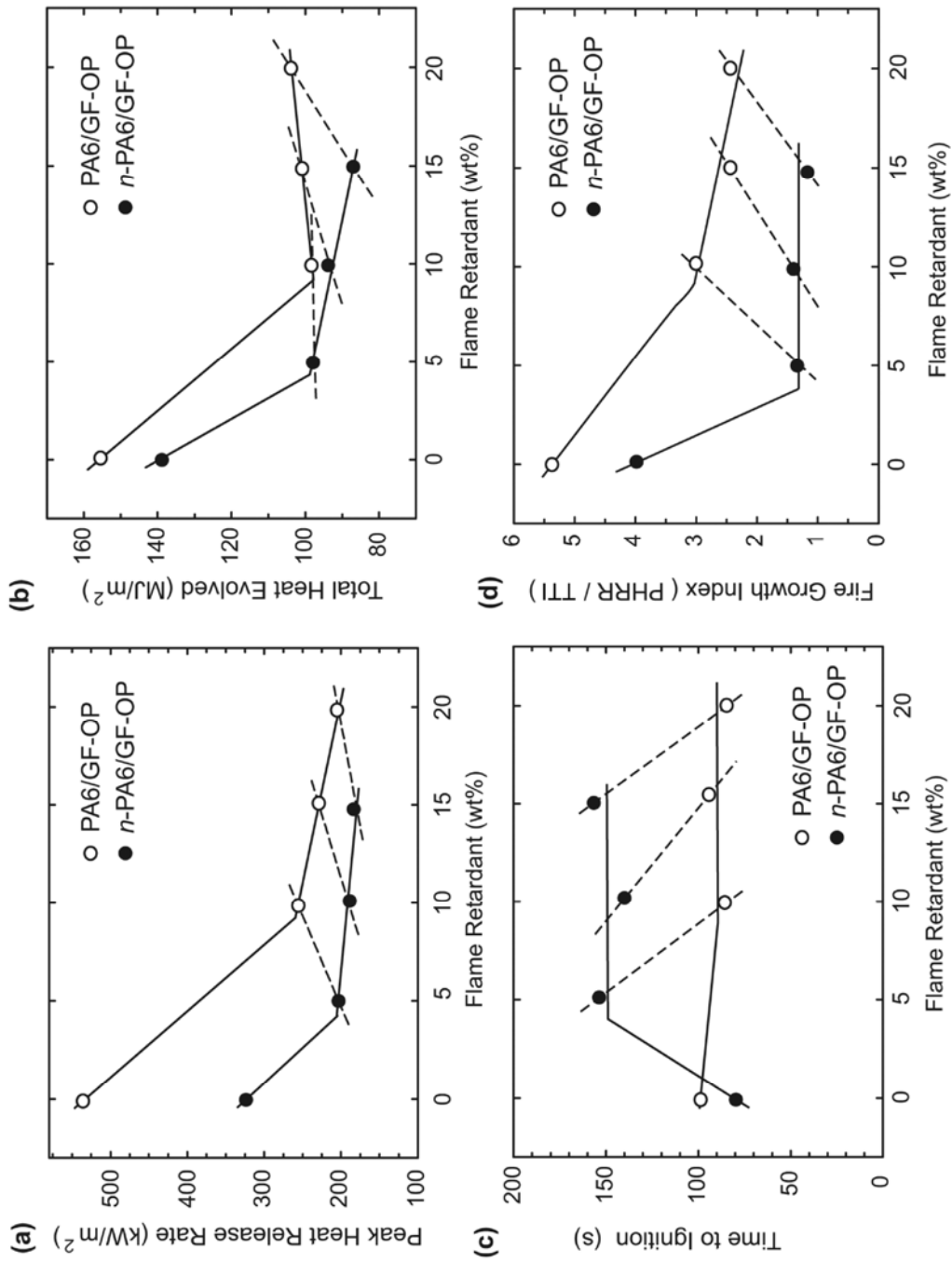


Figure 3.72 Mass loss calorimeter data as a function of organophosphorus flame retardant content, (a) peak heat release rate, (b) total heat evolved, (c) time to ignition, and (d) fire growth index. Dashed lines indicate equal nominal filler contents. i.e. organoclay + flame retardant

Table 3.20 Interpreted mass loss calorimeter data showing the effect of fiber reinforcement

	Peak Heat Release Rate - PHRR - (kW/m²)	Total Heat Evolved - THE - (MJ/m²)	Time to Ignition - TTI - (s)	Fire Growth Index - FGI - (kW/m²s)	Total-heat-evolved / Total-mass-loss - THE/TML - (MJ/m²g)
PA6	899	175	98	9.2	4.1
PA6/OP20	208	112	101	2.1	2.9
PA6/GF	532	156	99	5.4	3.9
PA6/GF-OP20	203	104	85	2.4	2.8
PA6/GF-OP15	228	101	97	2.4	2.7
PA6/GF-OP10	255	98	84	3.0	2.7
<i>n</i>-PA6/GF	320	139	80	4.0	3.7
<i>n</i>-PA6/GF-OP15	178	76	157	1.1	2.1
<i>n</i>-PA6/GF-OP10	191	94	141	1.4	2.6
<i>n</i>-PA6/GF-OP5	205	98	154	1.3	2.7

Comparing PA6/GF with the nanocomposite, total heat evolved (THE) values given in Figure 3.68(b) showed a minor reduction caused mainly by dilution of fuel via inorganic filler content, and stabilization of a certain PA6 fraction by catalytic charring. Total heat evolved was remarkably lowered with the addition of the flame retardant in PA6/GF and *n*-PA6/GF. It can be inferred from that total heat evolved was more or less independent of flame retardant content with PA6/GF-OP formulations, whereas a progressive reduction was obtained as a result of char enhancement and strengthening in presence of the nanoclay. Furthermore, regarding materials with same nominal filler content (dashed lines in Figure 3.68), increasing flame retardant loading leads to larger reductions in total heat evolved obtained by nanocomposite formulations.

Figure 3.68(c) shows that *n*-PA6/GF ignited earlier than PA6/GF as a result of acid catalyzed degradation of polyamides [131] via protonic sites formed within clay galleries upon degradation of the organic modifier [132-134]. However, for *n*-PA6/GF-OP formulations, an opposite effect was observed such that strong and consolidated char impeded the evolution of flammable volatiles. Consequently, ignition was delayed in nanocomposites when materials with same nominal filler content are considered. Time to ignition (TTI) values suggest that the flame retardant content imparted no change in ignitability for both PA6/GF-OP and *n*-PA6/GF-OP formulations.

It is followed from the work of Petrella [95] that a fire growth index (FGI) defined by $\text{PHRR}/t_{\text{ign}}$ makes a reasonable attempt at assessing the flame spread as a fire hazard. It can be inferred from Figure 3.68(d) that substitution of 5 wt% flame retardant with nanoclays significantly lowers FGI owing to reduced PHRR and delayed ignition.

It is also well established that the mechanism of flame retardancy can be addressed considering the ratio of total heat evolved to total mass loss (THE/TML). This ratio allows for the deduction of availability of gas phase action since it is a suitable measure for the effective heat of combustion of volatiles [130, 135].

THE/TML for PA6 was reduced from 4.1 MJ/m²g to 2.9 MJ/m²g with the addition of the flame retardant. PA6/GF gave a THE/TML value of 3.9 MJ/m²g, which was reduced on the average to 2.8 MJ/m²g with PA6/GF-OP formulations. Therefore, it was concluded that, in addition to a dominant condensed phase action by means of barrier formation, flame inhibition and dilution were also present as gas phase flame retarding mechanisms. Actually, Braun et al. [93] have shown that evolution of melamine, diethyl phosphinic acid and aluminum–zinc phosphinates constitute the gas phase action of OP.

Considering nanocomposites of PA6/GF-OP formulations, no significant alteration was observed in THE/TML values. The average value of 2.8 MJ/m²g for PA6/GF-OP became 2.6 MJ/m²g on the average for *n*-PA6/GF-OP formulations, the change being in the range of experimental error margin. Hence, combining the reductions in PHRR and unaltered THE/TML values, it was concluded that the condensed phase action is enhanced in the presence of nanoclays, mainly owing to the formation of a stronger boron/aluminum phosphate barrier reinforced at the nano-scale (as explained in the following section).

3.4.3 Flame Retardancy Mechanisms by Thermal Degradation

In order to investigate the flame retardancy mechanisms of samples, thermogravimetric analysis was performed. All compositions possessed single decomposition steps as shown in Figure 3.69. The main breakdown of PA6 results in release of water, ammonia, carbon monoxide, carbon dioxide and hydrocarbon fragments [136]. Although differential thermogravimetry (DTG) peak temperatures (T_{\max}) of PA6/GF and *n*-PA6/GF were almost the same, 10% mass loss temperature ($T_{10\%}$) is lowered by 8 K (Table 3.21).

Additionally, *n*-PA6/GF-OP15 possessed about 7°C and 28°C lower temperatures compared to PA6/GF-OP15 in terms of T_{\max} and $T_{10\%}$, respectively. Lower temperatures corresponding to maximal rate of decomposition and 10% mass loss were attributed to the catalytic activity in the presence of large surface area clay layers with protonic sites [132-134]. T_{\max} and $T_{10\%}$ for PA6/GF-OP15 were 30 K and 17°C lower, respectively, compared to PA6/GF as a consequence of decomposition of flame retardant constituents. Decomposition of melamine polyphosphate at around 350°C [137] and evolution of phosphinates and phosphinic acids into the vapour phase [93] result in lower degradation temperatures. In addition, it is clear from T_{\max} and $T_{10\%}$ for *n*-PA6/GF with varying OP content that the flame retardant shifted the degradation temperatures progressively to smaller values, material with the highest flame retardant content being the earliest to decompose.

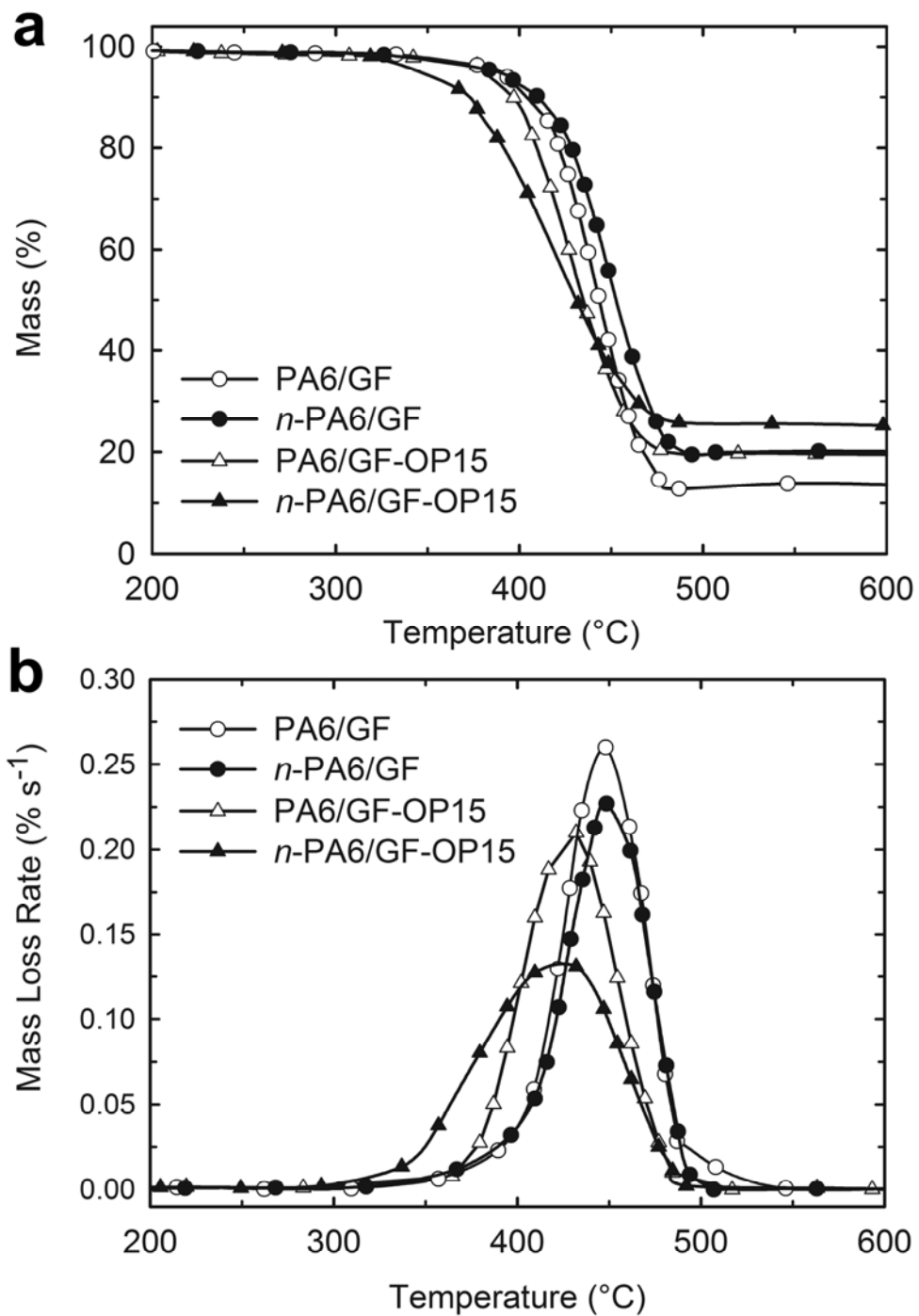


Figure 3.69 Thermogravimetric and differential thermogravimetric curves of flame-retarded glass fiber reinforced PA6 nanocomposites

Comparing the DTG curves for PA6/GF and PA6/GF-OP15, flame retardant decreased the maximal rate of mass loss by interfering with the main decomposition of PA6 with degrading flame retardant constituents. Formation of flame-retarded nanocomposite (*n*-PA6/GF-OP15) further suppressed the peak of mass loss rate for PA6/GF-OP15. Similarly, lower mass loss rates were obtained with *n*-PA6/GF compared to PA6/GF. These were attributed to the retardation of volatile evolution by means of the tortuous pathway formed by exfoliated, large aspect ratio clay layers.

It is shown in Table 3.21 that PA6/GF yielded a residue of 13.6% corresponding solely to glass fibers. In the case of PA6/GF-OP15, amount of char residue upon heating was 18.8 wt% while total concentration of additives was 30 wt%. Therefore it can be concluded that a significant fraction of the flame retardant volatilizes and acts in the gas phase. However, it should be noted that primary flame retardancy mechanism for organophosphorus flame retardant was stated to be a condensed phase action [55, 88].

Table 3.21 Thermogravimetric and differential thermogravimetric data of flame-retarded glass fiber reinforced PA6 nanocomposites

	$T_{\text{DTG-Peak}}$ (°C)	$T_{10\%}$ (°C)	% Residue
PA6/GF	455	416	13.6
PA6/GF-OP15	425	399	18.8
<i>n</i> -PA6/GF	455	408	19.6
<i>n</i> -PA6/GF-OP5	450	397	21.6
<i>n</i> -PA6/GF-OP10	435	384	22.2
<i>n</i> -PA6/GF-OP15	418	371	25.1

For *n*-PA6/GF, considering the weight fractions of nanoclay on silicate basis (3.5 wt%) and glass fiber residue from the reference measurement of PA6/GF (13.6 wt%), char yield of 19.6 wt% was higher than the total inorganic filler content. This is indicative of certain polymer fraction being retained as a result of charring induced in presence of nanoclay. Particularly, comparing PA6/GF-OP15 and *n*-PA6/GF-OP15, 6.3 wt% higher char yield was obtained with the flame-retarded nanocomposite recalling that the inorganic residue from nanoclay was approximately 3.5 wt%. In fact, for materials with same nominal filler content, i.e. PA6/GF-OP15 and *n*-PA6/GF-OP10, char yield was still higher with nanocomposites.

3.4.4 Flame Retardancy Mechanisms by Residue Analysis

Further investigations to understand flame retardancy mechanisms by ATR-FTIR on mass loss calorimeter char residues (termed as fire residues) revealed the underlying reasons behind increased amounts of char residues with nanocomposites of both PA6/GF and PA6/GF-OP formulations. Considering *n*-PA6/GF-OP with different flame retardant contents, it is clearly seen in Table 3.21 that the amount of char residue was increased with increasing flame retardant content.

The ATR-FTIR spectrum of PA6/GF residue (Figure 3.70a) includes a diffuse band around 930 cm^{-1} which corresponds to the superposition of bridging oxygen in Si–O–Si and terminal Si–O stretching vibrations [138]. The small band around 680 cm^{-1} was attributed to bending vibrations of Si–O–Si bridging oxygen atoms, and an additional small band around 1400 cm^{-1} corresponds also to glass fibers [93].

The spectra recorded from PA6/OP20 residue (Figure 3.70b) involve a sharp peak at 1080 cm^{-1} and a shoulder around 1020 cm^{-1} which were attributed to asymmetric stretching (ν_3) of PO_4^{3-} in boron phosphates [96]. Small shoulder appearing near 960 cm^{-1} arises from symmetric stretching vibrations (ν_1) of PO_4^{3-} . Small signal at 780 cm^{-1} matches with the most intense signal of neat organic phosphinate (characterized by reference measurements) which indicates that certain amount of flame retardant additive might have remained without decomposing.

An additional broad peak appeared at 1600 cm^{-1} which indicates the formation of an aromatic ring breathing mode or C=C of conjugated polyene structure. It was shown by Holland and Hay [139] that it is practically impossible to identify whether the band at 1600 cm^{-1} corresponds to aromatic or conjugated species. Nonetheless, aromatic or conjugated species indicates a partial stabilization of polymer degradation products in the condensed phase by the act of OP flame retardant. Spectrum for the residue of PA6/GF-OP15 (Figure 3.70c) contained an additional shoulder around 930 cm^{-1} characteristic of glass fibers when compared with the residue of PA6/OP20 (Figure 3.70b).

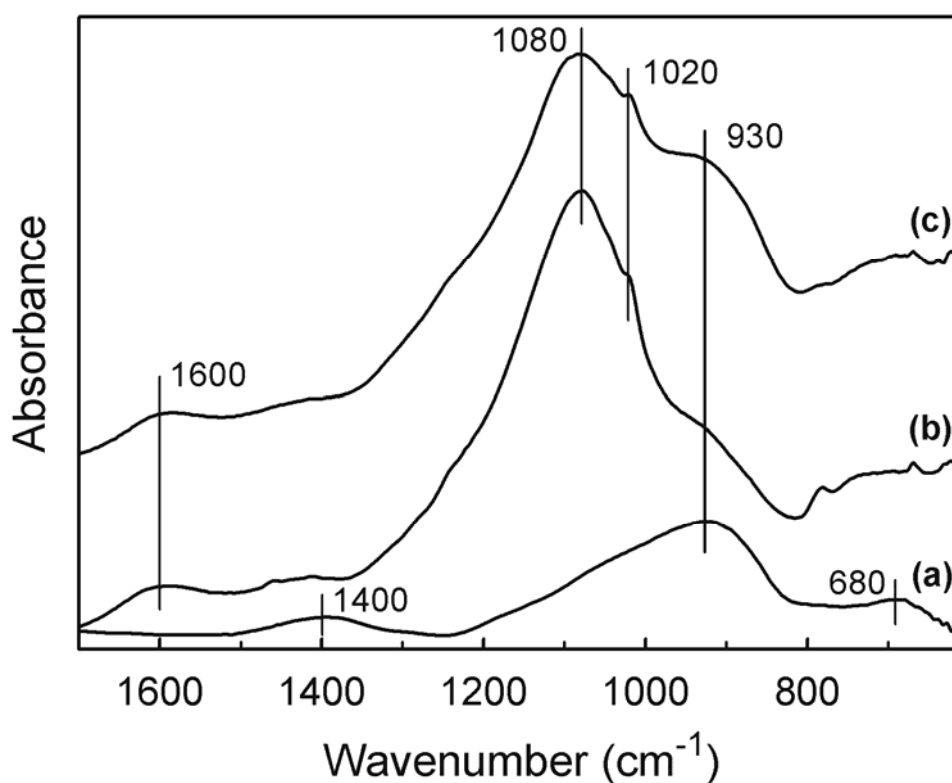


Figure 3.70 ATR-FTIR spectra of combustion residues from mass loss calorimeter char residues without nanoclay; (a) PA6/GF, (b) PA6/OP20, and, (c) PA6/GF-OP15

Figure 3.71 shows the spectra of fire residues from *n*-PA6/GF-OP15, *n*-PA6/GF, and PA6/GF. Absorption band for Si–O stretching in montmorillonite is at 1030 cm^{-1} determined by measuring reference spectra and from literature [99]. Spectrum for the residue of *n*-PA6/GF given in Figure 3.71(b) contains a sharp peak around 1030 cm^{-1} characteristic of montmorillonite and a shoulder around 930 cm^{-1} corresponding to Si–O–Si and Si–O stretching in glass fibers. Similar to previous discussions regarding materials with no nanoclays, formation of a band at 1600 cm^{-1} indicates the presence of aromatic or conjugated degradation products of polyamide-6 stabilized in the residue.

Considering the residue of *n*-PA6/GF-OP15 (Figure 3.71c), an additional shoulder appeared around 1115 cm^{-1} as an evidence for the formation of aluminum phosphates such as aluminum ortho-, pyro- and poly-phosphates [93]. Here, bands for phosphate absorption in boron phosphates were masked from the strong absorption of montmorillonite in nanoclay containing residue. This restricts further conclusions on the composition of residue in terms of the relative amounts of aluminum and boron phosphates. Nevertheless, the nanoclay can be said to have altered the reactivity of aluminum phosphinate, melamine polyphosphate and zinc borate flame retarding species in such a way that aluminum phosphates were preferentially formed in addition to boron phosphates contrary to the materials without the nanoclay.

The mechanism for the observed phenomenon can be explained by considering the well-known barrier effect of nano-dispersed clay layers. Diffusion of volatile species generated at elevated temperatures attained in cone test was restricted by the tortuous pathway formed by the clay layer network [140]. Of particular interest to our case, retardation of gaseous aluminum phosphinate evolution by means of the labyrinth effect of exfoliated clay layers provided that a larger portion of aluminum phosphinate reacts with the synergist flame retardant components to form aluminum phosphates in the char residue.

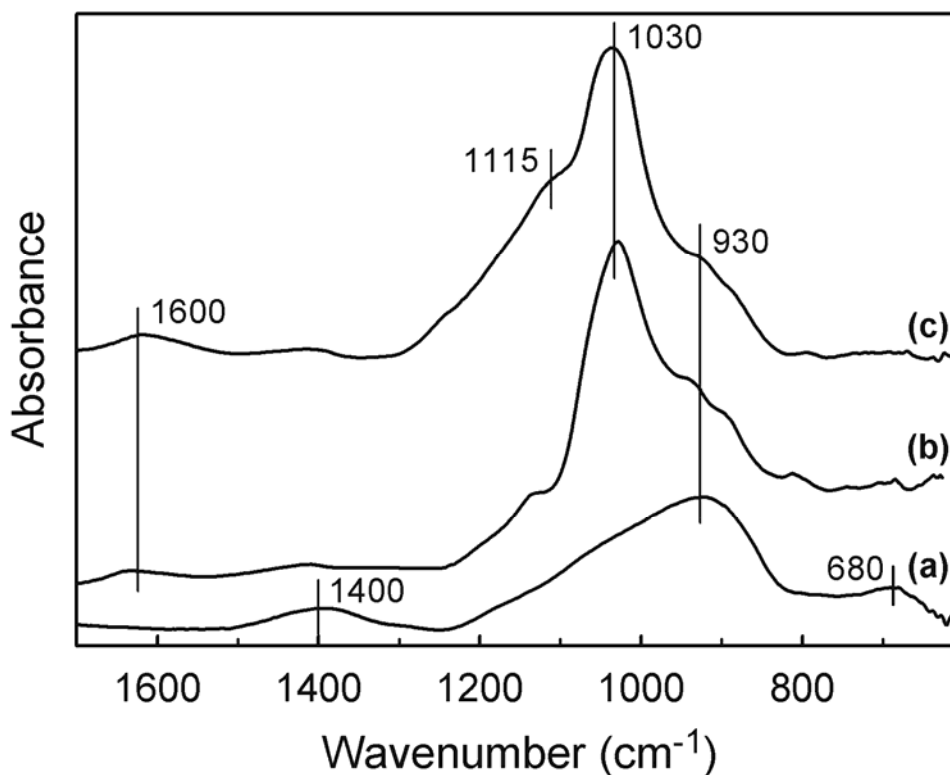


Figure 3.71 ATR-FTIR spectra of fire residues from materials with nanoclay, (a) PA6/GF, (b) *n*-PA6/GF, and (c) *n*-PA6/GF-OP15

Similarly, Braun et al. [93] showed through the utilization of large external heat fluxes in the cone test that vaporization of aluminum phosphinate is minimized and aluminum phosphates are formed in addition to boron phosphates. In particular, a boron/aluminum phosphate barrier was reported to act superior as a protective layer against heat and mass transport to that composed only of aluminum phosphates.

The diffuse reflections in XRD patterns given in Figure 3.72 indicate the formation of a char residue mainly possessing amorphous structure. The diffractograms of char residues from nanocomposites differ from those of conventional composites only in that the pattern contains crystal reflections from layered silicates as expected. Inorganic substances, such as aluminum and boron phosphates, may exist in crystalline state of long-range crystalline order as well as in amorphous state with short range order confined to polyhedral coordination. In order to allow for crystallization, crystalline transformation temperatures should be reached and prolonged times are required for compositional homogenization. In addition,

relatively slow cooling is necessary to allow for crystallization on cooling. However, in the case of fire tests, reached temperatures are low and the time allowed is short which results in the formation of a glassy char residue.

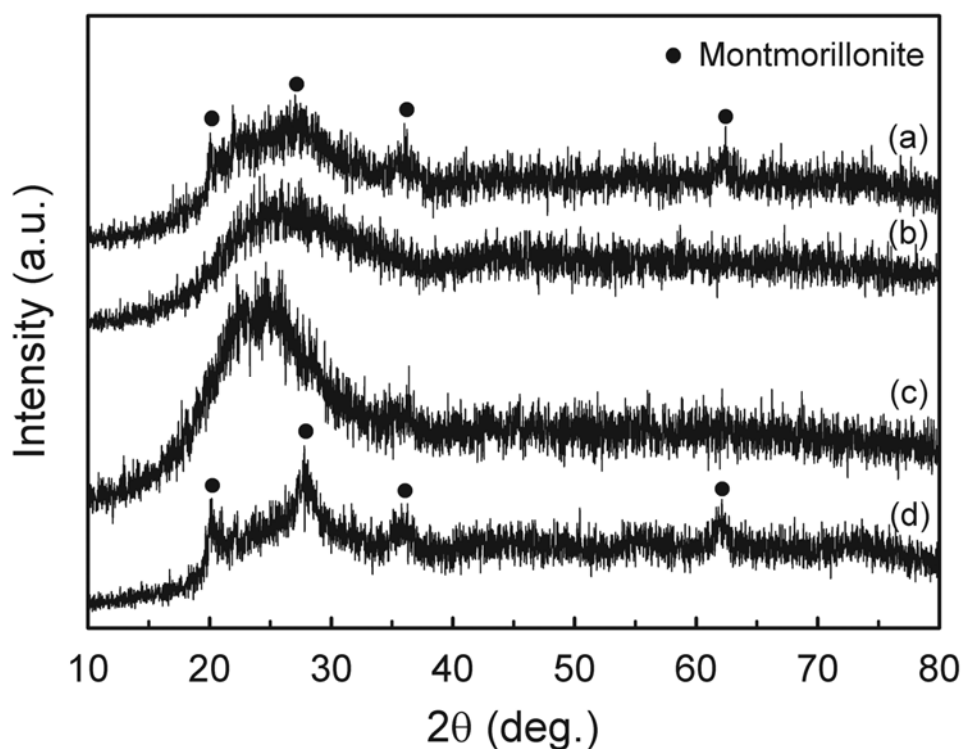


Figure 3.72 XRD patterns showing the amorphous structure of fire residues from (a) *n*-PA6/GF-OP15, (b) PA6/GF-OP15, (c) PA6/OP20 and (d) *n*-PA6/GF

Interestingly, clay basal reflections from the residues of *n*-PA6/GF and various *n*-PA6/GF-OP occurred either at noticeably different angles or the pattern was silent as shown in Figure 3.73. Basal spacing of clays in the residue of glass fiber reinforced nanocomposite attained a value of 1.3 nm as a result of almost complete collapse of montmorillonite layers upon volatilization of intra-gallery features, i.e. polymer and organic modifier. Recalling that neat organoclay and Na-MMT have basal spacings of 1.8 nm and 1.1 nm (from reference measurements), a certain amount of stable residue from degradation of polyamide (aromatic or conjugated species detected by ATR-FTIR) can be said to have remained in the intra-gallery region.

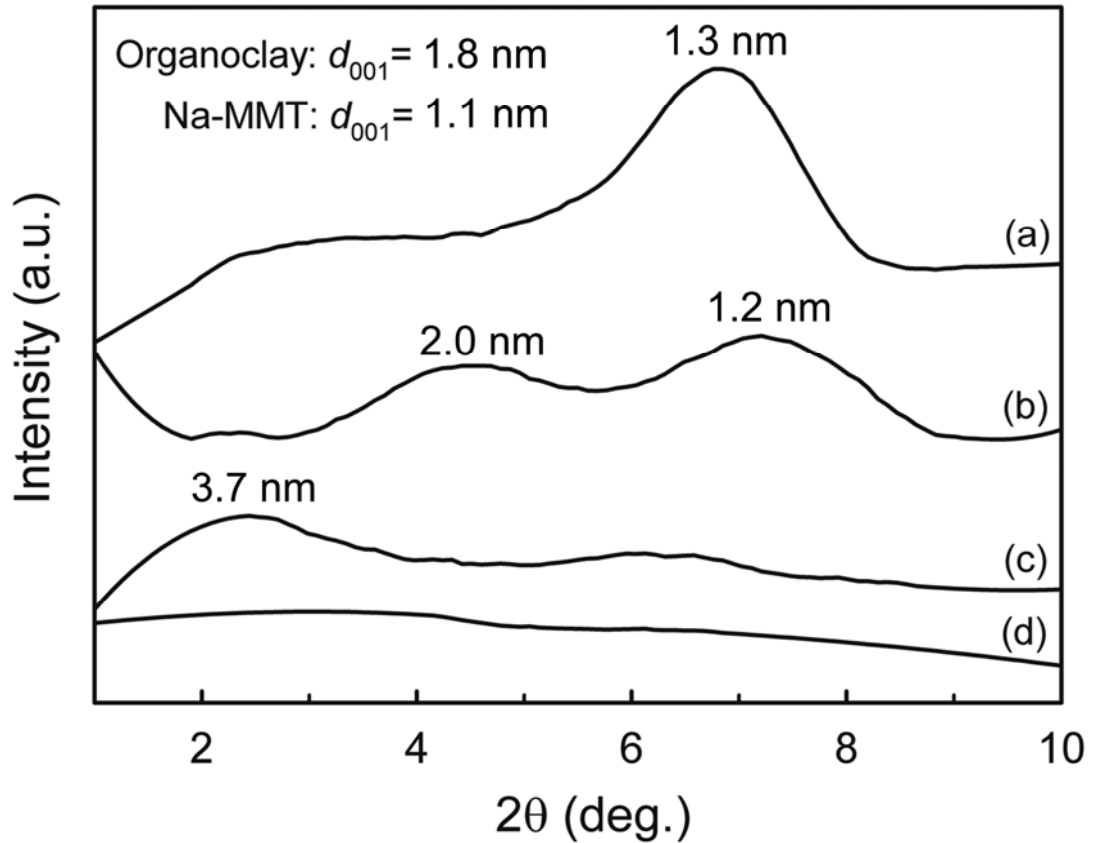


Figure 3.73 XRD patterns showing the clay nanomorphology in char residues from (a) *n*-PA6/GF, (b) *n*-PA6/GF-OP5, (c) *n*-PA6/GF-OP10, and (d) *n*-PA6/GF-OP15

Basal spacings of clays in the residues from *n*-PA6/GF-OP5 and *n*-PA6/GF-OP10 were 2.0 nm (1.2 nm) and 3.7 nm, whereas for the highest flame retardant content, i.e. *n*-PA6/GF-OP15, clay layer registry was still absent resembling the original state of the nanocomposite (Figure 3.73). It is seen that basal spacing of clays in the residue was either larger or no layer registry existed when an effective flame retardant that enhances strong charring was present in glass fiber reinforced nanocomposites. An intriguing reason could be the formation of a stable residue within the clay galleries as well as in the extra-gallery region during flaming combustion. Consequently, a double network structure develops which is an interpenetration of clay and boron/aluminum phosphate networks. The double network forming upon the explained phenomenon possesses a consolidated, crack-free and mechanically strong structure owing to the reinforcement of the flame retarding barrier at the nano-scale.

Figure 3.74 shows the TEM micrographs of char residue formed by combustion of *n*-PA6/GF-OP15 in the mass loss calorimeter. The residue contains mostly nano-dispersed montmorillonite layers with almost no long range stacking order. The inset in Figure 3.74(a) shows the selected area diffraction pattern containing polycrystalline reflections indicative of randomly oriented montmorillonite crystallites within the amorphous char matrix. It can be stated that, facilitated by rapid charring during combustion and well-exfoliated initial nanostructure, montmorillonite layers can be said to preserve to some extent their initial dispersion state in the matrix resulting in retained exfoliation in the char. Nanostructure formation in char residues can be thought to be controlled by factors such as the initial montmorillonite dispersion, loading level of flame retardant additive and effectiveness of additive in promoting charring reactions as well as combustion conditions and pyrolysing melt viscosity.

Figure 3.75(a-b) contains high magnification SEM images of chars showing the coexistence of relatively coarse/hollow spheres and fine spherical-like particles of amorphous aluminum/boron phosphates formed by combustion of PA6/GF-OP15. The nanostructured residue formed from *n*-PA6/GF-OP15 displayed in Figure 3.75(c-d) contains re-assembled montmorillonite platelets forming dense barrier layers where spherical particle morphology of the amorphous phosphate char could not be seen. Elemental analysis of the nanostructured char revealed the presence of montmorillonite by increased weight ratios of Al/P (from 0.43 to 0.62) and Si/P (from 0.62 to 1.16) in addition to detection of Fe as a minor constituent in the char from *n*-PA6/GF-OP15.

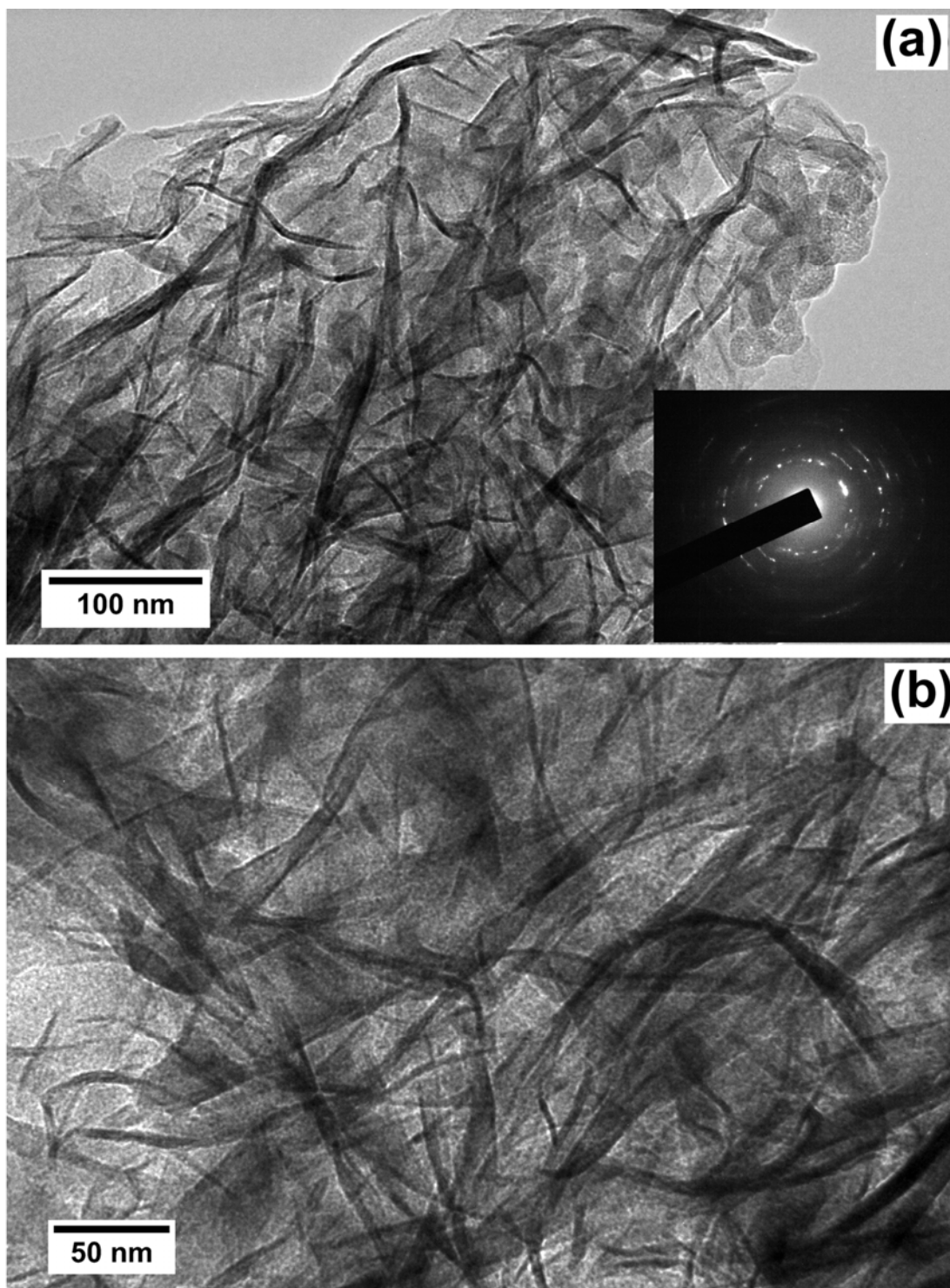


Figure 3.74 (a-b) TEM images of mass loss calorimeter residue of *n*-PA6/GF-OP15

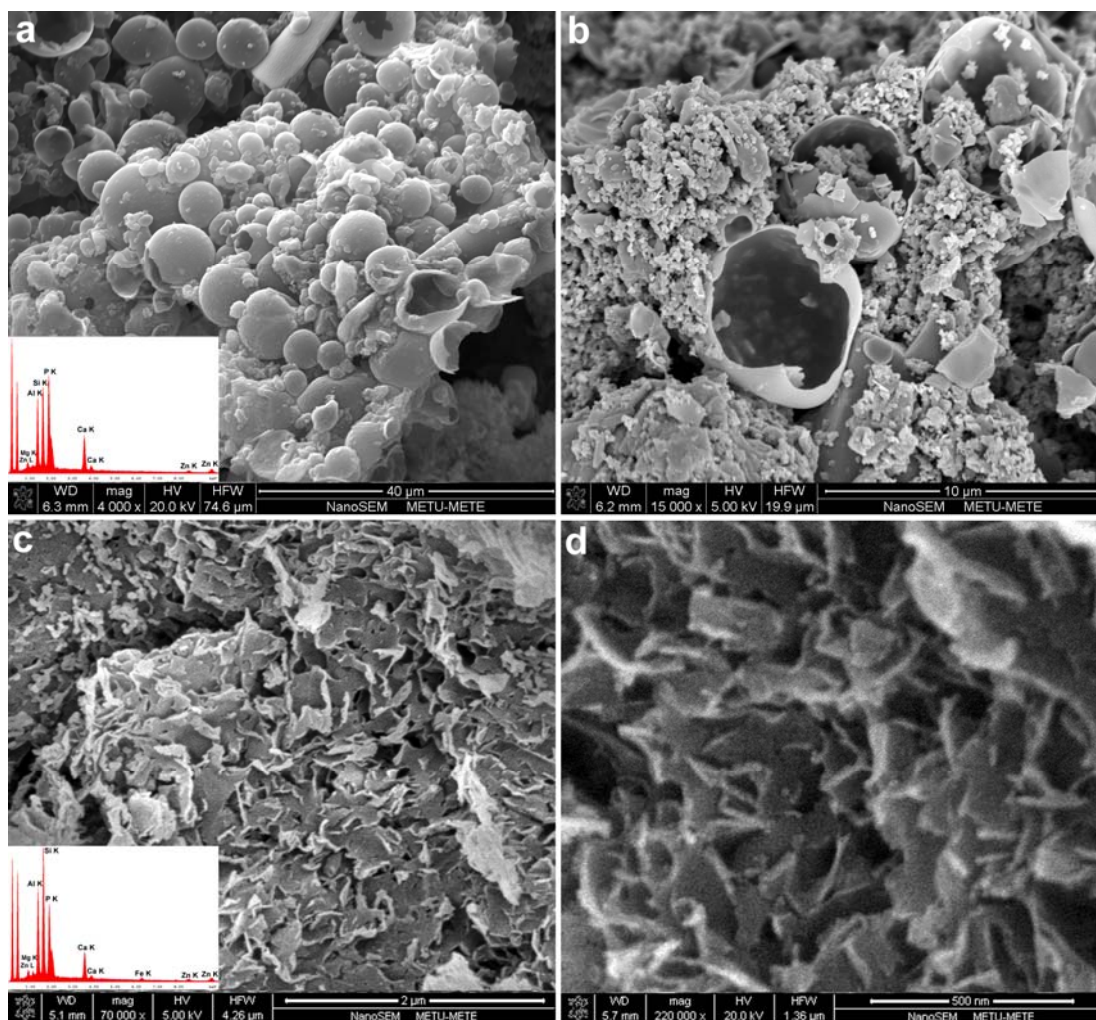


Figure 3.75 SEM images of mass loss calorimeter residues formed by combustion of (a-b) PA/GF-OP15 and (c-d) *n*-PA/GF-OP15

The macroscopic appearances of char residues serving as barriers during cone calorimetric fire tests are given in Figure 3.76 and also as SEM micrographs in Figure 3.77. Residue from PA6/OP20 displayed in Figure 3.77(a) shows intumescence. Figure 3.76 and Figure 3.77 show that the residue of *n*-PA6/GF possesses a loose structure suffering from major cracks. Residue from PA6/GF-OP15 possessed intumescent character with the carbonaceous char being thin and mechanically weak. It is clear that the residues were somewhat reinforced at the nano-scale shown in Figure 3.76(c-d) and Figure 3.77(d) and demonstrated more effective barrier properties against mass and heat transfer when compared to residues without the nanoclay shown in Figure 3.76(b) and Figure 3.77(c). Comparing Figure 3.76(c) and Figure 3.77(d) reveals that the structure of the barrier was improved with increasing flame retardant content associated with the larger basal spacing (or absence of basal spacing) of nanoclay in the residue. The strong nature of the chars formed from flame-retarded/glass fiber reinforced nanocomposites provides the significant improvements in flame retardancy as discussed above.

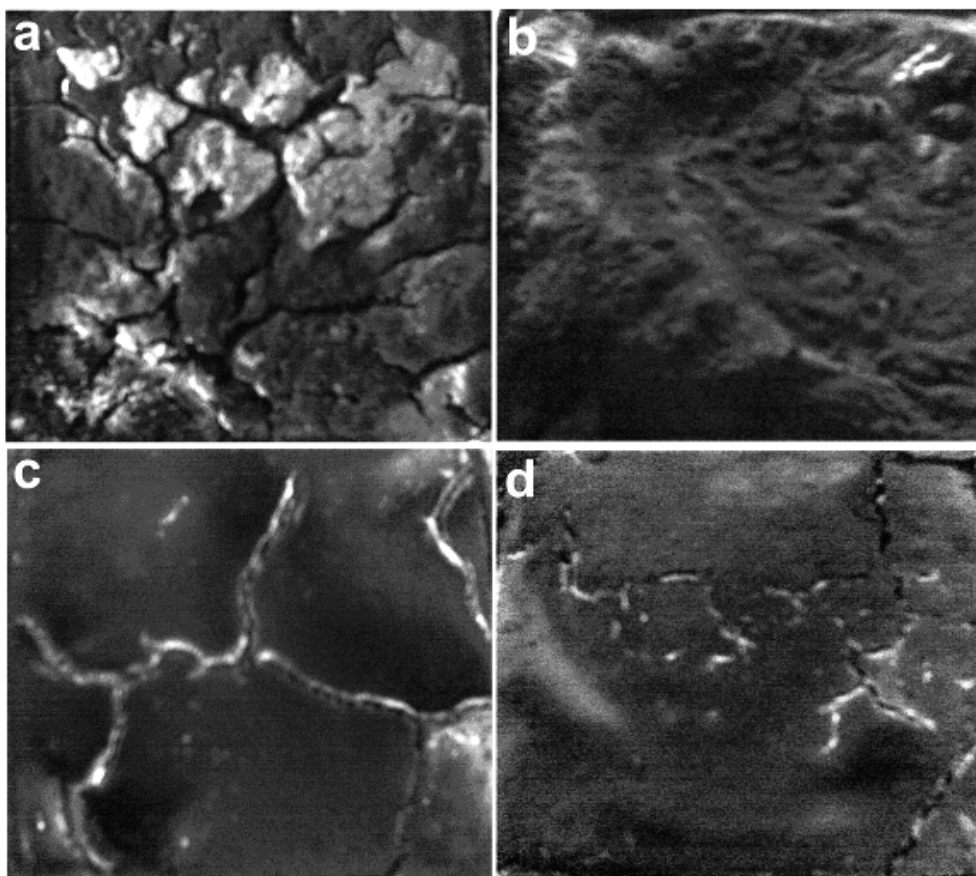


Figure 3.76 Macroscopic appearances of fire residues after mass loss calorimetry; (a) *n*-PA6/GF, (b) PA6/GF-OP15, (c) *n*-PA6/GF-OP5, and (d) *n*-PA/GF-OP15

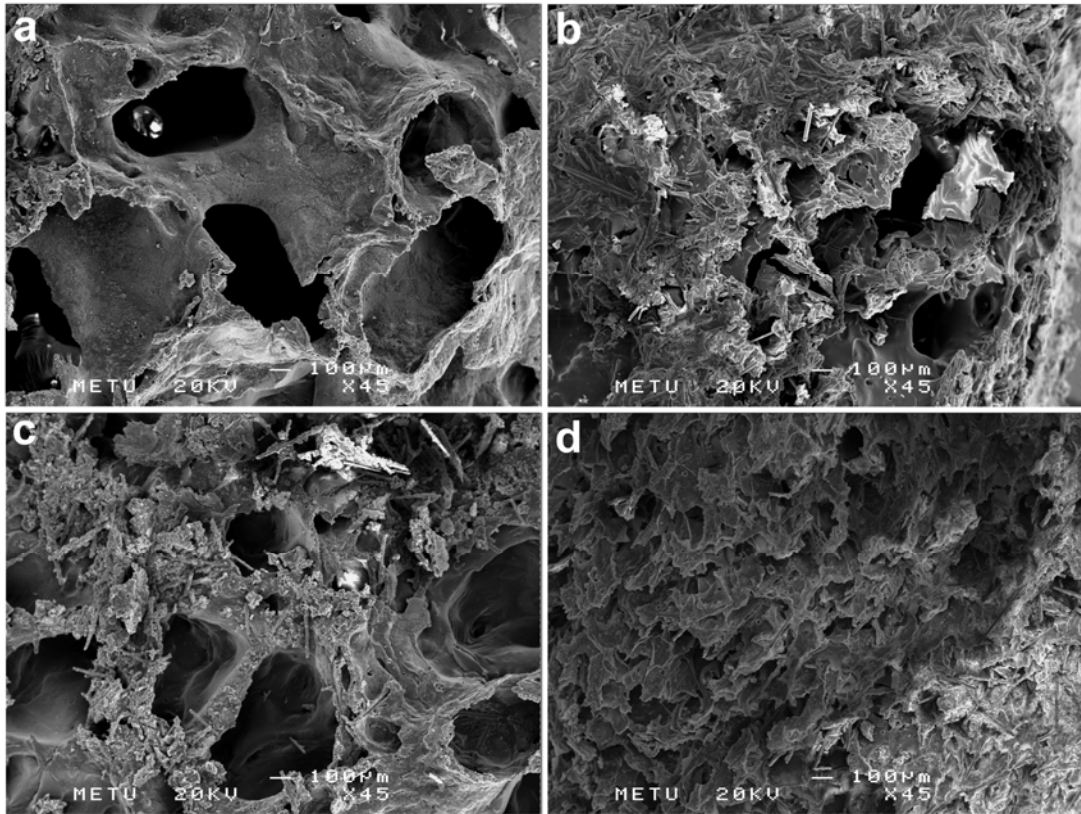


Figure 3.77 SEM micrographs displaying the fire residue morphologies of (a) PA6/OP20, (b) *n*-PA6/GF, (c) PA6/GF-OP15, and (d) *n*-PA6/GF-OP15

3.4.5 Mechanical Properties

Flame retardant additives are generally incompatible with the host polymer matrix resulting in discontinuities at particle/matrix interface, i.e. debonding (Figure 3.78). Strength of a particulate reinforced polymer is determined by the decreased effective cross-sectional area of load bearing polymer matrix. Consequently, there was a loss in tensile strength (σ) with the incorporation of OP flame retardant into neat PA6 as shown in Figure 3.79(a). In fact, decreasing tendency of strength in proportion to flame retardant content was observed for glass fiber reinforced PA6 (Figure 3.79b) and nanocomposites (Figure 3.79c). Additionally, the organophosphorus flame retardant used in the current study was also shown to deteriorate the apparent interfacial strength between glass fibers and matrix in the case of flame retarded/glass fiber reinforced PA6.

On the other hand, reinforcing fillers such as nanoclays and glass fibers provide effective strengthening as shown in Figure 3.79(a). Recalling the much lower volume fraction of nanoclays compared to that of short glass fibers, reinforcement at the nano-scale was much more effective than that at the micro-scale in terms of composite strength. This was attributed to an order of magnitude larger average aspect ratio of clays compared to short glass fibers. Additionally, the molecular level entanglements between polymer chains and nanoclays of very large surface area ensure highly efficient stress transfer from matrix to reinforcement. Substantial improvement in Young's modulus (E) was obtained especially with glass fiber reinforced PA6 nanocomposites in comparison to neat PA6.

Young's moduli were improved progressively with the incorporation of flame retardant additive aside from poor interfacial interactions as shown in Figure 3.79(b-c). At low strains encountered by the matrix in linear elastic region of modulus measurements, the mechanism of stress transfer at the particulate/matrix interface is inoperative. As a matter of fact, elastic modulus of a particulate reinforced composite was shown to be dictated by the volume fraction, particle size and stiffness of the filler whereas it is not noticeably affected by the interfacial strength between filler and matrix [141].

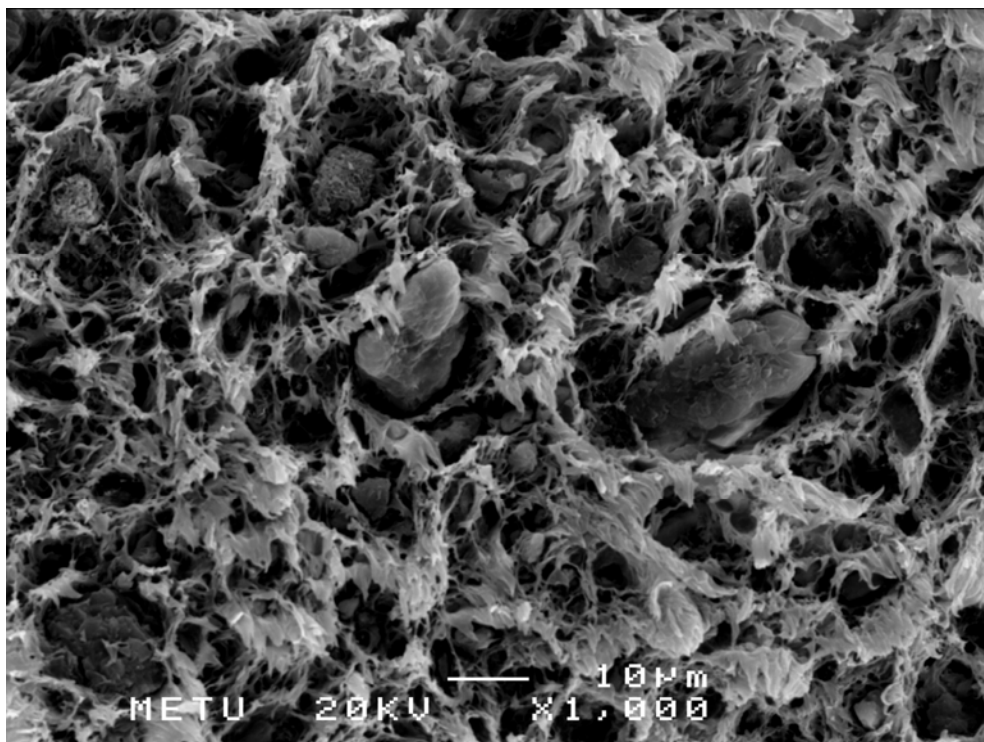


Figure 3.78 Debonding of flame retardant additive / polymer matrix interface as a consequence of poor adhesion

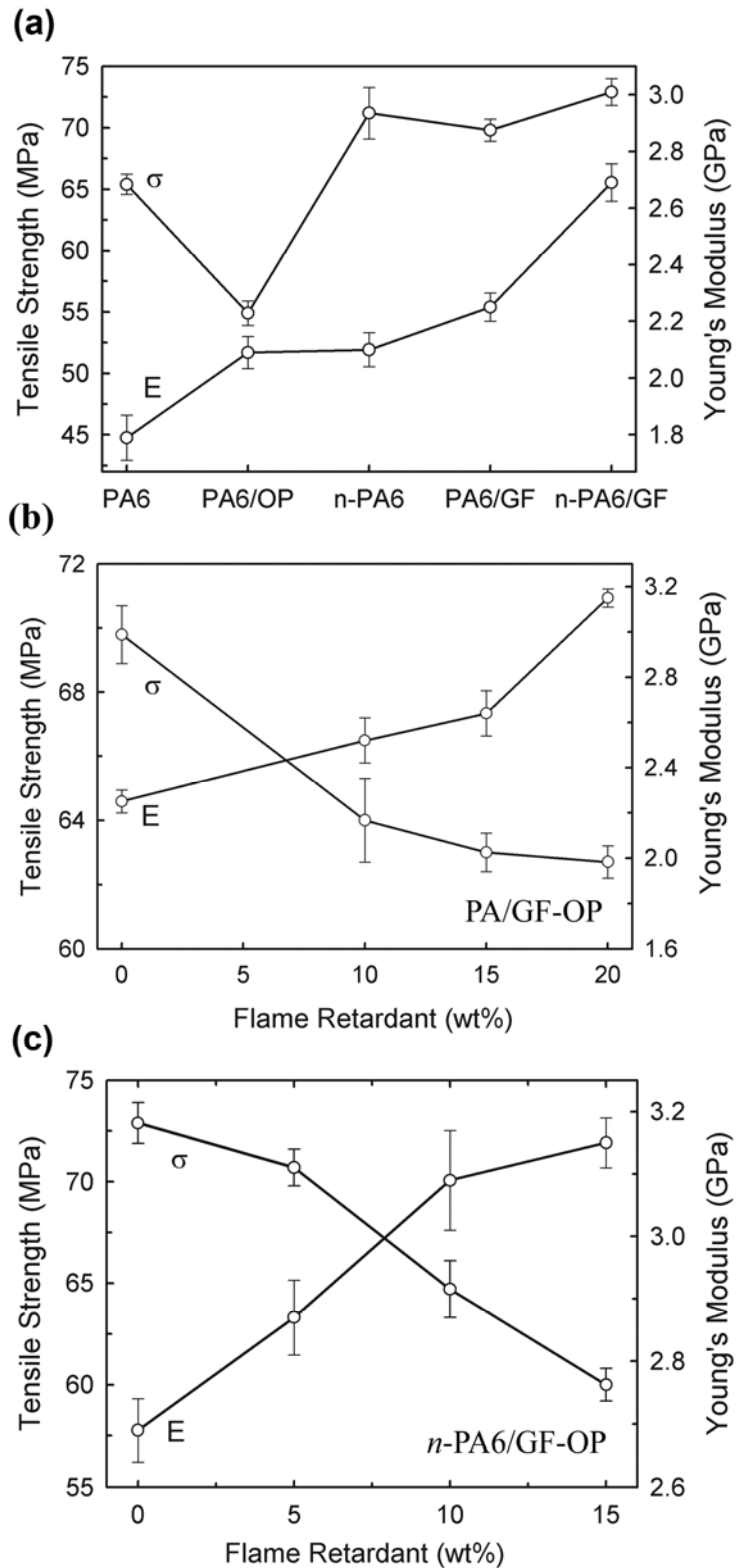


Figure 3.79 Mechanical properties of samples showing (a) the effect of GF, OP and nanofiller alone in the matrix, (b) the effect of OP content in GF reinforced PA6 composites, and (c) the effect of OP content in GF reinforced PA6 nanocomposites

3.5 INTERFACIAL INTERACTIONS

As an additional fifth purpose of this thesis, it was aimed to reveal the influence of nanofillers and flame retardant additives on fiber/matrix interfacial interactions. Firstly, an extension was developed to earlier theoretical micromechanics approach by Bader and Bowyer [142, 143] as a new continuum micromechanics model. Then, this model was evaluated for two experimental nanocomposite systems based on (i) short glass fiber reinforced amorphous matrix composites and (ii) short glass fiber reinforced semi-crystalline matrix composites. Both systems contained suitable flame retardant additives as micro-scale fillers and organically modified layered silicates as nano-scale fillers.

3.5.1 Micromechanical Modeling

The earlier work of Bowyer and Bader have shown that important micromechanical parameters, interfacial shear strength (τ), and fiber orientation distribution (FOD) efficiency, η_{FOD} , can be derived by simply utilizing the experimental stress–strain curves of polymer matrix and the composite together with the residual fiber length distribution (FLD) in the composite. The characterization of fiber length distribution has been the subject of detailed studies conducted by Fu et al. [144, 145].

Comprehensive work has recently been undertaken [146-149] on the realization of the developed method of Bowyer and Bader. In this thesis, emphasis is placed on developing and using a continuum micromechanics approach to derive the apparent interfacial strength and η_{FOD} in a more accurate manner compared to the original proposal and its follow-ups.

The strength of a composite material can be described in terms of the fraction and strength of constituent phases by the simple rule of mixtures approach having linear nature. However, several assumptions are made there to simplify the case which, in turn, cause the equation to be deficient in terms of representing the strength of real composites. The strengthening rate induced by the reinforcing fibers can be reduced via corresponding efficiencies associated with fiber length and orientation distributions. The fiber length distribution efficiency (η_{FLD}) arises from the shear lag analysis of Cox [150] which was followed by Kelly and Tyson's [151] proposal of critical fiber length concept and derivation of the average stress that can be transmitted from the matrix to a fiber of given length. Later, the concept was extended such that the critical fiber length is treated also as strain dependent aside from fiber strength, diameter and fiber/matrix interfacial shear strength [142, 143].

The modified rule of mixtures for short fiber reinforced composites which involves the effects of fiber length and orientation distributions on composite tensile strength can be written as a function of strain as:

$$\sigma_c(\varepsilon) = \eta_{\text{FOD}} \eta_{\text{FLD}}(\varepsilon) E_f \varepsilon V_f + \sigma_m(\varepsilon)(1 - V_f) \quad (1)$$

where $\sigma_c(\varepsilon)$ is the composite stress as a function of strain, η_{FOD} is the fiber orientation distribution factor, η_{FLD} is the fiber length distribution factor, E_f is the fiber tensile modulus, V_f is the volume fraction of fibers and $\sigma_m(\varepsilon)$ is the matrix stress as a function of strain.

The extension of the model by Kelly and Tyson to include the stress-strain relation for composites was developed by Bowyer and Bader and can be written as:

$$\sigma_c(\varepsilon) = \eta_{\text{FOD}} \left[\sum_i^{\ell_i < \ell_c} \frac{\tau}{d} \ell_i V_i + \sum_i^{\ell_i > \ell_c} E_f \varepsilon \left(1 - \frac{\ell_c}{2\ell_i} \right) V_i \right] + E_m \varepsilon (1 - V_f) \quad (2)$$

$$\ell_c = \frac{E_f \varepsilon d}{2\tau} \quad (3)$$

where ℓ_c is the critical fiber length, d is the fiber diameter, τ is the interfacial shear strength (IFSS) and E_m is the matrix tensile modulus.

The critical fiber length in Eq. (3) denotes the lower limit for the reinforcement to be stressed up to its highest load bearing capacity at the given strain. The fragmented form of experimental FLD is known to be well defined by a Weibull-type probability density function [145, 152-154] as denoted in Eq. (4). Accordingly, the discrete summations in Eq. (2) can be converted to integrals over all fiber lengths via introducing Eq. (4) into Eq. (2) yielding Eq. (5).

$$P_\ell = Kn\ell^{n-1}e^{-K\ell^n} d\ell \quad (4)$$

where P is probability, K is the scale parameter, n is the shape parameter and l is the fiber length.

$$\sigma_c(\varepsilon) = \eta_{\text{FOD}} Kn \left[\int_0^{\ell_c} \frac{\tau}{d} \ell^n e^{-K\ell^n} d\ell + \int_{\ell_c}^{\infty} E_f \varepsilon \left(1 - \frac{\ell_c}{2\ell}\right) \ell^{n-1} e^{-K\ell^n} d\ell \right] V_f + \sigma_m(\varepsilon)(1 - V_f) \quad (5)$$

When Eqs. (2) and (5) are compared, it can be seen that the contribution of matrix to the composite strength in Eq. (2) is converted to a non-linear function of ε ; $\sigma_m(\varepsilon)$, since the matrix or matrix components do not necessarily behave as Hookean solids. Then, considering Eqs. (1) and (5),

$$\begin{aligned} \eta_{\text{FLD}}(\varepsilon) &= \frac{Kn}{E_f \varepsilon} \left[\int_0^{\ell_c} \frac{\tau}{d} \ell^n e^{-K\ell^n} d\ell + \int_{\ell_c}^{\infty} E_f \varepsilon \left(1 - \frac{\ell_c}{2\ell}\right) \ell^{n-1} e^{-K\ell^n} d\ell \right] \\ &= \frac{Kn}{E_f \varepsilon} \left[\left(\frac{\tau}{d} \right) \frac{-n\ell e^{-K\ell^n} - \ell (K\ell^n)^{-1/n} \Gamma\left(\frac{1}{n}, K\ell^n\right)}{Kn^2} \Big|_0^{\ell_c} - \frac{E_f \varepsilon e^{-K\ell^n}}{Kn} \Big|_{\ell_c}^{\infty} - \frac{E_f \varepsilon \Gamma\left(1 - \frac{1}{n}, K\ell^n\right)}{2nK^{1-1/n}} \Big|_{\ell_c}^{\infty} \right] \quad (6) \end{aligned}$$

where $\Gamma(a)$ is the gamma function and $\Gamma(a, b)$ is the incomplete gamma function.

Since $\lim_{\ell \rightarrow \infty} \Gamma\left(1 - \frac{1}{n}, K\ell^n\right) = 0$, and $\lim_{\ell \rightarrow \infty} \left(e^{-K\ell^n}\right) = 0$, Equation 6 becomes;

$$\eta_{\text{FLD}}(\varepsilon) = \frac{\tau}{E_f \varepsilon d} \left[-\ell_c e^{-K\ell_c^n} - \frac{\Gamma\left(\frac{1}{n}, K\ell_c^n\right) - \Gamma\left(\frac{1}{n}\right)}{nK^{1/n}} \right] + e^{-K\ell_c^n} - \frac{\ell_c}{2} K^{1/n} \Gamma\left(1 - \frac{1}{n}, K\ell_c^n\right) \quad (7)$$

Following that a unified parameter which is readily useable in Eq. (1) can be proposed for fiber length distribution efficiency by using Eq. (3) as;

$$\eta_{\text{FLD}}(\varepsilon, K) = \frac{1}{2} \left[e^{-K\ell_c^n} - \frac{\Gamma\left(\frac{1}{n}, K\ell_c^n\right) - \Gamma\left(\frac{1}{n}\right)}{\ell_c n^{1/n} \sqrt{K}} - \ell_c \sqrt{K} \Gamma\left(1 - \frac{1}{n}, K\ell_c^n\right) \right] \quad (8)$$

Now that, since η_{FLD} is known as a function of applied strain, modified rule of mixtures (Eq. (1)) is rendered applicable. This approach allows modeling of the composite tensile strength as a function of strain at certain volume fraction of fibers possessing a pre-defined length distribution scaled by parameter K .

A simplistic approach to the problem of estimating τ is considering the limits of the composite's stress-strain curve. In the vicinity of unstrained condition, the constituent elements of a composite invariably attain Hookean solid nature which can be quantified by proportional limit moduli given as $E = \lim_{\varepsilon \rightarrow 0} \frac{d\sigma}{d\varepsilon}$. Consequently, as $\varepsilon \rightarrow 0$, the MROM in terms of moduli can be rearranged as:

$$\eta_{\text{FOD}} = \left[E_c - E_m (1 - V_f) \right] / \eta_{\text{FLD}} E_f V_f \quad (10)$$

It was discussed by Curtis et al. [155] that very low strains provide all the fibers to be sufficiently longer than the critical fiber length since such strain values yield very small critical fiber lengths regarding Eq. (3). This is algebraically validated by the proposed function of η_{FLD} in Eq. (8), through which the unstrained boundary condition provides $\lim_{\varepsilon \rightarrow 0} \eta_{\text{FLD}} = 1$. This is the result of the fact that shear-lag vanishes and the material resembles a misaligned continuous-fiber composite in such a case. Consequently, knowing all proportional limit moduli in Eq. (10), η_{FOD} can be calculated by setting η_{FLD} as unity. Now, one can move on to the failure (or yield) boundary condition where Eq. (1) can be rearranged as:

$$\eta_{\text{FLD}}^{\text{b}} = \left[\sigma_{\text{c}}^{\text{b}} - \sigma_{\text{m}}^{\text{b}} (1 - V_{\text{f}}) \right] / \eta_{\text{FOD}} E_{\text{f}} \varepsilon_{\text{b}} V_{\text{f}} \quad (11)$$

Having calculated η_{FOD} , Eq. (11) can be used to calculate η_{FLD} at the strain of break; *i.e.* $\eta_{\text{FLD}}^{\text{b}}$. Finally, knowing $\eta_{\text{FLD}}^{\text{b}}$ allows Eq. (8) to be solved iteratively to estimate $\ell_{\text{c}}^{\text{b}}$ and interfacial strength.

$$\ell_{\text{c}}^{\text{b}} = \frac{E_{\text{f}} \varepsilon_{\text{b}} d}{2\tau} \quad (12)$$

The relation for η_{FOD} in Eq. (10) can be inserted into Eq. (11) since η_{FOD} is assumed to be strain independent. Then the equation for $\eta_{\text{FLD}}^{\text{b}}$ becomes:

$$\eta_{\text{FLD}}^{\text{b}} = \left[\sigma_{\text{c}}^{\text{b}} - \sigma_{\text{m}}^{\text{b}} (1 - V_{\text{f}}) \right] / \left[(E_{\text{c}} - E_{\text{m}} (1 - V_{\text{f}})) \varepsilon_{\text{b}} \right] \quad (13)$$

Eq. (13) will enable us to proceed with provision of a graphical interpretation instead of the mentioned iterative solution to estimate τ . A simple construction and utilization of a chart enables direct interpretation of τ without the need for an iterative solution. By using Eqs. (8) and (13), one can construct the diagram given in Figure 3.80. Subsequently, by simply utilizing tension test data in combination with the determined residueal fiber length distributions represented by scale parameter K ,

one may obtain ℓ_c^b and corresponding interfacial strength on the vertical axis of the chart.

As it is depicted in Figure 3.80, less fiber breakage during production (lower K values) allows higher η_{FLD} to be attained at a given critical fiber length; and the dependence of η_{FLD} on interfacial shear strength is less pronounced when compared to that at increased fiber breakage (higher K values). For instance, corresponding doubling of ℓ_c^b (from 500 to 1000 μm) by halving the interfacial shear strength will generate ~ 55 , 45, and 25 % losses in η_{FLD} , at K values of 10^{-6} , 10^{-7} and 10^{-8} , respectively. A process design yielding the lowest fiber length reduction will produce composites which are more tolerant to alterations in interfacial shear strength between the matrix and reinforcing fibers.

Figure 3.80 is a universal chart which can be employed for interfacial shear strength estimation in any fiber/matrix combination. A wide range of K values (10^{-9} to 10^{-5}) has been considered to represent both extensive and insignificant fiber length reduction cases. Moreover, broad critical fiber length interval has been used to construct the chart which provides representation of a wide range of interfacial shear strength, composite strain at break, fiber modulus and diameter.

Based on the chart provided in Figure 3.80, trends regarding the critical fiber length, fiber length degradation, fiber length efficiency or interfacial shear strength observed by varying glass fiber content, polymer blend composition, extrusion processing conditions, and, presence of micro-fillers and nano-fillers were followed using the design chart. Figure 3.81 is a compilation of results of those studies.

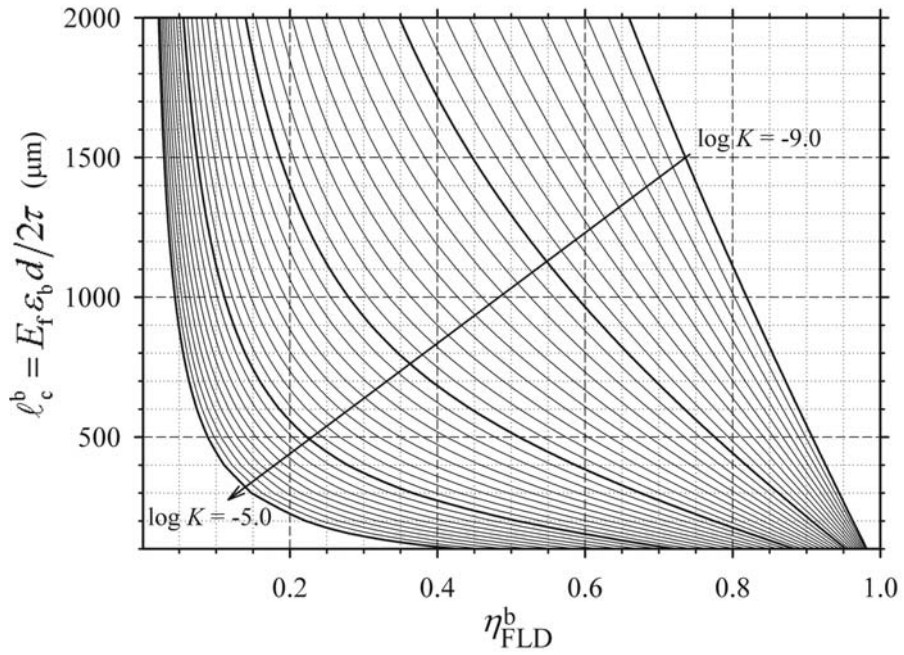


Figure 3.80 Chart for graphical interpretation of interfacial shear strength

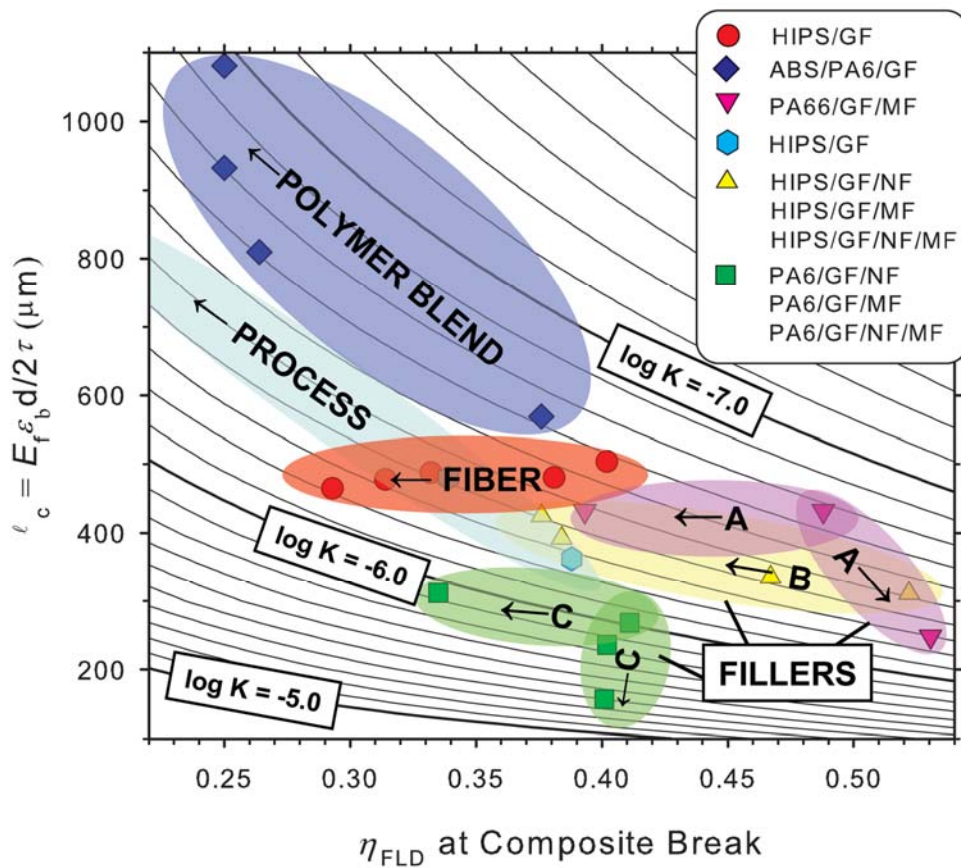


Figure 3.81 Compilation of interfacial shear strength estimations of experimental short glass fiber reinforced composite systems

3.5.2 Short Fiber Reinforced Amorphous Matrix Nanocomposites

Presence of fibers and fillers may have a significant influence on the physical properties of polymer matrix. A change in the conformational state is induced through geometrical hindrance or favorable interactions between polymer and filler surfaces. End-tethering can occur when polymer end-groups strongly interact or form covalent bonds with the reactive groups on filler/fiber surfaces. Crystallinity can be imposed by forced alignment on flat, impenetrable filler walls which considerably restricts conformational degree of freedom of polymer chains. In addition, varying fiber and/or filler content can alter the overall thermal conductivity, which may induce different proportions of polymer polymorphs in matrix. This is a particular problem if one needs to ideally investigate the influence of fiber content on fiber/matrix interface, since matrix components become dissimilar in every different composition.

However, with an amorphous polymer matrix such as high-impact polystyrene, property alterations can be conveniently minimized since it does not show considerable enthalpic interactions with the utilized silane-treated glass fibers. Moreover, it shows no stereoregularity meaning it is non-crystallizable; thus, fiber content has no practical effect on matrix morphology. Consequently, one major component of interfacial shear strength can be related to the radial compressive stress (through narrowing down the fiber-matrix contact zone and promoting frictional resistance to shear) developing from the thermal expansion mismatch of the host polymer and fiber during post-processing.

(i) Effect of Fiber Reinforcement

The micromechanical model developed in this thesis was first experimentally evaluated by exploring the effect of short glass fibers (GF) with different loading levels (10, 20, 30, 40 and 50 wt%) in high-impact polystyrene (HIPS) amorphous matrix.

Figure 3.82(a) shows cumulative fiber length distribution curves for short glass fiber reinforced high-impact polystyrene (HIPS/GF) composites with varying glass fiber contents. Distributions are shifted progressively to shorter lengths with larger volume fraction (V_f) of reinforcing fibers arising from the increased probability of attrition contacts. The variation of the scale parameter K with fiber content is essentially linear, as shown in the inset of Figure 3.82(a), provided that processing conditions are kept constant. Besides, changes in compounding conditions and accompanying degradation in fiber lengths are also well-represented with the scaling parameter, K , as plotted in Figure 3.82(b) for varying extrusion screw speed.

Figure 3.83(a) shows that interfacial strength values determined for HIPS/GF system were independent of fiber content and reflect the shear yield strength of HIPS, the reason for which is that matrix morphology, interface chemistry and the thermal contraction of chains in the close vicinity of fiber surfaces are not affected by the increasing fiber content. HIPS is an amorphous polymer containing dispersed second phase rubber particles; thus, it possesses two glass transitions, higher temperature one being around 115°C and lower being considerably below zero around -80°C. It contains dispersed second phase rubber particles, and this rubber phase induces significant reduction in rigidity below the glass transition for polystyrene, which allows the relaxation of axial or radial residual stresses on fibers during cooling regardless of fiber content.

It can be generalized that variations in interfacial strength in composite systems can be qualitatively followed from SEM micrographs by critically observing the fiber-polymer interfacial regions, as given in Figure 3.84 for the HIPS/GF system. No significant change can be seen in the micrographs of composites with varying fiber contents, fibers being surrounded by dark rings for all fiber loading levels. This means that during the transfer of applied stress to the fiber, interface failure (debonding) has occurred prior to composite failure at all fiber contents.

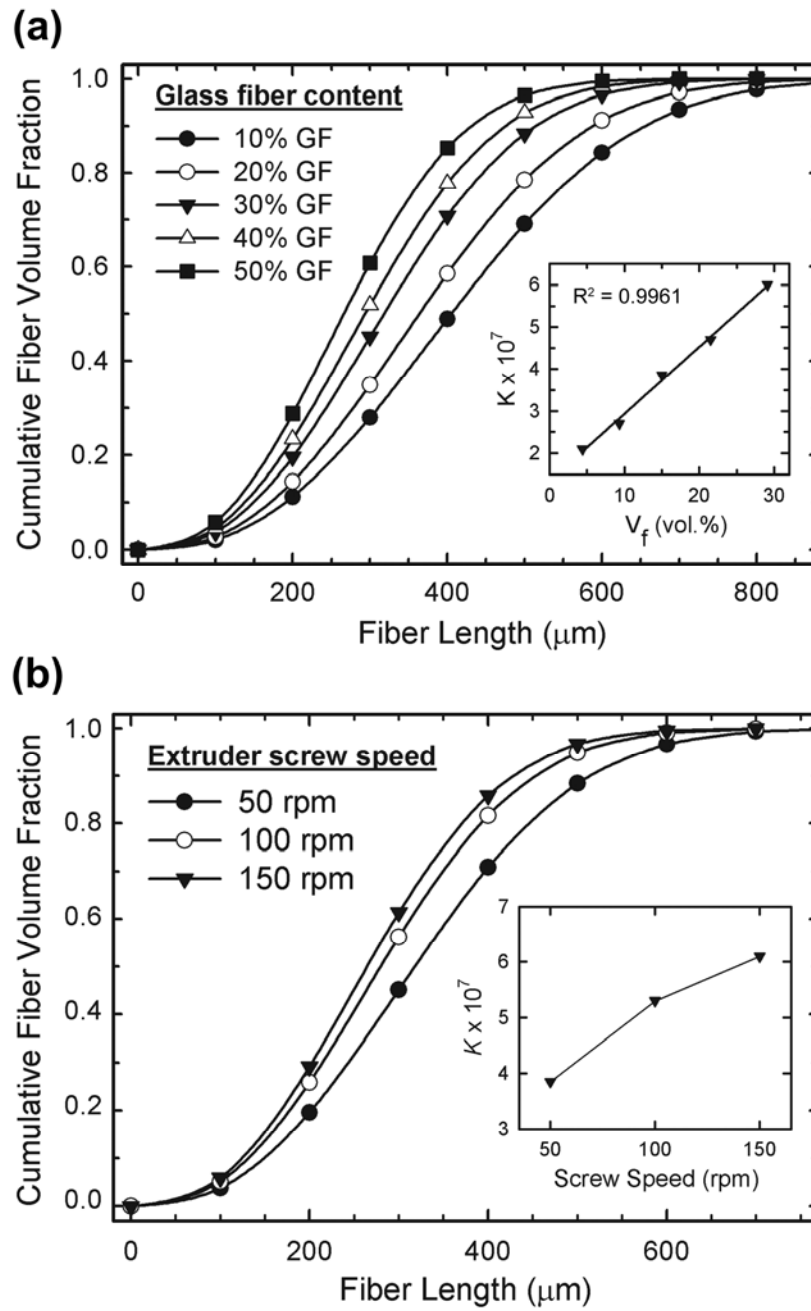


Figure 3.82 Variation of fiber length distribution in HIPS/GF composites with (a) fiber content, and, (b) screw speed in extrusion

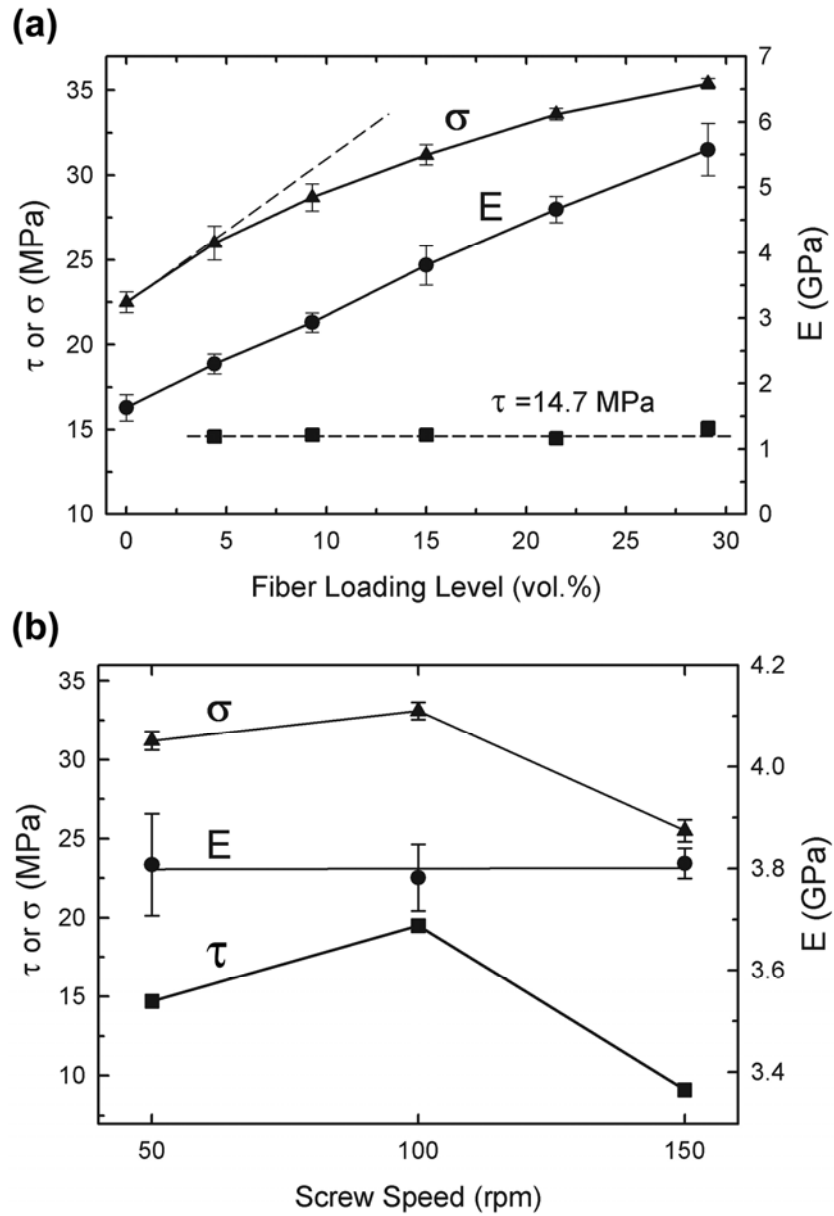


Figure 3.83 Variation of composite tensile strength (σ), interfacial shear strength (τ) and Young's modulus (E) of HIPS/GF composites with (a) fiber volume fraction and (b) screw speed in extrusion

Regarding the processing conditions examined at $V_f = 0.15$ in Figure 3.83(b), an optimum in respect of interfacial shear strength and tensile strength is found which ensures good wetting and provides homogenous dispersion. There appears to be a compromise between fiber-breakage (increase in K) and extent of good wetting/mixing as the extrusion screw speed is increased, revealing the observed optimum.

Since chemical effects are minimized, the experimentally evidenced loss in strengthening rate (non-linear increase in composite strength) with increasing fiber content in HIPS/GF system (Figure 3.83a)) is mainly related to load transfer efficiency and can be modeled with the employed micromechanics approach which involves two efficiency parameters accounting for fiber length and orientation effects

Fiber length distribution efficiency can be continuously investigated as a function of applied strain as illustrated in Figure 3.85(a). These are plotted according to Eq. (8) by considering the interfacial strength and K values for each composite sample. Curves start from unity meaning that all fibers are longer than the critical fiber length for an initial infinitesimal strain. As strain develops, ℓ_c increases linearly according to $\ell_c = E_f \varepsilon d (2\tau)^{-1}$, and η_{FLD} decreases in the nonlinear form dictated by Eq. (8).

It can be inferred from Figure 3.85(b) that the experimental stress-strain responses of composites are well-reproduced by theoretical micromechanics approach with determined interfacial strength, K and η_{FOD} values. The nonlinear nature of these stress-strain curves originates from the combination of loss in fiber length efficiency with strain in Figure 3.85(a) and nonlinear contribution of the thermoplastic matrix itself.

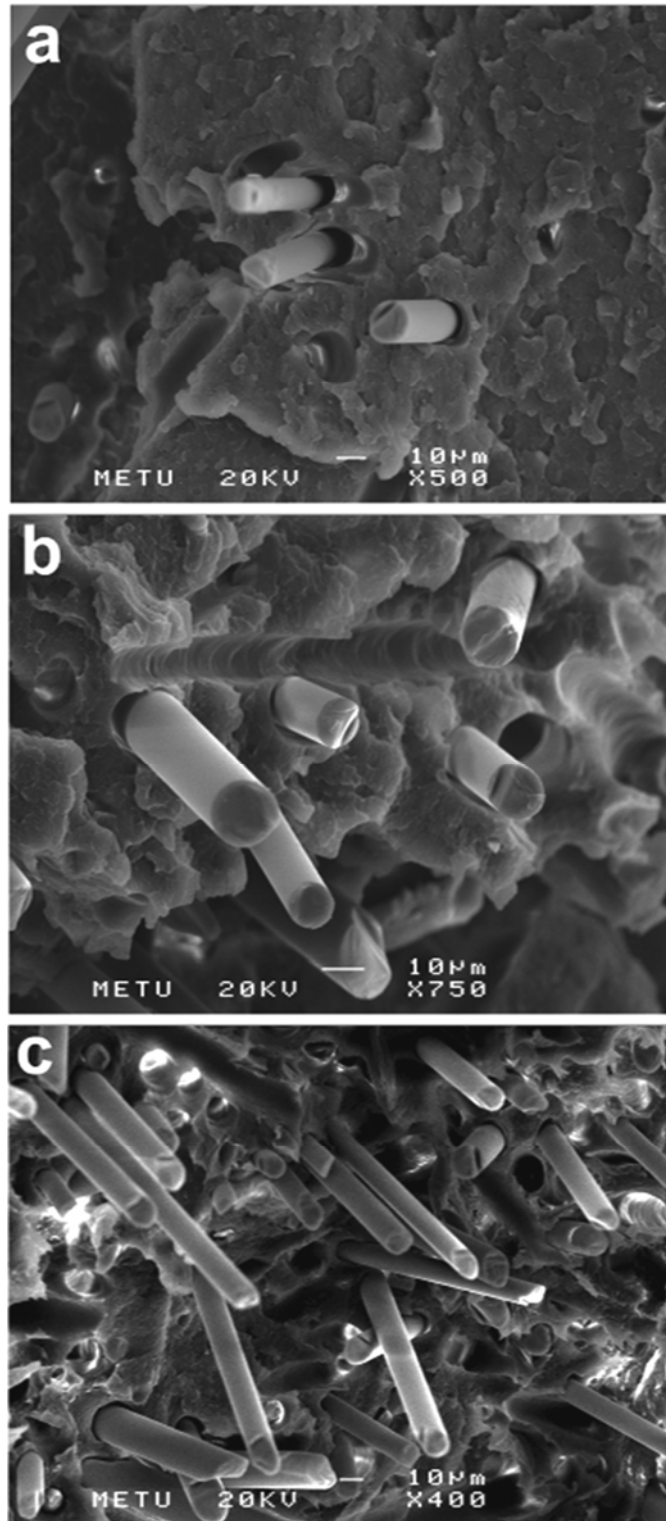


Figure 3.84 SEM images of fracture surfaces of HIPS/GF composites with short glass fiber contents of (a) 10 wt%, (b) 30 wt%, and, (c) 50 wt%

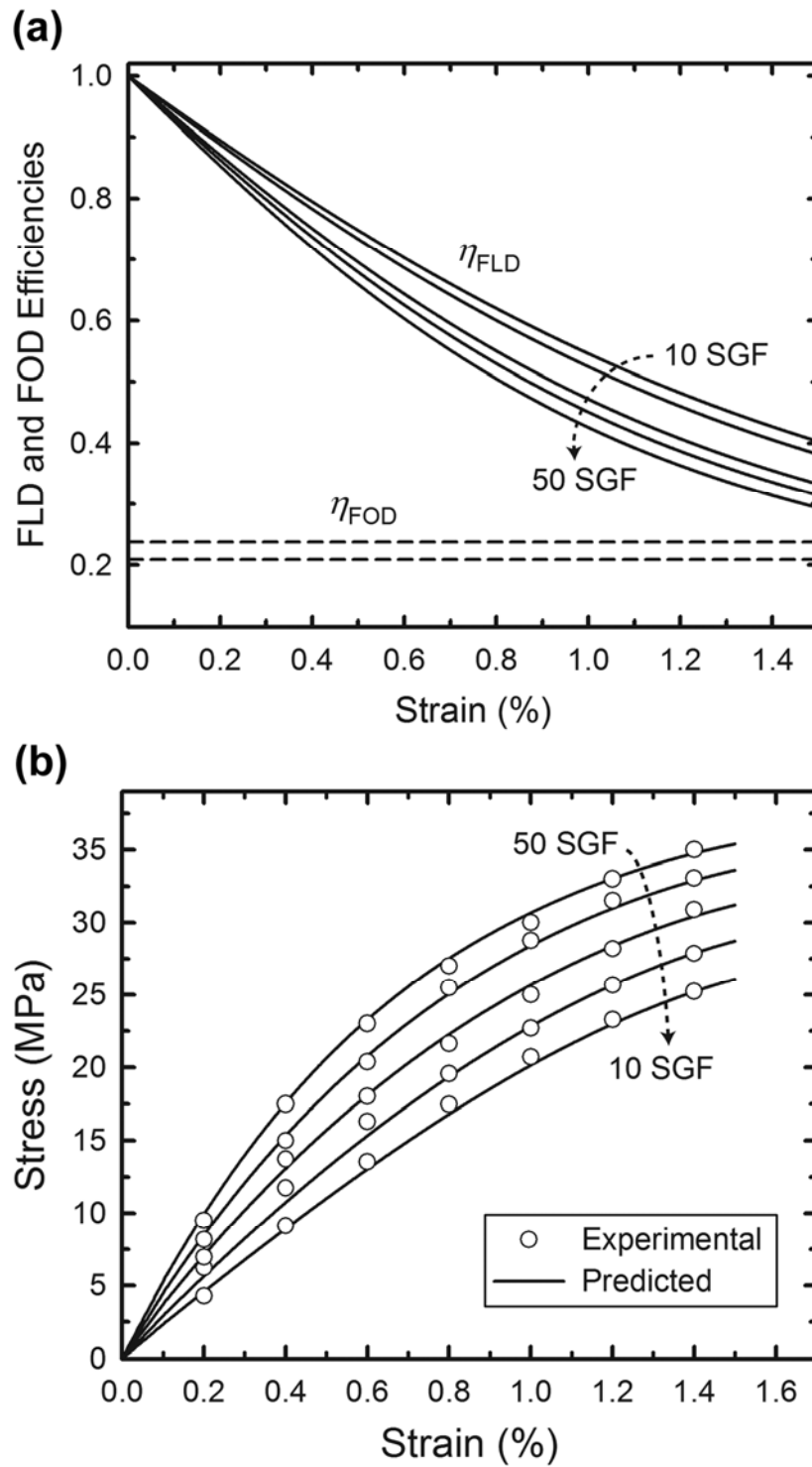


Figure 3.85 (a) η_{FLD} and η_{FOD} vs. strain, and, (b) experimental and predicted stress vs. strain curves of HIPS/GF composites

(ii) Effect of Nanofiller and Flame Retardant Additive

In the previous section, the micromechanical model was experimentally evaluated for HIPS/GF composites with various fiber loading levels, where properties of the matrix (such as morphology, thermal expansion, mechanical behavior etc.) were held almost fixed. This allowed trends observed in apparent interfacial shear strength to be directly attributed to micromechanical parameters and interfacial shear strength turned out to be independent of fiber volume fraction. Now, in this section, the effects of altering properties of the matrix polymer (without crystallization) at different length scales with micro- and/or nano-fillers on the fiber/matrix interface are discussed. Table 3.22 lists the designations and compositions of investigated materials.

Table 3.22 Designation and compositions (wt.%) of studied materials to reveal the influence of micro- and nano-fillers on interfacial interactions

	HIPS	Glass Fiber (GF)	Micro-filler (MF)	Nano-filler (NF)
HIPS	100	-	-	-
HIPS/MF	85	-	15	-
HIPS/NF	97	-	-	3
HIPS/MF/NF	82	-	15	3
HIPS/GF	80	20	-	-
+MF	65	20	15	-
+NF	77	20	-	3
+MF/NF	62	20	15	3

GF: silane treated short glass fiber

MF: aluminum tri-hydroxide flame retardant additive

NF: Cloisite 10A organically modified montmorillonite clay

Besides the main fiber-fiber attrition, introduction of MF and/or NF into the extruder results in fiber-filler attritions and increased melt viscosity during production. These can easily induce larger K values as shown in Figure 3.86(a). Although MF loading is much larger than that of NF, the latter induced nearly the same degradation in fiber lengths relative to the reference HIPS/GF. This may be due to the higher potential of NF to influence melt viscosity and more severe attrition effect of finely dispersed NF on fiber surfaces during processing. Introduction of MF and NF together brings about a cumulative effect and causes further shifting of the FLD to shorter lengths, as expected.

Although MF results in fiber breakage to nearly the same extent as NF, it has no significant effect on interfacial shear strength (IFSS) (Figure 3.86b). Accordingly, tensile strength of +MF hybrid composite slightly increases due to the gain in stiffness relative to HIPS/GF. However, NF modification reduces the IFSS and composite strength. The recovery of composite modulus and the slight increase of IFSS in +MF/NF addition with respect to +NF compensate the extensive K increase and yield a slight recovery in composite strength. The probability of micron-sized particles to locate in the vicinity of a fiber/matrix interface is relatively low due to large expected filler-fiber spacings. However, in the case of NF, due to dispersion of clay aggregates into finer crystallites upon melt-processing as shown by the TEM image in Figure 3.87, the effect of NF on fiber/matrix interfacial zone can be more pronounced than that of MF.

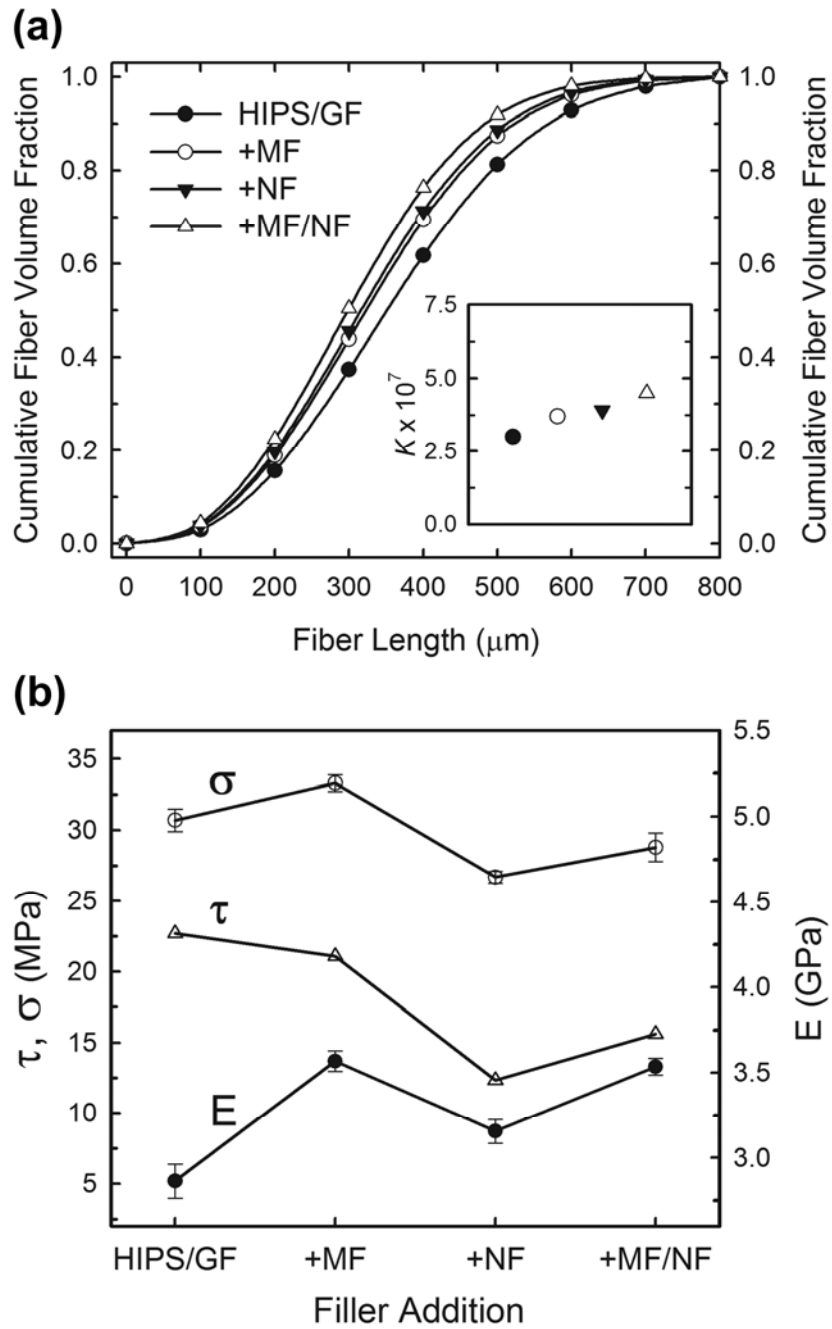


Figure 3.86 Variation of (a) fiber length distribution, and, (b) tensile strength, interfacial shear strength and Young's modulus of micro-filler (+MF), nano-filler (+NF) and micro + nano-filler (+MF/NF) modified HIPS/GF composites

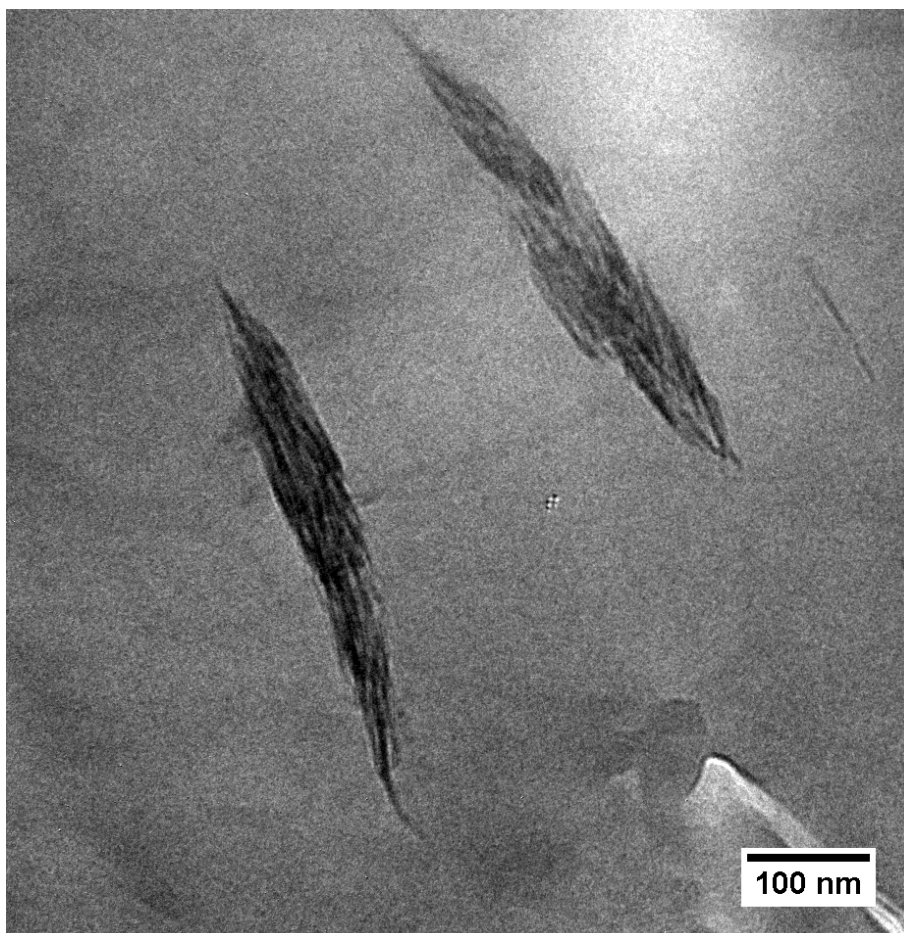


Figure 3.87 TEM micrograph of HIPS/clay composite showing coarse clay aggregates

Since NF is able to be located in the vicinity of fiber/matrix interfaces as well as in the bulk of the matrix, it can be postulated that considerable alteration of polymer matrix properties at the interfacial zone are expected which might be the cause of decreased IFSS. One explanation could be the thermal contraction of polymer chains in close vicinity of fiber/matrix interface being restricted in the presence of NF as a result of decreased thermal expansion coefficient. The presence of finely dispersed nano-fillers with large aspect ratio, high modulus, and low thermal expansion coefficient is known to significantly decrease the linear thermal expansion coefficient of thermoplastic polymer matrices even at very low loading levels. This would greatly reduce the thermal residual stresses developing during post-processing due to thermal expansion coefficient mismatch between ceramic fibers and polymer matrix and could directly show up as lowered apparent IFSS.

Comparing Figure 3.88(a) and Figure 3.88(b), it can be seen that there exists no significant influence of micro-filler on matrix morphology, while introduction of nano-filler (with or without micro-filler in Figure 3.88(c) and (d), respectively) alters the matrix morphology significantly near fibers, resulting in more severe fiber/matrix debonding upon loading. To sum up, reduced tensile strength in the presence of NF is due to the combination of effects of NF on fiber lengths, IFSS and especially the physical properties of polymer matrix.

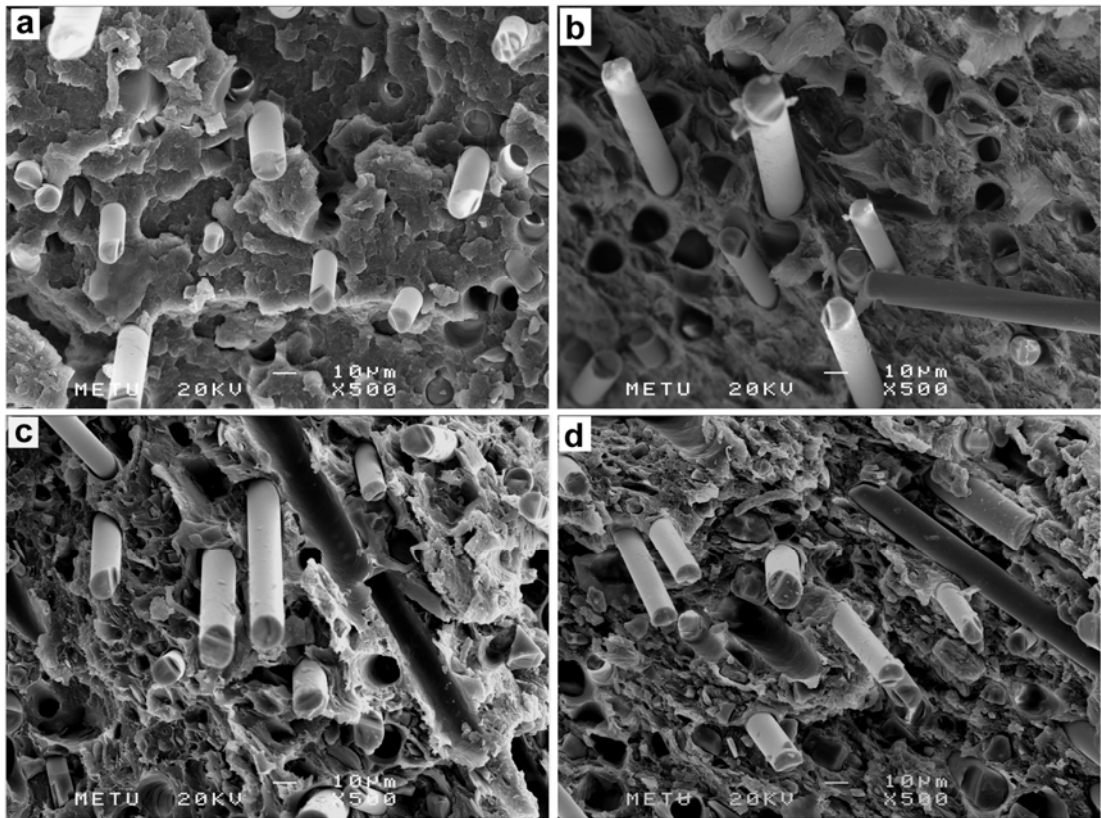


Figure 3.88 SEM images of fracture surfaces of (a) HIPS/GF, (b) +MF, (c) +NF and (d) +MF/NF composites, showing the direct correspondence of estimated interfacial shear strength values and fracture morphology of interfacial zones

3.5.3 Short Fiber Reinforced Semi-Crystalline Matrix Nanocomposites

Progress has recently been made on the concept of continuous fiber composites in which the matrix is a nanocomposite, often being an epoxy-clay nanocomposite [156-159] except a few studies with polyamide-6 by Vlasveld et al. [160, 161]. Influence of nanoclay in a continuous fiber composite is usually on properties dominated by matrix or fiber/matrix interface such as compressive strength, flexural strength, transverse tensile strength and in-plane shear strength.

So far, fiber/matrix interface of a fiber reinforced thermoplastic composite with nanocomposite matrix was investigated in a single study [162]. The fiber/matrix interface, assessed by single fiber fragmentation tests, was found to be degraded with the incorporation of nanoclay which was related to poor fiber wetting. Earlier work on the use of nanoclays and short fibers together as reinforcements in thermoplastic matrices is limited to a few studies [163, 164]. In particular, there seems to be no publications concerned with the effect of nanoclay on the interfacial properties of a short glass fiber reinforced polymer composite.

Thus, in this section, exfoliated clay nanocomposites of flame retarded/glass fiber reinforced polyamide-6 (PA6/GF) were prepared aiming to strengthen the fiber/matrix interfacial shear strength. Designations and compositions of studied materials are listed in Table 3.23. Nano-filler dispersion was examined by TEM. Degree of polymer crystallinity and relative amounts of crystalline species in molded specimens were determined by XRD. Then, the micromechanical model developed in this thesis was evaluated experimentally for PA6/GF composites.

Table 3.23 Designations and compositions (wt.%) of studied materials

	Polyamide-6 (PA6)	Glass Fiber (GF)	Micro-filler (MF)	Nano-filler (NF)
PA6/GF	85	15	-	-
PA6/MF	85	-	15	-
PA6/NF	95	-	-	5
PA6/MF/NF	80	-	15	5
+MF	70	15	15	-
+NF	80	15	-	5
+MF/NF	65	15	15	5

GF: silane treated short glass fiber

MF: organophosphorus flame retardant additive

NF: Cloisite 30B organically modified montmorillonite clay

TEM micrograph given in Figure 3.89 shows that silicate platelets are homogeneously distributed as individual nanometer size reinforcing fillers in PA6/organoclay nanocomposites. Polymer intercalation into clay galleries and subsequent clay layer exfoliation are strongly favored during high-shear extrusion processing. The key factors in achieving complete layer exfoliation are effective polar and hydrogen bonding interactions between PA6 chains and clay organic surface modifier [126].

In extrusion compounding, glass fibers cannot retain their initial lengths and are continuously broken into a distribution of lengths as a consequence of fiber surface attrition through fiber-fiber, fiber-filler and fiber-machine interactions. Larger attrition effect of the nano-filler is clear from Figure 3.90 compared to the micro-filler despite the significantly lower loading level of the former in matrix. This can be attributed to nano-scale dispersion in the case of exfoliated nanocomposite morphologies which increases the probability of fiber-filler interactions during extrusion compounding. Intense fiber length reduction in +MF/NF nanocomposite is associated with the combined effects of fiber-filler interactions and significant deterioration of the melt flow behavior at large filler loading.

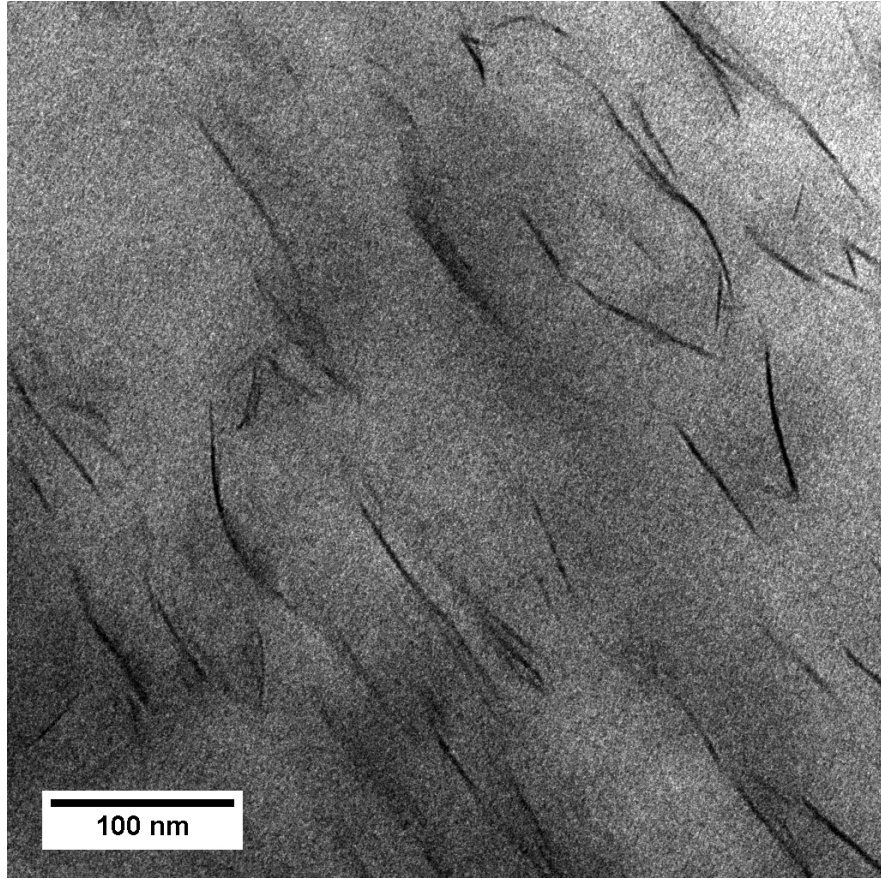


Figure 3.89 TEM micrograph of PA6/organoclay nanocomposite

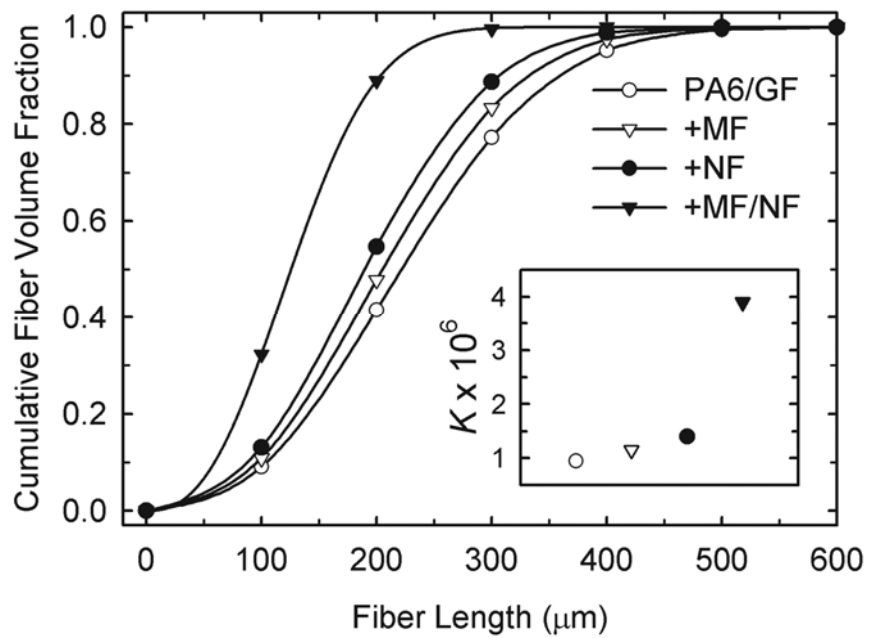


Figure 3.90 Fiber length distributions in short glass fiber reinforced PA6/organoclay nanocomposites

The chart given in Figure 3.91 illustrates the graphical interpretation of the critical fiber length and interfacial shear strength from known fiber length distributions and tensile properties. Table 3.24 contains the estimated fiber length efficiency, critical fiber length and most importantly the fiber/matrix interfacial strength of the investigated composites. It is seen that fiber length efficiency is similar for PA6/GF and +NF composites despite the shorter fibers in +NF. This is provided by lower critical fiber length and enhanced interfacial strength in the presence of the nano-filler.

The incorporation of the micro-filler lowers the fiber length efficiency to a considerable extent which is mainly attributed to the increased critical fiber length associated with degraded interface. Interestingly, fiber length efficiency is recovered in presence of the nano-filler in +MF/NF nanocomposite despite the notable reduction in fiber lengths. In other words, the critical fiber length is reduced and strengthening of the fiber/matrix interface takes place by the act of nano-filler in +MF/NF nanocomposite.

Figure 3.92 displays the fracture morphologies of PA6/GF and +NF composites being direct evidences of strong interfaces through absence of debonding, which validates the large interfacial strength values estimated above (Table 3.24). This is attributed to favorable energetic interactions between PA6 chains and aminosilane treated short glass fibers. Moreover, it was shown by Cartledge and Baillie [165] that the induced transcrystallinity in presence of glass fibers may have a positive contribution to fiber/matrix interface in PA6/GF composites. It is clear that the nano-filler has no significant influence on fiber/matrix.

Failure of the fiber/matrix interface in the form of debonding is depicted in Figure 3.93(a) for +MF composites. On the other hand, contrary to the case with +MF composite, fracture morphology of +MF/NF nanocomposite (Figure 3.93b) resembles those of PA6/GF and +NF composites (Figure 3.92) with regards to fiber/matrix interface, i.e. no remarkable interfacial debonding. In short, nanoclay assisted interfacial strength improvement deduced from the micromechanical estimation is confirmed by fracture surface morphologies.

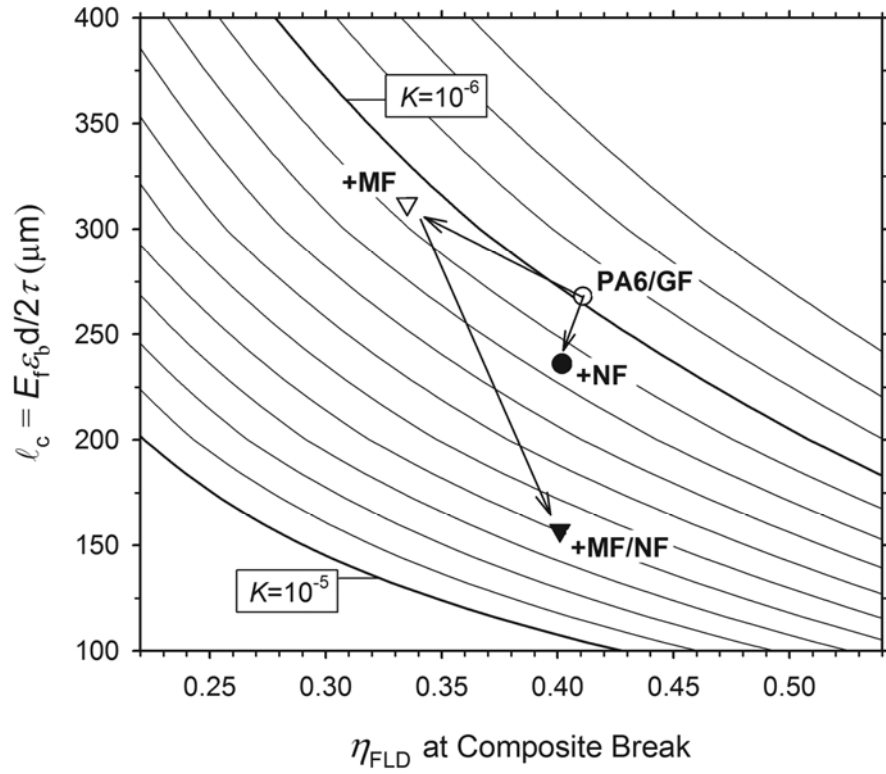


Figure 3.91 Graphical interpretation of critical fiber length and interfacial shear strength of investigated composites

Table 3.24 Estimated micromechanical parameters

	IFSS (MPa)	l_c (μm)	η_{FLD}^b
PA6/GF	83	268	0.411
+NF	86	236	0.402
+MF	62	312	0.335
+MF/NF	88	157	0.401

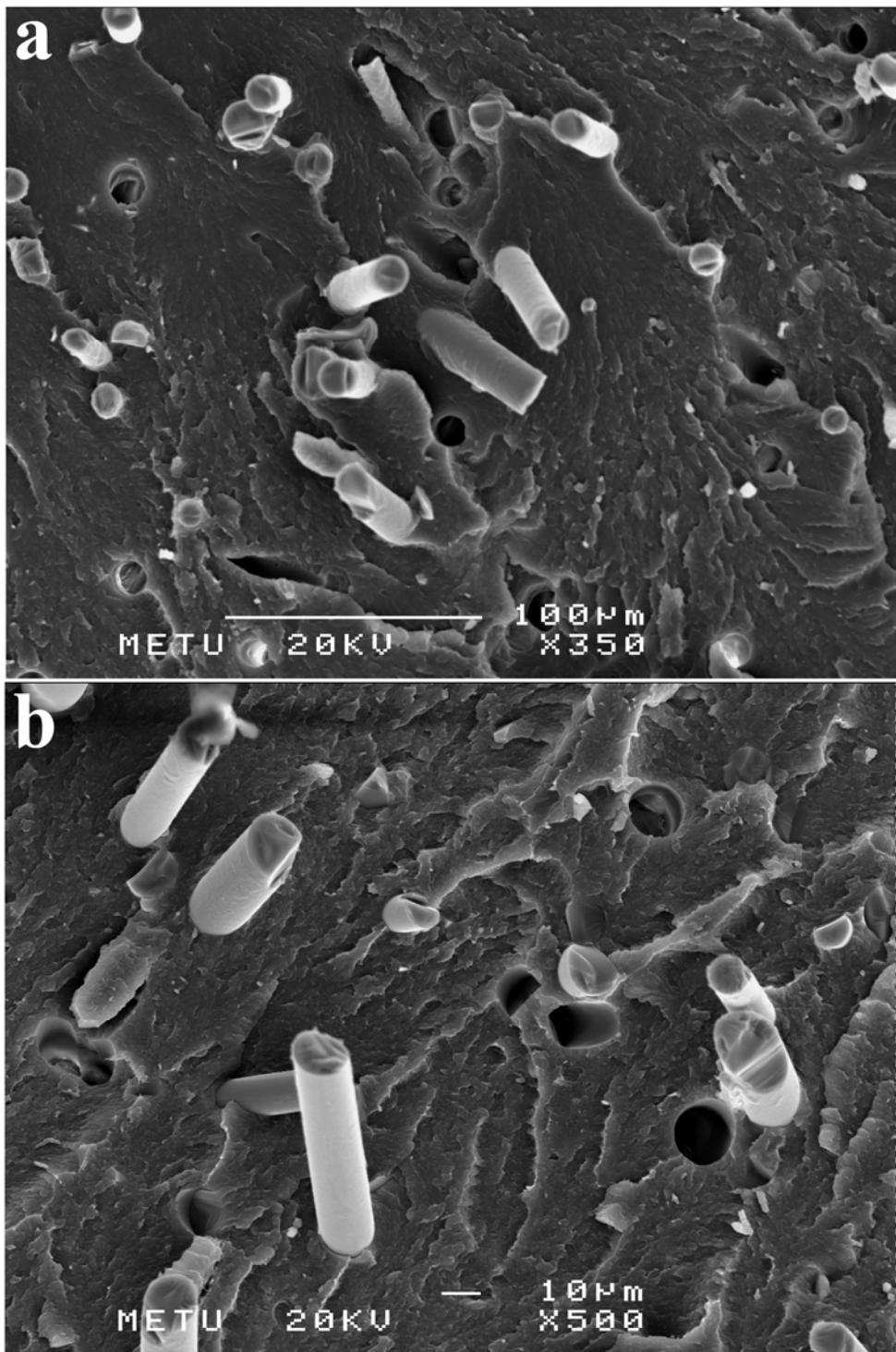


Figure 3.92 SEM images of the fracture surface morphologies of (a) PA/GF, and, (b) +NF composites

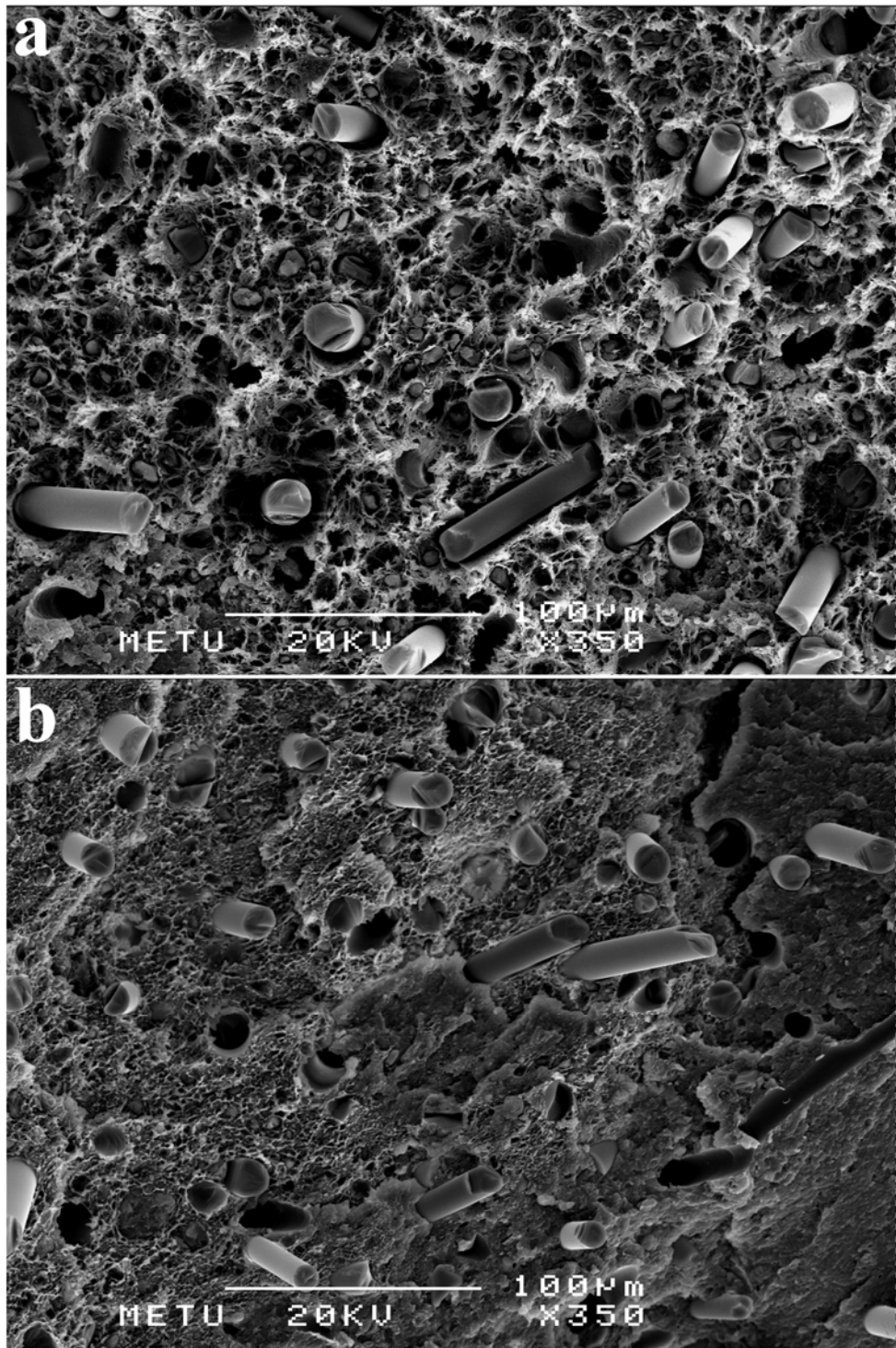


Figure 3.93 SEM images of the fracture surface morphologies of (a) +MF, and, (b) +MF/NF composites

Apparent degrees of polymer crystallinity were calculated by carrying out peak deconvolution of superimposed crystalline reflections and amorphous halo observed in XRD patterns (Figure 3.94). Crystalline peaks from montmorillonite and micro-filler, determined from reference XRD patterns for each, were neglected during the deconvolution procedure.

Polyamide 6 is known to crystallize predominantly in α - and γ - crystalline phases, depending on polymer processing conditions and presence of nucleating agents. Chains in the former phase are in extended conformation arranged in an anti-parallel manner. The latter phase has a parallel chain arrangement and amide groups on chains are rotated about 60° from the planar extended conformation. Crystallites of the α -phase are comprised of folded chains whereas those of γ -phase contain unfolded chains [166, 167]. Particularly, α -crystalline phase is known to be thermodynamically more stable, whereas γ -crystalline phase is kinetically favored [168].

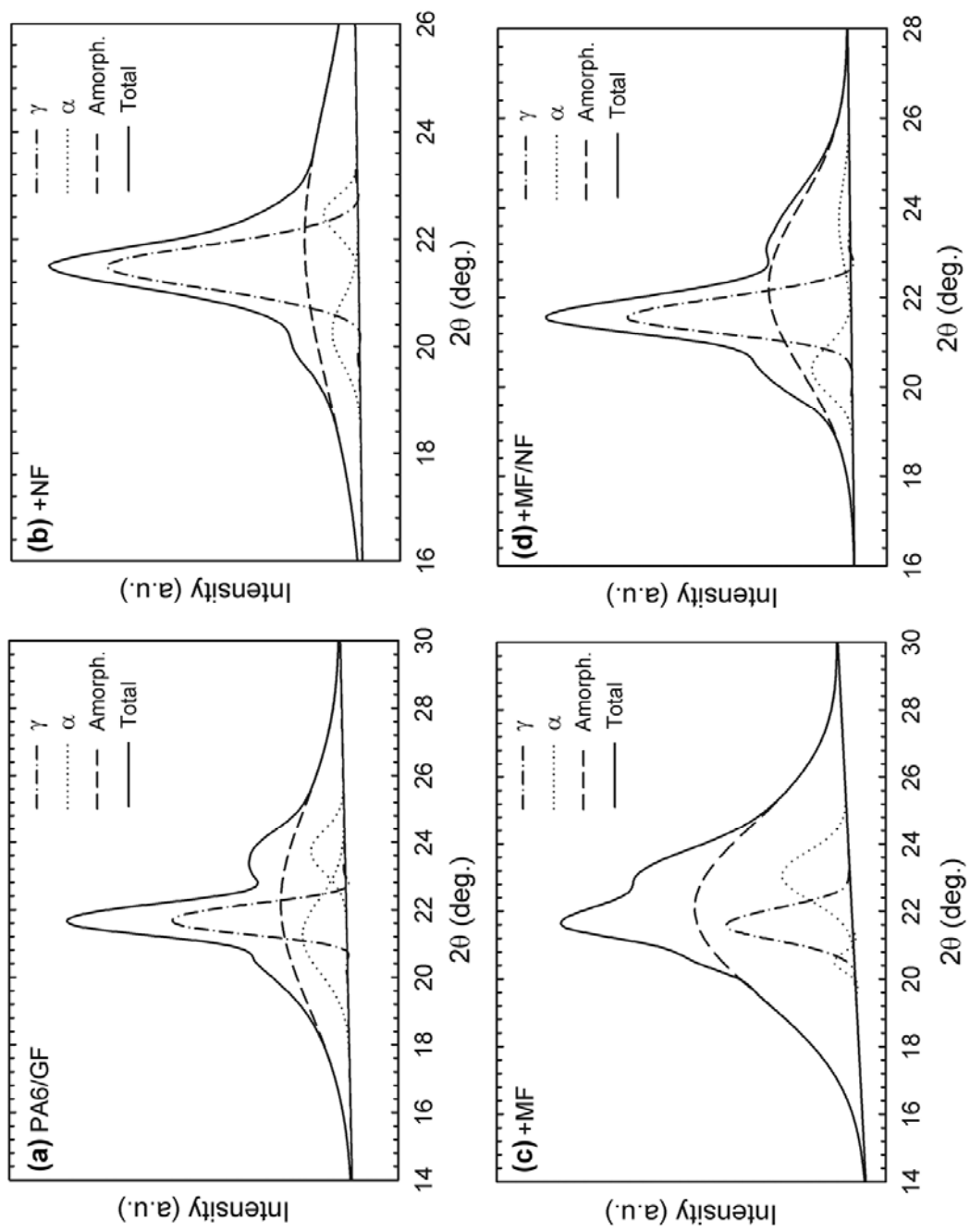


Figure 3.98 Deconvoluted XRD patterns using Gaussian peak profile and linear background; (a) PA6/GF, (b) +NF, (c) +MF, and, (d) +MF/NF

Table 3.25 summarizes the apparent degrees of crystallinity and relative amounts of crystalline phases in the composites. It is clear that the incorporation of the nano-filler in PA6/GF (+NF) and in +MF composites (+MF/NF) enhance crystallinity and favor the crystallization of γ -phase. The micro-filler is thought to impede crystallization either by reducing the segmental chain mobility or increasing the cooling rate during solidification. Interestingly, low degree of crystallinity in the case of +MF composite is completely recovered in the presence of nano-filler.

Promotion of overall crystallinity could be simply based on effective heterogeneous nucleation on large surface area clay layers. Most particularly, polymer chains are confined at the nano-scale, termed as nanoconfinement, between the well-oriented flat impenetrable clay walls with fine clay interlayer spacings in the nanocomposite (Figure 3.89). This plays a major role in hindering chain folding by lowering the conformational degree of freedom. In fact, polymer chains in the nanoconfined environment constitute the major fraction of the nanocomposite since an extremely large surface area of polymer-clay interaction is provided by the nano-dispersed, high aspect ratio clay layers. Crystallization is optimized in such a way that unfolded chain crystallites, characteristic of the γ -crystalline phase, are preferentially formed. Stabilization of the γ -phase in presence of nanoclays was shown by Lincoln et al. [166] depending on the fact that polymer did not undergo γ - to α - phase transformation upon annealing, and retained as γ -phase until melting.

Table 3.25 Degree of crystallinity and relative amounts of crystalline phases

	Degree of crystallinity (%)	γ -phase (%)	α -phase (%)
PA6/GF	41.8	48.9	51.1
+NF	47.8	78.3	21.7
+MF	21.9	52.7	47.3
+MF/NF	42.9	73.0	27.0

Fiber/matrix interfacial strength is a function of compressive residual stresses at fiber/matrix interface since other mechanisms such as primary bonding, hydrogen bonding and van der Waals interactions act less in polymer-inorganic fiber interactions. Accordingly, interfacial strength depends on factors such as thermal expansion mismatch between the glass fiber and polymer matrix in the vicinity of the glass fiber, and the amount of undercooling and rigidity below crystallization temperature [169]. An increase in the overall crystallinity enhances the trans-crystalline region in expense of the soft amorphous phase. Upon crystallization from melt, a highly rigid structure forms at the interfacial zone which cools and shrinks creating large compressive stresses on fibers compared to that would form by the contraction of amorphous matrix during cooling. Therefore, degree of polymer crystallinity has a remarkable influence on fiber/matrix interfacial strength, which was also explored in the literature [71, 165, 170].

Considering the estimated interfacial strength (Table 3.24) and degrees of crystallinity (Table 3.25), a strong correlation can be observed. The recovered degree of crystallinity in the presence of nano-filler, especially when +MF and +MF/NF are compared, recovers the poor fiber/matrix interface of +MF composite. Correlation of interfacial strength and degree of polymer crystallinity can be seen in Figure 3.95.

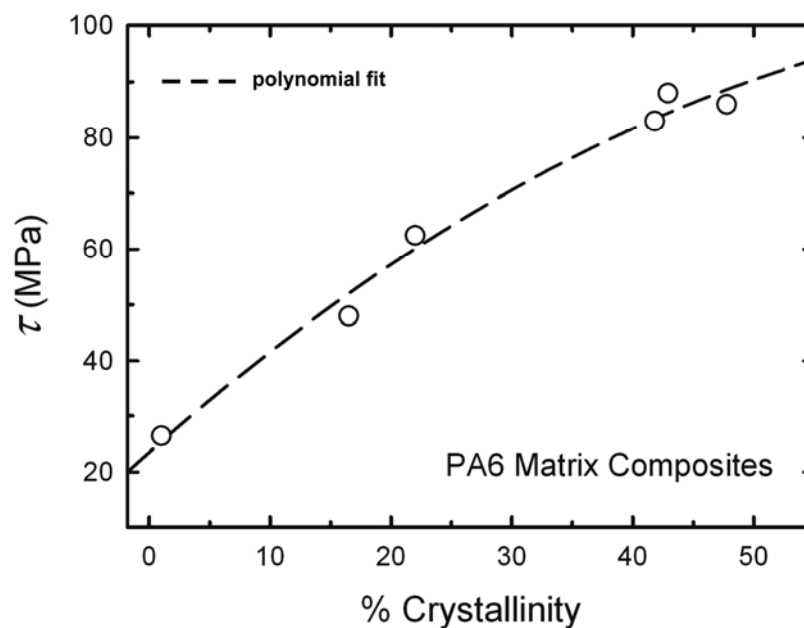


Figure 3.95 Variation of interfacial strength with degree of PA6 crystallinity

CHAPTER 4

CONCLUSIONS

Tremendous effort is being exerted both in the academic field and the plastics/additives industries on the development of novel environmentally friendly, halogen-free flame retarded polymer compounds that could outperform halogenated counterparts. In order to attain such high flame retardancy without halogenated additives, the current understanding is that it is essential to exploit synergistic fire retardancy arising between filler nanoparticles and halogen-free flame retardant additives.

Therefore, in this dissertation, a number of factors that influence the synergistic interactions of halogen-free flame retardant additives and nanofillers were investigated. Parameters such as nanofiller type, quality of nanofiller dispersion in the matrix, nanofiller geometry, and, the presence of short fiber reinforcement were evaluated in terms of nanocomposite morphology, flame retardancy, thermal stability and mechanical properties of flame retarded nanocomposites. In addition, it was also attempted to understand the role of nanofillers in fiber/matrix interactions in short fiber reinforced polymers containing flame retardant additives. The major conclusions drawn from each part of the dissertation are as follows.

(i) Effect of Nanofiller Type

- Nanocomposites were prepared based on neat PMMA and organophosphorus flame retarded PMMA with the incorporation of organically modified montmorillonite clay mineral (nanoclay) and multi-walled carbon nanotubes

as nanofillers of different types. An adequate dispersion technique specific to each nanofiller was utilized in order to achieve fine nano-scale filler dispersion in the polymer matrix.

- The organophosphorus flame retardant, consisting of aluminum diethylphosphinate, melamine polyphosphate and zinc borate, was found to act both in the condensed phase by intumescent char formation, and in the gas phase by dilution and flame inhibition mechanisms.
- The intumescent character of the organophosphorus flame retardant additive was restricted through the cage effect exerted by strong and continuous nanotube networks formed on the flaming surfaces at early stages during combustion, i.e. prior to initiation of intumescent charring. Consequently, a larger effective heat flux was encountered by the samples containing carbon nanotubes compared to those with nanoclay and without nanofillers.
- Contrary to the case with carbon nanotubes, nanoclays physically reinforced and consolidated the inorganic phosphate barriers without disrupting their intumescent character. Although nanoclay migration to the pyrolysis zone was apparent to some extent, the formed accumulate was not continuous and intact. Therefore, nanoclay accumulation on sample surface did not affect the viscosity of pyrolyzing melt and therefore did not hinder swelling of the char during combustion.
- Formulations with nanoclays were superior to those with carbon nanotubes as far as important mass loss calorimeter fire properties such as peak heat release rate, peak mass loss rate, fire residue and fire growth index are concerned.
- Critical degradation temperatures representing onset, halfway and maximum degradation were all shifted to higher temperatures with the incorporation of nanoclay and carbon nanotubes in neat- and flame retarded PMMA.

Nanofillers, particularly carbon nanotubes, had a remarkable effect on delaying the onset of degradation of organophosphorus flame retarded PMMA.

- Examining the differential thermogravimetric curves where three-stage degradation was observed, carbon nanotubes shifted maximum degradation temperature for the initial stage to a significantly higher temperature while nanoclays markedly decreased the mass loss corresponding to the initial stage with no apparent change in maximum degradation temperature. Incorporation of carbon nanotubes in flame retarded PMMA increased the mass loss corresponding to late stage degradation indicating that the amount of thermally stable products formed during the course of degradation was increased.
- Pyrolysis mass spectrometry revealed the evolution of diethylphosphinic acid, and melamine and its decomposition products from the organophosphorus additive. Considering organophosphorus flame retarded PMMA, the evolution of PMMA based products was almost identical to those recorded during the pyrolysis of neat PMMA. Depending on the appearance of new peaks in the recorded pyrograms, it is thought that the reactions between phosphinic acid and methyl ester groups of PMMA generated new products that with anhydride links leading to carbonization. Reactions between NH_2 groups of melamine and methacrylic acid units were shown to form isocyanic acid and products with unsaturated linkages.
- In the presence of nanoclay and carbon nanotubes, thermal decomposition pathway via random cleavages yielding also low mass oligomers was enhanced. The increased yield of products between PMMA and phosphinic acid or melamine is indicative of increased possibility of these reactions in nanocomposites.
- Nanoclay and carbon nanotubes did not impart significant changes in glass transition temperature of PMMA, but increased the heat capacity change

upon glass transition. Tensile strength of PMMA was adversely affected by both nanofillers due to increased brittleness caused by nanofiller agglomerates acting as stress concentration sites.

(ii) Effect of Nanofiller Dispersion

- High-power ultrasound assisted solution mixing and twin screw extrusion melt mixing techniques were used to disperse nanoclays in neat- and aluminum hydroxide flame retarded HIPS. In depth characterization of nanoclay dispersion by TEM and XRD revealed ultrasound assisted solution mixing provided intercalated nanocomposite formation and fine dispersion of nanofiller. Contrarily, phase-separated microcomposite morphology and poor dispersion of the nanofiller was seen for melt-mixed samples.
- Mass loss calorimeter fire tests indicated that intercalated nanocomposites considerably increase the amount of char residue, and provide remarkably larger reductions in the peak rates of heat release and mass loss compared to those obtained with phase-separated microcomposites. In conjunction with fire performance, intercalated nanocomposites demonstrated superior limiting oxygen index and lower burning rates.
- Higher performance of nanocomposites over microcomposites was attributed to the increases in carbonaceous char formation and retarded volatilization during combustion by the nanoconfinement and tortuous pathway effects of well-dispersed high aspect-ratio clay layers. Enhanced charring and condensed phase stabilization effect by organoclays was verified by infrared spectroscopy. Former allowed for the establishment of thicker and more consolidated protective carbonaceous layers that, in addition, contain collapsed montmorillonite particles and $\gamma\text{-Al}_2\text{O}_3$ phase from the decomposition of aluminum tri-hydroxide.

- Young's moduli were typically improved by 40–50% for both neat- and flame-retarded compounds with the use of nanoclay at a low loading level in the matrix. Intercalated nanocomposites allowed for the recovery of tensile strength reductions caused by high loadings of the conventional flame retardant additive which is incompatible with polymer matrix.

(iii) Effect of Nanofiller Geometry

- Aluminum diethylphosphinate flame retardant containing PLA compounds and corresponding nanocomposites with varying nanofiller geometries were produced by twin screw extrusion melt mixing process. Fumed silica was used as an iso-dimensional (0-D) nanofiller, halloysite and montmorillonite nanoclays were used as nano-rods (1-D) and nano-platelets (2-D), respectively.
- Transmission electron microscopy revealed homogenous dispersion of silica nanoparticles with some agglomeration and presence of halloysite particles almost completely as aggregates in the sub-micron scale. Characterization of montmorillonite nanocomposites by X-ray diffraction indicated that samples had a mixed intercalated/exfoliated nanomorphology.
- Incorporation of aluminum diethylphosphinate increases fire retardancy of PLA by improving the limiting oxygen index and UL-94 performance and reduces fire risks with lower peak heat release rate and peak mass loss rate in mass loss calorimeter fire tests. It was concluded that aluminum diethylphosphinate operates predominantly in the condensed phase by the formation of an intumescent aluminum phosphate fire residue.
- While 0-D and 1-D nanofillers provided no remarkable improvements in fire retardancy regarding fire parameters such as peak heat release rate, peak mass loss rate and fire growth index, the 2-D nanofiller enabled large reduction in fire risks, e.g. ~36% reduction in peak heat release rate compared to

conventional flame retarded PLA. Fire behavior was remarkably modified such that heat release and mass loss rates showed strongly suppressed plateaus owing to a pronounced condensed phase barrier effect of well-dispersed high aspect-ratio nanofiller.

- The mechanism underlying enhanced fire retardancy by 2-D nanofiller incorporation was explained by rapid migration and accumulation of aluminosilicate platelets on the exposed surface hindering subsequent intumescent char formation. Significantly larger montmorillonite interlayer space close to the exposed surface compared to the untested nanocomposite indicated that exfoliated layers were first to accumulate on exposed surface while intercalated montmorillonite particles reside in lower parts much below the exposed surface in the char. Rapid migration of exfoliated platelets facilitated the formation of a thick and rigid residue composed of aluminum phosphate microspheres reinforced at the nano-scale by montmorillonite platelets. This eventually helped establishing an effective barrier to heat and mass transfer as combustion proceeds.
- PLA containing aluminum diethylphosphinate showed a two-step degradation behavior, the first step corresponds to complete pyrolysis of PLA whereas the distinct second step occurs mainly due to the decomposition of aluminum diethylphosphinate. Nanoparticles did not alter the two step decomposition behavior apart from slightly increasing the degradation temperatures corresponding to 10% and 50% mass loss, and maximum degradation rate.
- Mechanical properties (tensile strength and Young's modulus) were enhanced in the order of 0-D < 1-D < 2-D nanofillers which directly match their effective aspect ratios in the nanocomposite.

(iv) Effect of Fiber Reinforcement

- Organoclay nanocomposites were prepared based on short glass fiber reinforced PA6 composites containing and organophosphorus flame retardant additive. Exfoliated morphology of nanocomposites was revealed by TEM and XRD.
- Flammability was increased in the presence of short glass fibers in PA6 matrix due to the candlewick effect. Substitution of a certain fraction of organophosphorus flame retardant by nanoclay provided significant peak heat release rate reductions and remarkably delayed ignition in the mass loss calorimeter fire tests while substantial improvements in limiting oxygen index were obtained together with maintained UL94 ratings.
- Thermogravimetric analysis on glass fiber reinforced composites showed that char yields of flame retarded nanocomposites were higher compared to conventional flame retarded formulations regarding materials with the same nominal filler content (nanofiller + flame retardant additive). This was explained by the preferential formation of aluminum phosphates as well as boron phosphates by the act of clay layers dispersed at the nano-scale, revealed by ATR-FTIR.
- Degradation of glass fiber reinforced composites shifted to lower temperatures in the presence of nanoclays as a result of the catalytic activity of protonic sites within clay galleries. Evolution of volatiles was retarded by the action of the tortuous pathway formed by exfoliated clay layers, confirmed by mass loss rates in thermogravimetry.
- Macro- and microscopic observation of short glass fiber containing fire residues ascribed the enhanced flame retardancy to the formation of mechanically strong, consolidated and crack-free protective char layers owing to the reinforcement of the char at the nano-scale by well-dispersed clay layers.

- Fire residues of flame retardant additive containing glass fiber reinforced nanocomposites were analyzed by XRD, ATR-FTIR and TEM and it was found that carbonaceous inorganic phosphate residues contained montmorillonite layers dispersed at the nano-scale without complete collapse of layers, i.e. nanocomposite residue formation was evident. An increase in organophosphorus flame retardant level shifted the residue nanomorphology from intercalated to exfoliated state. In the absence of the flame retardant additive, montmorillonite layers completely collapsed upon the volatilization of intra-gallery features.
- The incorporation of organophosphorus flame retardant and nanoclay improved the Young's modulus of short glass fiber reinforced PA6. Conversely, tensile strength is reduced with organophosphorus flame retardant addition as a consequence of poor interfacial interactions and consequent debonding at particle/matrix interface upon loading. At the same nominal filler content (nanofiller + flame retardant additive), nanocomposite formulations demonstrated higher Young's modulus and tensile strength.

(v) Interfacial Interactions

- Fiber/matrix interfacial strength was determined by a micromechanical approach to understand the influence of micro-filler (flame retardant additive) and nano-filler on the interfacial properties of short glass fiber reinforced composites based on amorphous and semi-crystalline thermoplastic matrices.
- Interfacial shear strength values estimated for short glass fiber reinforced HIPS are independent of fiber content. Besides fiber-fiber attrition, incorporation of micro- and nano-fillers into the polymer matrix induces additional fiber-filler attritions during twin-screw extrusion leading to the shift of residual fiber lengths to shorter values. While micro-filler was found to have no significant effect on interfacial strength, nano-filler modification reduced the IFSS which was explained by the limited post-processing thermal

contraction of polymer matrix due to fine dispersion of rigid, high-aspect ratio nanofiller both within bulk of the matrix and near fiber/matrix interfaces.

- Fiber/matrix interfacial strength in short glass fiber reinforced composites based on PA6, flame retarded PA6 and PA6/clay nanocomposite was studied. Despite the shorter fibers obtained in the fiber reinforced nanocomposite, fiber length efficiency was maintained owing to enhanced interfacial strength through promotion of polymer crystallization. Micro-filler reduced the degree of polymer crystallinity and resulted in the deterioration of the fiber/matrix interface. The incorporation of the nanofiller recovered the degree of crystallinity to a great extent which provided strengthening of the interface. Well-dispersed high aspect-ratio clay layers were found to act as effective heterogeneous nucleation sites owing to their smooth and large surfaces. PA6 chains in the nanoconfined environment in between well-oriented exfoliated clay layers solidified preferentially in the γ -crystalline form that was otherwise (in the absence of nanofiller) energetically not favored.

REFERENCES

- [1] Kawasumi M. "The discovery of polymer-clay hybrids" Journal of Polymer Science Part A: Polymer Chemistry (2004), 42;4:819-824.
- [2] Cho J.W., Paul D.R. "Nylon 6 nanocomposites by melt compounding" Polymer (2001), 42;3:1083-1094.
- [3] Fornes T.D., Yoon P.J., Hunter D.L., Keskkula H., Paul D.R. "Effect of organoclay structure on nylon 6 nanocomposite morphology and properties" Polymer (2002), 43;22:5915-5933.
- [4] Kaynak C., Tasan C.C. "Effects of production parameters on the structure of resol type phenolic resin/layered silicate nanocomposites" European Polymer Journal (2006), 42;8:1908-1921.
- [5] Ozkoc G., Bayram G., Quaedflieg M. "Effects of microcompounding process parameters on the properties of ABS/polyamide-6 blends based nanocomposites" Journal of Applied Polymer Science (2008), 107;5:3058-3070.
- [6] Ozkoc G., Bayram G., Tiesnitsch J. "Microcompounding of organoclay-ABS/PA6 blend-based nanocomposites" Polymer Composites (2008), 29;4:345-356.
- [7] Costache M.C., Heidecker M.J., Manias E., Camino G., Frache A., Beyer G., Gupta R.K., Wilkie C.A. "The influence of carbon nanotubes, organically modified montmorillonites and layered double hydroxides on the thermal degradation and fire retardancy of polyethylene, ethylene-vinyl acetate copolymer and polystyrene" Polymer (2007), 48;22:6532-6545.
- [8] Costache M.C., Jiang D.D., Wilkie C.A. "Thermal degradation of ethylene-vinyl acetate copolymer nanocomposites" Polymer (2005), 46;18:6947-6958.

- [9] Costache M.C., Wang D., Heidecker M.J., Manias E., Wilkie C.A. "The thermal degradation of poly(methyl methacrylate) nanocomposites with montmorillonite, layered double hydroxides and carbon nanotubes" Polymers for Advanced Technologies (2006), 17;4:272-280.
- [10] Jang B.N., Wilkie C.A. "The effect of clay on the thermal degradation of polyamide 6 in polyamide 6/clay nanocomposites" Polymer (2005), 46;10:3264-3274.
- [11] Kashiwagi T., Harris Jr R.H., Zhang X., Briber R.M., Cipriano B.H., Raghavan S.R., Awad W.H., Shields J.R. "Flame retardant mechanism of polyamide 6-clay nanocomposites" Polymer (2004), 45;3:881-891.
- [12] Morgan A.B. "Flame retarded polymer layered silicate nanocomposites: A review of commercial and open literature systems" Polymers for Advanced Technologies (2006), 17;4:206-217.
- [13] Zhu J., Morgan A.B., Lamelas F.J., Wilkie C.A. "Fire properties of polystyrene-clay nanocomposites" Chemistry of Materials (2001), 13;10:3774-3780.
- [14] Fornes T.D., Paul D.R. "Modeling properties of nylon 6/clay nanocomposites using composite theories" Polymer (2003), 44;17:4993-5013.
- [15] Tamura K., Yokoyama S., Pascua C.S., Yamada H. "New age of polymer nanocomposites containing dispersed high-aspect-ratio silicate nanolayers" Chemistry of Materials (2008), 20;6:2242-2246.
- [16] Iijima S. "Helical microtubules of graphitic carbon" Nature (1991), 354;6348:56-58.
- [17] Laoutid F., Bonnaud L., Alexandre M., Lopez-Cuesta J.M., Dubois P. "New prospects in flame retardant polymer materials: From fundamentals to nanocomposites" Materials Science and Engineering R: Reports (2009), 63;3:100-125.

- [18] Gao H.L., Hu S., Han H.C., Zhang J. "Effect of Different Metallic Hydroxides on Flame-Retardant Properties of Low Density Polyethylene/Melamine Polyphosphate/Starch Composites" Journal of Applied Polymer Science (2011), 122;5:3263-3269.
- [19] Wang Z.Y., Liu Y.A., Wang Q. "Flame retardant polyoxymethylene with aluminium hydroxide/melamine/novolac resin synergistic system" Polymer Degradation and Stability (2010), 95;6:945-954.
- [20] Liu Y.A., Wang Q. "The Investigation of Melamine Cyanurate-Encapsulating Magnesium Hydroxide Flame Retarded Polyamide-66" Polymers & Polymer Composites (2010), 18;6:253-258.
- [21] Wang Z.Z., Qu B.J., Fan W.C., Huang P. "Combustion characteristics of halogen-free flame-retarded polyethylene containing magnesium hydroxide and some synergists" Journal of Applied Polymer Science (2001), 81;1:206-214.
- [22] Cui W.G., Guo F., Chen J.F. "Preparation and properties of flame retardant high impact polystyrene" Fire Safety Journal (2007), 42;3:232-239.
- [23] Chang S.Q., Xie T.X., Yang G.S. "Effects of interfacial modification on the thermal, mechanical, and fire properties of high-impact polystyrene/microencapsulated red phosphorous" Journal of Applied Polymer Science (2008), 110;4:2139-2144.
- [24] Gunduz H.O. "Flame Retardancy of Polyamide Compounds and Nanocomposites" [M.S. Thesis]. Ankara: METU; 2009.
- [25] Camino G., Costa L., Trossarelli L. "Study of the mechanism of intumescence in fire retardant polymers: Part II-Mechanism of action in polypropylene-ammonium polyphosphate-pentaerythritol mixtures" Polymer Degradation and Stability (1984), 7;1:25-31.
- [26] Bourbigot S., Le Bras M., Duquesne S., Rochery M. "Recent advances for intumescent polymers" Macromolecular Materials and Engineering (2004), 289;6:499-511.

- [27] Xie F., Wang Y.Z., Yang B., Liu Y. "A novel intumescent flame-retardant polyethylene system" Macromolecular Materials and Engineering (2006), 291;3:247-253.
- [28] Isitman N.A., Gunduz H.O., Kaynak C. "Nanoclay synergy in flame retarded/glass fibre reinforced polyamide 6" Polymer Degradation and Stability (2009), 94;12:2241-2250.
- [29] Jang B.N., Wilkie C.A. "The thermal degradation of polystyrene nanocomposite" Polymer (2005), 46;9:2933-2942.
- [30] Wang J., Du J., Zhu J., Wilkie C.A. "An XPS study of the thermal degradation and flame retardant mechanism of polystyrene-clay nanocomposites" Polymer Degradation and Stability (2002), 77;2:249-252.
- [31] Kim S., Wilkie C.A. "Transparent and flame retardant PMMA nanocomposites" Polymers for Advanced Technologies (2008), 19;6:496-506.
- [32] Bourbigot S., Duquesne S., Fontaine G., Bellayer S., Turf T., Samyn F. "Characterization and Reaction to Fire of Polymer Nanocomposites with and without Conventional Flame Retardants" Molecular Crystals and Liquid Crystals (2008), 486:325/[1367]-1339/[1381].
- [33] Bourbigot S., Fontaine G. "Flame retardancy of polylactide: an overview" Polymer Chemistry (2010), 1;9:1413-1422.
- [34] Kashiwagi T., Du F., Winey K.I., Groth K.M., Shields J.R., Bellayer S.P., Kim H., Douglas J.F. "Flammability properties of polymer nanocomposites with single-walled carbon nanotubes: Effects of nanotube dispersion and concentration" Polymer (2005), 46;2:471-481.
- [35] Isitman N.A., Kaynak C. "Nanoclay and carbon nanotubes as potential synergists of an organophosphorus flame-retardant in poly(methyl methacrylate)" Polymer Degradation and Stability (2010), 95;9:1523-1532.

- [36] Schartel B., Potschke P., Knoll U., Abdel-Goad M. "Fire behaviour of polyamide 6/multiwall carbon nanotube nanocomposites" European Polymer Journal (2005), 41;5:1061-1070.
- [37] Kashiwagi T., Du F., Douglas J.F., Winey K.I., Harris Jr R.H., Shields J.R. "Nanoparticle networks reduce the flammability of polymer nanocomposites" Nature Materials (2005), 4;12:928-933.
- [38] Bourbigot S., Samyn F., Turf T., Duquesne S. "Nanomorphology and reaction to fire of polyurethane and polyamide nanocomposites containing flame retardants" Polymer Degradation and Stability (2010), 95;3:320-326.
- [39] Lu H., Wilkie C.A. "Synergistic effect of carbon nanotubes and decabromodiphenyl oxide/Sb₂O₃ in improving the flame retardancy of polystyrene" Polymer Degradation and Stability (2010), 95;4:564-571.
- [40] Du B., Guo Z., Fang Z. "Effects of organo-clay and sodium dodecyl sulfonate intercalated layered double hydroxide on thermal and flame behaviour of intumescent flame retarded polypropylene" Polymer Degradation and Stability (2009), 94;11:1979-1985.
- [41] Ye L., Wu Q., Qu B. "Synergistic effects and mechanism of multiwalled carbon nanotubes with magnesium hydroxide in halogen-free flame retardant EVA/MH/MWNT nanocomposites" Polymer Degradation and Stability (2009), 94;5:751-756.
- [42] Zhu H.F., Zhu Q.L., Li J.A., Tao K., Xue L.X., Yan Q. "Synergistic effect between expandable graphite and ammonium polyphosphate on flame retarded polylactide" Polymer Degradation and Stability (2011), 96;2:183-189.
- [43] Chen X.L., Yu J., Lu S.J., Wu H., Guo S.Y., Luo Z. "Combustion Characteristics of Polypropylene/Magnesium Hydroxide/Expandable Graphite Composites" Journal of Macromolecular Science Part B-Physics (2009), 48;6:1081-1092.

- [44] Du L.C., Zhang Y.C., Yuan X.Y., Chen J.Y. "Combustion Characteristics and Synergistic Effect of Halogen-Free Flame-Retarded EVA/Hydrotalcite Blends with Expandable Graphite and Fumed Silica" Polymer-Plastics Technology and Engineering (2009), 48;10:1002-1007.
- [45] Thirumal M., Khastgir D., Singha N.K., Manjunath B.S., Naik Y.P. "Effect of Expandable Graphite on the Properties of Intumescent Flame-Retardant Polyurethane Foam" Journal of Applied Polymer Science (2008), 110;5:2586-2594.
- [46] Nyambo C., Kandare E., Wang D., Wilkie C.A. "Flame-retarded polystyrene: Investigating chemical interactions between ammonium polyphosphate and MgAl layered double hydroxide" Polymer Degradation and Stability (2008), 93;9:1656-1663.
- [47] Manzi-Nshuti C., Hossenlopp J.M., Wilkie C.A. "Comparative study on the flammability of polyethylene modified with commercial fire retardants and a zinc aluminum oleate layered double hydroxide" Polymer Degradation and Stability (2009), 94;5:782-788.
- [48] Zhao C.-X., Liu Y., Wang D.-Y., Wang D.-L., Wang Y.-Z. "Synergistic effect of ammonium polyphosphate and layered double hydroxide on flame retardant properties of poly(vinyl alcohol)" Polymer Degradation and Stability (2008), 93;7:1323-1331.
- [49] Zhang G., Ding P., Zhang M., Qu B. "Synergistic effects of layered double hydroxide with hyperfine magnesium hydroxide in halogen-free flame retardant EVA/HFMH/LDH nanocomposites" Polymer Degradation and Stability (2007), 92;9:1715-1720.
- [50] Zhang M., Ding P., Qu B.J. "Flammable, Thermal, and Mechanical Properties of Intumescent Flame Retardant PP/LDH Nanocomposites With Different Divalent Cations" Polymer Composites (2009), 30;7:1000-1006.

- [51] Tai Q.L., Chen L.J., Song L., Hu Y.A., Yuen R.K.K. "Effects of a Phosphorus Compound on the Morphology, Thermal Properties, and Flammability of Polystyrene/MgAl-Layered Double Hydroxide Nanocomposites" Polymer Composites (2011), 32;2:168-176.
- [52] Ye L., Ding P., Zhang M., Qu B.J. "Synergistic effects of exfoliated LDH with some halogen-free flame retardants in LDPE/EVA/HFMH/LDH nanocomposites" Journal of Applied Polymer Science (2008), 107;6:3694-3701.
- [53] Vannier A., Duquesne S., Bourbigot S., Castrovinci A., Camino G., Delobel R. "The use of POSS as synergist in intumescent recycled poly(ethylene terephthalate)" Polymer Degradation and Stability (2008), 93;4:818-826.
- [54] Chigwada G., Jash P., Jiang D.D., Wilkie C.A. "Fire retardancy of vinyl ester nanocomposites: Synergy with phosphorus-based fire retardants" Polymer Degradation and Stability (2005), 89;1:85-100.
- [55] Laachachi A., Cochez M., Leroy E., Ferriol M., Lopez-Cuesta J.M. "Fire retardant systems in poly(methyl methacrylate): Interactions between metal oxide nanoparticles and phosphinates" Polymer Degradation and Stability (2007), 92;1:61-69.
- [56] Gallo E., Scharrel B., Acierno D., Russo P. "Flame retardant biocomposites: Synergism between phosphinate and nanometric metal oxides" European Polymer Journal In Press, Corrected Proof.
- [57] Cinausero N., Azema N., Lopez-Cuesta J.M., Cochez M., Ferriol M. "Synergistic effect between hydrophobic oxide nanoparticles and ammonium polyphosphate on fire properties of poly(methyl methacrylate) and polystyrene" Polymer Degradation and Stability (2011), 96;8:1445-1454.
- [58] Beyer G. "Flame Retardancy of Nanocomposites - from Research to Technical Products" Journal of Fire Sciences (2005), 23;1:75-87.

- [59] Hu Y., Wang S., Ling Z., Zhuang Y., Chen Z., Fan W. "Preparation and combustion properties of flame retardant Nylon 6/montmorillonite nanocomposite" Macromolecular Materials and Engineering (2003), 288;3:272-276.
- [60] Kiliaris P., Papaspyrides C.D., Pfaendner R. "Polyamide 6 filled with melamine cyanurate and layered silicates: Evaluation of flame retardancy and physical properties" Macromolecular Materials and Engineering (2008), 293;9:740-751.
- [61] Zhang J., Lewin M., Pearce E., Zammarano M., Gilman J.W. "Flame retarding polyamide 6 with melamine cyanurate and layered silicates" Polymers for Advanced Technologies (2008), 19;7:928-936.
- [62] Samyn F., Bourbigot S., Jama C., Bellayer S. "Fire retardancy of polymer clay nanocomposites: Is there an influence of the nanomorphology?" Polymer Degradation and Stability (2008), 93;11:2019-2024.
- [63] Zhang J., Jiang D.D., Wilkie C.A. "Fire properties of styrenic polymer-clay nanocomposites based on an oligomerically-modified clay" Polymer Degradation and Stability (2006), 91;2:358-366.
- [64] Yasmin A., Luo J.J., Abot J.L., Daniel I.M. "Mechanical and thermal behavior of clay/epoxy nanocomposites" Composites Science and Technology (2006), 66;14:2415-2422.
- [65] Cai G.P., Dasari A., Yu Z.Z., Du X.S., Dai S.C., Mai Y.W., Wang J.Y. "Fire response of polyamide 6 with layered and fibrillar nanofillers" Polymer Degradation and Stability (2010), 95;5:845-851.
- [66] Hapuarachchi T.D., Peijs T. "Multiwalled carbon nanotubes and sepiolite nanoclays as flame retardants for polylactide and its natural fibre reinforced composites" Composites Part a-Applied Science and Manufacturing (2010), 41;8:954-963.
- [67] Yang F., Nelson G.L. "Combination effect of nanoparticles with flame retardants on the flammability of nanocomposites" Polymer Degradation and Stability (2011), 96;3:270-276.

- [68] Bodzay B., Bocz K., Bárkai Z., Marosi G. "Influence of rheological additives on char formation and fire resistance of intumescent coatings" Polymer Degradation and Stability (2011), 96;3:355-362.
- [69] Zhao B., Hu Z., Chen L., Liu Y., Liu Y., Wang Y.Z. "A Phosphorus-Containing Inorganic Compound as an Effective Flame Retardant for Glass-Fiber-Reinforced Polyamide 6" Journal of Applied Polymer Science (2011), 119;4:2379-2385.
- [70] Isitman N.A., Gunduz H.O., Kaynak C. "Halogen-free Flame Retardants that Outperform Halogenated Counterparts in Glass Fiber Reinforced Polyamides" Journal of Fire Sciences (2010), 28;1:87-100.
- [71] Gunduz H.O., Isitman N.A., Aykol M., Kaynak C. "Interfacial Interactions and Flammability of Flame-Retarded and Short Fiber-Reinforced Polyamides" Polymer-Plastics Technology and Engineering (2009), 48;10:1046-1054.
- [72] Braun U., Bahr H., Sturm H., Schartel B. "Flame retardancy mechanisms of metal phosphinates and metal phosphinates in combination with melamine cyanurate in glass-fiber reinforced poly(1,4-butylene terephthalate): the influence of metal cation" Polymers for Advanced Technologies (2008), 19;6:680-692.
- [73] Zhao C.S., Huang F.L., Xiong W.C., Wang Y.Z. "A novel halogen-free flame retardant for glass-fiber-reinforced poly(ethylene terephthalate)" Polymer Degradation and Stability (2008), 93;6:1188-1193.
- [74] Liu Y., Deng C.L., Zhao J., Wang J.S., Chen L., Wang Y.Z. "An efficiently halogen-free flame-retardant long-glass-fiber-reinforced polypropylene system" Polymer Degradation and Stability (2011), 96;3:363-370.
- [75] Perret B., Schartel B., Stoss K., Ciesielski M., Diederichs J., Doring M., Kramer J., Altstadt V. "A New Halogen-Free Flame Retardant Based on 9,10-Dihydro-9-oxa-10-phosphaphenanthrene-10-oxide for Epoxy Resins and their Carbon Fiber Composites for the Automotive and Aviation Industries" Macromolecular Materials and Engineering (2011), 296;1:14-30.

- [76] Liu Y., Wang Q. "Melamine cyanurate-microencapsulated red phosphorus flame retardant unreinforced and glass fiber reinforced polyamide 66" Polymer Degradation and Stability (2006), 91;12:3103-3109.
- [77] Liu Y., Wang Q., Fei G.X., Chen Y.H. "Preparation of polyamide resin-encapsulated melamine cyanurate/melamine phosphate composite flame retardants and the fire-resistance to glass fiber-reinforced polyamide 6" Journal of Applied Polymer Science (2006), 102;2:1773-1779.
- [78] Chen Y.H., Wang Q. "Preparation, properties and characterizations of halogen-free nitrogen-phosphorous flame-retarded glass fiber reinforced polyamide 6 composite" Polymer Degradation and Stability (2006), 91;9:2003-2013.
- [79] Ferry L., Cuesta J.M.L., Chivas C., Hoy G.M., Dvir H. "Incorporation of a grafted brominated monomer in glass fiber reinforced polypropylene to improve the fire resistance" Polymer Degradation and Stability (2001), 74;3:449-456.
- [80] Pisanova E., Zhandarov S., Mader E., Ahmad I., Young R.J. "Three techniques of interfacial bond strength estimation from direct observation of crack initiation and propagation in polymer-fibre systems" Composites Part A: Applied Science and Manufacturing (2001), 32;3-4:435-443.
- [81] Desaegeer M., Verpoest I. "On the use of the micro-indentation test technique to measure the interfacial shear strength of fibre-reinforced polymer composites" Composites Science and Technology (1993), 48;1-4:215-226.
- [82] Marotzke C. "Influence of the fiber length on the stress transfer from glass and carbon fibers into a thermoplastic matrix in the pull-out test" Composite Interfaces (1993), 1:153-166.
- [83] Piggott M.R. "Failure Processes in the Fibre/Polymer Interphase" Composites Science and Technology (1991), 42;11:57-76.
- [84] Piggott M.R. "Why interface testing by single-fibre methods can be misleading" Composites Science and Technology (1997), 57;8:965-974.

- [85] Piggott M.R., Dai S.R. "Fiber pull out experiments with thermoplastics" Polymer Engineering and Science (1991), 31;17:1246-1249.
- [86] Piggott M.R., Reboredo M.M. "Durability of Kevlar-epoxy interfaces" Composite Interfaces (1995), 2;6:457-471.
- [87] Brandrup J., Immergut E.H., Grulke E.A. Polymer Handbook: John Wiley & Sons; 1999.
- [88] Samyn F., Bourbigot S., Jama C., Bellayer S., Nazare S., Hull R., Fina A., Castrovinci A., Camino G. "Characterisation of the dispersion in polymer flame retarded nanocomposites" European Polymer Journal (2008), 44;6:1631-1641.
- [89] Jash P., Wilkie C.A. "Effects of surfactants on the thermal and fire properties of poly(methyl methacrylate)/clay nanocomposites" Polymer Degradation and Stability (2005), 88;3:401-406.
- [90] Zhu J., Start P., Mauritz K.A., Wilkie C.A. "Thermal stability and flame retardancy of poly(methyl methacrylate)-clay nanocomposites" Polymer Degradation and Stability (2002), 77;2:253-258.
- [91] Jang B.N., Costache M., Wilkie C.A. "The relationship between thermal degradation behavior of polymer and the fire retardancy of polymer/clay nanocomposites" Polymer (2005), 46;24:10678-10687.
- [92] Beyer G. "Flame retardancy of nanocomposites based on organoclays and carbon nanotubes with aluminum trihydrate" Polymers for Advanced Technologies (2006), 17;4:218-225.
- [93] Braun U., Scharrel B., Fichera M.A., Jager C. "Flame retardancy mechanisms of aluminium phosphinate in combination with melamine polyphosphate and zinc borate in glass-fibre reinforced polyamide 6,6" Polymer Degradation and Stability (2007), 92;8:1528-1545.

- [94] Ramani A., Hagen M., Hereid J., Zhang J., Bakirtzis D., Delichatsios M. "Interaction of a phosphorus-based FR, a nanoclay and PA6-Part 1: Interaction of FR and nanoclay" Fire and Materials (2009), 33;6:273-285.
- [95] Petrella R.V. "The Assessment of Full-Scale Fire Hazards from Cone Calorimeter Data" Journal of Fire Sciences (1994), 12;1:14-43.
- [96] Ternane R., Cohen-Adad M.T., Boulon G., Florian P., Massiot D., Trabelsi-Ayedi M., Kbir-Ariguib N. "Synthesis and characterization of new oxyborapatite. Investigation of the ternary system CaO-P2O5-B2O3" Solid State Ionics (2003), 160;1-2:183-195.
- [97] Mekky W., Nicholson P.S. "Nano-aluminum-phosphate via a polymerized organic-inorganic complex route" Journal of Materials Processing Technology (2007), 190;1-3:393-396.
- [98] Avalos F., Ortiz J.C., Zitzumbo R., Lopez-Manchado M.A., Verdejo R., Arroyo M. "Phosphonium salt intercalated montmorillonites" Applied Clay Science (2009), 43;1:27-32.
- [99] Madejova J. "FTIR techniques in clay mineral studies" Vibrational Spectroscopy (2003), 31;1:1-10.
- [100] Kaynak C., Nakas G.I., Isitman N.A. "Mechanical properties, flammability and char morphology of epoxy resin/montmorillonite nanocomposites" Applied Clay Science (2009), 46;3:319-324.
- [101] Kashiwagi T., Inabi A., Hamins A. "Behavior of primary radicals during thermal degradation of poly(methyl methacrylate)" Polymer Degradation and Stability (1989), 26;2:161-184.
- [102] Manring L.E. "Thermal degradation of poly(methyl methacrylate). 4. Random side-group scission" Macromolecules (1991), 24;11:3304-3309.

- [103] Uyar T., Nur Y., Hacaloglu J., Besenbacher F. "Electrospinning of functional poly(methyl methacrylate) nanofibers containing cyclodextrin-menthol inclusion complexes." Nanotechnology (2009), 20;12:art. no. 125703.
- [104] Ferriol M., Gentilhomme A., Cochez M., Oget N., Mieloszynski J.L. "Thermal degradation of poly(methyl methacrylate) (PMMA): modelling of DTG and TG curves" Polymer Degradation and Stability (2003), 79;2:271-281.
- [105] Grady B.P., Paul A., Peters J.E., Ford W.T. "Glass transition behavior of single-walled carbon nanotube - Polystyrene composites" Macromolecules (2009), 42;16:6152-6158.
- [106] Morgan A.B., Harris J.D. "Exfoliated polystyrene-clay nanocomposites synthesized by solvent blending with sonication" Polymer (2004), 45;26:8695-8703.
- [107] Li Y., Ishida H. "Solution intercalation of polystyrene and the comparison with poly(ethyl methacrylate)" Polymer (2003), 44;21:6571-6577.
- [108] Zheng X., Wilkie C.A. "Nanocomposites based on poly (ε-caprolactone) (PCL)/clay hybrid: Polystyrene, high impact polystyrene, ABS, polypropylene and polyethylene" Polymer Degradation and Stability (2003), 82;3:441-450.
- [109] Wang D.Y., Liu Y., Wang Y.Z., Artiles C.P., Hull T.R., Price D. "Fire retardancy of a reactively extruded intumescent flame retardant polyethylene system enhanced by metal chelates" Polymer Degradation and Stability (2007), 92;8:1592-1598.
- [110] Chen K., Wilkie C.A., Vyazovkin S. "Nanoconfinement revealed in degradation and relaxation studies of two structurally different polystyrene-clay systems" Journal of Physical Chemistry B (2007), 111;44:12685-12692.
- [111] Bourbigot S., Gilman J.W., Wilkie C.A. "Kinetic analysis of the thermal degradation of polystyrene-montmorillonite nanocomposite" Polymer Degradation and Stability (2004), 84;3:483-492.

- [112] Morgan A.B., Harris Jr R.H., Kashiwagi T., Chyall L.J., Gilman J.W. "Flammability of polystyrene layered silicate (clay) nanocomposites: Carbonaceous char formation" Fire and Materials (2002), 26;6:247-253.
- [113] Miyagawa H., Drzal L.T. "The effect of chemical modification on the fracture toughness of montmorillonite clay/epoxy nanocomposites" Journal of Adhesion Science and Technology (2004), 18;13:1571-1588.
- [114] Pluart L.L., Duchet J., Sautereau H. "Epoxy/montmorillonite nanocomposites: Influence of organophilic treatment on reactivity, morphology and fracture properties" Polymer (2005), 46;26:12267-12278.
- [115] Crosby A.J., Lee J.Y. "Polymer nanocomposites: The "nano" effect on mechanical properties" Polymer Reviews (2007), 47;2:217-229.
- [116] Singh B. "Why does halloysite roll? - A new model" Clays and Clay Minerals (1996), 44;2:191-196.
- [117] Du M.L., Guo B.C., Jia D.M. "Newly emerging applications of halloysite nanotubes: a review" Polymer International (2010), 59;5:574-582.
- [118] Joussein E., Petit S., Churchman J., Theng B., Righi D., Delvaux B. "Halloysite clay minerals - A review" Clay Minerals (2005), 40;4:383-426.
- [119] Pack S., Si M., Koo J., Sokolov J.C., Koga T., Kashiwagi T., Rafailovich M.H. "Mode-of-action of self-extinguishing polymer blends containing organoclays" Polymer Degradation and Stability (2009), 94;3:306-326.
- [120] Pluta M. "Melt compounding of polylactide/organoclay: Structure and properties of nanocomposites" Journal of Polymer Science Part B-Polymer Physics (2006), 44;23:3392-3405.
- [121] Pluta M., Jeszka J.K., Boiteux G. "Polylactide/montmorillonite nanocomposites: Structure, dielectric, viscoelastic and thermal properties" European Polymer Journal (2007), 43;7:2819-2835.

- [122] Brehme S., Schartel B., Goebbels J., Fischer O., Pospiech D., Bykov Y., Döring M. "Phosphorus polyester versus aluminium phosphinate in poly(butylene terephthalate) (PBT): Flame retardancy performance and mechanisms" Polymer Degradation and Stability (2011), 96;5:875-884.
- [123] Braun U., Schartel B. "Flame retardancy mechanisms of aluminium phosphinate in combination with melamine cyanurate in glass-fibre-reinforced poly(1,4-butylene terephthalate)" Macromolecular Materials and Engineering (2008), 293;3:206-217.
- [124] Zammarano M., Gilman J.W., Nyden M., Pearce E.M., Lewin M. "The role of oxidation in the migration mechanism of layered silicate in poly(propylene) nanocomposites" Macromolecular Rapid Communications (2006), 27;9:693-696.
- [125] Endo T., Mortland M.M., Pinnavaia T.J. "Properties of Silica-Intercalated Hectorite" Clays and Clay Minerals (1981), 29;2:153-156.
- [126] Vaia R.A., Giannelis E.P. "Lattice model of polymer melt intercalation in organically-modified layered silicates" Macromolecules (1997), 30;25:7990-7999.
- [127] Bartholmai M., Schartel B. "Layered silicate polymer nanocomposites: New approach or illusion for fire retardancy? Investigations of the potentials and the tasks using a model system" Polymers for Advanced Technologies (2004), 15;7:355-364.
- [128] Lewin M., Zhang J., Pearce E., Gilman J. "Flammability of polyamide 6 using the sulfamate system and organo-layered silicate" Polymers for Advanced Technologies (2007), 18;9:737-745.
- [129] Shanmuganathan K., Deodhar S., Dembsey N., Fan Q., Calvert P.D., Warner S.B., Patra P.K. "Flame retardancy and char microstructure of nylon-6/layered silicate nanocomposites" Journal of Applied Polymer Science (2007), 104;3:1540-1550.
- [130] Schartel B., Hull T.R. "Development of fire-retarded materials - Interpretation of cone calorimeter data" Fire and Materials (2007), 31;5:327-354.

- [131] Levchik S.V., Weil E.D., Lewin M. "Thermal decomposition of aliphatic nylons" Polymer International (1999), 48;6-7:532-557.
- [132] Song L., Hu Y., Lin Z., Xuan S., Wang S., Chen Z., Fan W. "Preparation and properties of halogen-free flame-retarded polyamide 6/organoclay nanocomposite" Polymer Degradation and Stability (2004), 86;3:535-540.
- [133] Dasari A., Yu Z.Z., Mai Y.W., Cai G., Song H. "Roles of graphite oxide, clay and POSS during the combustion of polyamide 6" Polymer (2009), 50;6:1577-1587.
- [134] Morgan A.B., Chu L.L., Harris J.D. "A flammability performance comparison between synthetic and natural clays in polystyrene nanocomposites" Fire and Materials (2005), 29;4:213-229.
- [135] Scharrel B., Knoll U., Hartwig A., Putz D. "Phosphonium-modified layered silicate epoxy resins nanocomposites and their combinations with ATH and organo-phosphorus fire retardants" Polymers for Advanced Technologies (2006), 17;4:281-293.
- [136] Hornsby P.R., Wang J., Rother R., Jackson G., Wilkinson G., Cossick K. "Thermal decomposition behaviour of polyamide fire-retardant compositions containing magnesium hydroxide filler" Polymer Degradation and Stability (1996), 51;3:235-249.
- [137] Jahromi S., Gabrielse W., Braam A. "Effect of melamine polyphosphate on thermal degradation of polyamides: A combined X-ray diffraction and solid-state NMR study" Polymer (2002), 44;1:25-37.
- [138] Stoch L., Sroda M. "Infrared spectroscopy in the investigation of oxide glasses structure" Journal of Molecular Structure (1999), 511-512:77-84.
- [139] Holland B.J., Hay J.N. "Thermal degradation of nylon polymers" Polymer International (2000), 49;9:943-948.

- [140] Adame D., Beall G.W. "Direct measurement of the constrained polymer region in polyamide/clay nanocomposites and the implications for gas diffusion" Applied Clay Science (2009), 42;3-4:545-552.
- [141] Fu S.Y., Feng X.Q., Lauke B., Mai Y.W. "Effects of particle size, particle/matrix interface adhesion and particle loading on mechanical properties of particulate-polymer composites" Composites Part B: Engineering (2008), 39;6:933-961.
- [142] Bader M.G., Bowyer W.H. "The mechanical properties of thermoplastics strengthened by short discontinuous fibres" Journal of Physics D: Applied Physics (1972), 5:2215-2225.
- [143] Bowyer W.H., Bader M.G. "On the re-inforcement of thermoplastics by imperfectly aligned discontinuous fibres" Journal of Materials Science (1972), 7;11:1315-1321.
- [144] Fu S.Y., Lauke B. "Effects of fiber length and fiber orientation distributions on the tensile strength of short-fiber-reinforced polymers" Composites Science and Technology (1996), 56;10:1179-1190.
- [145] Fu S.Y., Yue C.Y., Hu X., Mai Y.W. "Characterization of fiber length distribution of short-fiber reinforced thermoplastics" Journal of Materials Science Letters (2001), 20;1:31-33.
- [146] Thomason J.L. "Micromechanical parameters from macromechanical measurements on glass reinforced polyamide 6,6" Composites Science and Technology (2001), 61:2007-2016.
- [147] Thomason J.L. "Micromechanical parameters from macromechanical measurements on glass-reinforced polybutyleneterephthalate" Composites Part A: Applied Science and Manufacturing (2002), 33;3:331-339.
- [148] Thomason J.L. "Interfacial strength in thermoplastic composites - at last an industry friendly measurement method?" Composites Part A: Applied Science and Manufacturing (2002), 33:1283-1288.

- [149] Sui G.X., Wong S.-C., Yang R., Yue C.Y. "The effect of fiber inclusions in toughened plastics - Part II: determination of micromechanical parameters" Composites Science and Technology (2005), 65;2:221-229.
- [150] Cox H.L. "The elasticity and strength of paper and other fibrous materials" British Journal of Applied Physics (1952), 3;3:72-79.
- [151] Kelly A., Tyson W.R. "Tensile Properties of Fibre-Reinforced Metals--Copper/Tungsten and Copper/Molybdenum" Journal of Mechanics and Physics of Solids (1965), 13;6:329-350.
- [152] Chin W.K., Liu H.T., Lee Y.D. "Effects of fiber length and orientation distribution on the elastic modulus of short fiber reinforced thermoplastics" Polymer Composites (1988), 9;1:27-35.
- [153] Fu S.Y., Mai Y.W., Ching E.C.Y., Li R.K.Y. "Correction of the measurement of fiber length of short fiber reinforced thermoplastics" Composites Part A: Applied Science and Manufacturing (2002), 33;11:1549-1555.
- [154] Ulrych F., Sova M., Vokrouhlecký J., Turcic B. "Empirical relations of the mechanical properties of polyamide 6 reinforced with short glass fibers" Polymer Composites (1993), 14;3:229-237.
- [155] Curtis P.T., Bader M.G., Bailey J.E. "The stiffness and strength of a polyamide thermoplastic reinforced with glass and carbon fibres" J Mater Sci (1978), 13:377-390.
- [156] Kornmann X., Rees M., Thomann Y., Necola A., Barbezat M., Thomann R. "Epoxy-layered silicate nanocomposites as matrix in glass fibre-reinforced composites" Composites Science and Technology (2005), 65;14:2259-2268.
- [157] Tsai J.L., Wu M.D. "Organoclay effect on mechanical responses of glass/epoxy nanocomposites" Journal of Composite Materials (2008), 42;6:553-568.

- [158] Bozkurt E., Kaya E., Tanoglu M. "Mechanical and thermal behavior of non-crimp glass fiber reinforced layered clay/epoxy nanocomposites" Composites Science and Technology (2007), 67;15-16:3394-3403.
- [159] Avila A.F., Morais D.T.S. "Modeling nanoclay effects into laminates failure strength and porosity" Composite Structures (2009), 87;1:55-62.
- [160] Vlasveld D.P.N., Bersee H.E.N., Picken S.J. "Nanocomposite matrix for increased fibre composite strength" Polymer (2005), 46;23:10269-10278.
- [161] Vlasveld D.P.N., Daud W., Bersee H.E.N., Picken S.J. "Continuous fibre composites with a nanocomposite matrix: Improvement of flexural and compressive strength at elevated temperatures" Composites Part A: Applied Science and Manufacturing (2007), 38;3:730-738.
- [162] Vlasveld D.P.N., Parlevliet P.P., Bersee H.E.N., Picken S.J. "Fibre-matrix adhesion in glass-fibre reinforced polyamide-6 silicate nanocomposites" Composites Part A: Applied Science and Manufacturing (2005), 36;1:1-11.
- [163] Akkapeddi M.K. "Glass fiber reinforced polyamide-6 nanocomposites" Polymer Composites (2000), 21;4:576-585.
- [164] Wu S.H., Wang F.Y., Ma C.C., Chang W.C., Kuo C.T., Kuan H.C., Chen W.J. "Mechanical, thermal and morphological properties of glass fiber and carbon fiber reinforced polyamide-6 and polyamide-6/clay nanocomposites" Materials Letters (2001), 49;6:327-333.
- [165] Cartledge H.C.Y., Baillie C.A. "Studies of microstructural and mechanical properties of Nylon/Glass composite: Part II The effect of microstructures on mechanical and interfacial properties" Journal of Materials Science (1999), 34;20:5113-5126.
- [166] Lincoln D.M., Vaia R.A., Wang Z.G., Hsiao B.S., Krishnamoorti R. "Temperature dependence of polymer crystalline morphology in nylon 6/montmorillonite nanocomposites" Polymer (2001), 42;25:9975-9985.

[167] Ramesh C., Bhoje Gowd E. "High-temperature X-ray diffraction studies on the crystalline transitions in the \hat{I}^{\pm} - and \hat{I}^3 -forms of nylon-6" Macromolecules (2001), 34;10:3308-3313.

[168] Murthy N.S. "Hydrogen bonding, mobility, and structural transitions in aliphatic polyamides" Journal of Polymer Science, Part B: Polymer Physics (2006), 44;13:1763-1782.

[169] Nairn J.A. "Thermoelastic analysis of residual stresses in unidirectional, high-performance composites" Polymer Composites (1985), 6;2:123-130.

[170] Li L., Li B., Tang F. "Influence of maleic anhydride-grafted EPDM and flame retardant on interfacial interaction of glass fiber reinforced PA-66" European Polymer Journal (2007), 43;6:2604-2611.

CURRICULUM VITAE

Nihat Ali İŞİTMAN

Research/Teaching Assistant

Dept. of Metallurgical and Materials Engineering
Polymers and Nanocomposites Laboratory
Middle East Technical University
Ankara / Turkey

PERSONAL INFORMATION

Date of Birth : **May 10, 1985**
Tel : **+90 533 339 5956**
E-mail : **aisitman@metu.edu.tr ; ali.isitman@gmail.com**
Web : **www.metu.edu.tr/~aisitman ; www.metu.edu.tr/~e134661**

EDUCATION

2006 - 2012 **Ph.D. on B.S. Metallurgical and Materials Engineering,**
Middle East Technical University
▪ Highest GPA (3.96/4.00), Course Performance Award
▪ Thesis title: “*Flame Retardancy of Polymer Nanocomposites*”
Thesis Advisor: Prof. Dr. Cevdet Kaynak

2002 – 2006 **B.S. Metallurgical and Materials Engineering,**
Middle East Technical University
▪ Highest GPA (3.73/4.00), High Honor Degree

ACADEMIC EXPERIENCE

2006 – 2011 **Research / Teaching Assistant**
Dept. of Metallurgical and Materials Engineering, METU

2009 – 2011 **Project Assistant**
▪ “*Widespread Utilization of Turkish Boron Compounds as Flame Retardant Additives in Plastics and Composites*”
National Boron Research Institute (BOREN)

2007 – 2009 **Project Assistant**
▪ “*Development of High Flame Retardancy Carbon Nanotube and Clay Reinforced Polymer Nanocomposites*”
The Scientific and Technological Research Council of Turkey (TUBITAK-1001)

ACADEMIC HONORS AND AWARDS

- Young Researcher Award
15th International Metallurgy and Materials Congress, 2010
- Plastics Technology Research Award
Turkish Plastics Industry Association, 2010
- Highest CGPA (3.96 / 4.00) in Ph.D. on B.S. Program, 2009
- Integrated Ph.D. Performance Award, 2009
- Highest CGPA (3.73 / 4.00) in B.S., 2006
- High Honor in Seven Semesters of B.S., 2002 – 2006

SPECIAL SKILLS

- Polymer Processing
 - ✓ Twin Screw Extrusion
 - ✓ Injection and Compression Molding
- Thermal Analysis
- Materials Characterization
 - ✓ Advanced Scanning Electron Microscopy
 - ✓ X-Ray Diffraction
 - ✓ Transmission Electron Microscopy Sample Preparation
- Mechanical Testing
 - ✓ Tension, Bending, Compression and Impact Tests
- Wet Chemical Techniques
 - ✓ Solution Processing, Functionalization, Viscometry
 - ✓ Planetary Ball-milling
- Scientific Software
 - ✓ Rigaku, OPUS, Instron, SigmaPlot, PeakFit, Mathematica

JOURNAL PUBLICATIONS

SCI Articles Directly Related to PhD Thesis

1. **N.A. Isitman**, M. Dogan, E. Bayramli and C. Kaynak, "Role of Filler Nanoparticle Geometry in Fire Retardancy: Organophosphorus Flame-Retardant Polylactide Nanocomposites", (submitted, under review)
2. T. Orhan, **N.A. Isitman**, J. Hacaloglu, and C. Kaynak, "Thermal Degradation Mechanism of Organophosphorus Flame-Retardant Poly(methyl methacrylate) Nanocomposites Containing Nanoclay and Carbon Nanotubes", *Polymer Degradation and Stability*, 97 (3), 273-280 (March 2012)
3. **N.A. Isitman**, M. Aykol, and C. Kaynak, "Interactions at Fiber/Matrix Interface in Short Fiber Reinforced HIPS Composites Modified with Micro- and Nano-Fillers", *Journal of Materials Science*, 47 (2), 702-710 (January 2012)
4. **N.A. Isitman** and C. Kaynak, " Nanostructure of Montmorillonite Barrier Layers: A New Insight into the Mechanism of Flammability Reduction in Polymer Nanocomposites ", *Polymer Degradation and Stability*, 96 (12), 2284-2289 (December 2011)
5. T. Orhan, **N.A. Isitman**, J. Hacaloglu, and C. Kaynak, "Thermal Degradation Mechanisms of Aluminium Phosphinate, Melamine Polyphosphate and Zinc Borate in Poly(methyl methacrylate)", *Polymer Degradation and Stability* 96 (10), 1780-1787 (October 2011)
* This article was featured in SciVerse ScienceDirect Top25 Hottest Articles under Materials Science, Polymer Degradation and Stability.
6. **N.A. Isitman** and C. Kaynak, "Tailored Flame Retardancy via Nanofiller Dispersion State: Synergistic Action Between a Conventional Flame-Retardant and Nanoclay in High-Impact Polystyrene", *Polymer Degradation and Stability* 95 (9), 1759-1768 (September 2010)
* This article was featured in SpecialChem R&D Highlights.

7. **N.A. Isitman** and C. Kaynak , “Nanoclay and Carbon Nanotubes as Potential Synergists of an Organophosphorus Flame-Retardant in Poly(Methyl Methacrylate)”, *Polymer Degradation and Stability* 95 (9), 1523-1532 (September 2010)
* This article was featured in SciVerse ScienceDirect Top25 Hottest Articles under Materials Science, Polymer Degradation and Stability.
8. **N.A. Isitman**, M. Aykol, and C. Kaynak, “Nanoclay Assisted Strengthening of the Fiber/Matrix Interface in Functionally Filled Polyamide 6 Composites”, *Composite Structures* 92 (9), 2181-2186 (August 2010)
9. **N.A. Isitman** and M. Aykol, “Continuum Micro-mechanics of Estimating Interfacial Shear Strength in Short Fiber Composites”, *Composite Interfaces* 17 (1), 49-58 (January 2010)
10. **N.A. Isitman**, H.O. Gunduz and C. Kaynak, “Nanoclay Synergy in Flame Retarded / Glass Fiber Reinforced Polyamide 6”, *Polymer Degradation and Stability* 94 (12), 2241 -2250 (December 2009)
* This article was featured in SciVerse ScienceDirect Top25 Hottest Articles under Materials Science, Polymer Degradation and Stability.

Other SCI Articles in the Subject Area

11. H. Balakrishnan, A. Hassan, **N.A. Isitman** and C. Kaynak, “On the Use of Magnesium Hydroxide Towards Halogen-Free Flame-Retarded Polyamide-6/Polypropylene Blends”, (submitted, under review)
12. **N.A. Isitman** and C. Kaynak, “Combinations of Aluminum Hydroxide and Hydrated Calcium Borate Towards Low Density Polyethylene with Improved Flame Retardancy”, (submitted, under review)

13. **N.A. Isitman**, B.M. Sipahioglu and C. Kaynak, “Nanomorphology and Fire Behaviour of Polystyrene/Organoclay Nanocomposites Containing Brominated Epoxy and Antimony Oxide”, *Polymers for Advanced Technologies*, (accepted for publication, available online)
14. C. Kaynak and **N.A. Isitman**, “Synergistic Fire Retardancy of Colemanite, A Natural Hydrated Calcium Borate, in High-Impact Polystyrene Containing Brominated Epoxy and Antimony Oxide”, *Polymer Degradation and Stability* 96 (5), 798-807 (May 2011)
15. **N.A. Isitman**, M. Dogan, E. Bayramli and C. Kaynak, “Fire Retardant Properties of Intumescent Polypropylene Composites Filled with Calcium Carbonate”, *Polymer Engineering & Science* 51 (5), 875-883 (May 2011)
16. C. Kaynak, H.O. Gunduz and **N.A. Isitman**, “Use of Nanoclay as an Environmentally Friendly Flame Retardant Synergist in Polyamide-6”, *Journal of Nanoscience and Nanotechnology* 10 (11), 7374-7377 (November 2010)
17. **N.A. Isitman**, M. Aykol, G. Ozkoc, G. Bayram, and C. Kaynak , “Interfacial Strength in Short Glass Fiber Reinforced Acrylonitrile-Butadiene-Styrene / Polyamide 6 Blends”, *Polymer Composites* 31 (3), 392-398 (March 2010)
18. **N.A. Isitman**, H.O. Gunduz and C. Kaynak, “Halogen-Free Flame Retardants That Outperform Halogenated Counterparts in Glass Fiber Reinforced Polyamides”, *Journal of Fire Sciences* 28 (1), 87-100 (January 2010)
19. C. Kaynak, G.I. Nakas and **N.A. Isitman**, “Mechanical Properties, Flammability and Char Morphology of Epoxy Resin / Montmorillonite Nanocomposites”, *Applied Clay Science* 46 (3) , 319 -324 (November 2009)
20. H.O. Gunduz, **N.A. Isitman**, M. Aykol, and C. Kaynak, “Interfacial Interactions and Flammability of Flame Retarded and Short Fiber Reinforced Polyamides”, *Polymer-Plastics Technology and Engineering* 48 (10), 1046 -1054 (October 2009)

21. C. Kaynak, E. Akgul and N.A. **Isitman**, “Effects of RTM Mold Temperature and Vacuum On the Mechanical Properties of Epoxy/Glass Fiber Composite Plates”, *Journal of Composite Materials* 42 (15), 1505-1521 (July 2008)
22. M. Aykol, N.A. **Isitman**, E. Firlar and C. Kaynak, “Strength of Short Fiber Reinforced Polymers: Effect of Fiber Length Distribution”, *Polymer Composites* 29 (6), 644-648 (June 2008)

Invited Papers

1. N. A. **Isitman**, M. Dogan, E. Bayramli, and C.Kaynak, "Is calcium carbonate still reasonable as cheap and inert filler?", *SPE Plastics Research Online*, 10.1002/spepro.003569
2. N.A. **Isitman** and C. Kaynak, “Yangına Direnen Polimerler”, *TÜBİTAK Bilim ve Teknik*, 512 (92-95), (July 2010); in Turkish.

Conference Proceedings / Abstracts

1. N.A. **Isitman**, F. Unlu, C. Kaynak, “Use of Colemanite as a Synergistic Fire Retardant Additive in High Impact Polystyrene/Brominated Epoxy Oligomer/Antimony Oxide Compounds”, **Book of Abstracts of the International Symposium Boron, Borides and Related Materials**, Istanbul, Turkey (11-17 September 2011)
2. C. Kaynak and N.A. **Isitman**, “Flame Retardancy Synergism by Using Aluminum Tri-Hydroxide (ATH) and Nanoclay in High-Impact Polystyrene (HIPS)”, **Extended Abstracts of the SPE Society of Plastics Engineers ASIATEC 2011 Conference**, SPE Japan Section, Tokyo , 2 pages on CD , (15-17 February 2011)

3. **N. A. Isitman** and C. Kaynak, “Do Filler Nanoparticles Always Act as Synergists in Flame Retardant Polymers? Investigations on Potentials of Functionally - filled Novel Polymer Nanocomposites”, **Book of Abstracts of the Materials Research Society MRS 2010 Fall Meeting**, Boston, USA (29 November - 3 December 2010)
4. **N. A. Isitman** and C. Kaynak, “Tailored Flame Retardancy via Nano - filler Dispersion State: Nanomorphology and Reaction to Fire of High - impact Polystyrene/Aluminum Tri - Hydroxide/Organoclay Nanocomposites”, **Book of Abstracts of the Materials Research Society MRS 2010 Fall Meeting**, Boston, USA (29 November - 3 December 2010)
5. **N.A. Isitman**, C. Kaynak, “*Applied Interfacial Strength Estimations in Short Fiber Reinforced Composites*”, **e-Proceedings of the 13. International Materials Symposium – IMSP 2010**, Pamukkale University, Denizli/Turkey, 6 pages on CD (13-15 October 2010)
6. **N.A. Isitman**, H.O. Gunduz, B.M. Kuscuoglu, C. Kaynak, “*High Flame Retardancy Carbon Nanotube and Clay Reinforced Polymer Nanocomposites*”, **e-Proceedings of the 15. International Metallurgy-Materials Congress - IMMC 2010**, UCTEA Chamber of Metallurgical Engineers, Istanbul/Turkey, 8 pages on CD (11-13 November 2010)
7. **C. Kaynak** and **N.A. Isitman**, “*Effects of Nanoclays and Carbon Nanotubes on the Flame Retardancy of Poly(methyl methacrylate)*”, **Book of Abstracts of the 10. International Conference on Nanostructured Materials – NANO 2010**, Rome, Italy (13-17 September 2010)
8. H.O. Gunduz, **N.A. Isitman** and **C. Kaynak**, “*Influences of Nanoclays on the Flammability Behaviour of Polyamide Compounds*”, **Book of Abstracts of the 7. International Conference on Nanosciences & Nanotechnologies – NN 2010**, Ouranopolis Halkidiki, Greece (11-14 July 2010)

9. **N.A. Isitman**, C. Kaynak, “*Improvement of the Nanomorphology and Nanodispersion in Polymer Nanocomposites*”, **e-Proceedings of the 9. National Chemical Engineering Conference**, Gazi University, Ankara/Turkey, 4 pages on CD (22-25 June 2010)

10. **N.A. Isitman** and C. Kaynak, “*Functionally Filled Polymer Nanocomposites: A Novel Class of Flame-Retardant Materials*”, **Book of Abstracts of the 6. Nanoscience and Nanotechnology Conference – NANO TR-VI** , Izmir Institute of Technology, Izmir, Turkey (15-18 June 2010)

11. **N.A. Isitman** and C. Kaynak, “*Tailoring the Interfacial Properties and Flame Retardancy of Polymer/Short-Fiber Composites through a Reinforcement at Nano-Scale*”, **Book of Abstracts of the 14. European Conference on Composite Materials**, Budapest, Hungary (7-10 June 2010)

12. **N.A. Isitman**, C. Kaynak, “*Nanoclay Assisted Strengthening of the Fiber/Matrix Interface in Functionally Filled Polyamide-6 Composites*”, e-Proceedings of the **3. National Polymer Science and Technology Conference**, Kocaeli University, Kocaeli/Turkey, 7 pages on CD (12-14 May 2010)

13. **N.A. Isitman**, G.I. Nakas, C. Kaynak, “*Improved Flame Retardancy and Mechanical Properties with organically modified Montmorillonite / Polymer Nanocomposites*”, **Proceedings Book of the 14. National Clay Symposium**, pages 794-800, Karadeniz Technical University, Trabzon/Turkey (1-3 October 2009)

14. H.O. Gunduz, **N.A. Isitman** and C. Kaynak, “*Use of Nanoclays as an Environmentally Friendly Flame Retardant Synergist in Polyamide*”, **Book of Abstracts of the International Conference on Nanoscience and Technology – ChinaNANO 2009**, pp 36, Beijing, China (1-3 September 2009)

15. **N.A. Isitman**, C. Kaynak and M. Aykol, “*Applied Interfacial Strength Estimations in Reinforced Polymers*” , **e-Proceedings of the 15. International Conference on Composite Structures – ICCS 15** , 2 pages on CD, Porto, Portugal (15-17 June 2009)
16. **N.A. Isitman**, C. Kaynak and H.O. Gunduz, “*Flame Retardancy of Polyamide 6 and 6.6*”, **Book of Abstracts of the European Polymer Congress – EPF 2009** , pp 198, Graz, Austria (12-17 July 2009)
17. **E. Akgul**, C. Kaynak, **N.A. Isitman**, “*Effects of Mold Temperature, Resin Temperature and Vacuum on the Resin Transfer Molding (RTM) Process*”, **e-Proceedings of the 14th International Metallurgy-Materials Congress - IMMC 2008**, UCTEA Chamber of Metallurgical Engineers, Istanbul , pp: 267 - 276 , (16-18 October 2008)
18. **N.A. Isitman**, M. Aykol, C. Kaynak, “*Effect of Fiber Length Distribution on Theoretical Strength of Short Fiber Reinforced Polymer Composites*”, **e-Proceedings of the 2. National Polymer Science and Technology Conference**, Harran University, Sanlurfa/Turkey, 3 pages on CD (30 April - 2 May 2008)

MEMBERSHIPS

- Society of Plastics Engineers (SPE)
- Materials Research Society (MRS)

REFEREEING

- Polymers for Advanced Technologies (Wiley)
- Composite Structures (Elsevier)
- Composite Interfaces (Brill)
- Materials Science and Engineering B (Elsevier)

CITATIONS (ISI WEB OF KNOWLEDGE)

ARTICLE	Times Cited
N.A. Isitman, H.O. Gunduz and C. Kaynak, “ <i>Nanoclay Synergy in Flame Retarded / Glass Fiber Reinforced Polyamide 6</i> ”, Polymer Degradation and Stability 94 (12) , 2241 -2250 (December 2009)	23
C. Kaynak, G.I. Nakas and N.A. Isitman, “Mechanical Properties, Flammability and Char Morphology of Epoxy Resin / Montmorillonite Nanocomposites”, Applied Clay Science 46 (3) , 319 -324 (November 2009)	10
H.O. Gunduz, N.A. Isitman, M. Aykol, and C. Kaynak, “ <i>Interfacial Interactions and Flammability of Flame Retarded and Short Fiber Reinforced Polyamides</i> ”, Polymer-Plastics Technology and Engineering 48 (10) , 1046 -1054 (October 2009)	9
M. Aykol, N.A. Isitman, E. Firlar and C. Kaynak, “ <i>Strength of Short Fiber Reinforced Polymers: Effect of Fiber Length Distribution</i> ”, Polymer Composites 29 (6), 644-648 (June 2008)	6
N.A. Isitman and C. Kaynak, “Tailored Flame Retardancy via Nanofiller Dispersion State: Synergistic Action Between a Conventional Flame-Retardant and Nanoclay in High-Impact Polystyrene”, Polymer Degradation and Stability 95 (9), 1759-1768 (September 2010)	5
N.A. Isitman and C. Kaynak , “Nanoclay and Carbon Nanotubes as Potential Synergists of an Organophosphorus Flame-Retardant in Poly(Methyl Methacrylate)”, Polymer Degradation and Stability 95 (9), 1523-1532 (September 2010)	4
N.A. Isitman, M. Aykol, and C. Kaynak, “Nanoclay Assisted Strengthening of the Fiber/Matrix Interface in Functionally Filled Polyamide 6 Composites”, Composite Structures 92 (9), 2181-2186 (August 2010)	3
C. Kaynak, H.O. Gunduz and N.A. Isitman, “Use of Nanoclay as an Environmentally Friendly Flame Retardant Synergist in Polyamide-6”, Journal of Nanoscience and Nanotechnology 10 (11), 7374-7377 (November 2010)	3
N.A. Isitman, H.O. Gunduz and C. Kaynak, “Halogen-Free Flame Retardants That Outperform Halogenated Counterparts in Glass Fiber Reinforced Polyamides”, Journal of Fire Sciences 28 (1), 87-100 (January 2010)	2
C. Kaynak, E. Akgul and N.A. Isitman “ <i>Effects of RTM Mold Temperature and Vacuum On the Mechanical Properties of Epoxy/Glass Fiber Composite Plates</i> ”, Journal of Composite Materials 42 (15), 1505-1521 (July 2008)	1
N.A. Isitman, M. Aykol, G. Ozkoc, G. Bayram, and C. Kaynak , “Interfacial Strength in Short Glass Fiber Reinforced Acrylonitrile-Butadiene-Styrene / Polyamide 6 Blends”, Polymer Composites 31 (3), 392-398 (March 2010)	1
N.A. Isitman and M. Aykol, “Continuum Micro-mechanics of Estimating Interfacial Shear Strength in Short Fiber Composites”, Composite Interfaces 17 (1), 49-58 (January 2010)	1
TOTAL	68